

Annual Report 2022

Institut für Kernphysik · COSY

Jül-4435

Annual Report 2022

Institut für Kernphysik / COSY

DIRECTORS AT THE IKP

Experimental Hadron Structure (IKP-1, IKP-2):
Theory of the Strong Interactions (IKP-3/IAS-4):
Large-Scale Nuclear Physics Equipment (IKP-4):

Prof. James Ritman
Prof. Ulf-G. Meißner
Dr. Ralf Gebel (managing director)

EDITORIAL BOARD

Dr. Christian Böhme
Dr. Ralf Gebel
Prof. Frank Goldenbaum
Dr. Dieter Grzonka
Prof. Christoph Hanhart
Dr. Volker Hejny
Dr. Andro Kacharava
Dr. Vsevolod Kamedzhiev
Prof. Andreas Lehrach
Prof. Livia Ludhova
Prof. Thomas Luu
Prof. Ulf-G. Meißner
Prof. James Ritman
Susan Schadmand, Ph.D. habil.
Dr. Thomas Sefzick

Cover picture: The cover picture shows the sensitivity at a 90% confidence level for excluding oscillating electric dipole moments (EDMs) of the deuteron induced by axion-like particles as measured by the JEDI collaboration. The frequency range shown is 120–121.4 kHz, corresponding to an axion mass range of 0.495–0.502 neV/c². The exclusion region is represented by the lighter filled areas, while the darker lines indicate the upper limit of the oscillating EDM. The green and blue colors are used to distinguish between two experimental settings, with the green and blue areas representing measurements with a momentum change per cycle of $\Delta p = 0.112 \text{ MeV}/c$ and $\Delta p = 0.138 \text{ MeV}/c$, respectively. More detailed information can be found in Sect. 2.1.

Contents

Preface	vi
1 Experimental Activities for FAIR	1
1.1 E reconstruction with realistic track finders for PANDA	1
1.2 Beamtime (Phase-0) at HADES	2
1.3 KOALA Experiment	3
2 Storage Ring Based EDM Search	3
2.1 Axion Searches	4
2.2 Electric Dipole Moment (EDM) Searches	5
2.3 Proof of Principle of the Pilot Bunch Technique	6
2.4 Investigation of Proton Spin Coherence Time	7
2.5 Beam and Spin Tracking	8
2.6 Design Study of a Dedicated EDM Ring	9
2.7 Outlook: Experiments with Polarized Beams and Targets at the GSI/FAIR Storage Rings	10
3 Neutrino Physics	10
3.1 Borexino latest results with solar neutrinos	10
3.2 Towards completion of the JUNO detector	13
3.3 Online Scintillator Internal Radioactivity Investigation System (OSIRIS) of JUNO	15
4 Accelerator Research	16
4.1 Developments at COSY	16
4.2 Progress of the HESR	18
5 Further Activities	20
5.1 LHCb Polarized Target Experiment	20
5.2 A new Method to polarize Atoms, Molecules and their Ions	21
6 Theoretical Investigations	23
6.1 Introduction	23
6.2 Emergent geometry and duality in the carbon nucleus	23
6.3 Hyperon-nucleon interaction in chiral EFT	24
6.4 Charge-symmetry breaking in $A = 7$ and $A = 8$ hypernuclei	25
6.5 Prediction of five-flavoured penta-quarks	26
6.6 Do near-threshold molecular states mix with neighboring $\bar{Q}Q$ states?	26
6.7 Localization of electron wavefunctions in hybrid nanoribbons	27
6.8 Criticality in brain dynamics	28
A Beam Time at COSY in 2022	29
B Committees	31
B.1 CBAC – COSY Beam Time Advisory Committee	31
B.2 Committee Service	31
C Publications	33
C.1 Journal Articles	33
D Talks, Colloquia and Proceedings	39
D.1 Conference and Workshop Contributions	39
D.2 Colloquia	45
E Academic Degrees	47
E.1 Dissertation / PhD Theses	47
E.2 Master Theses	48
E.3 Bachelor Theses	48
F Awards	49

G	Third Party Funded Projects	50
H	Collaborations	51
I	Conferences and Outreach Activities (Co-)Organized by the IKP	52
I.1	PSTP2022 Workshop	52
I.2	Georgian-German Science Bridge: 9th GGSWBS Workshop in Tbilisi and Kutaisi: <i>"Health as a Global Challenge: contributions by GGSB and its SMART\ Labs"</i>	52
I.3	Particle physics academy and training program for high school students 2022	53
I.4	Eighth Annual Meeting of the Programme "Matter and Technologies"	53
I.5	HESR Get Together Workshops	54
J	Teaching Positions	55
K	Personnel	56
L	Individual Contributions	59
	Accelerator Research	61
	Experimental Activities for FAIR	77
	Further Activities	90
	Storage Ring Based EDM Search	97
	Neutrino Physics	112

Preface

This Annual Report 2022 compiles the joint activities of the Institute for Nuclear Physics (IKP) of the FZ-Jülich (FZJ) and the departments FAIR Research at NRW (FFN) and HESR of GSI-FAIR together with international collaborations at COSY as well as experiments of our scientists at other laboratories. This has been the second year of the incremental transfer of most of the activities at IKP and the corresponding resources from FZJ to GSI, a process called TransFAIR. Two new departments have been established at GSI. The experimental activities at IKP-1 and IKP-2 and part of the infrastructure activities are transferred into the department FFN (FAIR-Forschung-NRW). The accelerator-related and the remaining infrastructure activities are transferred to the department HESR and other organizational units at FAIR. Despite these organizational changes, the following experimental, theoretical and accelerator highlights have been achieved:

The contributions of FFN and the IKP theory feature prominently in the newly approved network of experimental and theoretical groups within NRW (Bochum, Bonn, Jülich, Münster, Wuppertal and GSI-Darmstadt as associated partner). The network is called NRW-FAIR and has over 16 MEUR available for the upcoming four years, and also provides a basis to establish of a significant part of FFN at universities in NRW.

A four week beam time was successfully performed as part of FAIR Phase0 to study the production and decay of excited hyperons with two new, PANDA-type Straw Stations, in the upgraded HADES spectrometer. The new detectors operated stably without failures and the electronic readout of the straw signals were constant with low noise levels up to the highest particle rates of a few 10^5 s^{-1} per straw.

The KOALA experiment was designed and built to precisely measure the total and elastic cross section of antiproton-proton elastic scattering. In commissioning experiments at COSY, it was learned that the results depend significantly on the beam alignment and the vacuum in the scattering chamber, which is now being studied in further detail with simulations.

The performance of Ξ reconstruction with realistic track finders for PANDA has been substantially improved. Hyperon reconstruction requires a high track finding efficiency for both primary tracks and secondary tracks, i.e. originating from a displaced secondary vertex. The new track finders improve the full event reconstruction rate for hyperons by as factor four.

The JEDI- and CPEDM collaborations continued towards their goal to provide a scientific infrastructure for the search for charged-particle electric dipole moments. In September 2022 the Advanced Grant "Search for electric dipole moments using storage rings" (srEDM, #694340) of the European Research Council was successfully concluded. A design study of the prototype storage ring is envisaged as the next step.

In 2019 the JEDI Collaboration explored a new method to search for axions or axion-like particles (ALPs) in storage rings using an in-plane polarized deuteron beam. The experiment entailed a scan of the spin precession frequency. In 2022 the data analysis was finished, and a corresponding publication was submitted. No ALP resonance was observed and upper limits of the oscillating EDM component of the deuteron and the corresponding axion coupling constants are provided.

The main goal of the JEDI precursor experiment is to make the first direct measurement of the deuteron EDM. This includes performing experiments on prolonging and understanding the spin coherence time (SCT) of cooled and bunched deuterons at a beam momentum of $p = 970 \text{ MeV}/c$. It has been shown that sextupole configurations leading to small chromaticities in the horizontal and vertical plane result in long SCTs in the order of $\tau = 1000 \text{ s}$. A first run on proton SCT was performed at the beginning of 2022. Detailed beam and spin dynamics simulations have been performed to explain experimental results with polarized deuterons and protons at COSY and determine the optimal setting for polarized protons.

Together with the INFN Section of Ferrara, IKP has developed storage cells for gaseous targets, with significant impact in the field of experimental hadronic physics. This competence is being made available to LHCspin, which aims at installing a polarized gas target to bring spin physics at LHC for the first time. With strong interest and support from the international theoretical community, LHCspin offers unique opportunities by complementing both existing facilities and the future Electron-Ion Collider.

A Letter of Intent entitled "Towards experiments with polarized beams and targets at the GSI/FAIR storage rings" has been submitted to the GPAC. The committee encouraged the authors to submit a full proposal. Among the physics topics proposed are axion/ALP searches and the measurement of parity even time-reversal odd analyzing power in polarized proton tensor polarized deuteron scattering.

Together with the Borexino collaboration, the IKP neutrino group published the first precise measurement of the Earth’s orbital parameters based solely on solar neutrinos. In 2022, the first measurement of sub-MeV solar neutrinos using their associated subdominant Cherenkov radiation was presented by Borexino. To investigate neutrinos from Fast Radio Bursts (FRBs) a search for an excess in the number of events produced by neutrino-electron elastic scattering and the inverse beta-decay on protons (IBD) has been performed using the full exposure Borexino data set. No statistically significant increase in the number of events over the backgrounds was observed. Furthermore, the strongest upper limits on FRB-associated neutrino fluences of all flavors is obtained in the 0.5 to 50 MeV neutrino energy range. JUNO will be the first multi-kton Liquid Scintillator (LS) detector currently under construction in Jiangmen, China. The success of JUNO strongly depends on the levels of radiopurity that will be achieved. The achieved level of LS radiopurity will be tested in 20 ton detector of OSIRIS (Online Scintillator Internal Radioactivity Investigation System). Within OSIRIS, the neutrino group is responsible for the source insertion calibration system, a refurbished Automated Calibration Unit.

The IKP theory group studies the strong interactions in their various settings, spanning topics in hadron structure and dynamics, the nuclear many-body problem, symmetry tests in Quantum Chromodynamics (QCD), physics beyond the Standard Model, strongly correlated electronic systems and brain dynamics. The first focus of the theory group is the formulation and application of effective field theories for precision hadron and nuclear physics based on the symmetries of QCD. The second focus is related to high-performance computing in nuclear, hadronic and condensed matter physics, spear-headed by the work on nuclear lattice simulations. This year, we added machine-learning techniques to our toolbox.

Since July 2012, the group is heavily involved in the activities of the collaborative research center “Symmetries and the emergence of structure in QCD” (CRC 110) together with researchers from Bonn University, TU München, Ruhr-Universität Bochum, IHEP/CAS (Beijing, China), ITP/CAS (Beijing, China) and Peking University (China). This CRC is presently in its third and final funding period. A further strengthening of the group was achieved through the ERC Advanced Grant “EXOTIC” that began in November 2021. It focuses on precision calculations in nuclear and hypernuclear physics on the lattice and exploring fine-tunings in nuclear reactions and the role of anthropic considerations. Since this year, the IKP theory group is also involved in the NRW-FAIR network funded by the Ministry of culture and science of the state of Northrhine-Westfalia. Some of the highlights of all of these activities are discussed in this report.

One central element unifying IKP is the operation of and experiments with COSY. A second element is the realization of the High Energy Storage Ring (HESR) for the PANDA experiment. The completion of all accelerator components is coming to an end and all major systems are ready to be stored until installation starts for the completion of FAIR. All 46 bending dipole magnets have been equipped with the necessary vacuum chambers and delivered to the storage in Weiterstadt. This includes four magnets that were prepared for the SPARC experiment and therefore possess modified vacuum chambers, where a laser beam for the experiment can be passed in and out. One of the cavities for the HESR was installed in COSY for testing already in late 2021. In early 2022 some initial tests including the recording of calibration data were performed. Since then it has been used to accelerate the beam during the operation of COSY. As expected its stability and reliability could be demonstrated.

Researchers from JCNS at FZJ have achieved a breakthrough by delivering the first neutrons with a new powerful target/moderator technology developed in Jülich. Currently, the platform houses three beamlines: a detector test stand, a time-of-flight (ToF) diffractometer, and the HERMES neutron reflectometer from the decommissioned Orphée reactor, which was contributed through a collaboration with LLB (Saclay). Both thermal and cold neutrons were measured at all three positions around the TMR facility.

The success of our institute is built on the efforts of all its members, and with this report, we can share our achievements. We are pleased to express our sincere gratitude to everyone in the institute for their efforts during this challenging year. The achievements presented in this report would not have been possible without the dedication of our technicians and engineers, the service groups, our colleagues in the FZJ infrastructure, and the students who advanced the scientific work. We continued in COVID conditions followed by the effects of the Russian invasion of Ukraine. There were impressive results and progress across many activities. We thank all for their continued commitment and sense of responsibility, which enabled the institute to perform excellently this year despite highly challenging circumstances.

Jülich, March 2023

Ralf Gebel, Ulf-G. Meißner, Jim Ritman

1 Experimental Activities for FAIR

1.1 Ξ reconstruction with realistic track finders for PANDA

Hyperon reconstruction requires a high track finding efficiency not only for primary tracks but also for secondary tracks originating from a displaced secondary vertex. The reason is that hyperons have a long lifetime and often decay into Λ particles, which also have a long lifetime with a mean decay length of a few cm. Secondary track finding is a more computationally intensive task than primary track finding, where the interaction point (IP) can be used to simplify the calculation and to reduce the number of parameters. Therefore a combination of primary and secondary track finders leads to the best performance in terms of efficiency and computing time. In this work the combination of primary and secondary track finders were investigated by analyzing a benchmark hyperon reaction chain for PANDA: $p\bar{p} \rightarrow \Xi(1820)^-\Xi^+ \rightarrow \Lambda K^-\bar{\Lambda}\pi^+ \rightarrow p\pi^-K^-\pi^+\bar{p}\pi^+$. The reaction chain contains one primary particle (K^-) and five secondary particles (p , π^- , π^+ , \bar{p} , π^+). An example event display is shown in Fig. 1. Two different primary track finders were combined with a newly developed secondary tracker. The two investigated primary track finders are the currently used track finder in PANDA, which is called the standard tracker, and a newly developed track finder based on Hough transformations. The efficiencies are here always defined as the fraction of found tracks divided by the number of reconstructable tracks. A track is defined as reconstructable if it has at least four hits in the MVD or six hits in all tracking detectors (MVD, STT, GEM).

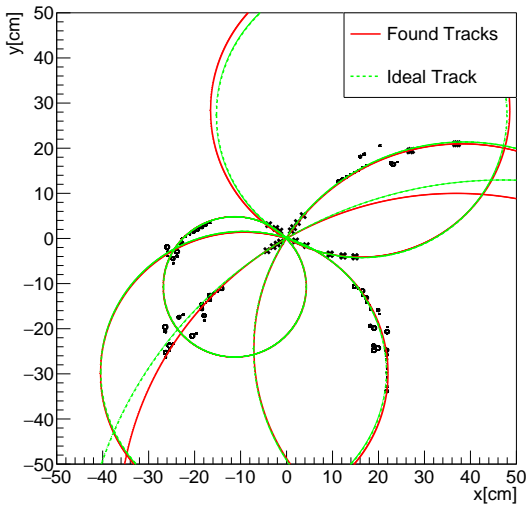


Figure 1: An example event of the $p\bar{p} \rightarrow \Xi(1820)^-\Xi^+$ reaction. The ideal tracks are shown in green, the tracks found by the combination of Hough and Secondary track finder are shown in red.

Comparing only the primary track finders for tracks in the target spectrometer shows that the standard tracker has a higher efficiency for the primary particle (Standard: 88.2 %, Hough: 82.4 %). However, the efficiency of the secondary particles is higher for the Hough track finder (table 1). The full event reconstruction rate for the Hough track finder is 5.9 %, which is more than twice that of the standard tracker with only 2.4 %. This is a consequence of the higher efficiencies for secondary tracks for the Hough track finder.

The combination of primary and secondary track finders (table 2) improves the reconstruction rate in the target spectrometer of the secondary tracks (Standard + Secondary: 56.0 % - 73.6 %, Hough + Secondary: 58.6 % - 78.3 %). Here the improvement of the standard tracker is larger than the improvement of the Hough track finder, since the Hough track finder itself had already a better efficiency. In both cases the secondary track finder improves the full event reconstruction rate. For the standard track finder an improvement by a factor of four could be reached (from 2.4 % to 9.9 %). The increase in efficiency for the Hough and secondary track finder is less pronounced with an improvement of about 40 % (from 5.9 % to 8.2 %). The reason for the slightly lower efficiency of the combination of Hough and secondary track finder compared to the combination of standard and secondary track finder is that the Hough track finder itself has a much better reconstruction rate for secondary tracks. However, the momentum resolution of these tracks is poorer. Consequently, the Hough track finder finds secondary tracks with a poor momentum resolution which then are not available for the secondary track finder anymore. Here, optimizing the Hough track finder to only find primary

	Standard	Hough
K^-	88.2	82.4
P	61.6	62.3
π^-	43.2	62.8
$\pi^+(\Xi^+)$	52.5	69.2
\bar{P}	50.9	51.9
π^+	32.3	51.6
Full event	2.4	5.9

Table 1: Reconstruction efficiencies of the final state particles found in the target spectrometer and reconstruction efficiency of the full event using only the primary track finder.

tracks promises a stronger improvement for the combination with the secondary track finder. The new track finders (Hough and Secondary track finder) both lead to an improvement of the full event reconstruction rate of the investigated hyperon decay. The full event reconstruction rate, which also takes the detector acceptance into account, could be improved by a factor of four to a reconstruction efficiency of 1.2 % for the combination of the standard and secondary track finders, compared to 0.3 % for the full event reconstruction rate reached with only the standard tracker.

Currently, both the Hough and the Secondary track finders reconstruct only the x-y-component of a particle track. The z-component is reconstruction using Monte Carlo information from the simulated tracks. The next step towards a realistic track finding in the target spectrometer is to combine the algorithms with a realist p_z -finder, which already exists in PANDA. Additionally, an online capability of the Hough track finder has already been tested by porting the algorithm to a GPU. A speed-up factor of four could be achieved with a medium size GPU. Of particular interest is also the investigation of the online capability of the Secondary track finder.

	Standard + Secondary	Hough + Secondary
K^-	88.8	86.5
P	71.5	70.4
π^-	65.7	73.5
$\pi^+(\Xi^+)$	73.6	78.3
\bar{P}	56.5	58.6
π^+	56.0	63.5
Full event	9.9	8.2

Table 2: Reconstruction efficiencies of the final state particles found in the target spectrometer and reconstruction efficiency of the full event using primary and secondary track finders.

1.2 Beamtime (Phase-0) at HADES

As part of the FAIR phase-0 program, a beam time of four weeks was successfully performed in spring 2022 to study the production and decay of excited hyperons with two new, PANDA-type Straw Stations (STS1 and STS2) in the upgraded HADES spectrometer. The proton beam with kinetic energy of 4.5 GeV was focused on a liquid hydrogen target. In addition to the new STS tracking stations, there was a new RPC detector for time-of-flight measurements covering the polar-angle range from about 0.7° up to 6.5° to complement the forward going tracks in the STS. A stable operation of the STS detectors without any failures and stable electronic readout of the straw signals with constant, low noise levels up to the highest particle rates of a few 10^5 s^{-1} per straw was achieved. This result verifies the various quality assurance methods and measurements during the preparation and set up of the systems, which will be adopted for the PANDA-STT. The calibration methods of both STS stations were developed and the calibration of the space – drifttime relation for each of the 1728 single straws in the STS has been completed for the beam time data. Fig. 2 shows as an example the result of the parametrized isochrones radius - drifttime relation $r(t)$ (red line) and the comparison with a simulation of ionizing proton tracks through a single straw (green line: fit of the track distance versus drifttime points). As expected, close to the wire the measurement of small track distances is distorted by the

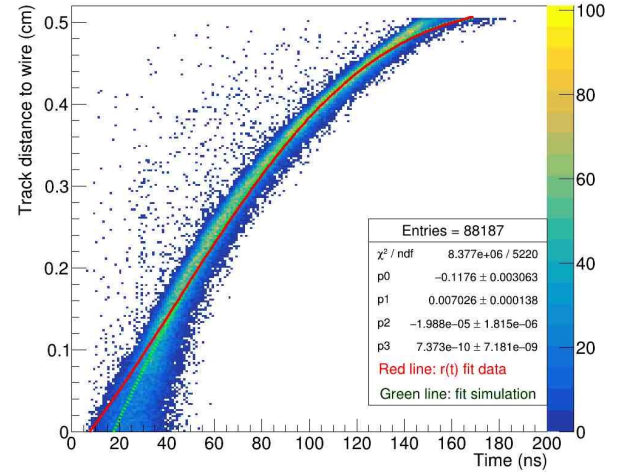


Figure 2: Drift time simulation (Garfield) of proton tracks passing through a single straw and $r(t)$ parametrization (green line: fit to the simulation, red line: $r(t)$ calibration for the in-beam data)

varying and Poisson-distributed distances of the ionization clusters along the track path, which limits the resolution in this region. Above a track-to-wire distance of about 0.6 mm the agreement between the simulated drift motion and $r(t)$ calibration of the data is very good.

Part of the calibration is the determination of the maximum drift time of a straw, which contains all smearing effects of the drifttime measurement and systematic errors, from the straw geometry, drift gas, electric field, electronic readout up to the drifttime extraction and calibration with a parametrization of the isochrone radius - drifttime relation $r(t)$. Fig. 3 shows the distribution of the maximum drifttime for all 704 straws in the STS1 with a mean value of 164 ns. The obtained very low spread of 3.2 ns (σ) of the distribution corresponds to very low differences in the maximum isochrone radius for all straws of less than 40 μm , which is less than 0.8% of the pressurized straw tube inner radius of 5.05 mm. The result confirms the precise geometry of the PANDA-type straw technology with self-supporting, pressurized and thin-wall film tubes.

Note, that a few straw channels in the region 150 to 155 ns in Fig. 3 have a low number of entries in the drifttime spectrum, where the determination of the start and end of the spectrum yields slightly lower values for the maximum drifttime.

Proton-proton elastic scattering events are used to determine the integrated luminosity for the production run. Events were selected that contain one proton in the STS tracking stations with a polar angle (θ) in the region of $3^\circ < \theta_{STS} < 6^\circ$ in coincidence with a proton in the polar angular range $70^\circ < \theta_H < 79^\circ$ measured by the main HADES spectrometer. Kinematic constraints are used to

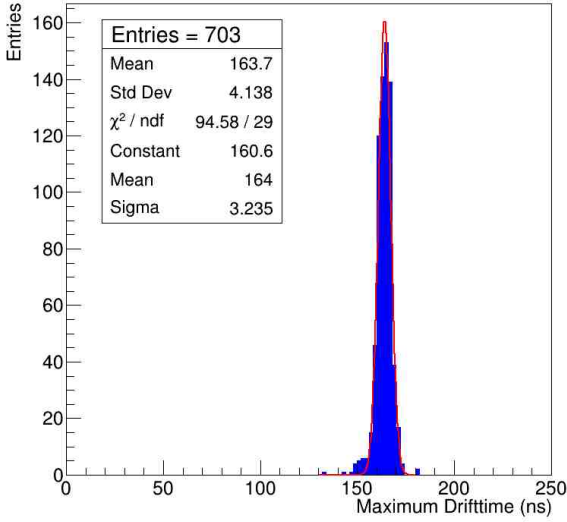


Figure 3: Distribution of the maximum drifttime (ns) for all straws in the STS1. A gaussian fit (red line) to the data obtained a mean value of 164 ns and width of 3.2 ns (σ).

suppress the background in the data sample. The cross-section of proton-proton elastic scattering into this angular range is $\sigma_{el} = 4.4^{+0.8}_{-0.3}$ mb as obtained by interpolation between measurements from other experiments. The reconstruction efficiency is determined by a comparison with proton-proton elastic events from simulation. The preliminary time integrated luminosity for the four week beamtime is $5.6 \pm 0.4 \text{ pb}^{-1}$ and will allow studies of *e.g.* hyperon production and decay channels and the experimentally unexplored process of hyperon Dalitz decays. More details about the proton-proton elastic scattering analysis and determination of the integrated luminosity are discussed in this annual report as a separate individual report by G. Perez-Andrade (see page 85).

1.3 KOALA Experiment

The KOALA experiment was designed and built to measure the antiproton-proton elastic scattering in order to gain precise knowledge of the total cross section as well as the elastic cross section. The main idea of KOALA is to measure the region covering the Coulomb-nuclear interference, in which Coulomb scattering can be used for an absolute normalization of the luminosity. KOALA consists of a hydrogen cluster-jet target, a recoil detector and a forward detector to obtain a wide range of squared four-momentum transfer, *i.e.*, $|t| = 0.0008 - 0.1 \text{ (GeV}/c)^2$. The recoil detector comprises four semiconductor strip energy sensors measuring the kinetic energy and emitting angle of the recoil protons. Four pairs of plastic scintillator bars as the forward detector are located symmetrically at the vertical and horizontal direction close to the beam axis. With the commissioning experiments at COSY, it

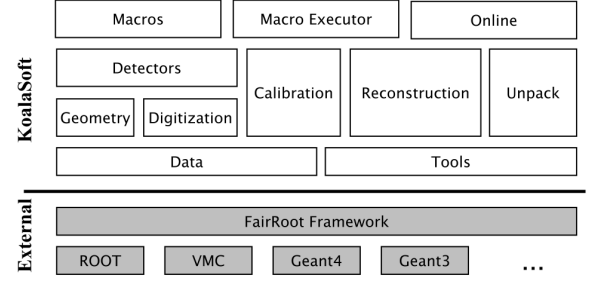


Figure 4: Schematic layout of the KoalaSoft framework.

was learned that the precision of the measurement is significantly impacted by the finite beam misalignment as well as the poor vacuum in the scattering chamber.

To pursue an even higher precision of the measurements, the current focus of KOALA is to investigate such constraints by software studies. Based upon FairRoot, which combines the VMC library and the ROOT package, the KoalaSoft framework has been developed for both data analysis and simulation study. As illustrated in Fig. 4, the KoalaSoft package has been devised to be modularized concerning a sustainable development and maintenance. In order to implement the same analysis codes either for simulated data or for experiment data, special attention has been paid for the data format. The unpacked experiment data as well as the simulated data after digitization can be further processed with the same analysis routines. Benefiting from the modularization, new features or developments can be readily added to the framework.

To enable investigations of the impact of the beam and target on the overall precision of the experiment, a preliminary simulation chain for proton-proton elastic scattering has been implemented. It can be used to generate proton-proton elastic events and reconstruct the t -distribution for further studies. The new features to simulate the beam misalignment and the beam halo or generate background from a poor vacuum from the hydrogen cluster target are being implemented.

2 Storage Ring Based EDM Search

The JEDI- and CPEDM-collaborations continued investigations and measurements towards their goal to provide a scientific infrastructure which enables the search for charged-particle electric dipole moments with unprecedented sensitivity. At the end of September 2022, a major milestone was reached with the successful conclusion of the Advanced Grant „Search for electric dipole moments using storage rings“ (srEDM, #694340) of the European Research Council with Principal Investigator Hans Ströher and additional beneficiaries University of Ferrara (Paolo Lenisa) and RWTH Aachen University

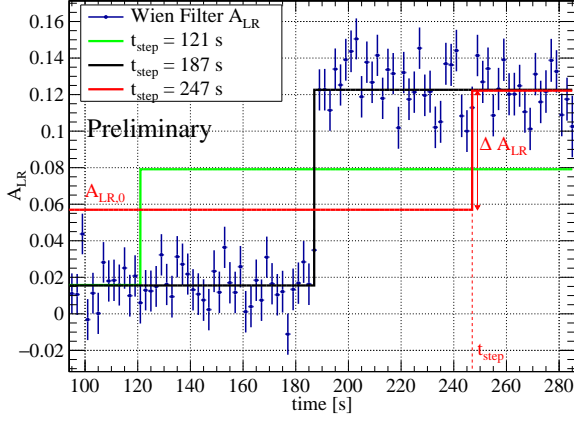


Figure 5: Examples of a step function fit to the Wien filter scan data for a single bunch from one cycle. The black line is a fit with the jump at the resonance crossing. The red and green curves show the results for other choices of the jump time. In the analysis, the time with the lowest χ^2 is chosen.

(Jörg Pretz). As the next step, the collaborations envisage a design study of the prototype storage ring.

2.1 Axion Searches

In 2019 the JEDI Collaboration performed a first measurement at COSY exploring a new method to search for axions or axion-like particles (ALPs) in storage rings by using an in-plane polarized deuteron beam. The experiment scanned momenta near 970 MeV/c and entailed a scan of the spin precession frequency. At resonance between the spin precession frequency of deuterons and the ALP-induced EDM oscillation frequency, there should be an accumulation of the polarization component out of the ring plane. The beam momentum and, consequently, the spin precession frequency were ramped to search for a vertical polarization change. During 2022 the data analysis has been finished, and a corresponding publication has been submitted¹. No ALP resonance was observed and upper limits of the oscillating EDM component of the deuteron and the corresponding axion coupling constants are provided.

The pseudoscalar nature of axions and ALPs allows interactions of the oscillating axion/ALP field $a(t)$ with the spin of nucleons and nuclei by two different mechanisms: coupling to the electric dipole moment of a non-self-conjugate particle with non-zero spin or by the gradient of the field, known as the axion-wind effect. The first coupling leads to an oscillating component d_{AC} of the particle's total EDM pointing parallel to the spin direction. The second coupling, the axion wind, causes the spin of a nucleon or nucleus to rotate about the gradient of the axion field, which is analogous to a magnetic field parallel to the particle momentum. Both effects cause res-

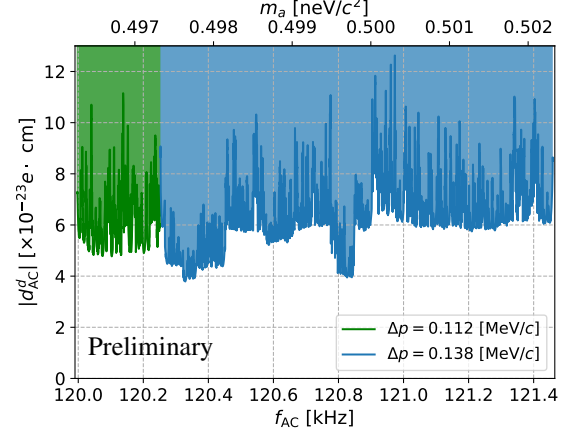


Figure 6: 90% confidence level sensitivity for excluding the ALPs induced oscillating EDM. The two colors indicate two different measurement intervals per scan.

onant rotation of the spin when the precession frequency of the spin matches the oscillation frequency of the axion field, resulting in a build-up of vertical polarization. The measurement principle is similar to a Froissart-Stora scan, in which the axion field is treated as an RF spin resonator scanning the spin precession frequency using a slow momentum ramp. In this way, most of the systematic effects that occur in a static EDM measurement are not present here.

During the experiment, a total of 103 partially overlapping frequency intervals were scanned, covering a range from 119.997 kHz to 121.457 kHz or an axion mass range of 4.95–5.02 neV/c². For each scan, the phase of the oscillating electric dipole moment relative to the in-plane precession motion is unknown. This could cause a ALP to be missed during a single scan, since the magnitude of the out-of-plane rotation is affected by this relative phase. To avoid this, four beam bunches were used simultaneously so that the spin directions are nearly orthogonal relative to the particle momentum in these four bunches. For each bunch, a step function was fit to the vertical polarization as function of time to describe the effect of a resonant spin rotation. An example of such a fit using the rf Wien filter as the spin rotator is shown in Fig. 5. Fig. 6 shows the resulting exclusion regions for the oscillating EDM d_{AC} for the measured frequency range.

The limits of the spin rotation can then be expressed as limits of the coupling of ALPs to the deuteron spin via the oscillating part of the deuteron EDM d_{AC} and/or via the axion wind effect. Since we cannot experimentally distinguish between these two sources, the coupling constants are calculated assuming that either one or the other process produces 100% of the effect. As an example, we show here the limits for the model-independent coupling

¹Preprint available at <https://arxiv.org/abs/2208.07293>.

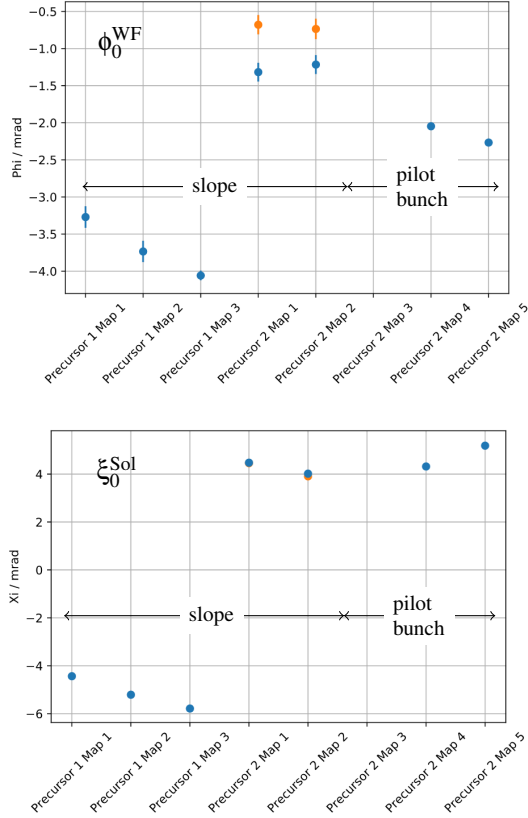


Figure 8: Overview of the current status of all measured maps during Precursor I & II. The upper and lower panel shows the radial and longitudinal component of the invariant spin axis, respectively. The two difference colors for Precursor II Map 1 & 2 represent the two bunches.

used, and the phase-lock feedback as well as the rf Wien filter were acting on the same particles. As the feedback system requires a minimum degree of in-plane polarization to work, the measurement stopped as soon as the out-of-plane spin rotation into the vertical direction was complete. In this setup the slope of the out-of-plane angle $\alpha(n)$ depends on the relative phase ϕ_{rel} between the Wien filter frequency and the spin precession. For Precursor run II, a system of fast switches were implemented at the Wien filter that allowed bunch-selective spin manipulations to be performed (see Sect. 2.3). We then used two bunches in the machine, one for the phase-lock feedback ("pilot bunch") and one for spin rotations by the RF Wien filter. Here, we directly measured the (phase independent) vertical oscillation frequency $f = \epsilon f_{rev}$. During both runs we measured several maps for systematic studies. We also had several campaigns to mechanically align the COSY components in between the two runs and also calibrated the beam position monitors using beam based alignment.

The results for the directions of \vec{n} for various maps are summarized in Fig. 8. There are a number of systematic effects that are currently under investigation.

2.3 Proof of Principle of the Pilot Bunch Technique

There are important spin-physics experiments in storage rings where it is imperative to maintain a large number of spin flips under continuous operation of an rf spin rotator. The pilot bunch approach developed by the JEDI collaboration at COSY (see IKP Annual Report, 2021) uniquely allows either to maintain the exact resonance condition or to fix the detuning of the rf spin rotator with respect to the spin precession frequency by operating in multi-bunch mode, where the spin rotator is gated out (decoupled) from the rf power when a particular (pilot) bunch passes through the spin rotator. The undisturbed (idle) precession of the horizontal polarization of the pilot bunch is continuously monitored using the beam polarimeter. The idle precession frequency is prone to drift, but feedback from the polarimeter is used to correct the spin rotation frequency and maintain either an exact resonance or fixed detuning. The results presented were obtained in 2020 with stored polarized 970 MeV/c deuterons, using the rf Wien filter (WF) employed as a spin rotator.

The case of weak detuning is of interest in its own right, as detuning provides a very interesting insight into the aspects of rf-driven spin rotations in storage rings that have not yet been fully exploited. Here we illustrate the main features of the pilot-bunch technique using the results for vertical polarization obtained in the two-bunch regime. Further details regarding the in-plane polarization and the phase walk are discussed in Vera Shmakova's contribution to this Annual Report (see page 98). The time structure of the gated rf magnetic field in the WF is shown in Fig. 9. The experiment used of two beam bunches stored simultaneously in COSY, as indicated in Fig. 10. The width of the gate in Fig. 9 is selected according to the bunch length.

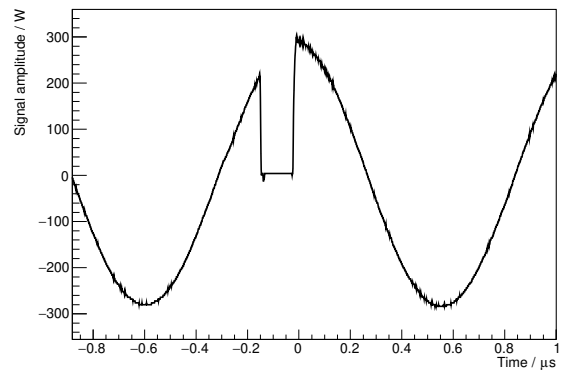


Figure 9: The effect of gating on the electromagnetic fields of the rf Wien filter on the signal amplitude.

Polarized beams are stored with vertical initial polarization. The polarizations for the WF-off cycles and those for the pilot-bunch cycles are shown in Fig. 11. In the case of exact resonance, the up-to-down and inverse spin

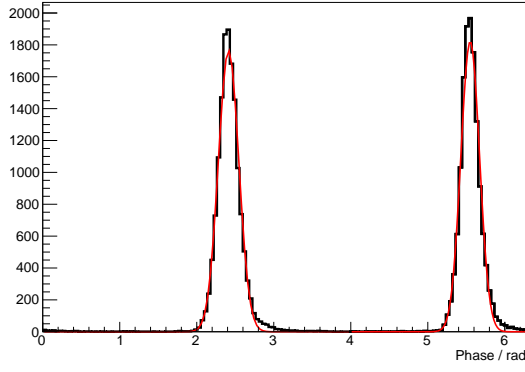


Figure 10: Pattern of the longitudinal beam intensity profiles of the two deuteron bunches orbiting in the ring.

flips of the active bunch would have been complete and with full amplitude. At finite detuning, the spin flip of the signal bunch would be a partial one with suppressed amplitude and finite offset. The internal polarimeter target only scrapes off the edge (periphery) of the beam that is outside the symmetry center of the polarimeter, which also contributes to the offset of the vertical polarization (see Fig. 11).

The time dependence of the vertical polarization of the pilot and signal bunches, irrespective of a possible detuning, serves as an irrefutable proof of principle for the pilot bunch technique. We fit the measured polarization asymmetries to a function $A(t) = a(t - t_0) + b + c \cos(\omega_{\text{SF}}(t - t_0) + \phi_{\text{SF}})$, where ω_{SF} indicates the spin-flip angular frequency and t_0 denotes the time when the WF was switched on. For the pilot bunch and the cycle with WF switched OFF, the oscillation amplitude c is consistent with zero.

2.4 Investigation of Proton Spin Coherence Time

During the last years the JEDI collaboration has performed a sequence of experiments on prolonging and understanding the spin coherence time (SCT) of cooled and bunched deuterons at a beam momentum of $p = 970 \text{ MeV}/c$. It has been shown that sextupole configurations leading to small chromaticities in the horizontal and vertical plane result in long SCTs in the order of $\tau = 1000 \text{ s}$. The long term strategy for EDM searches aims at an intermediate prototype ring as a demonstrator for key technologies for an electric ring as well as for frozen spin, and has as a final goal a high precision all-electric storage ring for protons with counter-rotating beams. For such EDM measurements on protons a successful realization of a long spin coherence time is a mandatory requirement.

A first run on proton SCT was performed at the beginning of 2022. During the experiment a number of challenging observations were made: the distribution of the spin-

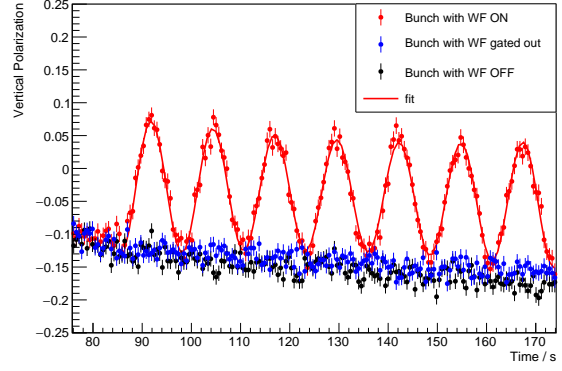


Figure 11: Experimental results for one cycle, with two stored bunches in the machine. The red points indicate the vertical polarization when the rf Wien filter (WF) is switched ON (at $t_0 \approx 86 \text{ s}$). The blue points reflect the case for the pilot bunch, *i.e.*, when the rf of the WF is gated out, as indicated in Fig. 9. Black points indicate the situation when, during a different cycle, the WF is completely switched OFF.

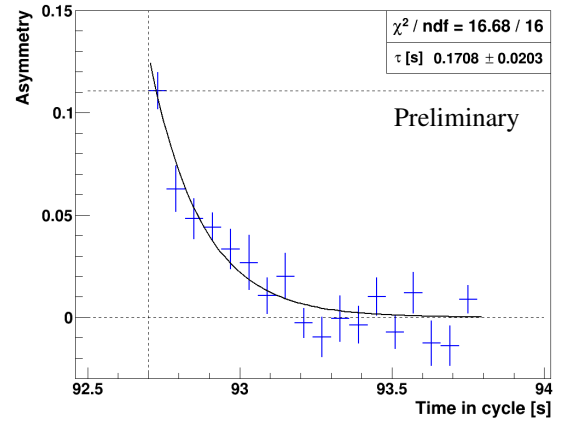


Figure 12: Example plot showing the time-evolution of the in-plane polarization of protons after the rotation into the horizontal plane. The vertical line indicates the time when the spin vector reaches the horizontal plane. The spin coherence time is well below 1 s.

resonance frequencies in the beam was too wide to be addressed by an RF solenoid running at fixed frequency, the synchrotron side bands (which played no role for deuterons) had a strong influence on the spin rotation and also other interference terms of unknown origin distorted the pattern of the spin rotation via a Froissart-Stora scan. The best results were achieved when using the RF Wien filter running on a 40 Hz wide frequency band. With this setup some first data were taken.

Fig. 12 shows an example of the in-plane polarization after rotation in the horizontal plane. The spin coherence time is well below 1 s and, at this stage, it cannot be ex-

cluded, that the slope contains some residual effects from the rotation.

For further planning, additional spin tracking simulations – including the rotation into the horizontal plane – in order to understand the observed features are mandatory. This is a prerequisite for any experimental optimization procedures to come. However, in view of the upcoming cessation of COSY operation by the end of 2023, the JEDI Collaboration has decided to focus on the concluding the precursor studies and not to continue with this topic at COSY.

2.5 Beam and Spin Tracking

Detailed beam and spin dynamics simulations have been performed to explain experimental results with polarized deuterons at COSY and to determine the optimal setting for a long SCT of polarized protons.

Spin tracking simulations in an accurate simulation model of COSY are required to understand the measured data from the precursor experiment with polarized deuterons. The EDM signal results in a tilt of the invariant spin axis from the original vertical direction to the horizontal plane and needs to be distinguished from systematic spin rotations that have the same signature. Therefore, an improved model of COSY was implemented using the Bmad software library. Systematic effects were considered by including magnet displacements, effective dipole shortenings, longitudinal fields, and junction beam deflections. These effects rotate the invariant spin axis in addition to the EDM and need to be analyzed and understood. Recent spin tracking results and methods for determining the invariant spin axis are presented by *M. Vitz*, page 101. The direct implementation of all measured systematic effects into the simulation model resulted in a tilt of the ISA (Invariant Spin Axis) that was one order of magnitude less than the measured values in the radial and longitudinal directions. As it is very unlikely that this large deviation in the radial direction is due to an EDM, an alternative explanation has to be found. This was recently done by examining the distribution of the ISA under a series of Gaussian distributed quadrupole misalignments. The result of this approach is shown in Fig. 13.

In order to get a complete picture of the ISA distribution under the influence of misalignments, it is necessary to consider the rotations of the quadrupoles as well as other displacements and rotations of the magnets. In Fig. 14 the simulation of an EDM resonance map is shown, taking into account all known and measured systematic effects such as misaligned magnets, multipole fields, etc.

To prepare for SCT optimization for polarized protons at COSY, modeling of the optical setting has been performed. Similar to the optical setting of deuterons, effects influencing the closed orbit, including magnet misalignments and effective dipole lengths, have been implemented in the software library Bmad. The results of the

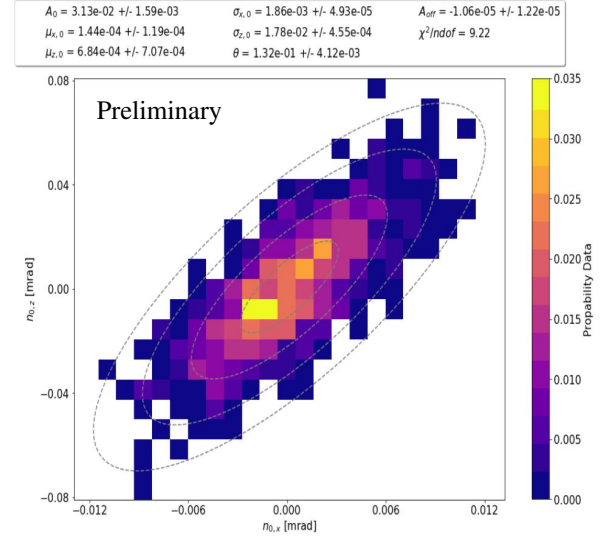


Figure 13: Distribution of the ISA (radial on the x-axis, long. on the y-axis) by assuming Gaussian distributed quadrupole offsets. A two-dimensional Gaussian fit was applied to the data and is indicated via the grey lines.

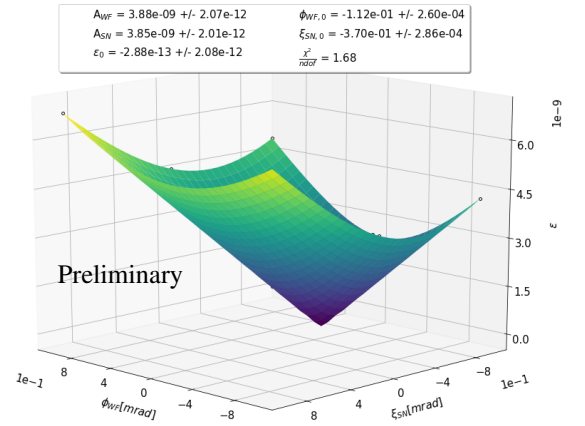


Figure 14: The simulated EDM resonance strength is plotted for all known and measured systematic effects versus different Wien filter ϕ_{WF} and solenoidal snake magnet ξ_{SN} rotation angles. The minimum ($\phi_{WF,0}$, $\xi_{SN,0}$) indicates the required Wien filter rotation and magnet strength of the snake magnet to align the ISA and EM fields with the corresponding resonance strength ϵ_0 . A_{WF} and A_{SN} are the spin rotation angles in the Wien filter respectively in the snake magnet, normalized by 4π .

experiments conducted in February and March 2022 are compared with a model comprising the real COSY settings for the analysis. Overall, it has been shown that the existing COSY simulation model is capable of describing measurements with protons at COSY by integrating additional systematic effects and implementing a com-

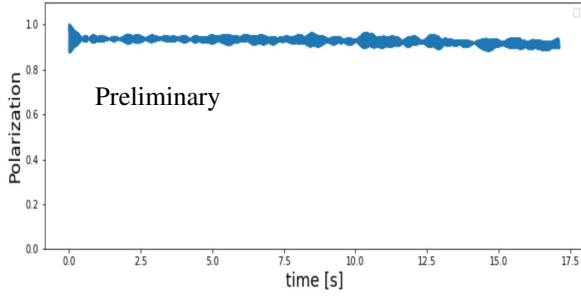


Figure 15: Spin coherence time for a polarized proton beam with optimal sextupole settings. The x-axis is the time and the y-axis is the total polarization.

plex fitting algorithm based on the calculation of an orbit response matrix. Additional effects that affect the accuracy of the model include the effective lengths of the quadrupoles, the displacements of the BPMs, the fringe fields, and the effects of the multipole components of the magnets. An improved model with an underlying fitting procedure requires additional beam time with protons. Reaching high values of SCT for protons is more challenging compared to deuterons due to a higher anomalous magnetic moment. It has been shown for protons that spin motion is strongly influenced by nearby intrinsic and integer spin resonances. The strengths of the lattice has been calculated for a typical COSY optical setting and the overall influence on SCT was predicted. Results for simulations also show that a long SCT with protons cannot be achieved by minimizing the chromaticities alone, as is the case for deuteron beams. The second-order momentum compaction factor must be optimized along with the horizontal and vertical chromaticities. After a 12 million turns spin tracking simulation (see Fig. 15), the total polarization remains above 0.9 (see *D. Gu*, page 102).

2.6 Design Study of a Dedicated EDM Ring

Further beam and spin dynamics simulations for a prototype proton EDM ring were carried out to study in detail the advantages and shortcomings of the current lattice. The main problem, which severely limits the optical flexibility of the second-order lattice, was found to be the arrangement of the sextupoles, which affects the overall configuration of the lattice. Furthermore, a robust method was developed to optimize the working point of the prototype ring for SCT above 1000 seconds. The established method is also useful to find the sextupoles settings for long SCT.

Simulations were performed using the Bmad software library to verify the relationship between some important parameters of the optical setting of the lattice and the SCT (see *R. Shankar*, page 103). Starting from the assumption of a linear system of equations, the optimal arrangement for the three families of sextupoles in an ideal lattice was found by spin-tracking simulations. To optimize the

SCT, different values of the second-order optical parameters ξ_x (horizontal chromaticity), ξ_y (vertical chromaticity) and α_1 (second-order momentum compaction factor), which are determined linearly by the field strengths of the three available sextupole families, were adjusted at fixed quadrupole settings.

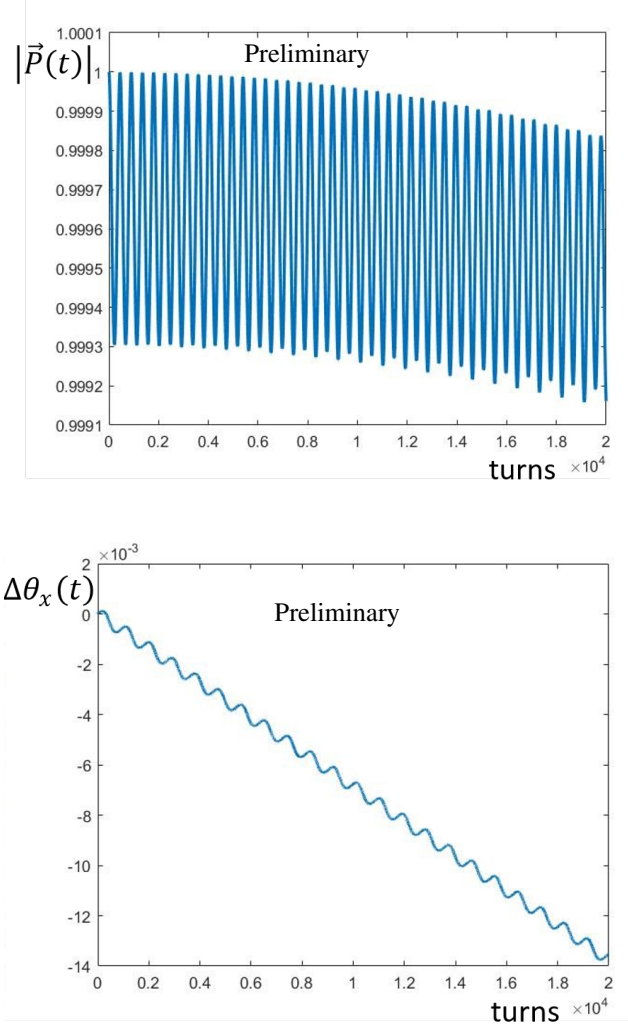


Figure 16: Evolution of the magnitude of the polarization vector $|\vec{P}(t)|$ of 1000 particles in a Gaussian distributed bunch as a function of the number of simulated turns (upper plot). The decoherence phenomenon is observed as a steady decrease in averaged value of the polarization after several turns. The spin tune spread $\Delta\theta(t)$ of the polarization vectors in the particle ensemble from the upper plot is simultaneously determined and plotted against the number of turns (lower plot).

The SCT was determined by fitting the steady decrease in the magnitude of the polarization vector $|\vec{P}(t)|$ of the particle ensemble in Fig. 16 (upper plot). The effect of path lengthening, on the other hand, manifests itself as oscillations in the directional shift of the polarization vector, as shown in Fig. 16 (lower plot). Using this analyz-

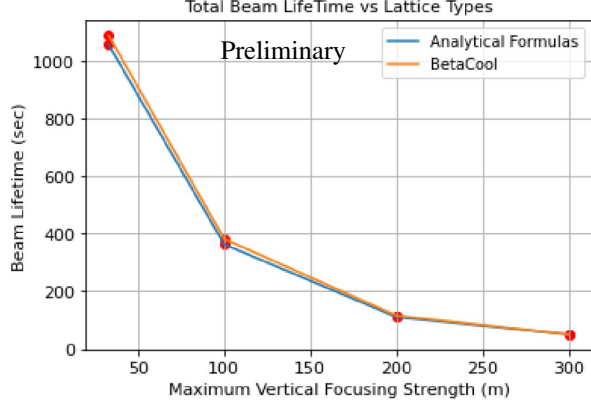


Figure 17: This plot shows a comparison of analytical formulas and BetaCool results in the form of beam lifetime vs lattice types (in terms of their maximum vertical focusing strength β_y^{max}).

ing method, several points with SCT above 1000 s were found.

Nevertheless, the small tolerances of the optimised operating point for meeting the sensitivity criterion are still quite tight and represent a high bar for sextupole precision. While it is envisaged that the lattice improvements investigated so far could relax these tolerances, it is currently unclear whether this will actually be the case. In addition, a deeper look into the mechanisms of decoherence seems to indicate that the spin tune spread varies differently in storage rings with a pure electrostatic bending field compared to those without.

In addition to the SCT, the particle beam in the prototype ring must also provide a sufficiently long beam lifetime. Four different lattices with different maximum focusing strengths, with a maximum Beta functions of $\beta_y^{max} = 33$ m, 100 m, 200 m, 300 m, were generated with the simulation program MADX and studied in the context of beam losses (see *S. Siddique*, page 104). The aim of these calculations was to find an optimized lattice with minimum systematic effects and maximum beam lifetime. First, four major effects which cause immediate beam loss in a storage ring called Hadronic interactions, Coulomb scatterings, Energy loss straggling, and Touschek effect, were studied and applied analytically. After obtaining results from rough analytical formulae using Wolfram Mathematica, the BetaCool simulation program was used to perform the beam loss calculations. BetaCool is used because it provides a more realistic description of the storage ring. Very good agreement was found between the analytical calculations and the BetaCool results, as shown in Fig. 17. As expected, these calculations also show that a lattice with stronger vertical focusing (which means smaller β_y^{max}) provides longer beam lifetimes. Next, a $30\mu\text{m}$ diameter carbon pellet was also introduced into the beam to scatter it towards the polarime-

ter for beam polarization measurements (see *S. Siddique*, page 104).

These studies have shown that increased beam focusing is beneficial for beam lifetime. In addition, as expected, the beam-target interaction results in significantly higher beam loss rates and a higher beam emittance growth rate. As the beam passes through the target, not all particles experience the same interaction with the target. Due to this inhomogeneous influence of the target on the beam, the beam particles are scattered at different angles and with different momenta. In order to extract the beam at a specific angle, it is necessary to study this interaction in more detail. For this purpose, beam tracking is being performed, including interaction with the target.

2.7 Outlook: Experiments with Polarized Beams and Targets at the GSI/FAIR Storage Rings

A Letter of in Intent (LoI) entitled "Towards experiments with polarized beams and targets at the GSI/FAIR storage rings" has been submitted to the GPAC. The committee encouraged the authors to submit a full proposal. Among the physics topics proposed are axion/ALP searches and the measurement of parity even time reversal odd analyzing power in polarized proton tensor polarized deuteron scattering.

The main goal for 2023 is the preparation of a full proposal for experiments with polarized beams and targets at GSI/FAIR storage rings.

3 Neutrino Physics

The neutrino group is specialized in low-energy neutrino physics with liquid-scintillator (LS) based detectors. Borexino (Sec.3.1), the world's radio-purest 280 ton LS detector in the Laboratori Nazionali del Gran Sasso in Italy took data from May 2007 until October 2021, focused on solar neutrinos, geoneutrinos, and searches for rare processes in coincidence with astrophysical events. JUNO (Sec.3.2) will be the first multi-kton LS detector and it is currently under construction in Jiangmen, China. Its completion is expected by the end of 2023. The success of JUNO strongly depends on the levels of radiopurity that will be achieved. German groups are leading the construction of the 20 ton OSIRIS detector (Sec.3.3), that will monitor the level of radio-purity of the LS during the several months long period of filling the 20 kton JUNO central detector.

3.1 Borexino latest results with solar neutrinos

The Sun is powered via the fusion of hydrogen to helium that can proceed via two distinct mechanisms. The dominant proton-proton (pp) chain is responsible for the production of $\sim 99\%$ of the solar energy. The remaining en-

ergy is produced via the sub-dominant carbon-nitrogen-oxygen (CNO) cycle, in which the fusion is catalyzed by the presence of C, N, and O. These two mechanisms are also associated with the emission of electron flavor neutrinos (ν_e). These so-called *solar neutrinos* are the only direct messengers about the nuclear reactions occurring in the core of the Sun. In Borexino, the detection of solar neutrinos is primarily based on the scintillation light produced by deposition of energy in scintillating medium by the recoiled electrons from neutrino-electron elastic scattering interaction.

3.1.1 Improved Measurement of CNO-cycle solar neutrinos and its implication for the Standard Solar Model

In 2020, Borexino provided the first observation of CNO solar neutrinos⁵. This represents the first experimental evidence of the existence of the CNO cycle in nature. While it is subdominant in the Sun, it is expected to be the dominant stellar hydrogen burning process in the universe. The measurement of CNO solar neutrinos is also relevant for solving one of the key issues of solar physics, the so-called "metallicity-puzzle", where metallicity refers to the abundance of heavy elements in the Sun.

In 2022, Borexino presented an improved measurement of the rate of interaction of CNO solar neutrinos. This measurement was used for the evaluation of the carbon + nitrogen abundance in the solar interior, using solar neutrinos for the first time. These results were firstly presented at the Neutrino 2022 conference, followed by the publication in *Physical Review Letters*⁶. This publication was selected by the journal as *Editors' Suggestion* and was also featured in *Physics*.

This analysis is based on the data-set collected in the so-called Phase-III period, which extends from January 2017 to October 2021. Several backgrounds contribute in the same energy range as the CNO signal. The latter is represented by a featureless recoiled electron energy spectrum with the end-point energy of 1.517 MeV and with the rate of few counts per day (cpd) in 100 tonnes of LS. Therefore, a multivariate fit is performed in order to disentangle the CNO neutrino signal from other solar neutrinos and backgrounds. Similar to the 2020 publication, this fit procedure uses constraints on the rates of *pep* solar neutrinos and the intrinsic ^{210}Bi background to break their spectral degeneracy with the CNO solar neutrinos. In particular, the new ^{210}Bi constraint is now estimated to be (10.8 ± 1.0) cpd/100 t via the counting of α -decays of its daughter ^{210}Po using pulse shape variable in the cleanest region of the detector, called the Low Polonium Field (LPoF). The LPoF was formed as the result of the detector's thermal stabilisation campaign performed between 2015 and

⁵Experimental evidence of neutrinos produced in the CNO fusion cycle in the Sun, *Nature* **587** (2020) 577.

⁶Improved Measurement of Solar Neutrinos from the Carbon-Nitrogen-Oxygen Cycle by Borexino and Its Implications for the Standard Solar Model, *Phys. Rev. Lett.* **129** (2022) 252701.

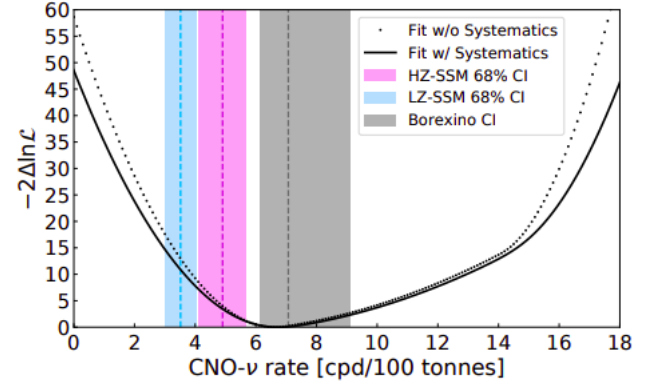


Figure 18: NO-neutrino rate negative log-likelihood profile obtained from the multivariate spectral fit (dashed black line) and after folding in the systematic uncertainties (black solid line). The blue, violet, and grey vertical bands show 68% confidence intervals (C.I.) for the low metallicity SSM B16-AGSS09met ((3.52 ± 0.52) cpd/100 tonnes) and the high metallicity SSM B16-GS98 ((4.92 ± 0.78) cpd/100 tonnes) predictions and the new Borexino result including systematic uncertainty, respectively.

2016, necessary to minimize the residual convection in the innermost parts of the detector that brought out-of-equilibrium ^{210}Po from peripheral sources to the fiducial volume. The updated ^{210}Bi constraint is now lower due to the removal of the 2016 data with high ^{210}Po rate and more precise than the previous value due to the inclusion of new period with stable LPoF after February 2020. After fitting, the CNO interaction rate with zero-threshold is estimated to be $6.7^{+2.0}_{-0.8}$ cpd/100 tonnes including systematic errors. The observed interaction rate can be converted to a flux of $6.6^{+2.0}_{-0.9} \times 10^8 \text{ cm}^{-2} \text{ s}^{-1}$ CNO neutrinos at Earth. This result confirms the existence of the CNO cycle at with about 7σ significance, which can be interpreted from Fig. 18.

The new result on CNO solar neutrinos is included in a global analysis of all solar neutrino data and KamLAND reactor data in order to investigate the compatibility of experimental measurements with the predictions of the Standard Solar Model (SSM). The resulting solar ν fluxes are found to be in agreement with the high-metallicity SSM (B16-GS98) predictions, while the comparison features a small tension with the low-metallicity SSM (B16-AGSS09met) model. Information on metallicity is also obtained by exploiting the direct dependence of CNO cycle on the C and N abundances in the solar core. The precise measurement of ^8B neutrino flux from the global analysis, which strongly depends on temperature, is used "as a thermometer" to decouple the CNO flux dependence on temperature from its dependence on metallicity. This provides the first-ever measurement of chemical abundances in the Sun's core using solar neutrinos. The C + N abundance with respect to the H in the photosphere is $(5.78^{+1.86}_{-1.00}) \times 10^{-4}$, obtained using extrapo-

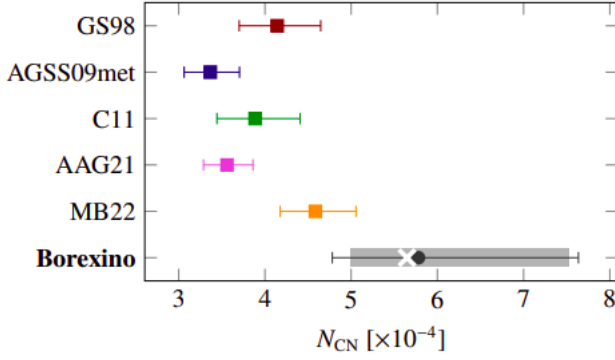


Figure 19: Comparison of abundance of (C+ N)/H in the solar photosphere, N_{CN} , from spectroscopy (squares) and using solar neutrinos (circle). The gray area highlights the uncertainty due to the precision of the CNO rate measurement. The white cross marks the result of the very same study repeated changing the reference SSM from the B16-GS98 to the B16-AGSS09met.

lation of the C + N abundance from the core to the photosphere. It was found that the abundance of C and N in the Sun determined with solar neutrinos is in good agreement with all high-metallicity photospheric measurements (MB22, GS98), while it shows $\sim 2\sigma$ tension with all the low-metallicity photospheric measurements (AGSS09met, C11, AAG21), as demonstrated in Fig. 19.

3.1.2 Search for Low-Energy Signals from Fast Radio Bursts

Fast Radio Bursts (FRBs) are millisecond radio transients observed at the extra-galactic or cosmological distances, with unclear nature of their source. The most popular class of models proposed to explain their origin involve the emission of neutrinos, which could be potentially detected by large Cherenkov or LS detectors. In this analysis, the search for an excess in the number of events produced by neutrino-electron elastic scattering and the inverse beta-decay on protons (IBD) has been performed using the full exposure Borexino data set, between 2007 and 2021. As a result, no statistically significant increase in the number of events over the backgrounds was observed. Furthermore, the strongest upper limits on FRB-associated neutrino fluences of all flavors is obtained in the 0.5–50 MeV neutrino energy range. In 2022, this work was published in European Physical Journal C⁷.

3.1.3 Independent determination of the Earth's orbital parameters with solar neutrinos

Borexino collaboration has published the first precise measurement of the Earth's orbital parameters based

⁷Search for Low-Energy Signals from Fast Radio Bursts with the Borexino Detector, *Eur. Phys. Journal C* 82 (2022) 278.

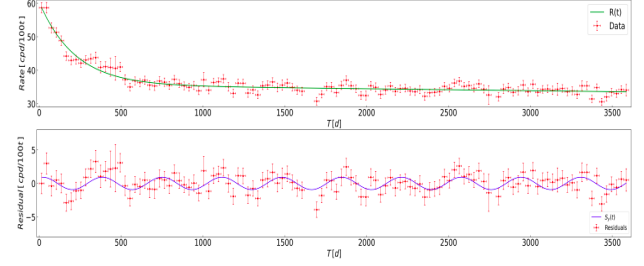


Figure 20: Top: Full Borexino rate time series in the RoI dominated by the ${}^7\text{Be}$ solar neutrino signal fitted to the trend model to remove background components. The rate in cpd/100 tonnes is binned in time intervals of 30 days with starting point of the time axis (in days) at 12:00 AM of December 11th 2011, in UTC time. Bottom: Residuals of the time series with respect to the trend model. The blue sinusoidal best fit of the residual rate indicates the presence of a significant annually modulated signal.

solely on solar neutrinos in *Astroparticle Physics*⁸ journal. This measurement represents an additional prove of the solar origin of the Borexino signal. The analysis estimates the Earth's orbit eccentricity exploiting the variation of the solar neutrino flux produced in the Sun's core and detected by Borexino on the Earth, caused by the Sun-Earth distance change as a function of time due to the non-circular shape of the orbit. The search for solar neutrino signal modulations in the frequency range between one cycle/year and one cycle/day using the generalized Lomb-Scargle method was performed on the time series of the Borexino measured rate as shown in Fig. 20. The used dataset period ranges from December 11th 2011 to October 3rd 2021. The chosen energy region of interest (RoI) is 300 - 827 keV with a dominant contribution from the mono-energetic ${}^7\text{Be}$ solar neutrinos and a subdominant contribution from *pep* and CNO neutrinos, including the backgrounds such as ${}^{210}\text{Bi}$ and ${}^{85}\text{Kr}$ β decays, γ -ray emitting external backgrounds, and cosmogenic ${}^{11}\text{C}$ decays. The estimated eccentricity is $\epsilon = 0.0184 \pm 0.0032$ (stat+sys). The hypothesis of no annual modulation of the solar neutrino signal due to the eccentricity of Earth's orbit is excluded with a significance greater than 5σ . No other significant modulation frequencies are found. Strong constraints are placed on the amplitudes of other frequencies of interest, such as day-night effects and correlations with the Sun's rotation around its axis. The limits for the percent diurnal modulation and the percent solar rotation day are $< 1.3\%$ (90% CL) and 1.8% (90% CL), respectively. These updated bounds are relevant in solar modelling and in constraining various non-standard neutrino interactions.

⁸Independent determination of the Earth's orbital parameters with solar neutrinos in Borexino, *Astroparticle Physics* 145 (2023) 102778.

3.1.4 First directional measurement of sub-MeV solar neutrinos

In 2022, the first measurement of sub-MeV solar neutrinos using their associated subdominant Cherenkov radiation was presented by Borexino. This work was jointly published in *Physical Review Letters*⁹ and *Physical Review D*¹⁰. This provided an experimental proof of principle for the exploitation of directional Cherenkov light in future LS-based neutrino experiments using a newly developed technique called *Correlated and Integrated Directionality* (CID). CID is based on constructing an angular distribution for the solar neutrino events in a energy region of interest (RoI) of 0.54 MeV - 0.74 MeV, dominated by ⁷Be solar neutrino events. The characteristic angle correlates the direction of first PMT hits of each event (defined between the hit PMT and the reconstructed event vertex) with the known direction from the Sun. The number of solar neutrino events ($N_{\text{solar-v}}$) is then statistically inferred from the contribution of Cherenkov photons correlated to the position of the Sun. The data-set used for the analysis extends from May 2007 to May 2010 referred to as Phase-I period. The extracted number of solar neutrino events in RoI from the best fit of first 2 hits of 19,904 data events is $N_{\text{solar-v}} = 10887^{+2386}_{-2103}(\text{stat}) \pm 947(\text{sys})$. Figure 21 shows the measured angular distribution for the first PMT hits of all selected events along with the best fit. The best fit result is well in agreement with the SSM expectation, rejecting the hypothesis of no neutrino signal at $>5\sigma$ confidence level. The extracted interaction rate of ⁷Be solar neutrinos in Borexino is $R_{\text{Be7}} = 51.6^{+13.9}_{-12.5}$ cpd/100 tonnes by fixing the sub-dominant *pep* and CNO solar neutrino contributions in RoI to their SSM predictions. It is well in agreement with both SSM predictions as well as Borexino spectral fit results in Phase-I. Furthermore, performing a dedicated calibration of the Cherenkov light is highly recommended for more precise solar neutrino measurements.

An effort is now ongoing to exploit the CID method for the measurement of CNO solar neutrinos using enlarged Borexino dataset. Furthermore, the inferred number of CNO + *pep* solar neutrinos will be applied as a constraint in the multivariate spectral fit to extract the CNO rate with and eventually even without ²¹⁰Bi constraint in a combined Phase II + Phase III dataset.

3.2 Towards completion of the JUNO detector

The Jiangmen Underground Neutrino Observatory (JUNO) is a multipurpose 20 kton liquid scintillator detector positioned 53 km from the Yangjiang and Taishan nuclear power plants in South China. It is currently under construction in an underground laboratory with a 650 m

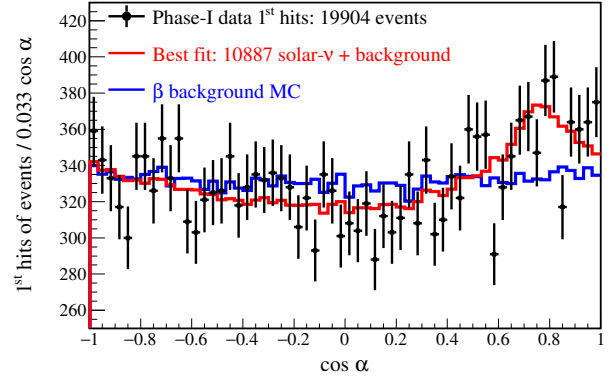


Figure 21: Directional measurement of solar neutrinos by Borexino: The $\cos \alpha$ distributions of the first hits of all the selected data events (black points) in RoI compared with the best fit curve (red) for the resulting number of solar neutrinos $N_{\text{solar-v}}$ plus background. All histograms are normalized to the data statistics. It can be seen that the data points cannot be explained by the background-only hypothesis (blue).

overburden and with a planned completion in 2023. The experiment is designed for the determination of the neutrino mass ordering, one of the key open questions in neutrino physics. This measurement will be based on the observation of vacuum oscillation pattern of antineutrinos from the two nuclear power plants at 53 km baseline. The unprecedented expected energy resolution of $3\%/\sqrt{E} [\text{MeV}]$ and the large fiducial volume, offer exciting opportunities for addressing many important topics in neutrino and astro-particle physics. The final design of the detector and the updated JUNO physics strategy are summarized in a recent review paper in *Progress in Particle and Nuclear Physics* journal¹¹.

The civil construction of the the JUNO site was completed in December 2021. The Central Detector (CD) will be filled with 20 kton of LS contained in a spherical acrylic vessel with a diameter of 35.4 m. The acrylic panels of the CD detector are being mounted from an installation platform, whose construction was completed in May 2022. The CD is supported by a stainless steel support structure that was finished in June 2022, as it is shown in Fig. 22. On the support structure will be mounted the PMTs with their front-end electronics. The CD will be characterized by high photocathode coverage of 78%, provided by 17,612 20-inch PMTs (LPMTs) and 25,600 3-inch PMTs (SPMTs). The Water Cherenkov Detector (WCD) will consist of 35 kton of ultra-pure water surrounding the CD and will be equipped with 2400 LMPTs. WCD will serve as an active veto of cosmic muons as well as a passive shield against external background. The further key steps towards completion of the JUNO detector are the finalisation of the acrylic vessel construc-

⁹First Directional Measurement of sub-MeV Solar Neutrinos with Borexino, *Phys. Rev. Lett.* **128** (2022) 091803.

¹⁰Correlated and Integrated Directionality for sub-MeV solar neutrinos in Borexino, *Phys. Rev. D* **105** (2022) 052002.

¹¹JUNO physics and detector, *Progress in Particle and Nuclear Physics*, **123** (2022) 103927.



Figure 22: Support structure of the central detector and the installation platform with the workers, photo from June 2022.

tion, PMTs installation, completion of the LS purification plants and OSIRIS pre-detector, and finally 6 months long filling of the LS into CD.

The JUNO LPMTs are of two kinds, about 1/3 is from Hamamatsu and the rest are multi-channel (MCP) PMTs produced by Northern Night Vision Technology (NNVT). All LPMTs have been produced, tested, and instrumented with waterproof potting. An extensive LPMT testing program began in 2017 and elapsed for about four years. A collaboration paper was published in the European Physical Journal C¹² presenting the design of the testing systems and demonstrating a good quality of all accepted PMTs. More than fifteen performance parameters (including the photocathode uniformity) were tested. This constitutes the largest sample of 20-inch PMTs ever produced and studied in detail to date.

The unprecedented size and energy resolution of JUNO enables it to make precise measurement of the oscillated spectrum of reactor antineutrinos, shown in Fig. 23, and to observe the so-called solar and atmospheric oscillation simultaneously. As a result, the measurement of the Δm_{31}^2 , Δm_{21}^2 , and θ_{12} neutrino oscillation parameters will reach better than sub-percent precision (see Fig. 24). This significant improvement is one of the primary physics goals of the experiment. The new sensitivity estimate for this measurement has been published in a collaboration paper in the Chinese Physics C¹³. These measurements will constitute an important input to other experiments, provide constraints for model building, and enable more precise searches for physics beyond the Standard Model in the neutrino sector.

The damping signatures at reactor spectrum expected in JUNO could be motivated by various new physics models, including quantum decoherence, $\nu 3$ decay, neutrino absorption, and wave packet decoherence. Their study was published in a collaboration paper in the Journal of

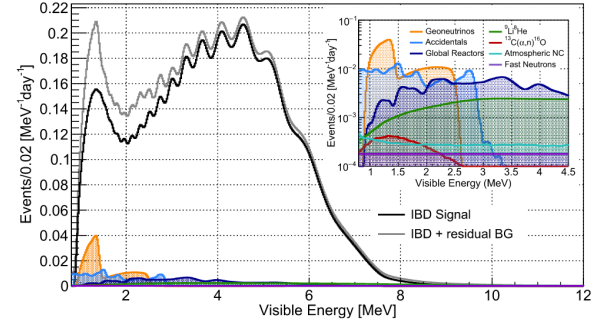


Figure 23: Visible energy spectrum expected in JUNO as measured with the LPMT system with (grey) and without (black) backgrounds.

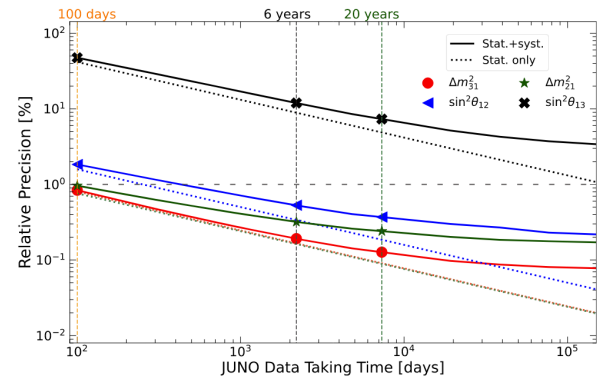


Figure 24: Relative precision of the neutrino oscillation parameters as a function of JUNO data taking time. The horizontal gray dashed line stands for 1% relative precision. The green dotted and red dotted lines are on top of each other since the statistical-only precision is essentially identical for the Δm_{31}^2 and Δm_{21}^2 parameters.

High Energy Physics¹⁴. Here the ability of JUNO to constrain these damping parameters and disentanglement of these different damping signatures have been reported.

Diffuse Supernova Neutrino Background (DSNB) neutrinos represent an integrated neutrino flux from the past supernova explosions in the visible Universe. DSNB has not been detected yet. A comprehensive study on the prospects for its discovery in JUNO was published as a collaboration paper in the Journal of Cosmology and Astroparticle Physics¹⁵. It reports that even for the pessimistic scenario with non-observation, JUNO would strongly improve the current best limits and exclude a significant region of the model parameter space. Together with the existing water-Cherenkov detector SK-Gd, it stands for the pioneering efforts to first observe the DSNB signal in the next decade. JUNO has a large dis-

¹²Mass Testing and Characterization of 20-inch PMTs for JUNO, *Eur. Phys. J. C* 82 (2022) 1168.

¹³Sub-percent Precision Measurement of Neutrino Oscillation Parameters with JUNO, *Chinese Physics C* 46 (2022) 123001.

¹⁴Damping signatures at JUNO, a medium-baseline reactor neutrino oscillation experiment, *J. High En. Phys.* 06 (2022) 062.

¹⁵Prospects for detecting the diffuse supernova neutrino background with JUNO, *JCAP* 10 (2022) 033.

covery potential of 3σ in 3 years of data taking for the nominal theoretical SN models.

JUNO has also potential to search for proton decay in $p \rightarrow \bar{\nu} K^+$ mode. The excellent energy resolution of JUNO permits to suppress the sizable background caused by other delayed signals. The sensitivity study was submitted to the Physical Review D¹⁶ as a collaboration paper.

The physics potential of detecting ^8B solar neutrinos is exploited at JUNO in a model independent manner by using three distinct channels of the charged-current (CC), neutral-current (NC), and elastic scattering (ES) interactions. Due to the largest-ever mass of ^{13}C nuclei in the liquid-scintillator detectors and the potential low background level, ^8B solar neutrinos would be observable in the CC and NC interactions on ^{13}C for the first time. This has been studied and reported in a collaboration paper¹⁷ submitted to the Astrophysical Journal.

The JUNO sensitivity to ^7Be , pep , and CNO solar neutrinos will highly depend on the achieved radio-purity level. Several radio-purity scenarios were considered in a recent study: from the level achieved by the Borexino experiment up to the IBD one (minimum required for the NMO determination), as demonstrated in Fig. 25. For ^7Be neutrinos, JUNO can reach the current precision of 2.7% achieved by Borexino after one year of data-taking. For the pep neutrinos, JUNO can improve the current best Borexino result of 17% after two years of data-taking (except for the IBD scenario when 6 years are needed). For the CNO neutrinos, constraint on the rate of pep neutrinos in the spectral fit remains crucial and can be achieved using the exiting data and theoretical assumptions. However, JUNO will be able to detect CNO solar neutrinos without the ^{210}Bi constraint applied in the Borexino analysis and to achieve 20% precision in two to four years (except for the IBD scenario). Additionally, JUNO might be able to distinguish the ^{13}N and ^{15}O CNO components for the first time. The neutrino group has a leading role in this analysis that was presented at the Neutrino 2022 conference. A collaboration paper about these studies is currently under internal review.

3.3 Online Scintillator Internal Radioactivity Investigation System (OSIRIS) of JUNO

JUNO physics potential strongly depends on the radiopurity levels of the LS that will be achieved. In order to meet the stringent requirements, e.g. U/Th concentration of 10^{-15} g/g (for the NMO determination) and 10^{-17} g/g (for solar neutrino measurement), a scintillator processing system has been built. The LS system includes four purification stages (Al_2O_3 column, distillation, water extraction, and steam stripping) as well as storage and

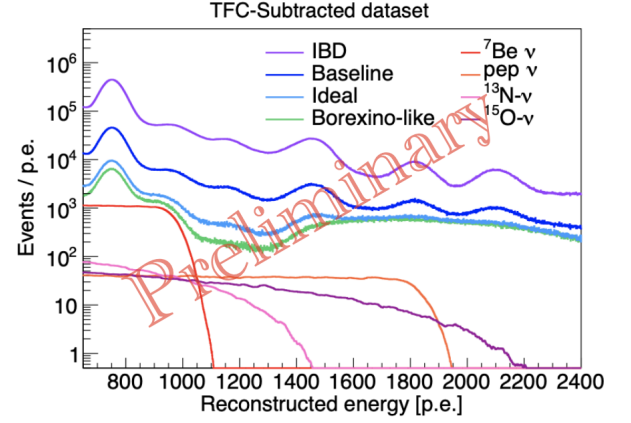


Figure 25: Various radiopurity scenarios, considered in the JUNO solar neutrino sensitivity study, compared to the expected spectra of ^7Be , pep , ^{13}N , and ^{15}O solar neutrinos for 1 year statistics.

mixing tanks. The achieved level of LS radiopurity will be tested in 20 ton detector of OSIRIS (Online Scintillator Internal Radioactivity Investigation System). The OSIRIS design has been optimized to evaluate LS contamination with ^{238}U and ^{232}Th via tagging the ^{214}Bi - ^{214}Po and ^{212}Bi - ^{212}Po delayed coincidences occurring in the respective decay chains. After a successful test of each purification batch, the LS will be filled into the CD. OSIRIS features an 18 ton LS target within an acrylic vessel of 3 m width and 3 m height. Sixty-four 20-inch Large Photomultiplier tubes (LPMs) mounted on a stainless steel frame instrument the watershielded target. Twelve additional LPMs are employed in the water Cherenkov muon veto of OSIRIS, which is separated from the inner detector by optical foils. The originally foreseen intelligent PMTs (iPMTs), a development of RWTH Aachen that was strongly supported by the neutrino group members, were found to be non-operational after transportation to China. Therefore, the iPMTs were replaced by JUNO LPMs.

Within OSIRIS, the neutrino group is responsible for the source insertion calibration system, a refurbished Automated Calibration Unit (ACU, see Fig. 26) provided by the Daya Bay collaboration. It features three independent wheels mounted on a turntable, allowing to lower calibration sources directly into the LS volume. In order to maximise the variation of the detector response at different heights, the ACU is placed 1.2 m off-center to the central axis of OSIRIS. Three calibration sources have been purchased by the neutrino group. A multi-gamma source consisting of ^{137}Cs , ^{60}Co , and ^{65}Zn with a combined activity of several kBq will be employed for the calibration of energy and vertex reconstructions. A 435 nm-LED allows the calibration of LPM timing and charge responses. By tuning its intensity, also higher p.e. occupancies can be investigated. The third source, a low-

¹⁶JUNO Sensitivity on Proton Decay $p \rightarrow \bar{\nu} K^+$ Searches, arXiv:2212.08502v2 (2022), submitted to Physical Review D.

¹⁷Model Independent Approach of the JUNO ^8B Solar Neutrino Program, arXiv:2210.08437 (2022), submitted to APJ.

activity ^{40}K ($\leq 1\text{ Bq}$) is used to continuously monitor the LS properties during normal operation.

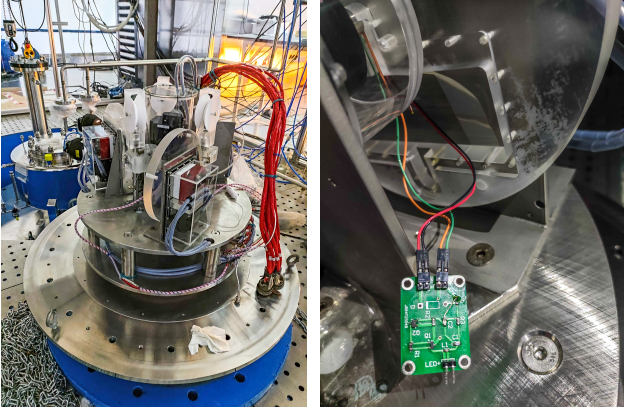


Figure 26: Left: Inside look of the opened ACU inside the top clean room of OSIRIS. Clearly visible are the three wheels on the turntable. The ACU is usually sealed from the outside by a Nitrogen-flooded bell jar. Right: Zoom on the LED driver board and the wheel cut-out in which it will be placed during normal operation. A special bearing allows continuous wheel rotations without shearing off the cables.

Since late September 2022, two members of the neutrino group have been heavily involved in the construction and commissioning of OSIRIS on-site in Jiangmen, China. The main focus is the preparation of the ACU for the upcoming commissioning and data-taking phases of OSIRIS. For this, the ACU control software as well as its control and readout hardware were tested to ensure proper functionality. The ACU itself was prepared for the installation of the calibration sources, planned for spring 2023.

Furthermore, the neutrino group is also involved in the data acquisition of OSIRIS. The so-called EventBuilder collects data streams from the LPMTs and combines them into events for further analysis. Due to the replacement of the iPMTs with LPMTs, the readout electronics as well as the acquisition software had to be adjusted. Here, the group performed various functionality tests of the whole LPMT readout chain and introduced software modifications reflecting the hardware changes. The understanding gained in these tests allows fast hardware checks during installation inside OSIRIS too.

Lastly, as the LPMTs differ in geometry from the iPMTs, the holders to mount them inside the detector had to be adapted as well. FEA-simulations and mechanical stability tests led to an improved assembly scheme which could be successfully employed in the installation of the first eight LPMTs (see Fig. 27). Together with the construction of a dedicated OSIRIS underground cleaning facility and the integration of a Daya Bay CCD system into OSIRIS, the neutrino group strongly contributed to the installation efforts. These installation works are currently ongoing, while a dedicated detector commissioning phase is planned to start in April 2023.



Figure 27: The first eight PMT modules of OSIRIS, which were installed above the acrylic vessel. The PMTs feature magnetic shieldings to reduce electronic noise and signal disturbances caused by the Earth's magnetic field. The white ropes visible on the bottom will be used to remove the protective cover of the acrylic vessel after the installation of measurement equipment has been completed.

4 Accelerator Research

4.1 Developments at COSY

In 2022 the COSY accelerator facility continued providing particle beams for its users (Fig. 45 and Table 3). New hardware installations and software developments were carried out to meet the requirements of the experiments and accelerator related studies envisaged for 2023.

4.1.1 Ion sources and JULIC

In order to optimize the beam polarization at the ion source while running the facility with un-polarized beam, a Lamb-shift Polarimeter was installed at the beam line of the polarized source II. Details are reported in "Polarised Beam Transport to the Lamb-Shift Polarimeter"; *Yu. Valdau et al.*, page 61.

4.1.2 Developments at the NESP beamline

For experiments related to the High Brightness Neutron Source (HBS) project, a dedicated low energy beam line (NESP) transporting particle beams from the cyclotron JULIC into the Big Karl experimental area (Fig. 28) has been built in 2018. This allowed for component testing and experimental validations of cross section for the HBS target development. With the installation of the Target-Moderator-Reflector-demonstrator (TMR) as well as the kicker and dipole magnets and a dedicated three field permanent magnet in 2022 the envisaged setup in the Big Karl area was completed. According to the proposed HBS-layout these newly built beamline, with the

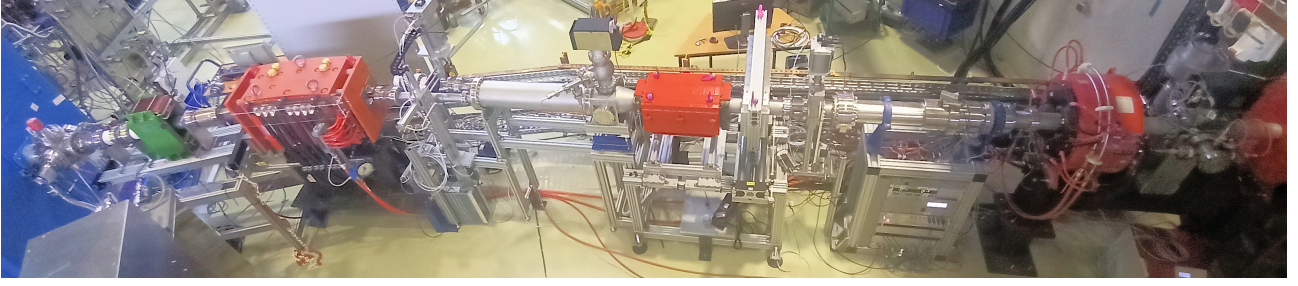


Figure 28: Beamline from JULIC into the BigKarl Area to do very first tests of cross section measurements.

additional magnets, provides the possibility to deflect the beam up to 40° for driving three target stations, scan the beam over targets, and to investigate timing related questions due to neutron production as well as for experimental setups.

The three-field permanent magnet (Fig. 29) is able to direct the beam onto three different paths. At the given beamline in the Big Karl area the permanent magnet can be shifted using a stepper motor for this purpose, so the beam enters the dedicated field region of the magnet. While the kicker magnet is used for testing the sophisticated timing scheme of HBS to run different target stations.

Beside the magnets, the beamline is equipped with beam current measurement devices as well as beam profile and position measurement instruments.

Beam profile measurements are done with a Multi Wire Proportional Chamber (MWPC) installed at the second beam exit window. This system is used for optimizing the beam spot on target. For vacuum safety reasons the accelerator and TMR vacuum are separated by a thin stainless steel foil. At this foil the negatively charged ions are stripped to positive ones. Measuring the current on this isolated foil allows for continuous monitoring of the beam being delivered onto the target. A second, isolated stainless steel exit window and a beam cup in the right-handed beam path give another current measurement possibility. Additional non-destructive beam instrumentation such as a Fast Current Transformer (FCT) and a Beam Position Monitor (BPM) will help operate the beamline at higher average beam current. Further details are described in "JULIC Neutron Platform"; *P. Zakalek et al.*, page 73 and on the poster "JULIC – driver accelerator for HBS"; *O. Felden et al.*, on page 77.

4.1.3 EPICS Integration

In the course of EPICS integration at COSY progress was achieved with various accelerator sub-systems. The effort to integrate the power supply control of the injection beamline (IBL) in collaboration with Cosylab d. d. was continued from last year. Furthermore the power supplies of the ion source beamline (QBL) were integrated in the EPICS control system.

In order to develop and test algorithmic access to the IBL,

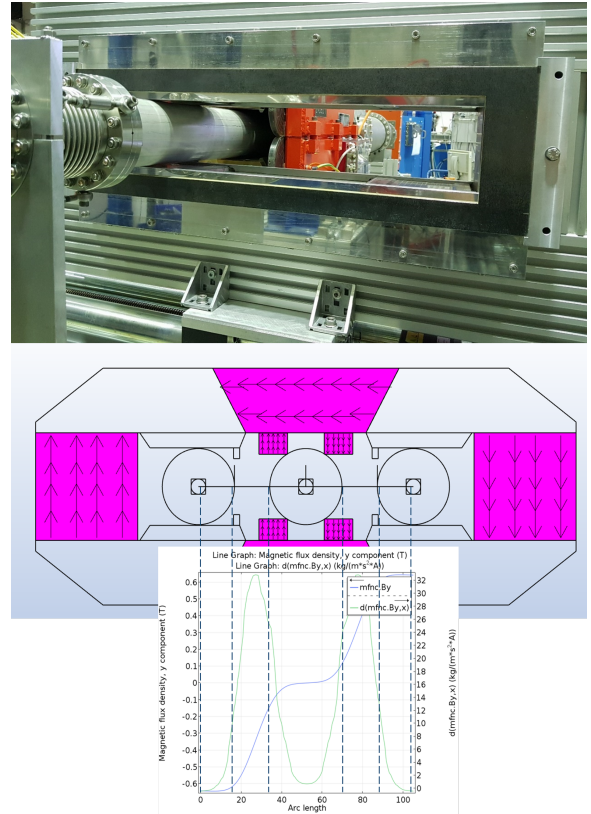


Figure 29: Three-field permanent magnet in position to bend the beam left-handed into the TMR. The lower sketch shows the dedicated field-regions and measured field-strength in the horizontal midplane.

an Simulator was developed. This is described in more detail in "The IBL Simulator - A Digital Twin for the IBL"; *J. Hetzel*, page 63.

To enable fast switching between the stripping foil and the viewer at injection location a stepper motor drive is built and tested. Controls software developed at iThemba LABS based on the DIAMOND Ethercat EPICS Master was adopted. The installation of the system in the COSY tunnel is scheduled for the spring 2023 in order to be used in the machine learning studies envisaged at COSY in 2023. This was also the motivation to upgrade the software that automatically reads and analyzes the viewer im-

ages in beamlines. This was done in collaboration with Cosylab d.d..

4.1.4 Power Converters

For the extraction of the beam towards one of the external beam lines, an electrostatic septum is used. To overcome instabilities of the old power converter a new one was tested and installed. The details are reported in "Upgrade of the COSY Extraction Septum Power Converter"; *K. Grigoryev et al.*, page 64. Ethernet capable interfaces were added to the power supplies of the injection and extraction beamlines.

Significant effort had to be made in cleaning and repairing numerous PS PCBs after water damage.

Thanks to the recent upgrades of the water cooling system independent operation of COSY and injector systems became possible. This enables additional energy saving.

4.1.5 ExB Deflector

An electrostatic deflector is one of the major components of the EDM prototype storage ring designed by the JEDI collaboration. To investigate the possibility of reaching desired electric field as well as to gain practical experience in handling such a device a full size deflector prototype was produced. The sophisticated infrastructure available at COSY was crucial for carrying out the studies. The details are described in "ExB - Deflector Tests at COSY"; *K. Grigoryev et al.*, page 66, while the developments towards an interlock system for the deflector are described in "ExB - Deflector Interlock and Control Systems"; *M. Schubert*, page 68.

4.1.6 Upgrade of Beam Current Diagnostics of the COSY Beamlines

The current readout electronics of numerous Faraday cups and collimators in the ion source, cyclotron and COSY injection beam lines have been replaced by modern commercially available devices. EPICS integration and the development of new operator interfaces was done in house. The new system provides much higher accuracy and time resolution. The controls of pneumatic drives of beam instrumentation devices have also been upgraded mainly for the reasons of seamless EPICS integration. The new hardware is based on EtherCat technology.

4.1.7 Model

Accompanying the integration of the IBL power supplies in EPICS a new on-line model has been developed. This model calculates the optical functions as well as the beam width. It is based on the actual current settings of the magnetic elements in the IBL but can as well be switched to an offline mode for test of a set of currents prior to its application.

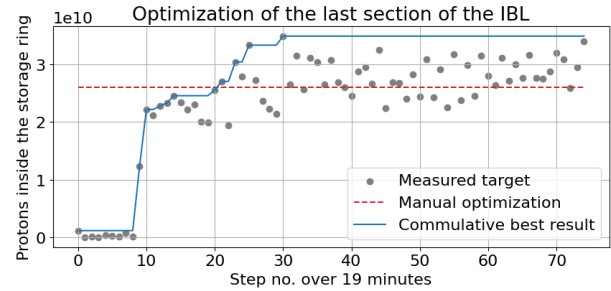


Figure 30: Evolution of the number of recorded particles in COSY during a run with the bayesian optimization method.

4.1.8 Injection Beamline Optimization

The EPICS framework allows for algorithmic access to the elements with an influence on beam properties as well as to the diagnosis element in the IBL. In a dedicated beam time the automated optimization of the IBL has been demonstrated. For this demonstration different algorithms have been prepared and tested. The most sophisticated optimization was done with Bayesian optimization, see Figure 30. This is described in more detail in "Injection optimization using machine learning at the Cooler Synchrotron COSY"; *A. Awal*, page 72.

4.1.9 Access to Accelerator Related Information

360° photo walk-through In order to have a 360° photo walk-through, the accelerator complex was photographed with a 360deg camera and later the photographs were put into a special software to create a walk-through experience. Most of the accelerator, not only COSY but also e.g. the cyclotron or the power supply rooms, are available. The walkthrough was shown at the open house with several VR googles and on several PCs, as a in-person walkthrough was not possible for radiation safety reasons. Legal clarifications, are ongoing to grand a general public access.

COSY Documentation which is still on paper, was continued to be scanned and the content beeing processed via OCR to be machine readable. Afterwards the documentation is put on a system hosted by the controls group to have it full text searchable.

4.2 Progress of the HESR

While FAIR continues its commitment towards the Modularized Starting Version (MSV) that includes the realisation of the HESR strong focusing is crucial for the success of the entire FAIR Project under current boundary conditions. In October 2022 the "First-Science and Staging Review of the FAIR Project" has been published. The review included the recommendation to prioritize projects in steps that were labeled as early science (ES),

first science (FS) and first science plus (FS+). It is anticipated that the Scientific Council of FAIR will follow the recommendations. As the HESR is not part of any of the mentioned steps, preparations to freeze the HESR sub-project are under way. The HESR related activities in Jülich are to be frozen in the manner that guaranties as little damage as possible for the sub-project assuming its reactivation once the resources became available. Most activities in 2023 will be focused on documentation and transport of components from Jülich to the storage in Weiterstadt. Progress achieved within the HESR work packages in 2022 is described below.

4.2.1 Work package Magnets and Pre-assembly

All 46 bending dipole magnets have been equipped with the necessary vacuum chambers and have been delivered to the storage in Weiterstadt. This includes four magnets which were prepared for the SPARC experiment and therefore possess modified vacuum chambers, where a laser beam for the experiment can be passed in and out. This laser beam will interact with the HESR beam. To move the dipoles to their dedicated positions in the tunnel an air cushion system will be used. This system (see Fig. 31) has successfully been tested at one of the dipole magnets. Each dipole weighs 34 tons.

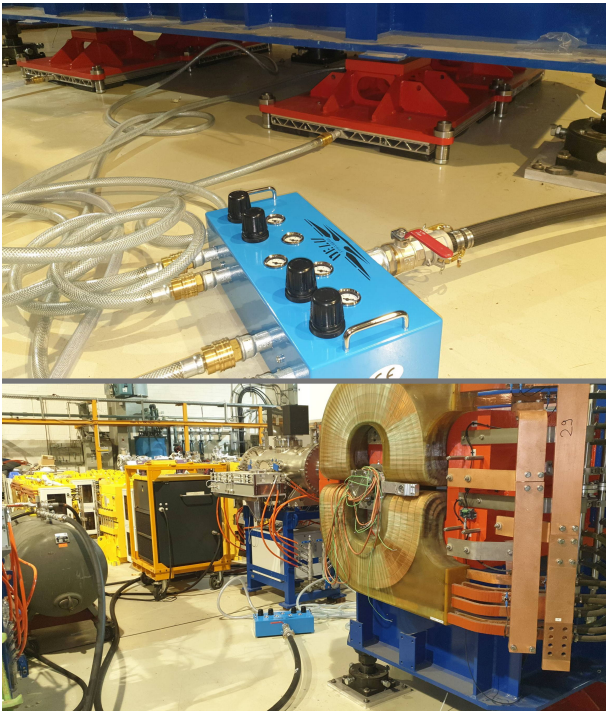


Figure 31: Installation of the air cushion system at the HESR dipoles for testing. Two of the four plates that lift the magnet are visible on the left photograph. The right image shows the dipole (red magnet) and the supporting equipment (compressor, tank).

4.2.2 Work Package RF System

One of the cavities for the HESR was installed in COSY for testing already in late 2021. In early 2022 some initial tests including the recording of calibration data have been performed (see Fig. 32). Since then it is used to accelerate the beam during the operation of COSY. As expected its stability and reliability could be demonstrated.

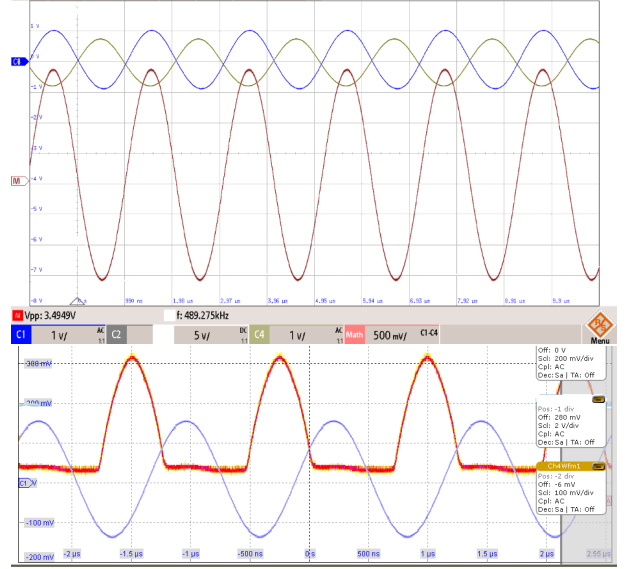


Figure 32: The measured gap voltage as seen by the beam is shown in the upper picture (red-brown curve, scale: 1:1000). The phase probe signal of the bunched COSY beam is shown in the lower plot (red curve). The bunching and acceleration was done with the HESR cavity.

4.2.3 Work Package Beam Diagnostics

Beam position monitor (BPM) Up to now 50 BPMs are delivered to Jülich. Calibration measurements on the test bench continued in order to achieve the required accuracy for the orbit measurements in the HESR. Details of the measurement method are described in "BPM Test Bench Operation for HESR"; A. Halama *et al.*, page 70. The BPMs are being installed in the quadrupole assemblies. For the comparably small electrical currents expected at the HESR, additional pre-amplifiers have to be installed in addition to the FAIR-wide pre-amplifier A110. The design was finished and a review was performed, which is still waiting for its formal acknowledgement. The additional pre-amplifier will be used not only with the BPMs in the HESR, but also at the CR, some HEBT beam-lines and the ESR. A total of 110 BPMs are planned to be equipped with these.

Ion clearing (IC) The ion clearing chambers were already delivered in 2021 and are waiting for the assembly in the quadrupole units mentioned above.

Viewer The mechanical design for viewers (see Fig. 33) and beam diffusors was finished and the production of the series has been completed in the IKP machine shop. The manufacturing of vacuum chambers, which are as well needed for storage, started at ZEA-1 machine shop.

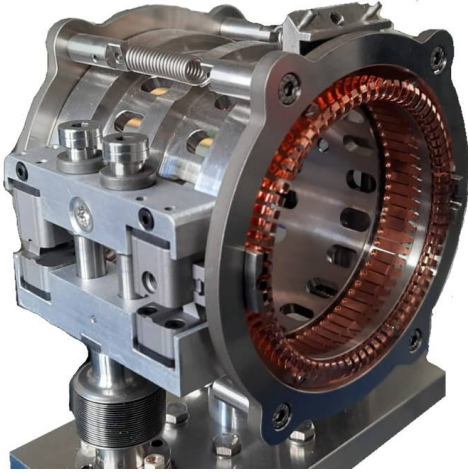


Figure 33: RF cage assembly, ready for installation into the viewer vacuum chamber.

Ionization beam profile monitor (IPM) The mechanical design is completed. The manufacturing of the 1st of series is nearly finished. The technological aspects of a fine stainless steel mesh being diffusion-welded to a frame have been worked out by ZEA. Parts of the mechanical construction are illustrated in Figure 34. All IPMs within GSI and FAIR will be equipped with these meshes. The mesh will be installed in front of the position sensitive detectors of IPMs as well as in front of the UV lamps which are used for detector calibration. The series production of the meshes is ongoing. The envisaged design review for the beam profile monitor is still pending.

Scraper The manufacturing of both scrapers is finished. The mechanical and electrical tests of the entire systems including the stepper motors and motor controllers have been performed successfully. The scrapers are being prepared for vacuum testing and baking.

Beam Loss Monitor (BLM) 20 scintillation detectors produced by GSI have been delivered to IKP. They are to be integrated in the FESA test system. The operation of the system is planned during the 2023 COSY beamtime.

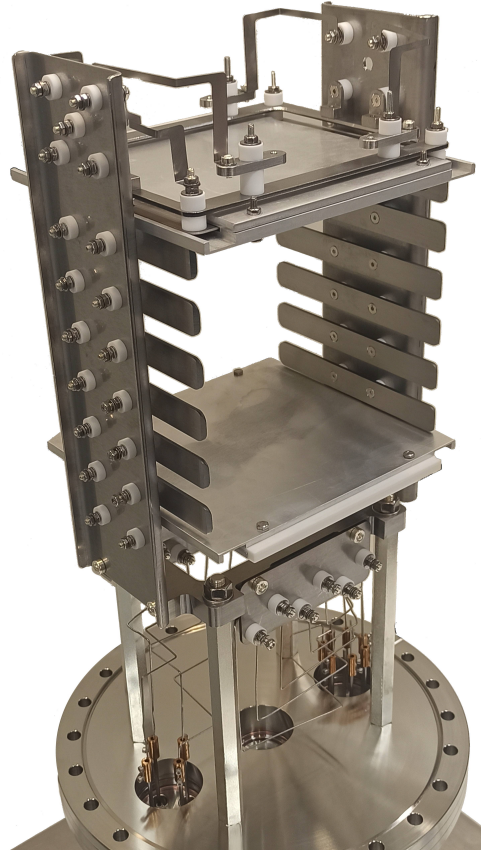


Figure 34: Inner parts of the IPM 1st of series during assembly in the IKP workshop. During assembly covers are mounted, therefore the openings for the UV light and ions are closed on the picture.

5 Further Activities

5.1 LHCb Polarized Target Experiment

Over the past 20 years, the Jülich group, together with the INFN Section of Ferrara, has developed a solid and acknowledged experience in the design and construction of storage cells for gaseous targets. The use of this technology has had a significant impact in the field of experimental hadronic physics. Examples of the application of this technology are the target of the HERMES experiment at HERA (DESY), operated from 1995 to 2007, that of the OLYMPUS experiment at DORIS (DESY), operated in the period 2012-2013, and that of the PAX/JEDI experiment, currently in operation at COSY (Forschungszentrum Jülich).

The storage cell, typically made of a 50-200 mm thick layer of aluminum with cylindrical geometry, is placed inside the beam-pipe of the accelerator, coaxially with the beam. The latter then intercepts directly the target gas contained into the cell, without interacting with other materials, as in the case of solid targets. Furthermore, with respect to the more traditional gaseous jet targets, the use of a storage cell allows to reach areal densities of

the order of $10^{13} - 10^{14} \text{ atoms/cm}^2$, i.e. up to two orders of magnitude higher.

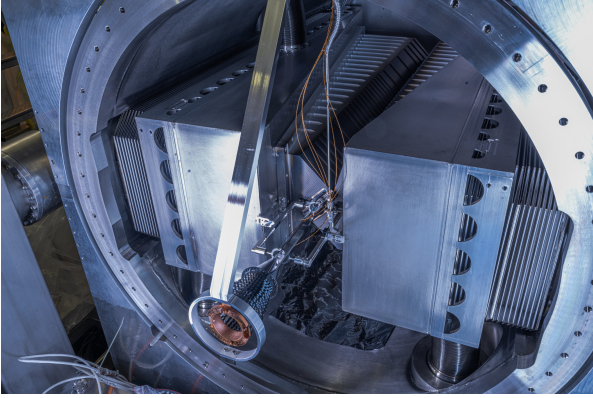


Figure 35: The target cell at the interaction point of LHCb.

The experience acquired in the framework of CSN3 experiments, has recently allowed to develop a storage cell for the LHCb experiment (see Fig. 35), SMOG2, which will be used for the LHCSpin project¹⁸, that aims at extending the LHCb fixed target program in Run4 (expected to start in 2028).

SMOG2 is a gas target confined within a 20 cm-long aluminium storage cell that is mounted at the upstream edge of the VELO detector, 30 cm from the main interaction point, and coaxial with the LHC beam. The storage cell technology allows a very limited amount of gas to be injected in a well defined volume within the LHC beam pipe, keeping the gas pressure and the density profile precisely controlled, and ensuring that the beam pipe vacuum level stays at least two orders of magnitude below the upper threshold set by the LHC. The cell is made of two halves, attached to the VELO with an alignment precision of 200 μm . Like the VELO halves, they can be opened for safety during LHC beam injection and tuning, and closed for data taking.

The storage cell was successfully installed upstream of the LHCb detector in Summer 2020. Starting from RUN3 (2021), LHCb is therefore the only LHC experiment to be provided with two distinct interaction points and the possibility of operating simultaneously in two collision modes: collider and fixed- target mode. The plot in Fig. 36 is the result of a preliminary LHCb analysis of 2022 data, which shows both the beam-gas target and the beam-beam collision peaks. The beam-gas collisions occurs at a center-of-mass energy of 115 GeV for proton beams and 72 GeV for lead beams. SMOG2 will allow to carry out precision studies in the field of QCD and astroparticle physics in essentially unexplored kinematic regions.

The fixed-target physics program at LHC has been greatly enhanced with the recent installation of the

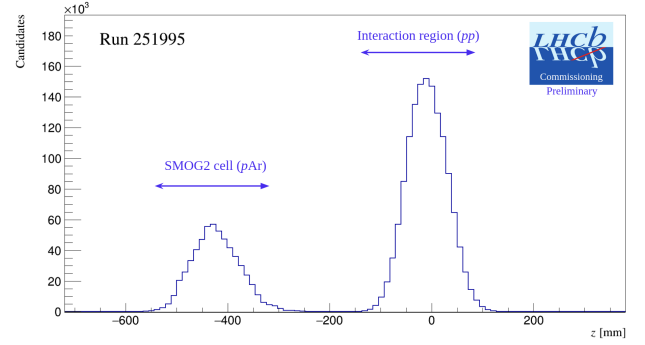


Figure 36: Preliminary LHCb analysis showing the beam-gas target and the beam-beam collision peaks.

SMOG2 setup at LHCb. LHCSpin is the natural evolution of SMOG2 and aims at installing a polarized gas target to bring spin physics at LHC for the first time, opening a whole new range of exploration. With strong interest and support from the international theoretical community, LHCSpin is a unique opportunity to advance our knowledge on several unexplored QCD areas, complementing both existing facilities and the future Electron-Ion Collider.

5.2 A new Method to polarize Atoms, Molecules and their Ions

A particle moving through a static but oscillating magnetic field with wavelength λ experiences an incoming electromagnetic wave in its inertial system at rest. Depending on its velocity the time-of-flight $\Delta t = \lambda/v$ and the frequency $f = 1/\Delta t$ is determined. Of course, the velocity of this electromagnetic wave will be $v \ll c$, but the equation $v = \lambda \cdot f$ still holds. For a typical beam energy of 1 keV ($v \sim 4 \cdot 10^5 \text{ m/s}$) and $\lambda = 20 \text{ cm}$ the frequency is about 2 MHz and the Planck-Einstein relation yields a photon energy of $\sim 8 \text{ neV}$ that can be used to induce magnetic dipole transitions, e.g. within the hyperfine substates of metastable hydrogen atoms¹⁹.

Until now, this technique was used to investigate such transitions between single hyperfine states of metastable hydrogen and deuterium atoms in a pre-polarized beam that was produced and analyzed with the components of a Lamb-shift polarimeter. The occupation numbers of single substates were observed as function of the magnetic field amplitude inside two coils with opposing magnetic field direction, which induce the longitudinal field oscillation. Figure 37 shows an example where a beam of deuterium atoms in the substates α_1 , α_2 and α_3 , i.e. $m_J = +1/2$ and $m_I = +1, 0, -1$, was passing through the oscillating field and the relative occupation number of the substate α_1 was measured. Five single measurements were carried out within five hours to demonstrate a reproducibility of better than 10^{-4} of these measurements.

¹⁸The LHC Spin Project, [arXiv:1901.08002 \[hep-ex\]](https://arxiv.org/abs/1901.08002)

¹⁹R. Engels et. al., Eur. Phys. J. D **75**, 257 (2021).

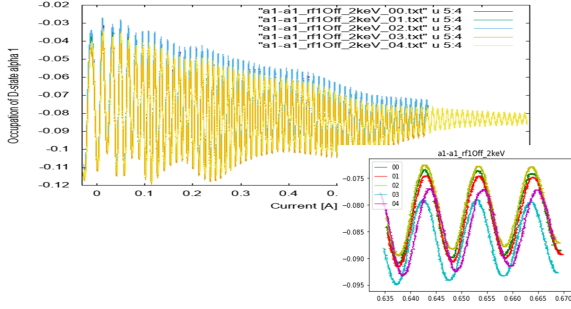


Figure 37: Relative occupation numbers of metastable deuterium atoms in the substate α_1 as function of the current in the Sona coils when a beam of atoms in the states α_1 , α_2 and α_3 at 1 keV is moving through. Here, the transition between the substates α_3 and β_4 is dominant.

One possible application of this method is the precise mapping of the Breit-Rabi diagram, i.e. the binding energy of the single substates as function of an external magnetic field. By that the QED corrections of the bound electron and proton/deuteron g -factors compared to the free particles can be measured.

In recent measurements with an unpolarized beam passing through the coils also oscillations between the hyperfine substates were observed. Amazingly, most of the atoms in the $F = 1$ multiplet are transferred in one substate and a nuclear polarization close to 0.95 was reached for dedicated magnetic field amplitudes in the coil center. Corresponding simulations solving the Schrödinger equation delivered the same result. In the photon model this behavior can be explained by correlations of the transitions between the $\alpha_1 \leftrightarrow \alpha_2$ and the $\alpha_2 \leftrightarrow \beta_3$ substate that happen in parallel and the interference of these transitions.

This universal method allows to produce hyperpolarization for many different, initially unpolarized, atoms, molecules and their ions that have a hyperfine structure. Thus, a patent was requested (Aktenzeichen 102022213860.0), because this method seems useful for several applications:

1.) Polarized $^3\text{He}^+$ Beam Source

The use of polarized $^3\text{He}^{2+}$ ions in storage rings opens a new window for the study of nuclear forces, since the spin-dependent part of the differential cross section of the observed reactions must mainly depend on the neutron spin. Therefore, nuclear polarized $^3\text{He}^{2+}$ beams can be considered as an ideal substitute for polarized neutron beams. Several groups around the world, e.g. at RHIC and RIKEN, have been working on the realization of an efficient polarized $^3\text{He}^{(+)}$ ion source for injection into storage rings. These concepts are based on fast ionization of optically pumped polarized ^3He gas with polarization values up to 0.8, but most of the ionization techniques

tested so far result in low polarization of the ion beams. Another recent approach is laser plasma acceleration of polarized ^3He gas, which was implemented by the JuSPARC group in 2021 at GSI's PHELIX facility²⁰. In a joint effort of the IKP and the Peter-Grünberg Institute it is planned to test this completely new approach to produce high-intensity ($\sim 10 \mu\text{A}$) polarized $^3\text{He}^+$ beams with up to 90% beam polarization, which can be used for stripping injection to feed storage rings (see Figure 38). The method itself can be extended to other ions, even heavy ions, and could open the door to a new generation of polarized ion sources.

This new type of polarized ion source can be built with components already used for similar experiments with metastable hydrogen and deuterium atoms. A $^3\text{He}^+$ ion beam at 4 keV will be produced with an ECR source and a following Wien filter to separate all other ions. When these ions are moving through the oscillating magnetic field of two opposite coils they experience dedicated photons that can induce transitions within the hyperfine structure that was recently published²¹.

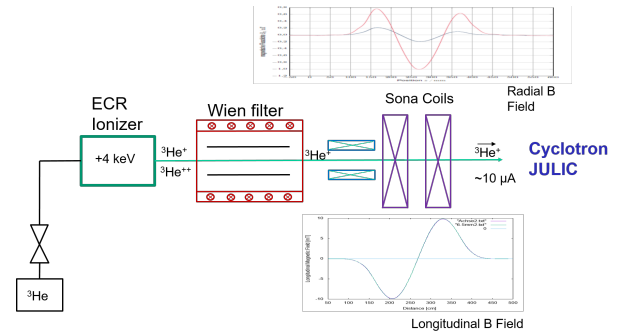


Figure 38: Proposed setup of a polarized $^3\text{He}^+$ ion source: After ionization of ^3He gas and acceleration to 4 keV the produced ions are separated by a Wien filter. A solenoidal magnetic field then defines the spin states with respect to the beam axis before they reach the Sona coils with opposite magnetic field directions. Here, the occupation numbers of the hyperfine substates with $F = 1$ are pumped into a single state by absorption of the coherent and monochromatic single radio-wave pulses.

Like for hydrogen the nuclear spin $I = 1/2$ and the total electron spin $J = 1/2$ interact with each other, but the hyperfine splitting energy and the g -factor of the nucleus are different. To prove the performance of this type of ion source, a polarization measurement has been proposed using the modified low-energy polarimeter behind the JULIC cyclotron at a beam energy above 100 MeV and the known analyzing powers of the elastic

²⁰P. Fedorets et al., Instruments **2022**, 6(2), 18 (2022).

²¹A. Schneider, B. Sikora, S. Dickopf et al., Nature **606**, 878–883 (2022)

scattering on protons at these energies ²².

2.) Polarized Fuel for Fusion Reactors

Some Tokamaks are fueled and heated with atomic beams in a fixed energy range between 100 to 200 keV. Again, when these atoms are moving through a sinusoidal magnetic field the corresponding transitions between the hyperfine substates are induced and can produce a nuclear polarization. All nuclear fusion reactions are spin-dependent and by choosing the optimum spin combinations their fusion rates and, therefore, the energy output of fusion reactors can be increased. The maximal achievable polarization values for the vector and tensor polarization of deuterium seem to be limited to smaller values as compared to hydrogen, because the oscillation between four hyperfine substates are less efficient to pump the atoms just into a single one. Nevertheless, polarization values above 0.5 are possible according to our simulations. An experiment to test such a setup is under discussion with collaborating groups in the US. The polarization values can be measured due to the known analyzing powers of the $d + d \rightarrow t + p$ in this low energy regime.

3) Production of Hyperpolarization in Samples

A fully equivalent approach to send a beam of particles through a static, but oscillating magnetic field is to induce a corresponding radio-wave signal into a probe at rest. Therefore, it seems possible to polarize probes by inducing the suitable radio-waves, if a proper hyperfine structure exists, i.e. the interaction of the nuclear spin with an electron spin, a rotational magnetic moment or with other nuclear spins. Of course, total electron spins and rotational magnetic moments will be zero within most solid and liquid materials. Thus, the proton/deuteron spin interaction with each other and the external magnetic field should be the reason for the hyperfine splitting. This means, that it might be possible to hyper-polarize for example ortho-deuterium ice and ortho-water in the human body. Even other materials that can be used for MRI as polarized tracers in medicine should be in range. Again, this can also be useful to polarized D₂, HD or DT molecules frozen as ice for pellet injection into Tokamaks or for laser-induced fusion, or into storage rings as a new type of dense polarized targets. Another option might be a new NMR method based on this technique: When at low magnetic fields the corresponding radio-wave are induced they should produce a polarization that is 5 orders of magnitude larger compared to normal NMR. Thus, it is simpler to detect the signal and no superconducting magnets are needed within the apparatus. This means that resolution and costs might be optimized by orders.

²²A. Watanabe, PhD thesis, Tohoku University, Sendai, Japan, Springer Theses, ISBN 978-981-15-9444-1 (2021).

6 Theoretical Investigations

6.1 Introduction

The IKP theory group studies the strong interactions in their various settings — spanning topics in hadron structure and dynamics, the nuclear many-body problem, symmetry tests in Quantum Chromodynamics (QCD), physics beyond the Standard Model, strongly correlated electronic systems and brain dynamics. The first focus of the theory group is the formulation and application of effective field theories for precision hadron and nuclear physics based on the symmetries of QCD. The second focus is related to high performance computing in nuclear, hadronic and condensed matter physics, spearheaded by the work on nuclear lattice simulations. Since July 2012, the group is heavily involved in the activities of the collaborative research center “Symmetries and the emergence of structure in QCD” (CRC 110) together with researchers from Bonn University, TU München, Ruhr-Universität Bochum, IHEP/CAS (Beijing, China), ITP/CAS (Beijing, China) and Peking University (China). This CRC is presently in its third and final funding period. A further strengthening of the group was achieved through the ERC Advanced Grant “EX-OTIC” that began in November 2021. It focuses on precision calculations in nuclear and hypernuclear physics on the lattice as well as exploring fine-tunings in nuclear reactions and the role of anthropic considerations. Since this year, the IKP theory group is also involved in the NRW-FAIR network funded by the ministry of culture and science of the state of Northrhine-Westfalia. Some of the high-lights of all of these activities are discussed in the following.

6.2 Emergent geometry and duality in the carbon nucleus

The carbon atom provides the backbone for the complex organic chemistry composing the building blocks of life. The physics of the carbon nucleus in its predominant isotope, ¹²C, is similarly full of multifaceted complexity. Some nuclear states of ¹²C can be preferentially treated as a collection of independent particles held by the mean field of the nucleus, while other states behave more as a collection of three alpha-particle clusters. But these two pictures are not mutually exclusive, and some states can be described in either fashion. In this work, we provide the first model-independent tomographic scan of the three-dimensional geometry of the nuclear states of ¹²C using the *ab initio* framework of nuclear lattice effective field theory. We use an SU(4) symmetric action including two- and three-body contact interactions with local and non-local smearing as well as the time-honoured next-to-next-to-leading chiral interaction, that features one- and two-pion exchanges and a number of four-nucleon terms with zero and two derivatives. This interaction was used in the first *ab initio* description of the Hoyle state in 2011. Both type of interactions give the same results, although

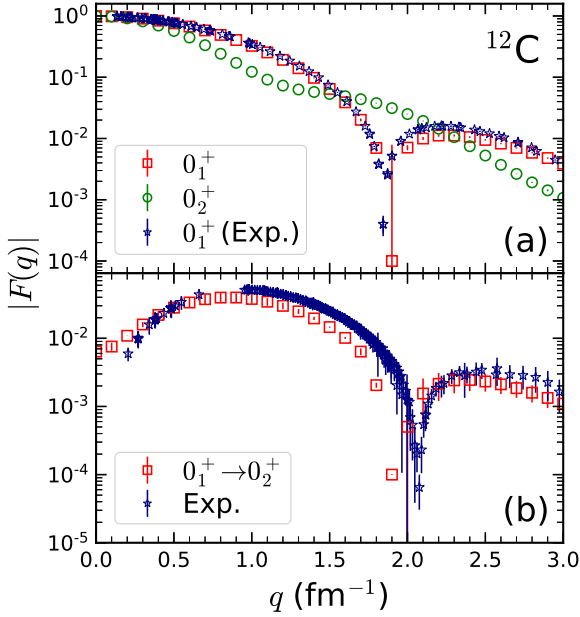


Figure 39: The absolute value of the charge form factor $F(q)$ versus momentum q . The top figure (a) shows the ground state (red squares) and Hoyle state (green circles), and the bottom figure (b) shows the transition from the ground state to the Hoyle state (red squares). The error bars correspond to one standard deviation errors. Experimental data (purple stars) are shown for comparison.

the uncertainties on the SU(4) interaction are smaller due to the stronger suppression of the “sign oscillations”.

We find that the well-known but enigmatic Hoyle state is composed of a “bent-arm” or obtuse triangular arrangement of alpha clusters. We identify all of the low-lying nuclear states of ^{12}C as having an intrinsic shape composed of three alpha clusters forming either an equilateral triangle or an obtuse triangle. From these basic structural formations, the various nuclear states correspond to different rotational and vibrational excitations as well as either distortions or large-amplitude displacements of the alpha clusters. The states with the equilateral triangle formation also have a dual description in terms of particle-hole excitations in the mean-field picture. We compare our theoretical calculations with experimental data for binding energies, quadrupole moments, electromagnetic transitions, charge densities, and form factors, see Fig. 39. The overall agreement is good, and further studies using higher-fidelity interactions are planned.

6.3 Hyperon-nucleon interaction in chiral EFT

SU(3) chiral effective field theory (EFT) is a powerful tool to explore the baryon-baryon (BB) interaction involving hyperons. In this approach a potential is established via an expansion in terms of small momenta and small Goldstone-boson masses, subject to an appropriate power

counting, so that the results can be improved systematically by going to higher orders, while at the same time theoretical uncertainties can be estimated. The resulting interaction potentials consist of contributions from an increasing number of pseudoscalar-meson exchanges (π , η , K), determined by the underlying chiral symmetry, and of contact terms which encode the unresolved short-distance dynamics and whose strengths are parameterized by a priori unknown low-energy constants (LECs).

Studies by us, performed up to next-to-leading order (NLO) in the chiral expansion, have shown that for the strangeness $S = -1$ (ΛN , ΣN) and $S = -2$ ($\Lambda\Lambda$, ΞN) sectors a consistent and satisfactory description of the available scattering data and other experimental constraints can be achieved within the assumption of (broken) SU(3) flavor symmetry. Applications of the resulting potentials in bound-state calculations for light hypernuclei led to results close to the empirical values. In addition, the exploration of neutron-star properties with the strangeness $S = -1$ interaction indicate the potential to resolve the so-called hyperon puzzle, when combined with consistently derived ΛNN and ΣNN three-body forces.

Now we have started to extend our ΛN - ΣN interaction to next-to-next-to leading order ($N^2\text{LO}$) in the chiral expansion. We also switched to a novel and more physically motivated regularization scheme with that already was applied successfully in the two-nucleon system. In the following we focus on the ΣN channel where a wealth of new data has become available from measurements at the J-PARC facility in Japan. Specifically, we show results for $\Sigma^+ p$ scattering which is of particular interest for theory. Since the total isospin is $I = 3/2$ there is no coupling to the ΛN channel which simplifies the dynamics. Moreover, SU(3) symmetry provides strong constraints on several partial wave amplitudes. To be concrete, space-spin antisymmetric states like 1S_0 , $^3P_{0,1,2}$, ... belong all to the $\{27\}$ irreducible representation of SU(3) symmetry and, thus, the corresponding interactions would be identical to that in the NN system provided that SU(3) symmetry is exactly fulfilled.

Indeed in case of the new NLO interaction, fixing the contact terms in accordance with SU(3) symmetry yields already a good description of the data taken at laboratory momenta $p_{\text{lab}} = 440\text{--}550$ MeV/c, cf. the dash-dotted line in Fig. 40 (right). For the $N^2\text{LO}$ interaction all P -wave LECs are fitted to the data. Actually, here we have explored two scenarios, one where the resulting angular distribution is similar to that obtained for NLO (solid line) and one which produces an overall more pronounced angular dependence (dashed line). The latter is clearly preferred by the available data in that momentum range. The predictions of our former NLO potential from 2019 (NLO19), included here for illustration and shown as a band that represents the regulator dependence, are clearly in disagreement with the data.

The integrated $\Sigma^+ p$ cross section is shown in Fig. 40 (left). Again the NLO19 potential does not reproduce the trend of the data for laboratory momenta $p_{\text{lab}} >$

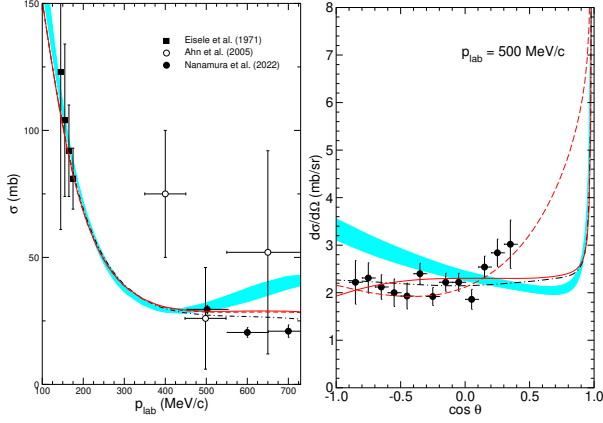


Figure 40: Σ^+p total (left) and differential (right) cross sections. The new data from the J-PARC facility are indicated by filled circles.

500 MeV/c. We believe that the rise of the cross section for larger p_{lab} could be an artifact of the employed regularization scheme. On the other hand, those momenta corresponds to a laboratory energy of $T_{\text{lab}} \gtrsim 150$ MeV so that we are certainly in a region where NLO and possibly even $N^2\text{LO}$ cannot be expected to be quantitatively reliable. Moreover, one should keep in mind that three-body channels like $\Lambda n\pi$ open around that energy which anyway marks the limit for the applicability of any two-body potential.

6.4 Charge-symmetry breaking in $A = 7$ and $A = 8$ hypernuclei

The hyperon-nucleon (YN) interaction ($Y=\Lambda, \Sigma$) is not accurately known because there are only few low-energy scattering data. Therefore, the known bound states of Λ hyperons and nuclei, so called hypernuclei, provide important additional information on the YN interaction. Of special interest is the Λ -neutron (Λn) interaction which contributes to the properties of neutron matter. Depending on the strength of this interaction, a sizable component of neutron stars could be Λ hyperons which very likely leads to inconsistencies of predictions for neutron matter and astrophysical observations. In order to further constrain the magnitude of this component, several experimental facilities, e.g. FAIR, J-PARC and J-Lab, are planning new experiments to study interactions of hyperons for this reason.

But the Λn interaction is particularly difficult to constrain by YN data. In standard approaches to model the YN interaction, it is therefore usually assumed that Λ -proton (Λp) and Λn interactions are identical. We have recently shown that the charge-symmetry breaking (CSB) difference of the Λp and Λn interaction can be predicted using the difference of Λ separation energies of the mirror hypernuclei ${}^4_\Lambda\text{H}$ and ${}^4_\Lambda\text{He}$, and that it is non-negligible.

In a new publication, we have now extended this study to pairs and triplets of $A = 7$ and 8 p-shell hypernuclei.

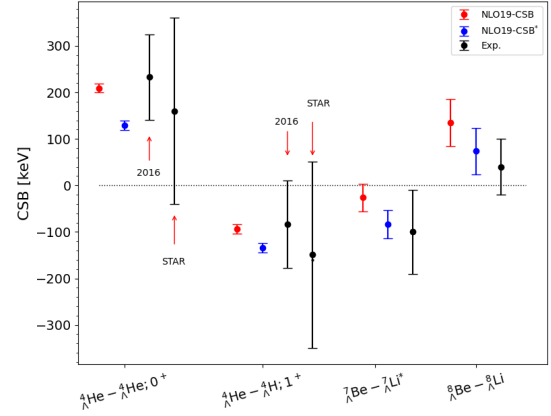


Figure 41: Theoretical predictions for CSB splittings of $A = 4$ to 8 hypernuclei compared to experiment.

The calculations have been performed with the Jacobi-No Core Shell Model (J-NCSM) for hypernuclei that we recently developed. In order to improve the accuracy of the calculations, we have now added for the first time Similarity Renormalization Group (SRG) evolved three-baryon interactions to our Hamiltonian and also extended the calculations to $A = 8$ hypernuclei.

Due to these advances in our simulations, we are now able to predict Λ separation energies for ${}^5_\Lambda\text{He}$, ${}^7_\Lambda\text{He/Li/Be}$ and ${}^8_\Lambda\text{Li/Be}$. We found that the description of the available experimental data is considerably better for one of the recent next-to-leading order (NLO) chiral YN interactions (NLO19) compared to another one (NLO13) indicating that chiral hyperon-nucleon-nucleon interactions are probably smaller for NLO19. We then used the experimental values of ${}^4_\Lambda\text{H/He}$ to determine the CSB difference of the Λp and Λn interactions and predict the differences for ${}^7_\Lambda\text{He/Li/Be}$ and ${}^8_\Lambda\text{Li/Be}$. The results are shown as red bars (NLO19-CSB) in Fig. 41 and compared to the experimental values (black bars). The results are in agreement within the large experimental uncertainties. Nevertheless, there is an indication that the CSB splittings are too small in magnitude for $A = 7$ and too larger for $A = 8$ hypernuclei. Interestingly, when fitting the CSB interaction to new $A = 4$ data from the STAR collaboration, a much better agreement with the data can be achieved (see blue bars, NLO19-CSB*).

As can be also seen in the figure, the experimental uncertainty is still much larger than the theoretical uncertainty of our calculations. Fortunately, new data for $A = 4$ hypernuclear can be expected from upcoming experiments at J-PARC. With such data, it will be possible to fix the strength of Λn interactions and make conclusive predictions for the contribution of Λ hyperons to neutron matter.

6.5 Prediction of five-flavoured pentaquarks

The search for and investigation of so-called exotic hadrons, that are states that do not fit into the conventional quark model, is one of the hottest topics in particle physics since two decades. In particular, the prediction and later observation of hidden-charm pentaquarks with and without strangeness, the P_c states, as well as the doubly charmed tetraquark state T_{cc}^+ have generated lots of theoretical investigations. A very promising approach to understand these states is the molecular scenario, where two (or three) hadrons are bound thus generating beyond the quark model states. Recently, there have been rather extensive studies of the possible formation of such molecular states from heavy-heavy and heavy-antiheavy hadrons.

We have provided theoretical evidence of the existence of $B^{(*)}\Xi_c^{(\prime)}$ bound states with charge $Q = +1$. On the one hand, the $B^{(*)}\Xi_c^{(\prime)}$ system is most likely to form bound states among several possible options. On the other hand, it is quite special that all the involved quarks have different flavors, since the quark content is $[q\bar{b}][q'sc]$ ($q^{(\prime)} = u, d$). Thus, this system appears to be the best option to search for a pentaquark state, which we call $\Lambda_{c\bar{b}}$, that includes five different quarks. We investigated the coupled channel effects in the $B^{(*)}\Xi_c^{(\prime)}$ system to search for possible bound states with $Q = +1$. The calculation was divided into two parts, namely the pseudoscalar meson-baryon (PB) interaction and the vector meson-baryon (VB) interaction. In each sector, there are in total four channels taken into consideration, $B^{(*)}\Xi_c$, $B^{(*)}\Xi'_c$, $B_s^{(*)}\Lambda_c$ and $B_c^{(*)}\Lambda$. However, because the $B_c^{(*)}(J^P = 1^-)$ state has not been confirmed experimentally so far, we have taken the average value of several theoretical predictions. We calculate the corresponding potentials $V_{PB \rightarrow PB}$ and $V_{VB \rightarrow VB}$ at tree-level, where P, V, B denote the groundstate octet of the pseudoscalar mesons, the vector mesons and the baryons, respectively. These potentials are then iterated in a regularized Lippmann-Schwinger equation and poles are searched for in the complex energy plane.

For the PB interaction, four channels $B\Xi_c$, $B\Xi'_c$, $B_s\Lambda_c$ and $B_c\Lambda$ are taken into consideration. We find there are two poles located at $z_0 = 7720.12 - i3.7\text{MeV}$ and $7847.60 - i2.2\text{MeV}$, just below the threshold of $B\Xi_c$ and $B\Xi'_c$, respectively, and their coupling strength with each corresponding channel is much greater than that with other channels. Thus we regard these two poles as $B\Xi_c$ and $B\Xi'_c$ bound states. The binding energies of these two states are about 30 MeV and 10 MeV. We remark that the quark content of these $\Lambda_{c\bar{b}}$ states is $[q\bar{b}][q'sc]$, where all the five involved quarks are different, a truly exotic hadron. Due to this unique feature, its decay to light-meson-light-baryon channels are only possible through the weak interaction, so that it is hard to observe them in light-meson-light-baryon channels. For the VB interactions, the $B^*\Xi_c$, $B^*\Xi'_c$, $B_s^*\Lambda_c$ and $B_c^*\Lambda$ channels are

considered. We find poles in the $B^*\Xi_c$ and $B^*\Xi'_c$ channels, whose locations are at $z_0 = 7768.86 - i3.6\text{MeV}$ and $7896.62 - i2.0\text{MeV}$, respectively. Finally, note that the existence of such $B^{(*)}\Xi_c^{(\prime)}$ bound states, which have the most diverse flavor composition, would extend the already rich spectrum of exotic hadrons. These states can be searched for in the $pp \rightarrow B_c\Lambda X$ or $pp \rightarrow B_s^{(*)}\Lambda_c X$ processes by the LHCb Collaboration in the $B_c\Lambda$ or $B_s^{(*)}\Lambda_c$ invariant mass spectrum.

6.6 Do near-threshold molecular states mix with neighboring $\bar{Q}Q$ states?

Since the beginning of the century a large number of states was discovered experimentally that does not fit into a classification as quark-antiquark states for mesons and three quark states for baryons. Most prominent in this context are probably charged mesons and baryons that decay to final states containing heavy quarkonia. Since the OZI rule strongly suppresses the emergence of the latter in the course of the decay, a $\bar{Q}Q$ state must be already a part of the wave function and accordingly the mentioned states qualify as four quark (tetraquark) or five quark (pentaquark) structures, respectively. In the literature different assignments for the underlying structure of those states are put forward. The most popular ones are compact tetraquarks made from diquark-antidiquark substructures, hadroquarkonia, formed from a compact quarkonium core surrounded by a light quark cloud, and hadronic molecules, where the quarks within the multi-quark structures cluster into color neutral substructures.

Besides the mentioned groups that are explicitly exotic, there are also states found in the meson sector that show properties inconsistent with the most simple quark model structure, however, still having quantum numbers consistent with a quark-antiquark state. Accordingly one would expect that these mix with nearby conventional states. If such a mixing occurs at all or how large it is is expected to depend on the assumed underlying structure. In the work reported here we investigated a possible mixing pattern of hadronic molecules with simple quark model states. In particular we argue that the mixing of quark model states and hadronic molecules should be very weak. The study is a follow-up of an earlier work now supplemented with analytic insights as well as a concrete application of the proposed scenario to observed open charm axial vector states.

Starting point of our investigation is a scenario where only stable quark-model states exist. Such a scenario is naturally reached in QCD as soon as the limit $N_c \rightarrow \infty$ is taken, since the coupling of quark-model states to two-body intermediate states scales as $1/\sqrt{N_c}$. If one now starts to introduce such a coupling, the individual quark model states will acquire a width, which is small as long as the coupling is small. In this scenario each state is described by a pair of poles located symmetrically as mirror images with respect to the real axis and the imaginary axis in the s -plane and the momentum-plane or k -plane,

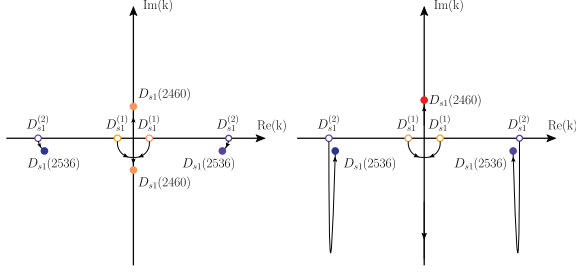


Figure 42: The trajectories of the lowest D_{s1} poles in the momentum plane for varying couplings to the continuum channel for the weak (left panel) and strong (right panel) coupling regimes.

respectively. The various quark model states do not feel their neighbors and the coupling to the continuum can be treated perturbatively. This regime we call the weak coupling limit. However, as the coupling is increased further, the individual states will now become increasingly broad. As soon as the width of the states gets of the order of the level spacing between two neighboring states, for most of the states the width starts to decrease again, as the coupling is increased further, to eventually decouple from the continuum in the infinite coupling limit. At the same time one state absorbs all the coupling strength to the continuum and will eventually turn into a hadronic molecule, with its single pole located naturally quite close to the continuum threshold. We demonstrated analytically that the second pole related to this state in the large coupling limit disappears to $-\infty$ in s or, equivalently, to $-\infty$ in k .

Candidates for exotic states not only appear in doubly heavy systems, but also in singly heavy systems. A prominent example are the open charm positive parity states $D_{s0}(2317)$ and $D_{s1}^*(2460)$. For the study here especially the latter state is of interest for in the same channel also another state, the $D_{s1}^*(2536)$ is observed. The latter axial vector state is found to be rather narrow, given that it is located above the KD threshold. The former is also narrow, however, for this state this is natural for the only kinematically allowed strong decay channel is suppressed by isospin symmetry. The existing data could now be explained both in the weak and the strong coupling regimes: In the first scenario the $D_{s1}^*(2536)$ is narrow, because its coupling to the KD channel is small (for example since it contains the light quark cloud with $j = 3/2$ - but even then one would expect a larger decay with because of a spin symmetry violating mixing with the $j = 1/2$ component that should be sizable in the charm sector). In this scenario the $D_{s1}^*(2460)$ is a $c\bar{q}$ state. The related pole trajectories are shown in the left panel of Fig. 42. In the second scenario, the heavier axial vector is narrow, because all the KD strength went into the $D_{s1}^*(2460)$, which in turn needs to be interpreted as a hadronic molecule — the pole trajectories are shown in the right panel of Fig. 42. Further research is necessary to better understand this intriguing system.

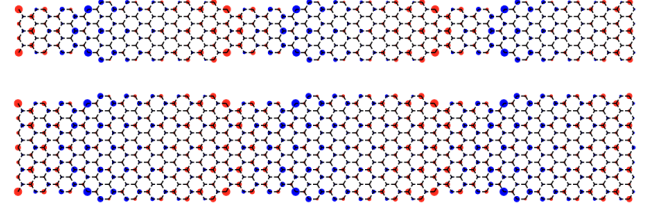


Figure 43: The electronic densities for the 7/9 (top) and 13/15 (bottom) periodic hybrid systems. The red and blue colors denote the densities on the two underlying sublattices. Note the concentration of these densities at the junctions between the different widths. This localization remains essentially unchanged in the presence of interactions.

6.7 Localization of electron wavefunctions in hybrid nanoribbons

Carbon nanoribbons are comprised of carbon ions arranged in a hexagonal lattice. They are basically strips of graphene cut along particular lines, resulting in two types defined by their edge geometries: armchair and zigzag. Recently it has been demonstrated that ribbons of different widths can be manufactured and mated, resulting in so-called hybrid nanoribbons. The possibility of engineering such systems has spurred research into their use for manufacturing novel electronic devices, such as quantum dots.

It was also shown that low-energy, localized electronic states can occur at the junction of two armchair nanoribbons of different widths that are topologically distinct. The presence of such symmetry-protected topological (SPT) localized states depends on their topological invariance, a property that is intrinsically related to the system's underlying geometry and symmetries. The presences of such SPT states potentially provides an avenue for obtaining fault-tolerant quantum computing.

Such SPT states are manifest in the non-interacting limit, which in this case corresponds to the tight-binding model. Furthermore, exact SPT occurs when the lengths of both ribbons extend infinitely from the single junction. The extent to which these SPT states remain low energy, as well as localized, in the strongly interacting regime is an open question, especially since any practical implementation of these hybrid systems will be finite in extent, or perhaps in a repeating lattice.

Our recent work on hybrid nanoribbons directly addressed this question. Here we investigated two hybrid nanoribbons, the so-called 7/9 and 13/15 hybrid systems, see Fig. 43. These particular systems comprise of armchair ribbons of specific widths with junctions that demarcate two topologically distinct regions. We placed these systems in a periodic lattice and introduced an Hubbard interaction term U . This allowed us to investigate the ‘finite-volume’ dependence of the energy of the SPT states, as well as their dependence on interactions. We

also devised a method to obtain the wavefunction densities of the SPT states which allowed us to investigate the states' localization.

Using Quantum Monte Carlo (QMC) methods, we showed that the energy of the SPT states did indeed have a strong dependence on the interaction parameter U . However, it remained the lowest energy in the spectrum. More importantly, we found that the localization remained essential unchanged, indicating that this feature is robustly maintained in the strongly interacting, finite volume regime, as shown in Fig. 43. These findings bode well for the possibility of using these systems for manufacturing novel electronic devices which are inherently finite in volume.

In addition to these findings, we also investigated these systems in the so-called 'symmetric-line limit' where we included a superconducting pairing term that had equal weight with the tight-binding hopping term. Our findings here also indicate that localization of these SPT states persisted in the presence of interactions. Finally, we showed how such localized states are the physical analogs of 'domain-wall' fermions in $2 + 1$ dimensions. This observation opens the way for formulating an effective field theory description of such states, which in turn should allow us to describe dynamical quantities of such systems. We are actively investigating this avenue of research.

6.8 Criticality in brain dynamics

Criticality is understood to play an essential role in the behavior of neural networks (NNs), providing a means for long-distance, collective signals required for memory and computation. However, there is an apparent dichotomy between criticality features that benefit memory and those that enhance computational capacity. Clearly, any model purported to satisfactorily describe brain dynamics must incorporate critical processes that enables both features.

Studies of critical brain dynamics have historically been confined to the realm of mean-field theories. As such, they provide descriptions that incorporate simple linear responses between modes of neuronal stimuli. This, in turn, has emphasized the optimal behavior of memory and signal separation near criticality, at the expense of computational capacity which requires non-linear interactions.

In our recent work we demonstrated a different behavior of criticality of neural networks, one of the Gell-Mann-Low type, that allows for optimization of both memory and non-linear computation. We analyzed the stochastic Wilson-Cowan rate model in $d = 2$ dimensions, which is a prototypical model of brain dynamics, and applied standard Wilsonian flow equations to understand the model's renormalization group (RG) behavior. This involved explicitly integrating out short-distance scales and observing how the couplings of the model evolved as one flowed to larger distance scales.

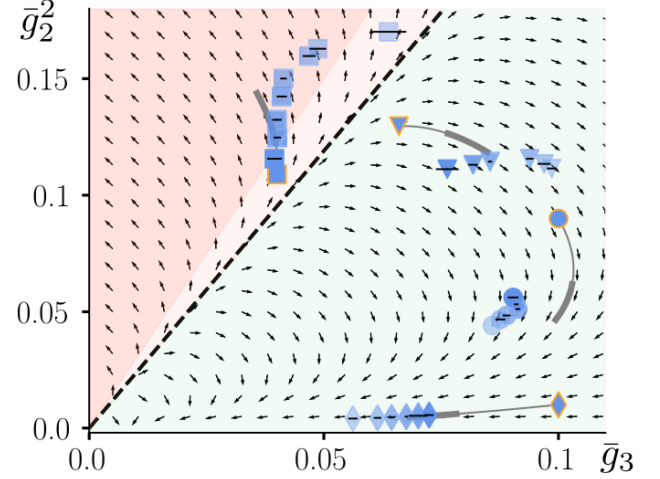


Figure 44: The flow behavior of the couplings of our NN. The arrows point the direction of flow as one integrates out short distance scales.

Our renormalization procedure correctly kept track of the flow of non-linear couplings within the model, and in so doing, we found that the model does indeed approach a Gaussian fixed point (indicating a phase transition), yet did so in a logarithmically slow fashion, see Fig. 44. This means that the non-linear couplings remained relevant at essentially all length scales, as opposed to what is found from a pure mean-field theory treatment. Thus both memory and computation can be accommodated and optimized near a critical phase transition, something which to date has not been observed in other NN models.

Finally, we strengthened our findings by explicitly constructing a neural network using this model and training it on tasks involving both memory and computation. We found that it performed equally well on these tasks. Our RG analysis, standard in field theory, represents a novel tool for the analysis of NNs and should provide new insights into other models of brain dynamics.

A Beam Time at COSY in 2022

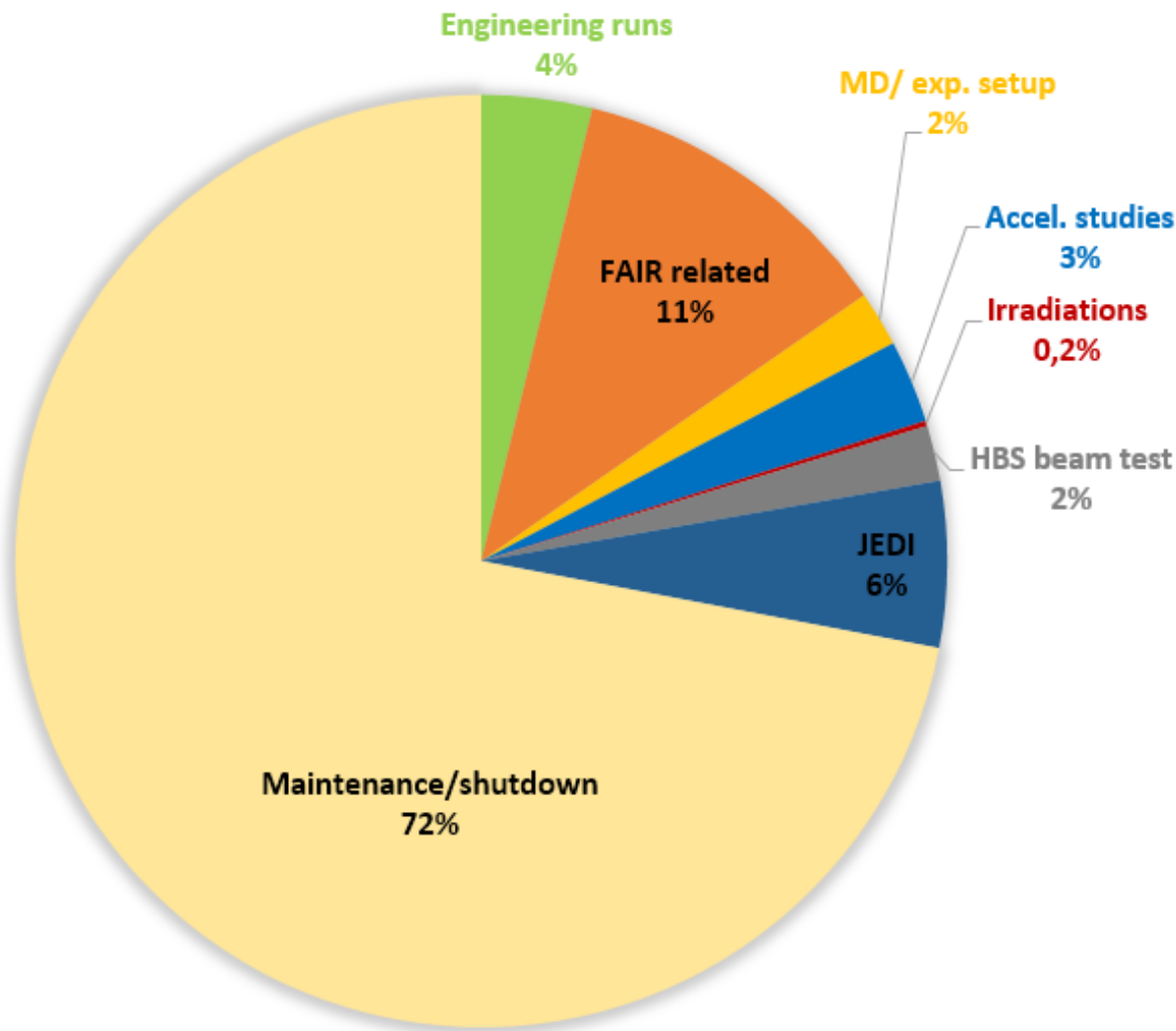


Figure 45: COSY beam-time statistics in 2022.

The distribution of user weeks and maintenance/shutdown periods is listed in Table 3.

Table 3: Overview COSY user beam time and EDM/FAIR weeks in 2022.

Date	Experiment	Duration	Reaction, experiment #
1.01.22.–16.01.22	Maintenance	2 weeks	
17.01.–23.01.	COSY	1 week	engineering run
24.01.–30.01.	MD/Maintenance	1 week	
31.01.–06.02.	MD/D016	1 weeks	D016 proton therapy (postponed to CW17)
07.02.–27.02.	EDM (JEDI)	3 weeks	JEDI Exp. E009.1
28.02.–06.03.	MD	1 week	
07.03.–13.03.	COSY	1 week	injection studies, Exp. A014.4
14.03.–20.03.	MD	1 week	
21.03.–27.03.	COSY	1 week	HI-MAPS, D019
28.03.–03.04.	COSY	1 week	LOEWE-NP, A017.2
04.04.–10.04.	MD	1 week	
11.04.–17.04.	COSY	1 week	electron cooling, Exp. A002.8
18.04.–24.04.	FAIR (Clust.)	1 week	FAIR Cluster Jet Target, Exp. D009.6
25.04.–04.12.	shutdown	33 weeks	finance driven shutdown
05.12.–09.12.	HBS	1 week	Beam and TMR Tests for HBS
10.12.–31.12.	shutdown	3 weeks	finance driven shutdown
user weeks 2022		9 weeks	
MD/maintenance		7 weeks	
finance driven shutdown		36 weeks	

B Committees

B.1 CBAC – COSY Beam Time Advisory Committee

Prof. K. Aulenbacher	Universität Mainz, Germany
Prof. O. Kester	TRIUMF, Canada
Prof. C.J. Schmidt	GSI Darmstadt, Germany
Prof. T. Stöhlker	HI-Jena, Jena, Germany
Prof. M. Weber (chair)	KIT, Karlsruhe, Germany

B.2 Committee Service

C. Ehrlich	- IKP Internal Steering Committee (ILA), FZ-Jülich GmbH, Germany
O. Felden	- WTR (Scientific and Technical Council), FZ-Jülich GmbH, Germany
R. Gebel	- International Organising Committee of the International Conference on Cyclotrons and their Applications
	- WTR (Scientific and Technical Council), FZ-Jülich GmbH, Germany
F. Goldenbaum	- Chair of the PANDA at FAIR collaboration board
	- WTR (Scientific and Technical Council), FZ-Jülich GmbH, Germany
	- Representatives' Assembly (WTV), FZ-Jülich GmbH, Germany
	- Scientific Secretary of COSY Beam Advisory Committee (CBAC), FZ-Jülich GmbH, Germany
J. Haidenbauer	- Theory advisory Group PANDA
C. Hanhart	- Theory advisory Group PANDA
	- Particle Data Group
	- Task coordinator (Precision calculations in non-perturbative QCD (I): Effective Field Theories, analyticity and dispersion relations) within STRONG2020
	- IKP Internal Steering Committee (ILA), FZ-Jülich GmbH, Germany
V. Hejny	- WTR (Scientific and Technical Council), FZ-Jülich GmbH, Germany
V. Kamedzhiev	- COSY Beamtime Advisory Committee (CBAC), FZ-Jülich GmbH, Germany
	- IKP Internal Steering Committee (ILA), FZ-Jülich GmbH, Germany
T. Lähde	- Representatives' Assembly (WTV), FZ-Jülich GmbH, Germany
A. Lehrach	- Institutional representative, European Network for Novel Accelerators (EuroNNAc)
	- Coordination, support and enhancement of training activities for accelerators in Europe, EU project ARIES (Accelerator Research and Innovation for European Science and Society)
	- Institutional representative, MT Executive Board, HGF Programme "Matter and Technologies"
	- Scientific Advisory Board (SAB), 13th International Particle Accelerator Conference (IPAC'22), Bangkok, Thailand, June 12 - 17, 2022
	- CA-D Machine Advisory Committee (MAC), Brookhaven National Laboratory, Upton (NY), USA
	- JuDocs Council, FZ Jülich GmbH, Germany
	- Representatives' Assembly (WTV), FZ-Jülich GmbH, Germany
L. Ludhova	- Institutional Board of Borexino
	- Steering Committee of Borexino
	- Physics Coordinator of Borexino
	- Institutional Board of JUNO
	- Analysis Coordination Committee of JUNO
	- Member of the International Advisory Committee (IAC) of Physics In Collision (PIC) conferences
	- Member of the IAC of "Symmetries in Subatomic Physics" (SSP 2022) conference

- | | |
|---------------|--|
| U.-G. Meißner | <ul style="list-style-type: none"> - WTR (Scientific and Technical Council), FZ-Jülich GmbH, Germany - Spokesperson DFG Review Board 309 "Particles, Nuclei and Fields" - Gründungsmitglied der Kommission für Ethik in der Forschung am Forschungszentrum Jülich - Scientific Advisory Committee of the Collaborative Research Center (SFB) 1245, "Nuclei: From fundamental interactions to structure and stars", TU Darmstadt - German/DFG delegate of NuPECC - Project coordinator, Regional Doctoral Program in Theoretical and Experimental Particle Physics (Bonn, Jülich, Siegen Tiflis, Yerevan), funded by Volkswagen Stiftung - Spokesperson of the Collaborative Research Center SFB/TR-110 "Symmetries and the Emergence of Structure in QCD" - Theory advisory Group PANDA - Particle Data Group |
| A. Nass | <ul style="list-style-type: none"> - Representatives' Assembly (WTV), FZ-Jülich GmbH, Germany - IKP Internal Steering Committee (ILA), FZ-Jülich GmbH, Germany |
| A. Nogga | <ul style="list-style-type: none"> - WTR (Scientific and Technical Council), FZ-Jülich GmbH, Germany |
| D. Prasuhn | <ul style="list-style-type: none"> - International Advisory Committee of the COOL Conferences (Beam Cooling) |
| J. Pretz | <ul style="list-style-type: none"> - Representatives' Assembly (WTV), FZ-Jülich GmbH, Germany |
| K. Reimmers | <ul style="list-style-type: none"> - Representatives' Assembly (WTV), FZ-Jülich GmbH, Germany |
| J. Ritman | <ul style="list-style-type: none"> - WTR (Scientific and Technical Council), FZ-Jülich GmbH, Germany - Scientific Coordinator of COSY - Co-Chair of the MESON biannual conference series - Chair of the Scientific Advisory Committee for FAIR-CZ - Co-Spokesperson of KLF (K-Long Facility at Jefferson Lab) |
| T. Sefzick | <ul style="list-style-type: none"> - IKP Internal Steering Committee (ILA), FZ-Jülich GmbH, Germany |
| R. Stassen | <ul style="list-style-type: none"> - Member of the Machine Advisory Committee for NICA (Nuclotron-based Ion Collider Facility), Joint Institute for Nuclear Research (JINR), Dubna, Russia |
| T. Stockmanns | <ul style="list-style-type: none"> - Computing coordinator PANDA - IKP Internal Steering Committee (ILA), FZ-Jülich GmbH, Germany |
| H. Ströher | <ul style="list-style-type: none"> - IAB KIU (International Advisory Board Kutaisi International University, Georgia) - ISPC (International Spin Physics Committee) - PGSB (Palestinian-German Science Bridge) Advisory Committee |

C Publications

C.1 Journal Articles

1. Y. Ünal *et al.*
Electric dipole moments of baryons with bottom quarks
Phys. Rev. D **105** 055026 (2022)
2. R. Abou Yassine *et al.*
Measurement of global polarization of Λ hyperons in few-GeV heavy-ion collisions
Phys. Lett. B **835** 137506 - (2022)
3. A. Abusleme *et al.*
Prospects for detecting the diffuse supernova neutrino background with JUNO
J. Cosmol. Astropart. P. **2022** 033 - (2022)
4. A. Abusleme *et al.*
Mass testing and characterization of 20-inch PMTs for JUNO
Eur. Phys. J. C **82** 1168 (2022)
5. S. Adhikari *et al.*
Search for photoproduction of axionlike particles at GlueX
Phys. Rev. D **105** 052007 (2022)
6. S. Adhikari *et al.*
Measurement of spin density matrix elements in Λ (1520) photoproduction at 8.2-8.8 GeV
Phys. Rev. C **105** 035201 (2022)
7. M. Agostini *et al.*
First Directional Measurement of Sub-MeV Solar Neutrinos with Borexino
Phys. Rev. Lett. **128** 091803 (2022)
8. M. Agostini *et al.*
Correlated and integrated directionality for sub-MeV solar neutrinos in Borexino
Phys. Rev. D **105** 052002 (2022)
9. S. Aiello *et al.*
Combined sensitivity of JUNO and KM3NeT/ORCA to the neutrino mass ordering
J. High Energ. Phys. **2022** 55 (2022)
10. H. Alharazin *et al.*
Gravitational form factors of the delta resonance in chiral EFT
Eur. Phys. J. C **82** 907 (2022)
11. A. Antognini, Y. Lin and U. Meißner
Precision calculation of the recoil-finite-size correction for the hyperfine splitting in muonic and electronic hydrogen
Phys. Lett. B **835** 137575 - (2022)
12. S. Appel *et al.*
Search for low-energy signals from fast radio bursts with the Borexino detector
Eur. Phys. J. C **82** 278 (2022)
13. S. Appel *et al.*
Independent determination of the Earth's orbital parameters with solar neutrinos in Borexino
Astropart. Phys. **145** 102778 (2022)
14. S. Appel *et al.*
Improved Measurement of Solar Neutrinos from the Carbon-Nitrogen-Oxygen Cycle by Borexino and Its Implications for the Standard Solar Model
Phys. Rev. Lett. **129** 252701 (2022)
15. V. Baru *et al.*
Is $Z_{cs}(3982)$ a molecular partner of $Z_c(3900)$ and $Z_c(4020)$ states?
Phys. Rev. D **105** 034014 (2022)

16. V. Baru *et al.*
Effective range expansion for narrow near-threshold resonances
Phys. Lett. B **833** 137290 - (2022)
17. B. Bhuyan *et al.*
Search for the decay $B_s^0 \rightarrow \eta\eta$
Phys. Rev. D **105** 012007 (2022)
18. L. Bieger *et al.*
Potential for a precision measurement of solar pp neutrinos in the Serappis experiment
Eur. Phys. J. C **82** 779 (2022)
19. T. Bloomfield *et al.*
Measurement of the branching fraction and CP asymmetry for $B \rightarrow \bar{D}\pi$ decays
Phys. Rev. D **105** 072007 (2022)
20. D.S. Carman *et al.*
Beam-recoil transferred polarization in K+Y electroproduction in the nucleon resonance region with CLAS12
Phys. Rev. C **105** 065201 (2022)
21. Y. Chen *et al.*
Measurement of Two-Particle Correlations of Hadrons in e+e- Collisions at Belle
Phys. Rev. Lett. **128** 142005 (2022)
22. C. Curceanu, J. Ritman and P. Salabura
Report on MESON2021
Nucl. Phys. News **32** 32 - 32 (2022)
23. T. Czank *et al.*
Search for $Z' \rightarrow \mu^+\mu^-$ in the $L_\mu - L_\tau$ gauge-symmetric model at Belle
Phys. Rev. D **106** 012003 (2022)
24. S. Diehl *et al.*
Multidimensional, High Precision Measurements of Beam Single Spin Asymmetries in Semi-inclusive π^+ Electroproduction off Protons in the Valence Region
Phys. Rev. Lett. **128** 062005 (2022)
25. M. Du *et al.*
Coupled-channel approach to T c c + including three-body effects
Phys. Rev. D **105** 014024 (2022)
26. S. Elhatisari *et al.*
Alpha-alpha scattering in the Multiverse
J. High Energ. Phys. **2022** 1 (2022)
27. E. Epelbaum *et al.*
Chiral theory of ρ -meson gravitational form factors
Phys. Rev. D **105** 016018 (2022)
28. E. Epelbaum *et al.*
Definition of Local Spatial Densities in Hadrons
Phys. Rev. Lett. **129** 012001 (2022)
29. H. Fu *et al.*
Update on strong and radiative decays of the $D_{s0}^*(2317)$ and $D_{s1}(2460)$ and their bottom cousins
Eur. Phys. J. A **58** 70 (2022)
30. X.Y. Gao *et al.*
Search for tetraquark states $X_{cc\bar{s}\bar{s}}$ in $D_s^+ D_s^+ (D_s^{*+} D_s^{*+})$ final states at Belle
Phys. Rev. D **105** 032002 (2022)
31. J. Golak *et al.*
Pion absorption from the lowest atomic orbital in ^2H , ^3H , and ^3He
Phys. Rev. C **106** 064003 (2022)

32. D. Grzonka *et al.*
A large area efficient trigger scintillator with SiPM read out
Nucl. Instr. Meth. Phys. Res. A **1041** 167410 - (2022)
33. C.K. Guruswamy, U. Meißner and C. Seng
Extracting the low-energy constant L_0 at three flavors from pion-kaon scattering
Commun. Theor. Phys. **74** 065202 - (2022)
34. C. Hadjivasiliou *et al.*
Search for B_0 meson decays into Λ and missing energy with a hadronic tagging method at Belle
Phys. Rev. D **105** L051101 (2022)
35. J. Haidenbauer and U. Meißner
Exploring the $\Sigma^+ p$ interaction by measurements of the correlation function
Phys. Lett. B **829** 137074 - (2022)
36. C. Hanhart and A. Nefediev
Do near-threshold molecular states mix with neighboring $\bar{Q}Q$ states?
Phys. Rev. D **106** 114003 (2022)
37. M. He *et al.*
Sub-percent Precision Measurement of Neutrino Oscillation Parameters with JUNO
Chinese Phys. C **46** 123001 (2022)
38. F. Hildenbrand *et al.*
Lattice Monte Carlo simulations with two impurity worldlines
Eur. Phys. J. A **58** 167 (2022)
39. S. Holz *et al.*
A dispersive analysis of $\eta' \rightarrow \pi^+ \pi^- \gamma$ and $\eta' \rightarrow \ell^+ \ell^- \gamma$
Eur. Phys. J. C **82** 434 (2022)
40. C.R. Howell *et al.*
International workshop on next generation gamma-ray source
J. Phys. G **49** 010502 - (2022)
41. K. Inami *et al.*
An improved search for the electric dipole moment of the τ lepton
J. High Energ. Phys. **2022** 110 (2022)
42. E.L. Isupov *et al.*
Polarized structure function $\sigma_{LT'}$ from $\pi^0 p$ electroproduction data in the resonance region at $0.4 \text{ GeV}^2 < Q^2 < 1.0 \text{ GeV}^2$
Phys. Rev. C **105** L022201 (2022)
43. H.B. Jeon *et al.*
Search for the radiative penguin decays $B_0 \rightarrow K_0 S K_0 S \gamma$ in the Belle experiment
Phys. Rev. D **106** 012006 (2022)
44. S. Jia *et al.*
Search for a Light Higgs Boson in Single-Photon Decays of $\Upsilon(1S)$ Using $\Upsilon(2S) \rightarrow \pi^+ \pi^- \Upsilon(1S)$ Tagging Method
Phys. Rev. Lett. **128** 081804 (2022)
45. N. Kaiser, Y. Lin and U. Meißner
Radiative corrections to elastic muon-proton scattering at low momentum transfers
Phys. Rev. D **105** 076006 (2022)
46. C. Kannis, J. Suarez and T.P. Rakitzis
Macroscopic production of spin-polarised hydrogen atoms from the IR-excitation and photodissociation of molecular beams
Mol. Phys. **120** e1975053 (2022)
47. B. Kaspschak and U. Meißner
Three-body renormalization group limit cycles based on unsupervised feature learning
Mach. Learn.: Sci. Technol. **3** 025003 - (2022)

48. F. Knechtli, T. Luu and C. Urbach
Erratum to: Topical issue on Lattice Field Theory during the Covid-19 pandemic
Eur. Phys. J. A **58** 47 (2022)
49. Y. Li *et al.*
Measurements of the branching fractions of $\Xi_c^0 \rightarrow \Lambda K_s^0$, $\Xi_c^0 \rightarrow \Sigma^0 K_s^0$, and $\Xi_c^0 \rightarrow \Sigma^+ K^-$ decays at Belle
Phys. Rev. D **105** L011102 (2022)
50. Y.B. Li *et al.*
First test of lepton flavor universality in the charmed baryon decays $\Omega_c^0 \rightarrow \Omega^- \ell^+ \nu_\ell$ using data of the Belle experiment
Phys. Rev. D **105** L091101 (2022)
51. Y. Lin, H. Hammer and U. Meißner
New Insights into the Nucleon's Electromagnetic Structure
Phys. Rev. Lett. **128** 052002 (2022)
52. Y. Lin, H. Hammer and U. Meißner
Differential cross section predictions for PRad-II from dispersion theory
Phys. Lett. B **827** 136981 - (2022)
53. Y. Lin, H. Hammer and U. Meißner
Dispersion-theoretical analysis of the electromagnetic form factors of the Λ hyperon
Eur. Phys. J. C **82** 1091 (2022)
54. J. Lozano *et al.*
Resonance form factors from finite-volume correlation functions with the external field method
J. High Energ. Phys. **2022** 106 (2022)
55. B. Lu *et al.*
Perturbative Quantum Monte Carlo Method for Nuclear Physics
Phys. Rev. Lett. **128** 242501 (2022)
56. T. Luu, U. Meißner and L. Razmadze
Localization of electronic states in hybrid nanoribbons in the nonperturbative regime
Phys. Rev. B **106** 195422 (2022)
57. N. Lyutorovich *et al.*
Self-consistent description of high-spin states in doubly magic Pb 208
Phys. Rev. C **105** 014327 (2022)
58. A. Magiera, A. Aggarwal and V. Poncza
Method to evaluate systematic uncertainties due to magnet misalignments in electric dipole moment measurements using a storage ring
J. Phys. G **49** 015004 - (2022)
59. M. Mai *et al.*
Coupled-channels analysis of pion and η electroproduction within the Jülich-Bonn-Washington model
Phys. Rev. C **106** 015201 (2022)
60. A. Malige *et al.*
Real-Time Data Processing Pipeline for Trigger Readout Board-Based Data Acquisition Systems
IEEE T. Nucl. Sci. **69** 1765 - 1772 (2022)
61. P. Maris *et al.*
Nuclear properties with semilocal momentum-space regularized chiral interactions beyond N²LO
Phys. Rev. C **106** 064002 (2022)
62. U. Meißner
Neutronen im Viererpack
Phys. J. **21** 26 (2022)
63. U. Meißner and B.C. Metsch
Probing nuclear observables via primordial nucleosynthesis
Eur. Phys. J. A **58** 212 (2022)

64. S. Morán *et al.*
Measurement of charged-pion production in deep-inelastic scattering off nuclei with the CLAS detector
Phys. Rev. C **105** 015201 (2022)
65. H. Mutuk and K. Azizi
Investigation of $\Delta^0\Delta^0$ dibaryon in QCD
Phys. Rev. D **105** 094021 (2022)
66. J.Y. Panteleeva *et al.*
Definition of electromagnetic local spatial densities for composite spin- 1 / 2 systems
Phys. Rev. D **106** 056019 (2022)
67. S. Patra *et al.*
Search for charged lepton flavor violating decays of Υ (1S)
J. High Energ. Phys. **2022** 95 (2022)
68. M. Rodekamp *et al.*
Mitigating the Hubbard sign problem with complex-valued neural networks
Phys. Rev. B **106** 125139 (2022)
69. D. Rönchen *et al.*
Light baryon resonances from a coupled-channel study including $K\Sigma$ photoproduction
Eur. Phys. J. A **58** 229 (2022)
70. M. Salajegheh *et al.*
Global QCD analysis of diffractive parton distribution function considering higher twist corrections within the xFitter framework
Phys. Rev. D **106** 054012 (2022)
71. C. Seng *et al.*
Update on $|V_{us}|$ and $|V_{us}/V_{ud}|$ from semileptonic kaon and pion decays
Phys. Rev. D **105** 013005 (2022)
72. C. Seng *et al.*
Complete theory of radiative corrections to $K_{\ell 3}$ decays and the V_{us} update
J. High Energ. Phys. **2022** 71 (2022)
73. C. Seng, W.J. Marciano and U. Meißner
Electron mass singularities in semileptonic kaon decays
Phys. Rev. D **106** 013006 (2022)
74. C. Shen and U. Meißner
Prediction of five-flavored pentaquarks
Phys. Lett. B **831** 137197 - (2022)
75. Y. Shi, U. Meißner and Z. Zhao
Resonance contributions in $B^- \rightarrow K^+ K^- \pi^-$ within the light-cone sum rule approach
Eur. Phys. J. C **82** 113 (2022)
76. Y. Shi *et al.*
 W -exchange contribution to the decays $\Xi_c^{++} \rightarrow \Xi^{+(\prime)} \pi^+$ using light-cone sum rules
Phys. Rev. D **106** 034004 (2022)
77. J. Stapmanns *et al.*
Erratum: Self-consistent formulations for stochastic nonlinear neuronal dynamics [Phys. Rev. E 101 , 042124 (2020)]
Phys. Rev. E **105** 059901 (2022)
78. G. Stellin, K. Speidel and U. Meißner
Magnetic dipole moments as a strong signature for α -clustering in even-even self-conjugate nuclei
Eur. Phys. J. A **58** 208 (2022)
79. L. Tiberi *et al.*
Gell-Mann-Low Criticality in Neural Networks
Phys. Rev. Lett. **128** 168301 (2022)

80. T. Tolba *et al.*
Irradiation studies of silicon photomultipliers with proton beam from the JULIC cyclotron
Nucl. Instr. Meth. Phys. Res. A **1025** 166130 - (2022)
81. T. Vonk, F. Guo and U. Meißner
Pion axioproduction: The Δ resonance contribution
Phys. Rev. D **105** 054029 (2022)
82. E. Waheed *et al.*
Study of $\bar{B}^0 \rightarrow D^+ h^-$ ($h = K/\pi$) decays at Belle
Phys. Rev. D **105** 012003 (2022)
83. B. Wang *et al.*
Measurement of B ($B_s \rightarrow D s X$) with B s semileptonic tagging
Phys. Rev. D **105** 012004 (2022)
84. J. Wang *et al.*
Damping signatures at JUNO, a medium-baseline reactor neutrino oscillation experiment
J. High Energ. Phys. **2022** 62 (2022)
85. X.L. Wang *et al.*
Study of $\gamma\gamma \rightarrow \gamma\psi(2s)$ at Belle
Phys. Rev. D **105** 112011 (2022)
86. Y. Wang *et al.*
Reaction $\pi N \rightarrow \omega N$ in a dynamical coupled-channel approach
Phys. Rev. D **106** 094031 (2022)
87. Z. Wang *et al.*
Resonances in heavy meson-heavy baryon coupled-channel interactions
Eur. Phys. J. C **82** 497 (2022)
88. R.L. Workman *et al.*
Review of Particle Physics
Prog. Theor. Exp. Phys. **2022** 083C01 (2022)
89. N. Zachariou *et al.*
Beam-spin asymmetry Σ for Σ^- hyperon photoproduction off the neutron
Phys. Lett. B **827** 136985 - (2022)
90. X. Zhang *et al.*
Remarks on non-perturbative three-body dynamics and its application to the $KK\bar{K}$ system
Eur. Phys. J. A **58** 20 (2022)
91. Z. Zhang *et al.*
Performance Study of a New Cluster Splitting Algorithm for the Reconstruction of PANDA EMC Data
Instr. (MDPI) **6** 34 - (2022)

D Talks, Colloquia and Proceedings

D.1 Conference and Workshop Contributions

1. A. Aliche, T. Stockmanns and J. Ritman
Track Finding with PANDA
DPG Frühjahrstagung 2022, online, Germany: 2022-03-28 - 2022-04-01
2. A. Aliche, T. Stockmanns and J. Ritman
Secondary Track Finding for PANDA
FAIR next generation scientists - 7th Edition Workshop, Paralía, Greece: 2022-05-23 - 2022-05-27
3. A. Aliche, T. Stockmanns and J. Ritman
Track Finding for the PANDA Experiment
Connecting the Dots 2022, Princeton University, USA: 2022-05-31 - 2022-06-02
4. A. Aliche, T. Stockmanns and J. Ritman
 Λ Reconstruction with Realistic Track Finding for PANDA
The Helmholtz program days Matter and the Universe 2022, Darmstadt, Germany: 2022-10-20 - 2022-10-21
5. A. Andres
The Search for Electric Dipole Moments of Charged Particles in Storage Rings
20th Conference on Flavor Physics and CP Violation, Oxford, Mississippi, USA: 2022-05-23 - 2022-05-27
arXiv:2207.02083
6. C. Böhme *et al.*
Status Overview of the HESR Beam Instrumentation
11th International Beam Instrumentation Conference, Krakow, Poland: 2022-09-11 - 2022-09-15
7. C. Böhme
Update on the Operational Experience of the LIBERA HADRON at COSY
Libera Workshop 2022, Solkan, Slovenia: 2022-05-11 - 2022-05-13
8. G. Ciullo *et al.*
Polarization REsearch for Fusion Experiments and Reactors - The PREFER Collaboration: Purposes and Present Status
24th International Spin Symposium (SPIN2021), Matsue, Japan (Hybrid): 2021-10-18 - 2021-10-22
9. R.W. Engels
How to produce nuclear-polarized hydrogen molecules and for what they can be used
DPG Frühjahrstagung AMOP, Erlangen, Germany: 2022-03-14 - 2022-03-18
10. R.W. Engels *et al.*
Initial storage cell coating R&D for LHCSpin
PBC mini-workshop on Vacuum, Coating and Surface technologies, CERN, Switzerland: 2022-04-06 - 2022-04-06
11. R.W. Engels
How to produce polarized Hydrogen/Deuterium Molecules in single Hyperfine Substates
StereoDynamics2022, Rethymnon, Crete, Greece: 2022-10-30 - 2022-11-04
12. R.W. Engels
Polarized H_2 , D_2 and HD molecules and their possible use to feed a polarized H_2^+ , D_2^+ or HD^+ ion source for stripping injection into storage rings
Workshop on polarized Sources, Targets and Polarimetry, Mainz, Germany: 2022-09-26 - 2022-09-30
13. R.W. Engels
Storage Cell Tests for the Polarized Target at LHCb
Workshop on polarized Sources, Targets and Polarimetry, Mainz, Germany: 2022-09-26 - 2022-09-30
14. R.W. Engels *et al.*
Polarized H_2 , D_2 and HD Molecules and Their Possible Use to Feed a Polarized H^+ , D^+ or HD^+ Ion Source for Stripping Injection into Storage Rings
24th International Spin Symposium (SPIN2021), Matsue, Japan (Hybrid): 2021-10-18 - 2021-10-22

15. W.A. Esmail
Investigation of the Σ^0 hyperon production in $p(3.5\text{GeV})+p$ collisions
 14th International Conference on Hypernuclear and Strange Particle Physics, Prag, Czech Republic: 2022-06-27 - 2022-07-01
16. N. Faatz
Hyperfine-spectroscopy measurement of metastable hydrogen atoms with a Sona-transition unit
 Workshop on polarized Sources, Targets and Polarimetry, Mainz, Germany: 2022-09-26 - 2022-09-30
17. P. Gibbon *et al.*
Experimental and numerical studies on laser-generated spin-polarized particle beams
 48th EPS Conference on Plasma Physics, Maastricht, Netherlands: 2022-06-27 - 2022-07-01
18. A. Göttel
JUST: A neutrino fit software for JUNO's solar analysis and sensitivity
 The 1st INFN School on Underground Physics, Online, Italy: 2021-06-28 - 2021-07-02
 Nuovo Cimento C 9
19. A. Göttel
JUNO potential in non-oscillation physics
 The European Physical Society Conference on High Energy Physics, Online conference, jointly organized by Universität Hamburg and the research center DESY: 2021-07-26 - 2021-07-30
20. A. Göttel
JUNO physics potential and status
 Deutsche Physikalische Gesellschaft, Online (Heidelberg), Germany: 2022-03-21 - 2022-03-25
21. E. Gregory *et al.*
Exotic states in the πD system
 The 38th International Symposium on Lattice Field Theory, Zoom/Gather@Massachusetts Institute of Technology, USA: 2021-07-26 - 2021-07-30
22. T. Gutberlet *et al.*
The HBS Project for a next generation accelerated based neutron source
 German Conference for Research with Synchrotron Radiation, Neutrons and Ion Beams at Large Facilities, Freie Universität Berlin, Germany: 2022-09-05 - 2022-09-07
23. J. Haidenbauer
Status of the hyperon-nucleon interaction in chiral effective field theory
 14th International Conference on Hypernuclear and Strange Particle Physics, Prague, Czech Republic: 2022-06-27 - 2022-07-01
24. J. Haidenbauer
Assorted aspects of the hyperon-nucleon interaction
 EXOTICO: EXOTic atoms meet nuclear COLLisions for a new frontier precision era in low-energy strangeness nuclear physics, Trento, Italy: 2022-10-17 - 2022-10-21
25. J. Haidenbauer
 $J/\psi p$ and $\Lambda_c p$ interactions reviewed
 Workshop on Femtoscopy "FemTUM22", Munich, Germany: 2022-08-31 - 2022-09-02
26. J. Haidenbauer and U. Meißner
Status of the hyperon-nucleon interaction in chiral effective field theory
 14th International Conference on Hypernuclear and Strange Particle Physics, Pra, Czech Republic: 2022-06-27 - 2022-07-01
 Eur. Phys. J. Web of Conferences 271 05001
27. C. Hanhart
What line shapes of resonances teach us about their nature
 Hadron Spectroscopy: The Next Big Steps, Mainz, Germany: 2022-03-14 - 2022-03-25
28. C. Hanhart
Coupled-channel approach to T_{cc}^+ including three-body effects
 The 15th International Workshop on Heavy Quarkonium, Darmstadt, Germany: 2022-09-26 - 2022-09-30

29. C. Hanhart
What lineshapes of resonances teach us about their nature
 4th Workshop on Future Directions in Spectroscopy Analysis, Newport News, USA: 2022-11-14 - 2022-11-16
30. L. Jokhovets *et al.*
Versatile free-running ADC-based data acquisition system for particle detectors
 Topical Workshop on Electronics for Particle Physics 2021, Zurich, online: 2021-09-20 - 2021-09-24
 J. Instrum. 17 C04022 -
31. J. Kannika, J. Ritman and T. Stockmanns
Machine Learning Approach for Track Finding Using Language Models
 Deutsche Physikalische Gesellschaft, Mainz, Germany: 2022-03-28 - 2022-04-01
32. C. Kannis
A NEW TYPE OF SPECTROSCOPY: Direct observation of hyperfine transitions with energy differences of 10 neV and below
 DPG Frühjahrstagung AMOP, Erlangen, Germany: 2022-03-14 - 2022-03-18
33. C. Kannis
Development of polarized sources based on molecular photodissociation
 Workshop on polarized Sources, Targets and Polarimetry, Mainz, Germany: 2022-09-26 - 2022-09-30
34. C.S. Kannis *et al.*
New Application of a Sona Transition Unit: Observation of Direct Transitions between Quantum States with Energy Differences of 10 neV and Below
 24th International Spin Symposium (SPIN2021), Matsue, Japan (Hybrid): 2021-10-18 - 2021-10-22
35. J. Kim and W. Unger
Error reduction using machine learning on Ising worm simulation
 The 39th International Symposium on Lattice Field Theory, LATTICE2022, Bonn, Germany: 2022-08-08 - 2022-08-13
 arXiv:2212.02365
36. J. Kim, P. Pattanaik and W. Unger
Nuclear Transition in the Strong Coupling Limit
 39th International Symposium on Lattice Field Theory, Bonn, Germany: 2022-08-08 - 2022-08-13
 arXiv:2212.03118
37. S. Kumaran
Directional analysis of sub-MeV 7Be solar neutrinos in Borexino
 The 1st INFN International School on Underground Physics (SoUP), online, online: 2021-06-28 - 2021-07-02
 Nuovo Cimento C 12
38. S. Kumaran
Recent solar and geoneutrino results from Borexino
 DPG Spring Meetings, Heidelberg (online), Germany: 2022-03-21 - 2022-03-25
39. J. Li *et al.*
Target activation and radiation safety for the HBS HiCANS
 First International Meeting on Challenges and Opportunities for HICANS, BCMaterials headquarters, Bizkaia Science & Technology Park, campus University Basque Country Leioa, Spain: 2022-06-20 - 2022-06-22
40. R. Liu
JUNO Experiment: Current Status and Physics
 The 28th International Nuclear Physics Conference, Cape Town, South Africa: 2022-09-11 - 2022-09-16
41. R. Liu *et al.*
Calibration and Trigger Studies for the OSIRIS pre-detector of JUNO
 Deutsche Physikalische Gesellschaft, Online (Heidelberg), Germany: 2022-03-21 - 2022-03-25
42. L. Ludhova
JUNO STATUS
 23rd International Workshop on Neutrinos from Accelerators, Salt Lake City, USA: 2022-07-31 - 2022-08-06

43. L. Ludhova
Borexino looks in the direction of solar neutrinos
 DPG Spring Meetings, Heidelberg (online), Germany: 2022-03-21 - 2022-03-25
44. L. Ludhova
Geoneutrinos from Borexino
 Passion for Earth - A new era for geoscience, Milano, Italy: 2022-10-27 - 2022-10-27
45. U. Meißner
Hypernuclear Physics from Nuclear Lattice EFT
 Second International Workshop on the Extension Project for the J-PARC Hadron Experimental Facility, J-PARC, Japan: 2022-02-16 - 2022-02-18
46. U. Meißner
Two-pole structures in QCD
 Workshop on "Hadronic molecules with heavy meson loops", Guangzhou, Peoples R China: 2022-02-16 - 2022-02-18
47. U. Meißner
Dispersive analysis of the nucleon's electromagnetic form factors
 International STRONG-2020 Workshop on the Proton Charge Radius and related topics, Paris, France: 2022-06-20 - 2022-06-23
48. U. Meißner
Aspects of strong CP-violation
 ECT* workshop on Neutron Electric Dipole Moment: from theory to experiment, Trento, Italy: 2022-08-01 - 2022-08-05
49. U. Meißner
Recent developments in Nuclear Lattice Effective Field Theory
 4th Meeting of the Low Energy Nuclear Physics International Collaboration, Bochum, Germany: 2022-08-24 - 2022-08-26
50. U. Meißner
The proton radius and its relatives
 International Nuclear Physics Conference 2022, Cape Town, South Africa: 2022-09-11 - 2022-09-16
51. U. Meißner
Axion-baryon couplings
 8th RDP workshop on "Recent Advances in Fundamental Physics", Tbilisi, Rep of Georgia: 2022-09-27 - 2022-10-01
52. U. Meißner
Molecular structures in hadron and nuclear physics
 Baiyan X Forum, Beijing, Peoples R China: 2022-10-28 - 2022-10-28
53. U. Meißner
Nuclear Lattice Effective Field Theory: Status A.D. 2022
 NIC Symposium 2022, Jülich, Germany: 2022-09-29 - 2022-09-30
54. N. Mohan *et al.*
Studies on the sensitivity for the Neutrino Mass Ordering Measurement of JUNO
 Deutsche Physikalische Gesellschaft, Online (Heidelberg), Germany: 2022-03-21 - 2022-03-25
55. A. Nogga
Hypernuclei based on chiral interactions
 19th International Conference on Hadron Spectroscopy and Structure, Mexico City, Mexico: 2021-07-26 - 2021-08-01
56. A. Nogga
Few-body hypernuclei
 Bethe Forum on "Multihadron Dynamics in a Box - A.D. 2022", Bonn, Germany: 2022-08-15 - 2022-08-19

57. A. Nogga
Constraints on the Lambda-neutron interaction from charge symmetry breaking of A=4 hypernuclei
 Modern equations of state and spectroscopy in neutron-star matter, Alcalá de Henares, Madrid, Spain: 2022-09-21 - 2022-09-23
58. A. Nogga
Relativistic corrections in the Faddeev-Yakubovsky framework
 The 4th Meeting of the Low Energy Nuclear Physics International Collaboration, Bochum, Germany: 2022-08-24 - 2022-08-26
59. L. Pelicci
Current status and prospects in solar neutrino field
 41st International Symposium on Physics in Collision, Tbilisi, Rep of Georgia: 2022-09-05 - 2022-09-09
60. L. Pelicci *et al.*
Solar neutrinos with JUNO: analysis strategy and sensitivity studies for Be7, pep and CNO neutrinos
 Deutsche Physikalische Gesellschaft, Online (Heidelberg), Germany: 2022-03-21 - 2022-03-25
61. L. Pelicci
Solar neutrino physics with JUNO: analysis strategy and sensitivity studies for Be7, pep and CNO neutrinos
 Neutrino 2022, Seoul (online), South Korea: 2022-05-30 - 2022-06-04
62. Ö. Penek
Observing our Sun with Borexino
 Blois 2022: 33rd Rencontres de Blois on "Exploring the Dark Universe", Château de Blois, Blois, Loire Valley, France: 2022-05-22 - 2022-05-27
63. G. Pérez Andrade *et al.*
Hyperon physics at HADES as a fair phase-0 experiment
 19th International Conference on Hadron Spectroscopy and Structure in memoriam Simon Eidelman, virtual, Mexiko: 2021-07-26 - 2021-07-31
64. G. Perez, P. Wintz and J. Ritman
THE NEW FORWARD TRACKER SYSTEM FOR THE HADES AND PANDA PHASE-0 EXPERIMENT
 DPG CONFERENCE MAINZ, Online-Mainz, Germany: 2022-03-28 - 2022-04-01
65. J. Pretz
Search for Electric Dipole Moments and Axions/ALPs at Storage Rings
 Trapped Charged Particles Conference 2022, Glashütten, Germany: 2022-09-26 - 2022-09-30
66. J. Pretz
Axion Searches at Storage Rings
 Workshop on Polarized Sources, Targets, and Polarimetry, Mainz, Germany: 2022-09-26 - 2022-09-30
67. J. Pretz
Towards experiments with polarized beams and targets at the GSI/FAIR storage rings
 Sparc Workshop, Jena, Germany: 2022-09-09 - 2022-09-09
68. J. Pretz
Event weighting vs. Event Counting
 RDP online PhD school and workshop 'Aspects of Symmetry', Online, Germany: 2021-11-08 - 2021-11-12
69. J. Pretz
Electric Dipole Moment Measurements at Storage Rings
 Proceedings of the 24th International Spin Symposium (SPIN2021), Matsue, Japan (Hybrid): 2022-10-18 - 2022-10-22
70. S.J. Pütz
Polarization measurement of a pulsed H^-/D^- ion Beam with a Lamb-shift Polarimeter
 Workshop on polarized Sources, Targets and Polarimetry, Mainz, Germany: 2022-09-26 - 2022-09-30
71. F. Rathmann
First direct hadron EDM measurement with deuterons using COSY
 Extreme Storage Rings Workshop, online, Switzerland: 2022-01-31 - 2022-02-08

72. M. Rifai *et al.*
Event reconstruction for the neutrino mass ordering measurement of JUNO
 Deutsche Physikalische Gesellschaft, Online (Heidelberg), Germany: 2022-03-21 - 2022-03-25
73. D. Rönchen
Baryon spectroscopy with the Jülich-Bonn dynamical coupled-channel approach
 DPG Frühjahrstagung Physik der Hadronen und Kerne (HK), online (Mainz), Germany: 2022-03-28 - 2022-04-01
74. D. Rönchen
Determination and status of the light baryon and hyperon spectrum
 The 9th International Conference on Quarks and Nuclear Physics, online, USA: 2022-09-05 - 2022-09-09
75. D. Rönchen
The light baryon resonance spectrum in a coupled-channel approach – recent results from the Juelich-Bonn model
 The 13th International Workshop on the Physics of Excited Nucleons, Santa Margherita Ligure, Italy: 2022-10-17 - 2022-10-21
76. D. Rönchen
Determination and status of the light baryon spectrum (Overview talk on PWA)
 International Conference on the Structure of Baryons, Online/Sevilla, Spain: 2022-11-07 - 2022-11-11
77. A. Saleev *et al.*
Spin Tune Response to Vertical Orbit Correction at COSY
 Proceedings of the 24th International Spin Symposium (SPIN2021), Matsue, Japan (Hybrid): 2021-10-18 - 2021-10-22
78. A. Schwab *et al.*
Time-of-flight measurements using a compact solid methan moderator
 German Conference for Research with Synchrotron Radiation, Neutrons and Ion Beams at Large Facilities, Freie Universität Berlin, Germany: 2022-09-05 - 2022-09-07
79. V. Shmakova
The search for electric dipole moments of charged particles using storage rings
 2nd Joint ECFA-NuPECC-ApPEC Symposium, Madrid, Spain: 2022-05-03 - 2022-05-06
80. V. Shmakova
Electric dipole moments of charged particles at storage rings
 DPG Frühjahrstagung, Mainz, Germany: 2022-03-28 - 2022-04-01
81. V. Shmakova
The search for electric dipole moment of charged particles using storage rings
 Workshop on Polarized Sources Targets and Polarimetry 2022, Mainz, Germany: 2022-09-26 - 2022-09-30
82. V. Shmakova
Search for the Electric Dipole Moment of Charged Particles Using Storage Rings
 European Nuclear Physics Conference 2022, Santiago de Compostela, Spain: 2022-10-24 - 2022-10-28
83. V. Shmakova
The Search for Electric Dipole Moments of Charged Particles Using Storage Rings
 Proceedings of the 24th International Spin Symposium (SPIN2021), Matsue, Japan (Hybrid): 2021-10-18 - 2021-10-22
84. A. Singhal
Analysis strategies used in the directional analysis of sub-MeV solar neutrinos in a liquid scintillator detector
 DPG Spring Meetings, Heidelberg (online), Germany: 2022-03-21 - 2022-03-25
85. A. Singhal
Recent results from Borexino: measurement of CNO solar neutrinos and directionality of sub-MeV solar neutrinos
 International Research Network Neutrino meeting, Annecy, France: 2022-06-29 - 2022-06-30

86. A. Singhal
Recent results from Borexino: measurement of CNO solar neutrinos and directionality of sub-MeV solar neutrinos
Matter and the Universe 2022, Darmstadt, Germany: 2022-10-20 - 2022-10-21
87. A. Singhal
First directional measurement of sub-MeV solar neutrinos in the liquid scintillator detector by Borexino
Neutrino 2022, Seoul (online), South Korea: 2022-05-30 - 2022-06-04
88. H. Smitmanns *et al.*
New Aspects of Storage Cell Developments for the Polarized Internal Target at LHCb
24th International Spin Symposium (SPIN2021), Matsue, Japan (Hybrid): 2021-10-18 - 2021-10-22
89. M.C. Vollbrecht
OSIRIS - The Online Scintillator Internal Radioactivity Investigation System of JUNO
Low Radioactivity Techniques, Rapid City, USA: 2022-06-14 - 2022-06-17
90. M.C. Vollbrecht *et al.*
Calibration of the JUNO pre-detector OSIRIS
Deutsche Physikalische Gesellschaft, Online (Heidelberg), Germany: 2022-03-21 - 2022-03-25
91. M. Westphal
Measurement of the occupation number of metastable atoms in the hyperfine-substate β_3 in an atomic hydrogen beam
Workshop on polarized Sources, Targets and Polarimetry, Mainz, Germany: 2022-09-26 - 2022-09-30
92. A. Weßel
Optimization of selection cuts for the directional analysis of sub-MeV solar neutrinos in Borexino
DPG Spring Meetings, Heidelberg (online), Germany: 2022-03-21 - 2022-03-25
93. A. Wirzba
Strong CP Problem
RDP online PhD school and workshop 'Aspects of Symmetry', Online, Rep of Georgia: 2021-11-08 - 2021-11-12

D.2 Colloquia

1. R.W. Engels
Status of recombination and depolarization studies at FZJ
32nd PBC-FT working group meeting, CERN, Switzerland: 2022-03-25 - 2022-03-25
2. J. Haidenbauer
Final state interaction of antiproton-proton in hadron decays
Beijing, Peoples R China: 2022-04-07
3. J. Hetzel
The High Energy Storage Ring HESR at FAIR
"Extreme Storage Rings" Workshop, online, Germany: 2022-01-31 - 2022-02-08
4. L. Ludhova
JUNO: the first multi-kton liquid scintillator based neutrino detector
London, UK: 2022-06-13
5. L. Ludhova
Geoneutrinos : A new tool to study the Earth
Colloquium at Université de Paris and Institut Universitaire de France, Paris, France: 2022-10-20
6. L. Ludhova
Updated geoneutrino measurement with Borexino
Grenoble (online), France: 2022-02-10
7. L. Ludhova
Geoneutrinos: a new tool to study the Earth
IOPB Online Colloquium, Bhubaneswar, Odisha (online), India: 2022-11-22

8. L. Ludhova
Solar neutrinos from the Carbon-Nitrogen-Oxygen fusion cycle: Borexino discovery and implications for the Standard Solar Model
Zeuthen, Germany: 2022-12-02
9. G. Perez, P. Wintz and J. Ritman
The new Forward Tracker System for the HADES FAIR Phase-0 experiment
FAIR next generation scientists - 7th Edition Workshop, **???—<PUB-LOCATION>—???**: 2022-05-23 - 2022-05-27
10. J. Pretz
Physik und Musik - Vom Gartenschlauch zur Posaune
Nacht der Wissenschaft, Duesseldorf, Germany: 2022-09-09
11. J. Pretz
Blick über den Tellerrand: Physik und Musik
Highlights der Physik, Regensburg, Germany: 2022-09-20

E Academic Degrees

E.1 Dissertation / PhD Theses

1. N. Canale
The SiPM Tracking Hodoscope for the JEDI Polarimeter
University of Ferrara
2. A. Göttel
Solar neutrino detection: CNO discovery with Borexino and preparations for success in JUNO and OSIRIS
RWTH Aachen
3. O. Javakhishvili
The Target System Development for an Electric Dipole Moment Measurement of Charged Particles at the Cooler Synchrotron COSY
Agricultural University of Georgia
4. F.A. Khan
An exploratory study for the $\omega - \pi$ transition form factor with WASA-at-COSY
Bergische Universität Wuppertal
5. S. Kumaran
Geoneutrinos and Solar neutrinos with the Borexino experiment
RWTH Aachen University

E.2 Master Theses

1. A. Asokan
Classification of Coupled Channel Amplitudes for Pole Extraction from LatticeQCD Studies
Bonn
2. D. Gu
Investigation of the Spin Coherence Time for measuring the Electric Dipole Moment of Protons in the COSY Cooler Synchrotron
RWTH Aachen
3. M. Manerova
Modeling of the Optical Setting for the Measurement of the Electric Dipole Moment of Protons at Cooler Synchrotron COSY
RWTH
4. C. Schneider
Renormalisation for coupled S-wave and D-wave contact potentials
Bonn
5. H. Smitmanns
Measurements of Transitions between Different Hyperfine Structure Substates of Hydrogen using a Sona Transition Unit
RWTH Aachen
6. A. Weßel
Directionality measurement of solar neutrinos CNO solar neutrino analysis with Borexino
RWTH Aachen University

E.3 Bachelor Theses

1. J. Ammon
Spin Tune Analysis using Machine Learning Methods
RWTH Aachen
2. S.V. Aswani
Optimization of the magnetic field configuration of a Sona transition unit
Forschungszentrum
3. O. Bilen
Preparation and Test of Carbon coated Storage Cells for the LHCspin Project
HHU Düsseldorf
4. C. Engelhardt
A Tool to Check the Analytic Structure of Amplitude Parametrisations
Bonn
5. L. Kunkel
Suche nach systematischen Effekten bei magnetisch induzierten Übergängen zwischen Hyperfeinstruktur-Unterzuständen
Forschungszentrum
6. S. Lehmann
Towards a systematic treatment of relativistic three-body systems
Bonn
7. C. Lörler
Width effects in QCD sum-rule analyses
Bonn
8. J. Salmann
Measurements of the Breit-Rabi Diagram of Deuterium with a Sona-Transition Unit
RWTH Aachen

F Awards

1. C. Hanhart
Recognition as Outstanding Referee for the American Physical Society.
2. U.-G. Meißner
Named Outstanding Reviewer of IOP Publishing.
3. Ludhova, L.
Listed among the **top Slovak scientists based on the h-index**.
4. Vollbrecht, M. C.
PhD research scholarship, sponsored by the Deutscher Akademischer Austauschdienst (DAAD), to support the 3-months long stay in China with the goal to contribute to the commissioning of the JUNO-OSIRIS detector.
5. Rifai, M.
Best poster in the Atmospheric Neutrinos field at the NEUTRINO 2022 conference.

G Third Party Funded Projects

Project	Responsible/Contact	Funded by
PGSB: Experimental tests of time-reversal NRW-FAIR	H. Ströher C. Hanhart	BMBF Ministry of Culture and Science of the state of NRW
SFB/TRR 110 Quantenchromodynamik TP A01	J. Haidenbauer	DFG/NSFC
SFB/TRR 110 Quantenchromodynamik TP A02	T. Luu	DFG/NSFC
SFB/TRR 110 Quantenchromodynamik TP A10	T. Luu	DFG/NSFC
SFB/TRR 110 Quantenchromodynamik TP B03	C. Hanhart	DFG/NSFC
SFB/TRR 110 Quantenchromodynamik TP B06	U.-G. Meißner	DFG/NSFC
SFB/TRR 110 Quantenchromodynamik TP B07	A. Nogga	DFG/NSFC
SFB/TRR 110 Quantenchromodynamik TP B09	T. Luu / U.-G. Meißner	DFG/NSFC
SFB/TRR 110 Quantenchromodynamik TP B11	D. Rönchen	DFG/NSFC
SFB/TRR 110 Quantenchromodynamik TP Z01	C. Hanhart	DFG/NSFC
SFB/TRR 110 Quantenchromodynamik TP Z02	C. Hanhart	DFG/NSFC
PANDA/ Straw Tube Tracker	J. Ritman	Industrieprojekt mit der GSI GmbH
PANDA/ Micro Vertex Detector	J. Ritman	Industrieprojekt mit der GSI GmbH
HESR - Dipole und Quadrupole	R. Tölle	Industrieprojekt mit der FAIR GmbH
HESR - sonstige Magnete	J. Böker	Industrieprojekt mit der FAIR GmbH
HESR - Netzgeräte	M. Retzlaff	Industrieprojekt mit der FAIR GmbH
HESR - Hochfrequenz	R. Stassen	Industrieprojekt mit der FAIR GmbH
HESR - Injektion	R. Tölle	Industrieprojekt mit der FAIR GmbH
HESR - Strahldiagnose	V. Kamedzhiev	Industrieprojekt mit der FAIR GmbH
HESR - Vakuum	F. Esser	Industrieprojekt mit der FAIR GmbH
HESR - Stochastische Kühlung	R. Stassen	Industrieprojekt mit der FAIR GmbH
HESR - Panda-Integration	D. Prasuhn	Industrieprojekt mit der FAIR GmbH
HESR - P1SR	R. Tölle	Industrieprojekt mit der GSI GmbH
Transnational Access to COSY TA1	D. Grzonka	EU (STRONG2020)
JRA2-FTE@LHC:	F. Rathmann	EU (STRONG2020)
JRA12-SPINFORFAIR: Spin for FAIR	F. Rathmann	EU (STRONG2020)
srEDM ERC Advanced Grant Management	H. Ströher	EU
srEDM ERC Advanced Grant Research	H. Ströher	EU
Bestimmung der Neutrino-Massenhierarchie	L. Ludhova	DFG

H Collaborations

- ATHENA Accelerator Technology Helmholtz Infrastructure
(https://www.athena-helmholtz.de/home/index_eng.html)
- Belle-II (B(meson) to lepton lepton (v.2))
(<https://www.belle2.org>)
- Borexino (Boron solar neutrino experiment, LNGS, Italy)
(<http://borex.lngs.infn.it>)
- CBM (Compressed Baryonic Matter)
(<https://www.gsi.de/work/forschung/cbmnqm/cbm.htm>)
- CLAS (CEBAF Large Acceptance Spectrometer, Jefferson Lab, USA)
(<https://www.jlab.org/Hall-B/clas-web>)
- CPEDM (Electric Dipole Moments, CERN)
(<http://pbc.web.cern.ch/edm/edm-org.htm>)
- ELENA (CERN) (Extra Low Energy Antiproton ring)
(<https://espace.cern.ch/elena-project/SitePages/Home.aspx>)
- GlueX (Gluonic Excitations Experiment, Jefferson Lab, USA)
(<https://www.jlab.org/Hall-D/>)
- HADES (High Acceptance DiElectron Spectrometer)
(<https://www-hades.gsi.de>)
- HBS (High Brilliance Neutron Source)
(https://www.fz-juelich.de/jcms/jcms-2/EN/Forschung/High-Brilliance-Neutron-Source/_node.html)
- JEDI (Jülich Electric Dipole moment Investigation, COSY)
(<http://collaborations.fz-juelich.de/ikp/jedi>)
- JUNO (Jiangmen Underground Neutrino Observatory, Jiangmen, China)
(<http://juno.ihep.cas.cn>)
- JuSPARC (Jülich Short-Pulsed Particle and Radiation Center)
(<https://jusparc.fz-juelich.de/>)
- KLF (K-long Facility, Jefferson Lab)
(https://wiki.jlab.org/klproject/index.php/December,_2020)
- LENPIC (Low Energy Nuclear Physics International Collaboration)
(<http://www.lenpic.org/>)
- PANDA (Anti-Proton Annihilation at Darmstadt, FAIR)
(<https://panda.gsi.de>)
- PAX (Polarized Antiproton eXperiments, COSY)
(<http://collaborations.fz-juelich.de/ikp/pax>)
- PDG (Particle Data Group)
(pdg.lbl.gov)
- PREFER (Polarization Research for Fusion Experiments and Reaktors)
- STRONG-2020 (The strong interaction at the frontier of knowledge: fundamental research and applications)
(www.strong-2020.eu)
- WASA-FRS (Wide Angle Shower Apparatus at FRS)
(<https://www-win.gsi.de/frs/index.htm>)
- WASA-at-COSY (Wide Angle Shower Apparatus at COSY)
(<http://collaborations.fz-juelich.de/ikp/wasa/>)

I Conferences and Outreach Activities (Co-)Organized by the IKP

I.1 PSTP2022 Workshop

The 19th International Workshop on Polarized Sources, Targets, and Polarimetry (PSTP 2022) took place at the Helmholtz-Institut Mainz (HIM) in Mainz (Germany) from September 26th to 30th, 2022. The scientific program of this workshop covered the following topics related to spin phenomena in particle and nuclear physics: polarized targets, polarized sources, polarimetry and spin manipulation, polarized neutrons, polarization applications for fundamental symmetry tests and new applications and developments, ongoing and upcoming spin physics facilities and experiments with polarized beams and targets (e.g., at BNL, COSY, JLAB, J-PARC, MESA, NICA, RIKEN, etc.). The Chairpersons for the workshop were Kurt Aulenbacher (HIM) and Frank Rathmann (IKP). The workshop has a long tradition and is organized every 3 years by world-wide labs working in the field of spin physics. It moves between Europe, USA, and Asia as suggested by the International Spin Physics Committee (ISPC). The predecessor (PSTP 2019) took place in Knoxville, Tennessee (USA). This time in Mainz, more than 50 participants registered and participated in the plenary sessions scheduled every day. Many excellent talks were presented in the tradition for this conference, which aims to cover a broad scientific program rather than only focus on a specific topic. All presentations are available at the PSTP conference web page <https://indico.him.uni-mainz.de/event/108/>. It is planned to publish the proceedings of PSTP2022 online in the Proceedings of Science (PoS) <https://pos.sissa.it>. The host institution for the next PSTP workshop (PSTP 2025) will be decided by the ISPC at the International Spin Symposium (SPIN 2023), planned to be held September 24-29, 2023, at the Durham Convention Center, Durham, NC (USA).



Figure 46: Participants of the PSTP2022 workshop in Mainz.

I.2 Georgian-German Science Bridge: 9th GGSWBS Workshop in Tbilisi and Kutaisi: *"Health as a Global Challenge: contributions by GGSB and its SMARTLabs"*

During September 12 – 16, 2022, Ivane Javakhishvili Tbilisi State University (TSU) and Kutaisi International University (KIU) hosted the 9th joint bi-annual meeting, called Georgian-German School and Workshop in Basic Science (GGSWBS'22; for details see: <http://collaborations.fz-juelich.de/ikp/cgswbp/cgswbp20/>) within the Georgian-German Science Bridge (GGSB). The following institutions participated: Forschungszentrum Jülich (FZJ, represented by IAS, IEK, INM, IKP and ZEA), Helmholtz Zentrum Dresden-Rossendorf e.V. (HZDR) and GSI Helmholtzzentrum für Schwerionenforschung (GSI) in Darmstadt as well as the universities of Aachen (RWTH) and Cologne – together with the Georgian partner universities (AUG, GTU, KIU and TSU). GGSWBS is a joint targeted program of Shota Rustaveli National Science Foundation of Georgia (SRNSFG) and FZJ. The primary subject discussed during this event was *"Health as a Global Challenge: contributions by GGSB and its SMARTLabs"*.

The school and workshop focused on the following topics:

- Research & Applications in Particle and Nuclear Physics
- Accelerator Research and Applications in Medicine
- Atmospheric Sciences and Environment
- Medical Imaging and Radionuclides for Life Sciences
- Machine Learning and Image Analysis
- Mechanical and Electrical Engineering

The meeting was attended by international experts of accelerator and particle physics, life sciences and scientists/engineers from technology institutes of various Helmholtz centres and international collaborations (such as CBM, JEDI, NuSTAR and PANDA) as well as BSc, MSc and PhD students from the Georgian universities. For FZJ, lectures were delivered by Hanno Scharr (IAS), Andreas Wahner (IEK), Jon Shah and Bernd Neumaier (INM), James Ritman and Hans Ströher (IKP/GSI) and Ghaleb Natour and Stefan van Waasen (ZEA) with contents fully covering the topics of the meeting. GGSWBS was highly appreciated by both students and professional participants. As part of the event, eleven excellent Georgian students were selected for internships stays of month each in Forschungszentrum Jülich. They come from

various scientific fields – Physics, Mathematics, Chemistry, Biology and Engineering Technology, corresponding to the inviting FZJ institutes. All presentations of the workshop together with additional information have been published in 2022 as “Schriften des Forschungszentrums Jülich, Key Technologies, Volume 263, ISBN 978-3-95806-664-9 (Eds.: A. Kacharava, E. Portius, J. Shah and H. Ströher).



Figure 47: Participants of the GGSWBS2022 workshop in Tbilisi (TSU).

I.3 Particle physics academy and training program for high school students 2022

In 2022 the CRC-110 presented for the fifth time its four-day particle physics academy for high school students (with 19 participants from 10th to 13th grade), which was again organized and largely executed by IAS4/IKP3. As venue served as in all previous years the Science College Overbach in Jülich, which provides an ideal environment since housing, lab and lecture hall are all on site. The program contained overview lectures as well as lectures on current issues in nuclear and particle physics - always with special emphasis on theoretical aspects which was very much appreciated by the participants. In addition, we presented demonstration experiments to illustrate the theoretical concepts and visited the COSY accelerator and the super computers at the research center Jülich. Moreover, we offered three projects to the students: In the first one they got a chance to get in touch with the fundamentals of quantum mechanics, in the second they learned how to simulate numerically the trajectory of the planet Mercury (including its perihelion motion) and in the third they discussed requirements of a scientific approach to philosophical issues like the anthropic principle. The feedback provided by the participants was extremely positive.



Figure 48: Participants of the High School student training program 2022.

I.4 Eighth Annual Meeting of the Programme "Matter and Technologies"

The 8th Annual Meeting of the Programme "Matter and Technologies" was hosted by DESY in Hamburg from Monday, September 26 to Tuesday, September 27, 2022 (see [website of the Annual MT Meeting](#)). Matter and Technologies (MT) is a programme in the Research Field Matter that is dedicated to enabling key technologies for accelerators, detectors and data science. The Helmholtz centres DESY, FZJ, GSI, HZB, HZDR, HZG and KIT cooperate in the MT programme. The MT topics are Accelerator Research and Development (ARD), Detector Technologies and Systems (DTS), and Data Management and Analysis (DMA). This was the first post-pandemic face-to-face meeting after three virtual meetings since 2020, with 271 scientists registered.

This meeting was followed by the eighth MT Student Retreat, where about 50 PhD students met to get to know each other and to exchange and discuss their scientific ideas and results (see [website of the MT Student Retreat](#)).



Figure 49: Participants of the 8th Annual Meeting of the Programme "Matter and Technologies".

Both meetings were jointly organised by DESY and the Forschungszentrum Jülich.

I.5 HESR Get Together Workshops

A series of in total six "HESR Get Together" workshops was organized and carried out in 2022 by IKP-4 and GSI. Half of the workshops were held at the GSI site in Darmstadt, the other half took place at the IKP in Jülich. With the exception of one workshop, where only IKP-4 staff was participating, the workshops were attended by staff from GSI and FZJ. One of the aims of the workshop was to integrate the HESR department as well as the individual staff members into the existing structures of FAIR/GSI. In addition several tandems were established to strengthen the cooperation between FZJ and GSI. These tandems consisted of each a GSI member and a (former) IKP-4 employee with a comparable area of responsibility. During the workshops the results of the tandem work was presented. Several laboratory tours where the participants had the opportunity to get into contact with each other and to see the working environment completed the programme of the workshops.

J Teaching Positions

Institute	Name	University
IKP-1	Prof. Dr. F. Goldenbaum	Bergische Univ. Wuppertal
	Prof. J. Ritman Ph.D.	Ruhr-Univ. Bochum
	Dr. T. Stockmanns	Ruhr-Univ. Bochum
IKP-2	Prof. Dr. L. Ludhova	RWTH Aachen
	Prof. Dr. J. Pretz	RWTH Aachen
IKP-3/IAS-4	Dr. E. Berkowitz	Rheinische Friedrich-Wilhelms-Univ. Bonn
	Univ. Doz. Dr. J. Haidenbauer	Univ. Graz
	Prof. Dr. C. Hanhart	Rheinische Friedrich-Wilhelms-Univ. Bonn
	Prof. Dr. T. Luu	Rheinische Friedrich-Wilhelms-Univ. Bonn
	Prof. Dr. Dr. h.c. U.-G. Meißner	Rheinische Friedrich-Wilhelms-Univ. Bonn
	Dr. A. Nogga	Rheinische Friedrich-Wilhelms-Univ. Bonn
	Dr. D. Rönchen	Rheinische Friedrich-Wilhelms-Univ. Bonn
	PD Dr. A. Wirzba	Rheinische Friedrich-Wilhelms-Univ. Bonn
IKP-4	Dr. O. Felden	FH Aachen
	Prof. Dr. A. Lehrach	RWTH Aachen

K Personnel

MSc. A. Aliche (IKP-1, until Sept. 30th 2022 and RUB/GSI-FFN, since Dec. 1st 2022)
MSc. A. Andres (IKP-2/ IKP-4)
MSc. A. Asokan (IKP-3/IAS-4)
BSc. S. Aswani (GSI-FFN, until April 30th 2022)
MSc. A. Awal (GSI-HESR)
C. Berchem (IKP-TA)
MSc. P. Bergmann (GSI-FNN, until March 31st 2022)
Dr. E. Berkowitz (IKP-3/IAS-4)
O. Bilen (GSI-FFN, until March 31st 2022)
Dr. C. Böhme (IKP-4)
M. Böhnke (IKP-4)
DI N. Bongers (IKP-4)
Dr. B. Breitkreutz (GSI-HESR)
P. Brittner (IKP-4)
F. Celik (GSI-HESR)
MSc. J. T. Chacko (IKP-3/IAS-4)
N. Chowdhury (GSI-FFN, since June 21st 2022 until Sept. 15th 2022)
W. Classen (IKP-4)
M. Comuth-Werner (IKP-TA/IAS-4)
DI F. U. Dahmen (IKP-4)
C. Deliege (IKP-4)
DI N. Demary (IKP-TA)
MBA A. Derichs (IKP-1)
MSc L. von Detten (IKP-3/IAS-4)
G. D'Orsaneo (IKP-2)
R. Dosdall (IKP-1)
C. Ehrlich (IKP-4)
T. El-Kordy (GSI-FFN, since Sept. 15th 2022)
Dr. R. Engels (IKP-2)
B. Erkes (IKP-4)
Dr. W. Esmail (GSI-FFN)
DI F.-J. Etzkorn (IKP-4)
N. Faatz (GSI-FFN, since April 1st 2022)
J. Fahnenschreiber (IKP-TA, GSI-HESR since March 1st 2022)
Dr. O. Felden (IKP-TA)
H. - W. Firmenich (IKP-TA)
Dr. A. Foda (GSI-FFN, since March 15th 2022)
MSc. C. Gäntgen (IKP-3/IAS-4)

Dr. R. Gebel (IKP-4, GSI-HESR)
J. Göbbels (IKP-TA)
MSc. A. Göttel (IKP-2, until Apr. 30th 2022)
Prof. Dr. F. Goldenbaum (IKP-1)
J. Gollub (RUB/GSI-FFN, since Oct. 1st 2022)
Dr. K. Grigoryev (GSI-HESR)
Dr. D. Grzonka (IKP-1)
M. Gülpen (IKP-TA)
D. Gu (GSI-HESR, until Oct. 31st, 2022)
T. Hahnrahts-von der Gracht (IKP-TA)
A. Halama (GSI-HESR)
E. Hall-Brunton (IKP-TA, until Nov. 31st 2022)
DI S. Hamzic (GSI-HESR)
Prof. Dr. C. Hanhart (IKP-3/IAS-4)
Dr. M. Hartmann (IKP-2)
DI R. Hecker (IKP-TA)
Dr. V. Hejny (IKP-2)
Dr. J. - H. Hetzel (GSI-HESR)
L. Heuser (IKP-3/IAS-4)
M. Holona (IKP-1)
Dr. A. Kacharava (IKP-2)
M. Kaczmarek (GSI-HESR, since April 21st 2022)
Dr. V. Kamerdzhev (IKP-4)
Dr. P. Kampmann (GSI-FFN, until April 30th 2022)
MSc. J. Kannika (IKP-1, GSI-FFN, since May 1st 2022)
MSc. C. Kannis (IKP-4, until Aug. 31st 2022)
A. Kelleners (IKP-TA)
Dr. I. Keshelashvili (GSI-FFN)
A. Kieven (IKP-4)
Dr. J. Kim (IKP-3/IAS-4)
S. Kistemann (IKP-TA)
Dr. R. Kliemt (RUB/GSI-FFN, since July 1st 2022)
B. Kuckelkorn-Klimczok (IKP-TA)
A. Kononov (GSI-FFN, since Aug. 1st 2022)
M. Kremer (IKP-TA)
DI T. Krings (IKP-TA)
M. Küven (IKP-4)
MSc. S. Kumaran (IKP-2, until March 30th 2022)
L. Kunkel (GSI-FFN, since April 15th 2022 until Oct. 31st 2022)
Dr. T. Lähde (IKP-3/IAS-4)

K. Laihem (GSI-HESR)	Dr. D. Rönchen (IKP-3/IAS-4)
K. - G. Langenberg (IKP-4)	G. Roes (IKP-TA)
Dr. H. Le Thi (IKP-3/IAS-4)	D. Ruhrig (IKP-4)
Prof. Dr. A. Lehrach (IKP-2)	G. Rupsch (GSI-HESR)
MSc. S. Liebert (GSI-HESR)	J. Salmann (GSI-FFN, until June 30 th 2022)
MSc. R. Liu (IKP-2)	Ph.D. habil. S. Schadmand (GSI-FFN)
Prof. Dr. L. Ludhova (IKP-2)	F. Scheiba (IKP-4)
Prof. T. Luu (IKP-3/IAS-4)	Dr. R. Schleichert (IKP-2)
M. Manerova (IKP-4, GSI-HESR since Nov. 1 st 2022)	M. Schmühl (IKP-4)
M. Marzen (IKP-4, GSI-HESR since June 14 th 2022)	MSc. C. Schneider (IKP-3/IAS-4)
M. Maubach (GSI-HESR, since Jan. 1 st 2022)	M. Schubert (GSI-HESR)
Prof. Dr. Dr. h. c. U.-G. Meißner (IKP-3/IAS-4)	Dr. T. Sefzick (IKP-TA)
MSc. A. Meraviglia (GSI-FFN, since May 13 th 2022)	H. Sharma (GSI-FFN, since Oct. 17 th 2022)
DI A. Messaaf (GSI-HESR)	Dr. S. Shen (IKP-3/IAS-4)
Dr. J. Messchendorf (GSI-FFN)	MSc. N. Shurkhno (GSI-HESR)
Dr. B. Metsch (IKP-3/IAS-4)	S. Siddique (GSI-FFN)
MSc. N. Mohan (GSI-FFN)	R. Similon (GSI-HESR)
Dr. H. Mutuk (IKP-3/IAS-4)	DI M. Simon (IKP-4)
Dr. A. Naß (IKP-2)	MSc. A. Singhal (IKP-2)
MSc. P. Niedermayer (GSI-HESR)	J. Slim (GSI-FFN, until July 31 st 2022)
Dr. A. Nogga (IKP-3/IAS-4)	J. Spelthann (GSI-HESR)
MSc. S. Pattnaik (GSI-FFN, since Feb. 1 st 2022)	D. Spölgen (IKP-2)
MSc. L. Pelicci (IKP-2)	Dr. R. Stassen (IKP-4)
Dr. O. Penek (IKP-2, until July 31 st 2022)	Dr. T. Stockmanns (IKP-1)
MSc. G. Perez-Andrade (IKP-1, GSI-FFN, since 9 th Oct. 2022)	Prof. Dr. Dr. h. c. mult. H. Ströher (GSI-FFN, until Sept. 30 th 2022)
Dr. A. Pesce (IKP-2)	MSc. R. Suvarna (GSI-FFN)
BSc J. T. Peters (IKP-4, until May 31 st 2022)	Dr. K. Suzuki (RUB/GSI-FFN, since Aug. 15 th 2022)
Dr. D. Prasuhn (GSI-HESR, until Nov. 30 th 2022)	MSc. M. Thelen (IKP-4)
Prof. Dr. J. Pretz (IKP-2)	Dr. R. Tölle (GSI-HESR, until Nov 30 th . 2022)
V. Priebe (IKP-TA, GSI-FFN)	Dr. Y. Valdau (GSI-HESR)
Dr. J. Pütz (IKP-1, GSI-FFN, until June 30 th 2022)	BSc. V. Verhoeven (GSI-FFN, since Aug. 1 st 2022)
S. Pütz (GSI-FFN)	MSc. M. Vitz (IKP-4)
S. Rasalingam (GSI-HESR, until June 30 th 2022)	MSc. C. Vollbrecht (IKP-2)
Dr. F. Rathmann (IKP-2)	BSc. A. Weißel (GSI-FFN, until April 30 th 2022)
MSc S. Rawat (IKP-3/IAS-4)	M. Westphal (GSI-FFN)
Dr. J. Regina (GSI-FFN, since March 1 st 2022)	Dr. P. Wintz (IKP-1)
DI K. Reimers (IKP-4)	D. Wirtz (IKP-TA)
MSc. M. Rifai (IKP-2)	PD Dr. A. Wirzba (IKP-3/IAS-4 until May 30 th 2022)
Prof. J. Ritman Ph.D (IKP-1, GSI-FFN)	Dr. H. Xu (IKP-1)
	H. Zens (IKP-4)

IKP-1	= Experimental Hadron Structure
IKP-2	= Experimental Hadron Dynamics
IKP-3/IAS-4	= Theory of the Strong Interactions
IKP-4	= Large-Scale Nuclear Physics Equipment
IKP-TA	= Technical Services and Administration
GSI-FFN	= GSI Helmholtzzentrum für Schwerionenforschung, FAIR Forschung NRW
GSI-HESR	= GSI Helmholtzzentrum für Schwerionenforschung, Hochenergiespeicherring
RUB	= Ruhr-Universität Bochum

L Individual Contributions

Contents

Accelerator Research	61
Polarised Beam Transport to the Lamb-Shift Polarimeter	61
The IBL Simulator - A Digital Twin for the IBL	63
Upgrade of the COSY Extraction Septum Power Converter	64
ExB – Deflector Tests at COSY	66
ExB – Deflector Interlock and Control Systems	68
BPM Test Bench Operation for HESR	70
Injection optimization using machine learning at the Cooler Synchrotron COSY	72
JULIC Neutron Platform	73
Poster: Status Overview of the HESR Beam Instrumentation	75
Poster: JULIC – driver accelerator for HBS	76
Experimental Activities for FAIR	77
Triggering AI and beam-target modeling in the PANDA software	77
A Partial Wave Analysis Framework for Hadron Physics	79
Towards a search for the N(1720) double resonance in pion-proton collisions with HADES	80
Hyperon-production studies in $p + p \rightarrow \Lambda + K_S^0 + p + \pi^+$ at 4.5 GeV with HADES at GSI	81
Hyperon reconstruction at HADES with kinematic fitting and forward detector upgrades	83
Investigation of proton irradiated SiPMs	84
Integrated Luminosity Determination for the FAIR Phase-0 Beamtime with HADES	85
Evaluating the Resolution of Track Candidates Reconstructed by a Language Model Based Track Finder	86
Acts tracking toolkit for PandaRoot	88
Deep Learning for Particle Identification at HADES	89
Further Activities	90
A new method to polarize atoms, molecules, and their ions	90
Actual Measurements with the Sona Transition Unit	91
Remote Control of the Lamb-Shift Polarimeter at the pulsed \bar{H}/\bar{D} Ion Source	92
Concept of a polarized $^3\text{He}^+$ ion source	93
Preparation of Storage Cell Tests for the Polarized Target at LHCb@CERN	94
A Transition Unit for the Bound-Beta Decay Experiment	95
Precision Physics with a Sona Transition Unit	96
Storage Ring Based EDM Search	97
Progress towards a direct measurement of the deuteron Electric Dipole Moment at COSY	97
Analysis of the second precursor experiment	98
Proton spin coherence time from March'22 measurement	99
Optimization of the COSY Simulation Model Using Orbit Matching Algorithm in Bmad	100
SCT optimization and determination of the Invariant Spin Axis in a COSY model using Bmad	101
Optimization of spin coherence time of protons with BMAD	102
Optimization of Spin Coherence Time at the Prototype Storage Ring	103
Study of Beam dynamics of a Prototype Electric Dipole Moment Storage Ring	104
Measurement of second-order momentum compaction factor at COSY	105
Rogowski Beam Position Monitor – Signal-to-Noise Ratio Investigation	107
Poster: The Search for Electric Dipole Moments of Charged Particles using Storage Rings	108
Poster: Spin-Tracking simulations in an idealized COSY model using Bmad	109
Poster: Optimization of Spin Coherence Time for Electric Dipole Moment measurements in a Storage Ring	110
Poster: Simulations of Beam Dynamics of Prototype EDM Storage Ring	111
Neutrino Physics	112
Source Insertion Calibration System of OSIRIS	112
Poster: Geoneutrinos and NMO sensitivity: an approach based on full Monte Carlo simulations	113
Poster: First directional measurement of sub-MeV solar neutrinos in the liquid scintillator detector by Borexino	114
Poster: OSIRIS: The Online Scintillator Internal Radioactivity Investigation System of JUNO	115
Poster: Solar neutrino physics with JUNO: analysis strategy and sensitivity studies for ^7Be , pep, and CNO neutrinos	116
Poster: Solar neutrino physics with JUNO: sensitivity studies for ^7Be , pep and CNO neutrinos	117
Poster: Atmospheric neutrino physics in JUNO: reconstruction of GeV interactions	118

Poster: Physics Prospects of The JUNO Experiment	119
Poster: Atmospheric Neutrinos Reconstructions	120

Polarised Beam Transport to the Lamb-Shift Polarimeter

Yury Valdau¹, Kirill Grigoryev¹, and Ralf Gebel¹

Colliding polarised atomic Beam Source (CBS), located in the basement of the cyclotron building, is routinely used for the COSY operations since already very long time. Beam preparation procedure at the polarised source can be subdivided into the following steps: switching on all the subsystems at Cs-side of CBS, Cs-beam development, switching on all the subsystems at atomic beam source, H-/D- beam development in the first beam cup (FB0), beam transport through the Source Beam Line (SBL) and cyclotron, and finally polarimetry studies at the Low-Energy Polarimeter (LEP) in the injection beam line of COSY. From the presented beam development plan one can see, that the polarisation measurements and hence atomic beam source optimization are only possible after all the subsystems of injector are set for the operation with polarised beam.

In this configuration, there is no possibility for the parallel operation of the cyclotron with unpolarised beam and at the same time polarisation optimization at the CBS using LEP. To overcome this limitation a Lamb-shift Polarimeter (LSP) has been build in the beam line of the polarised source II at the ground floor of the cyclotron building.

During experiment in April 2022 the H- polarised beam of the CBS has been transported to the LSP for the first measurements of the H- ion beam polarisation using Lamb-Shift polarimeter. Part of the SBL relevant for this experiment and LSP are schematically presented in Fig. 1. Polarised H- beam of 2 keV was prepared and optimised at the first Faraday Cup (FB0) of the source beam line. Transverse position of the beam in the SBL was carefully adjusted using screens at the first two cups (FB0 and FB1).

Angle and position of the beam in the beam line are especially crucial for this experiment due to the relatively large deflection angles during transport and short distances between the elements. Before beam arrives from the basement to the ground floor it was farther optimized after the first 135° electrostatic deflector (D1) (in vacuum chamber of MS4 magnet) using faraday cup (FB2') in the vertical section of the beam line. After the second beam deflection by 135° using electrostatic deflector D2 (in vacuum chamber of MS1 magnet) beam can was monitored and optimized using FB0' Faraday cup. The parameters of the SBL magnets and 135° deflectors (D1 and D2) are summarized in Table 1 and 2.

In this experiment a polarised beam from the CBS is rotated in the beam line by 360° using electrostatic and magnetic systems on the distance of about five meters. Therefore, from the ≈ 10 uA H- ions pro-

duced in the polarised source (FB0) only ≈ 0.5 uA arrive to the faraday cup in front of the Lamb-Shift polarimeter (FB1').

Due to relatively complicated geometry of LSP a beam transport through the polarimeter (schematically presented in Fig 1) requires very careful adjustment of all the subsystems and source beam line. To reach efficient beam transport through the central part of the LSP, where vertical level change is taking place, one of the electrodes of the first and second LSP electrostatic deflectors (LSP D1 and D2) have been used in beam development as a faraday cup and beam position monitors. Finally, beam intensity was optimized using all the LSP subsystems in the faraday cup (LSP-Cup) at the end of the Lamb-Shift polarimeter. Parameters of the LSP, relevant for the beam transport, are summarized in Table 3.

During the run in spring 2022 a polarised H- beam of ≈ 60 nA from the CBS in the basement of the building was delivered to the LSP at the upper floor using source beam line and two 135° electrostatic deflectors. Delivered beam intensity was sufficient for the first H- ion polarisation measurements using Lamb-shift polarimeter [1].

References

- [1] S.J. Pütz, et.al., Conference proceedings PSTP2022, in preparation.

¹ Currently at GSI Helmholtzzentrum für Schwerionenforschung, Darmstadt, Germany

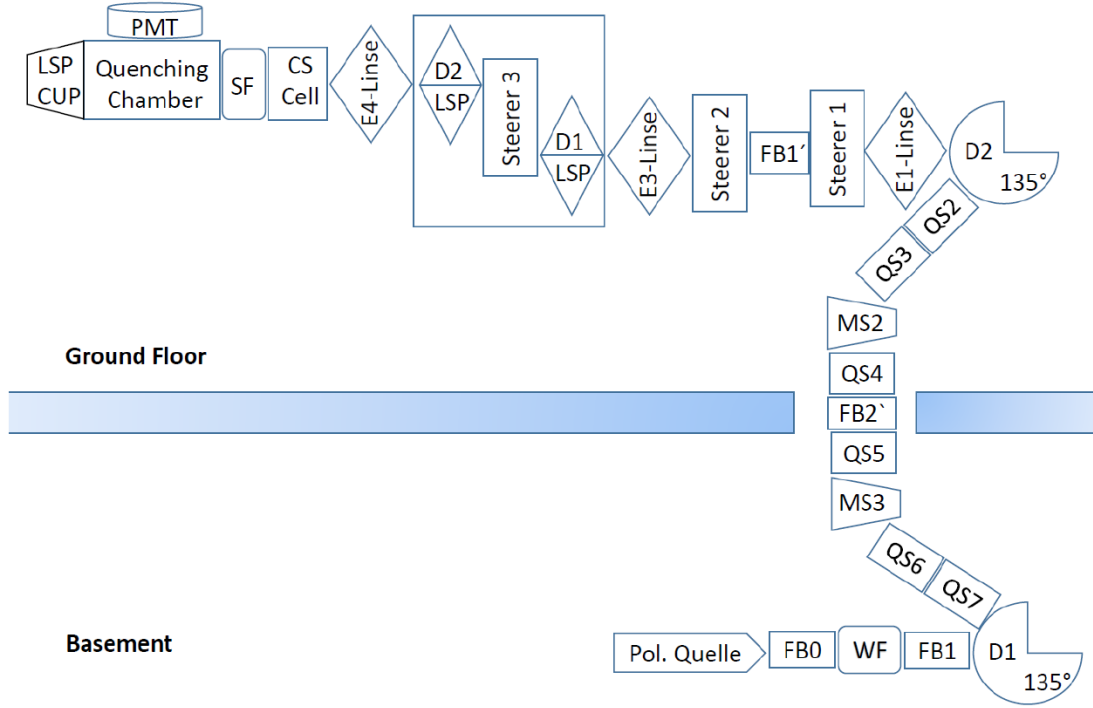


Figure 1: Schematic view of the source beam line between polarised source and the Lamb-Shift Polarimeter. The polarised beam is optimised at faraday cups (FB0 and FB1) and then deflected into the vertical section of the SBL using the first 135° deflector (D1). After beam optimisation in the faraday cup (FB2') the beam is again deflected by the second 135° deflector (D2) in to the horizontal plane for the beam transport through the LSP. With the help of the Steerer magnets (1-3) position of the beam in the LSP can be fixed on a geometrical axis. Set of electrostatic lenses (E1,E3, and E4) allows to focus the beam in the system. Two electrostatic deflectors (LSP D1 and LSP D2) are used to change vertical position of the beam in polarimeter from initial to the higher level. (In present configuration of the LSP it has no physical purpose.) Polarised H- beam is neutralised in Cs-Cell and after the Spin-Filter (SF) analysed with magnet field in the Quenching Chamber. Lyman- α photons produced in the quenching chamber (QC) are detected using a photo-multiplier mounted on the top of the chamber. Faraday Cups (FB1' and LSP) are used during the beam preparation for the optimisation.

Table 1: Parameters of the magnets in the source beam line during experiment in April 2022

WF [V]	WF [%]	MS2 [%]	MS3 [%]	QS13 [%]	QS24 [%]	QS57[%]	QS68[%]
179	2	24	23.9	-10.5	-7.3	-9.4	-6.6

Table 2: Parameters of the electrostatic 135° deflectors used during experiment in April 2022.

D1 _{Eingang} [V]	D1 ⁺ [V]	D1 ⁻ [V]	D1 _{Ausgang} [V]	D2 _{Eingang} [V]	D2 ⁺ [V]	D2 ⁻ [V]	D2 _{Ausgang} [V]
2800	1331	1331	999	1350	1245	1245	2000

Table 3: Parameters of the LSP beam transport system used during experiment in April 2022.

LSP D1 ⁺ [V]	LSP D1 ⁻ [V]	LSP D2 ⁺ [V]	LSP D2 ⁻ [V]	LSP _{Steerer} ^{Links} [V]	LSP _{Steerer} ^{Rechts} [V]
355	355	340	340	20	60

The IBL Simulator - A Digital Twin for the IBL

J. Hetzel

The injection beamline (IBL) is used to transfer the pre-accelerated particles from the JULIC cyclotron to the cooler synchrotron (COSY). It is about 94 m long and consists of several electromagnetic elements to guide and focus the beam. For diagnostic purposes several Faraday-cups (or beamcups (BC)) can be inserted at specific points along the beamline. They measure the beam intensity at the location of the cup. An upgrade of the of the IBL control system was started in late 2021 and completed in early 2022. The power supplies of all magnetic elements and the beam cups are now controlled and read-out via the EPICS interface [1]. This allows algorithmic access to the IBL, i.e. the development of algorithms that automatically optimize the settings of the IBL, see [2]. In order to test the algorithms before they are applied to the IBL, the IBL Simulator is developed.

The IBL simulator is written as a soft-IOC

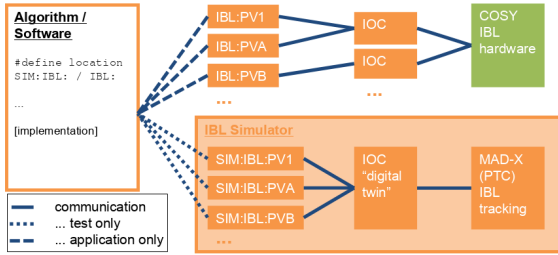


Figure 1: Simplified schematic of the communication of an algorithm with the IBL hardware and the IBL Simulator. Both provide a same set of PVs, only the namespace of the simulator is amended by the prefix "SIM:".

for EPICS. This means that it can be controlled and read in complete analogy to the real IBL but only exists as a software, as shown in Fig. 1. It is designed to be run on a local PC, so that several hypothetical developers can test their algorithms for the IBL in parallel. Like the control system of the real IBL, the simulator is controlled by and provides a set of process variables (PVs). In the context of EPICS each PV represents the state of a connected device, e.g. the actual output current of a power supply or (as a different PV) its set-value. To achieve maximum agreement between the IBL and the simulator, each PV that is used by the operator to control the IBL elements has its counterpart in the simulator. The name of the corresponding PVs differs by a prefixed SIM:. This prevents the algorithms to be tested from inter-

fering with the real machine when the algorithms are tested on a PC with access to the COSY network.

The IBL simulator is based on tracking calculations with the accelerator simulation tool MAD-X [3], specifically with its tracking component PTC. A simulation of 1000 particles can be performed in less than one second. Thus a typical cycle in test mode, which lasts 2 s, can be simulated in real-time. To do this, a randomly distributed set of phase-space coordinates of 1000 particles is generated every two seconds (larger cycletimes can be set via the corresponding PV, if desired). The underlying phase-space parameters for these random distributions can be controlled with dedicated PVs. The pre-set PVs roughly represent a typical distribution of particles as extracted from the cyclotron. The PTC-simulation is then started. To simulate the output of the Faraday cups, it is checked what fraction of the initial 1000 simulated particles reaches the location of the respective beam cup. Here the settings of all power supplies are incorporated in the simulation. The resulting number of particles reaching the beam cup is then scaled to a realistic number of particles of a real bunch and distorted with random noise to mimic the beam cup readout. The IBL simulator includes the process of ramping the power supplies to a desired value. For the simulation, this means that if a power supply has not reached its setpoint yet, the tracking is performed with a magnetic field corresponding to the actual value of the current during the ramp.

The IBL simulator has proven a useful tool to test algorithms as well as GUIs during their development phase. This has saved valuable time during the actual beam time at COSY, as most of the debugging could be done prior to the beam time.

References

- [1] R. Gebel et al., *4.1 Developments at COSY: EPICS Integration of the Injection Beam-line*, Annual Report 2021, IKP - COSY, Jül-4429, pp.17-18, (2022).
- [2] A. Awal, *Injection optimization using machine learning at the Cooler Synchrotron COSY*, Annual Report 2022, IKP - COSY (2023).
- [3] MADX, CERN Accelerator Beam Physics Group. Methodical Accelerator Design (MAD). <http://mad.home.cern.ch/mad>. online.

Upgrade of the COSY Extraction Septum Power Converter

K. Grigoryev¹, Yu. Valdau¹, M. F. Schubert¹, F. Dahmen, W. Classen

Particle physics experiments require testing of the detector prototypes, data acquisition systems and electronic equipment in a real environment with particles of certain energy. For this purpose a dedicated beamtimes with extracted beams are conducted at the COSY accelerator. During those experiments particles of known energy can be delivered from a storage ring to the detector test area at a desired moment and in predefined portion. This is done at COSY using ultra slow extraction system and magnetic (currents of up to 2000 A) and electrostatic (high voltages up to 200 kV) septa.

Meanwhile, experience have been collected in operation of a new Heinzinger 200 kV [2] oil-free power converters (Point 2 on the Fig.1) during tests of the ExB deflector [1]. To connect a new Heinzinger power converter to the old septa cable a special HV adapter has been build and installed in the septa power supply area (see Fig.2). Connector from the COSY septa cable, filled with oil, is inserted from the top in the adapter, while a new short flexible cable goes from the side and connect the adapter to the new power supply.

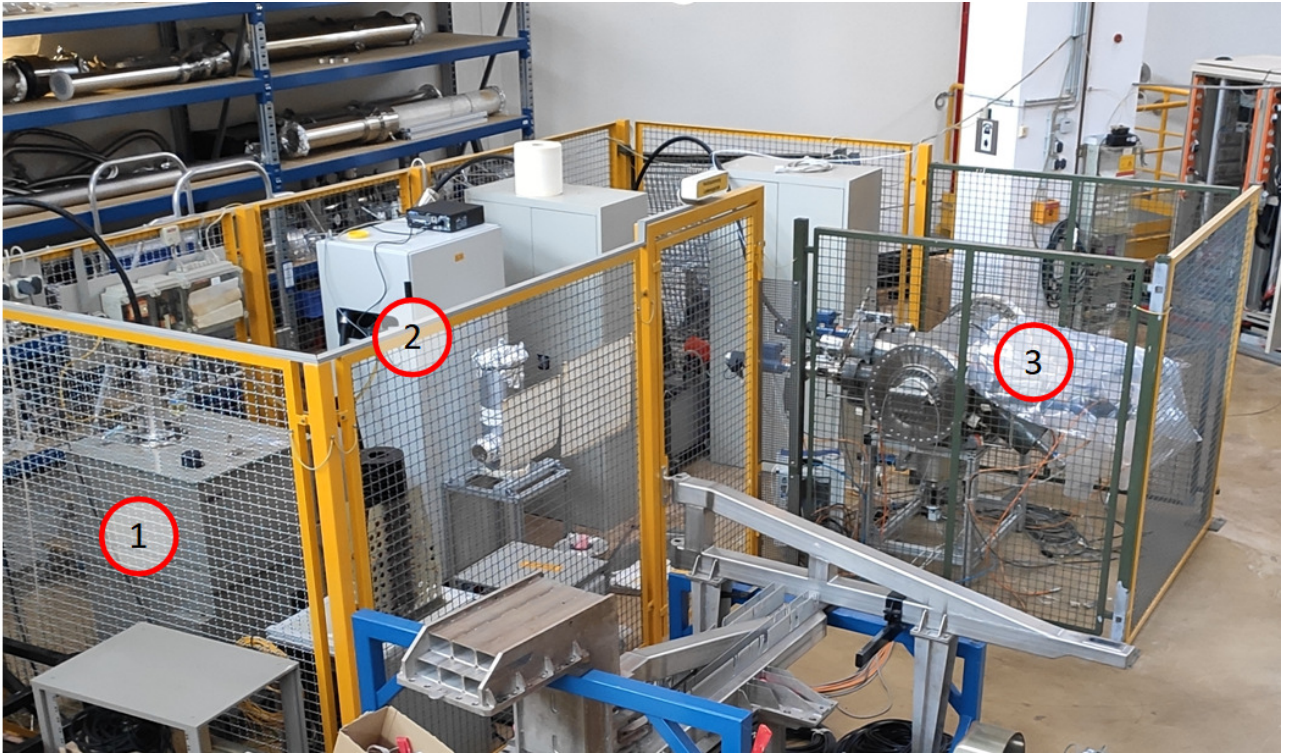


Figure 1: Experimental area for testing new oil-free HV power converter with spare electrostatic COSY-septum. Point 1 and 2 are old and new power converters, respectively. Point 3 - vacuum chamber of the test septum

During the last experiments with extracted beams many complications occurred in preparation and conditioning of the electrostatic septa. Power converter operation at high voltages was very unstable and require permanent attention. The old power converter and HV-feedthrough of COSY electrostatic septa are oil isolated. The diode cascade, electronic and connectors of the power converter are located in a temperature stabilised oil isolated tank presented in Fig.1 (Point 1)). A special cable connects power supply in the COSY area with a HV-feedthrough on the septum vakuum chamber installed in the COSY tunnel.

To test the performance of this system, a spare COSY septa (Point 3 on the Fig.1) was located near to the septa power supply area in COSY-eye and connected with a new Heinzinger power supply using adapter and short cables. After grounded fence has been build to protect an area from unauthorised access a series of experiments with spare septa have been done. The electrodes of the septa were positioned at the maximal distance larger than 60 mm. A vakuum system of the COSY spare septa has been taken into the operation and using additional turbomolecular pump chamber was evacuated to the 10^{-8} mbar, making a HV-tests feasible.



Figure 2: HV cable adapter of the new power supply.

Operation of the power converter and observation of the vacuum conditions was carried out remotely from accelerator control room, since unwanted X-ray emission is possible in case of HV-breakdown in the septa at the high voltages above 30 kV. The COSY extraction electrostatic septa is operated at constant voltages up to 156 kV, hence all tests were conducted in current limit mode of the power converter. The new power converter, cables, and adaptor have been commissioned together with a spare septa up to the high voltages of 180 kV without discharge and a dark currents below $10\text{ }\mu\text{A}$.

Hence, assuming better vacuum conditions around the electrostatic septa at the storage ring we can conclude that the system consist of a new Heinzinger power converter, new cables and adapter box can replace an old oil filled power supply for the coming COSY beamtime period without restriction on the septa operation voltages.

References

- [1] K. Grigoryev et al., "ExB Deflektor Tests at COSY", Contribution to Annual Report 2022, in preparation.
- [2] User Manual, "Precision High Voltage Power Supplies", V1.8, 2017, http://134.94.224.23/mediawiki/index.php?title=File:ExB_Heinzinger_Betriebsanleitung.pdf

¹ Currently at GSI Helmholtzzentrum für Schwerionenforschung, Darmstadt, Germany

ExB – Deflector tests at COSY

K.Grigoryev¹, Y.Valdau¹, M.Schubert¹, F.Dahmen, W.Classen, C.Ehrlich²

An electrostatic deflector is one of the major components for a new JEDI prototype storage ring [1]. To investigate possibility of reaching desired electric field strength (see Table 1) a deflector prototype was produced. Two real-size one meter long electrodes on ceramic insulators were mounted on the supporting flanges and precisely positioned inside the D2-Magnet vacuum chamber (see Fig. 1). Thin titanium foil stretched above and below the electrodes is foreseen to keep the distance to the grounded surface constant. As a byproduct it helps to protect the chamber walls from a damage during electric discharge.

Experiment conditions	E [MV/m]	B [mT]	D [mm]	HV [kV]
E Field 30MeV	6.67	-	60	400
ExB Field 30MeV	4.56	28.5	60	274
ExB Field 45MeV	7.00	32.7	60	400

Table 1: Deflector design parameters for JEDI prototype ring.

The setup was equipped with turbo-molecular, cryo and ion-getter pumps separated with valves (see Fig. 2). Initial pumping with a turbo pump will evacuate the chamber to the pressures up to 10^{-7} mbar. Further pumping of the system with cryopumps will help to make vacuum dry by removing water layers from the surface of the chamber.

The final experiment has to be conducted at pressures below 10^{-8} mbar with ion-getter pump only. All other pumps can be separated from the main vacuum chamber with gate valves and stopped in order to minimize environment vibrations. The vacuum conditions measured by the ion-getter pump parallel to its operation are also used in the interlock system.

Each deflector is connected to an individual precision bipolar high-voltage 200 kV power converter. In order to reach designed conditions with pure electric field at the distance of 60 mm it is obligatory to run the system at maximum voltage (see Table 1). But operation above 30 kV between the electrodes requires protection from X-rays, which can be produced during discharge. Therefore the experiment operation interlock (see individual report on ExB Deflector interlock) is monitoring not only vacuum and high-voltage conditions, but also the absence of the persons in the COSY experimental area.

First attempts to condition the electrodes were conducted without magnetic field. The distance between the electrodes is mechanically limited to 91 mm by the vacuum chamber and support elements dimensions. The field strength of 1.75 MV m^{-1} was achieved at 80 kV with a dark current below 100 nA.

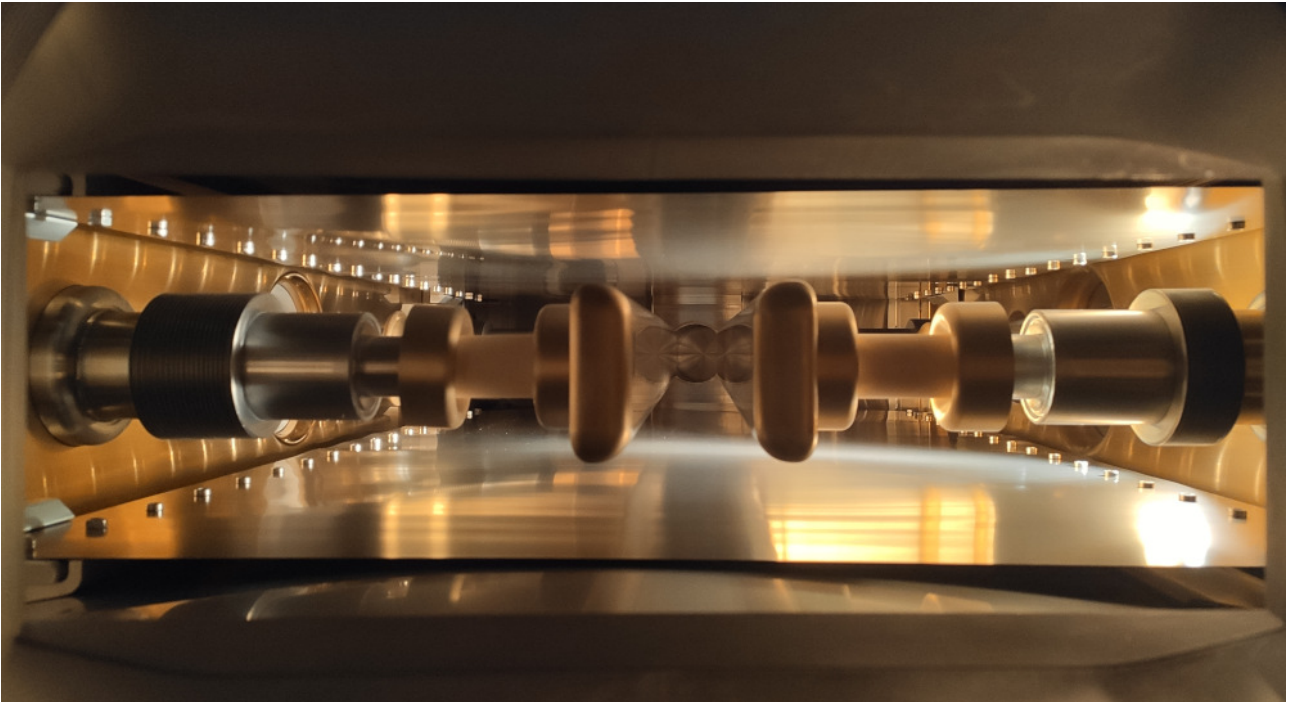


Figure 1: The electrodes inside the vacuum chamber.

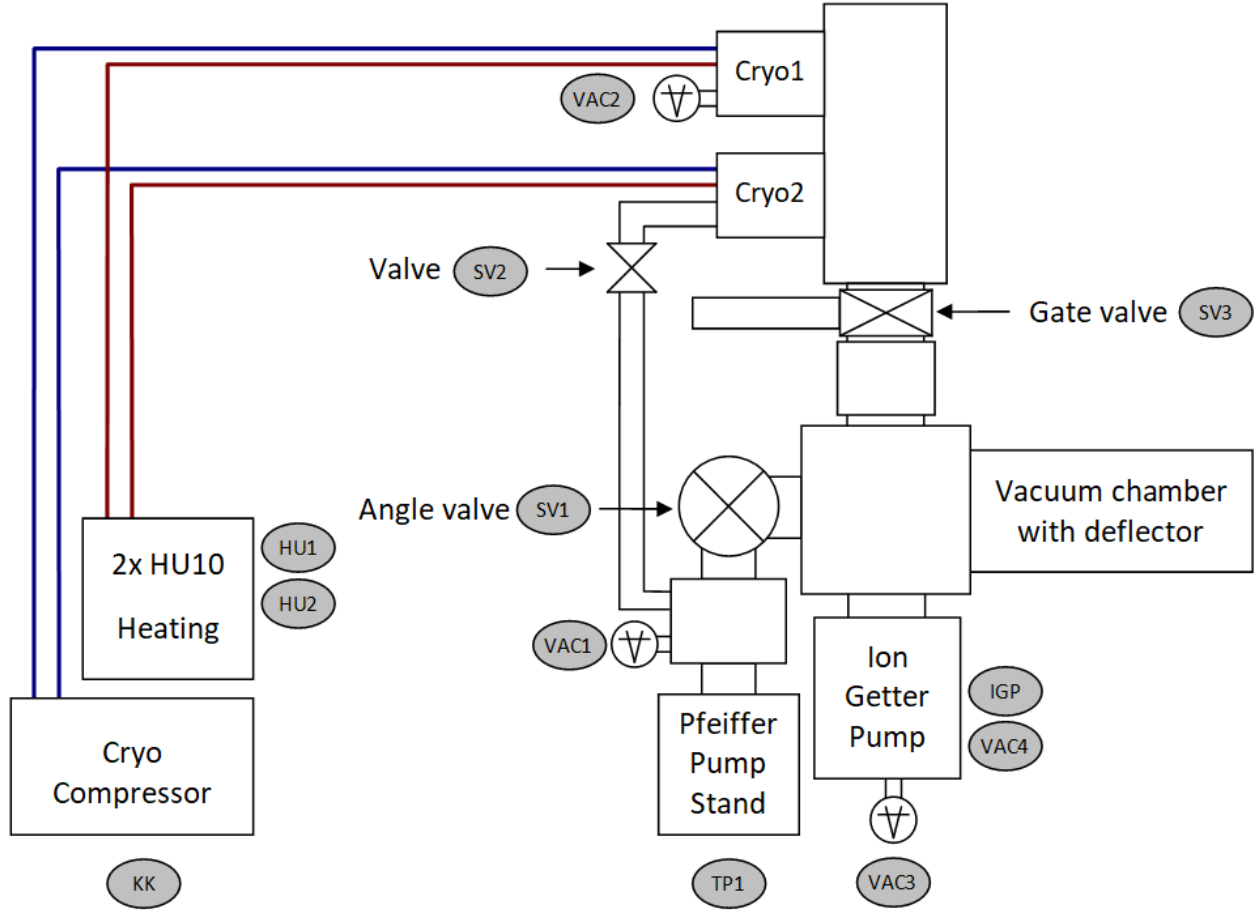


Figure 2: Vacuum layout of the ExB deflector setup.

Further tests were made with a presence of magnetic field of the D2 magnet. This was done in order to avoid electron bombardment of the electrodes during discharges. Free electrons between the plates guided by the magnetic field will reach the grounded titanium protection foil and do not damage the electrodes. During operation, D2 magnet coils are cooled by a mobile cooling system located nearby.

For the measurement the distance between the electrodes was changed to 60 mm - design parameters of the JEDI prototype deflector (see Table 1). During the measurements the dark current do not exceed 100 nA whereas during ramping it was limited to 1 μ A for safety reasons. Currently electric field strength of 2.5 MV m⁻¹ was reached.

References

- [1] F. Abusaif, et.al., arXiv:1812.08535 (2019).

¹ Currently at GSI Helmholtzzentrum für Schwerionenforschung, Darmstadt, Germany

² Currently at INW-IT, Forschungszentrum Jülich, Jülich, Germany

ExB – Deflector Interlock and Control Systems

Maurizio Fabian Schubert¹

The JEDI experiment requires the development of a new accelerator element with combined electric and magnetic fields [1]. During ExB deflector tests, discussed in Ref. [2], a high voltages of up to 200 kV per power supply [3] will be used. Such systems, with electric fields above 30 kV, are not only dangerous due to the possible high voltage shock but also are a source of unwanted X-ray radiation. Therefore a special ExB deflector interlock system has been build to meet safety precautions in place.

The interlock system of the ExB deflector, located in the COSY MeT area, is based on a Siemens Logo (see Fig.2) electronics. Interlock system controls: signal-”lights” of the MeT area safety system (”red”- area is secured and no access is granted, ”green” - access is granted), the COSY-PSA (COSY Persoenliche Sicherheits Anlage) control signal (”true” - if there are no people in COSY closed area) and analog voltage measurements of the deflector power supplies (0–10 V linear corresponds to 0–200 kV at the exit of the power supply). The ExB deflector interlock system is directly connected to the power converters as an interlock signal.

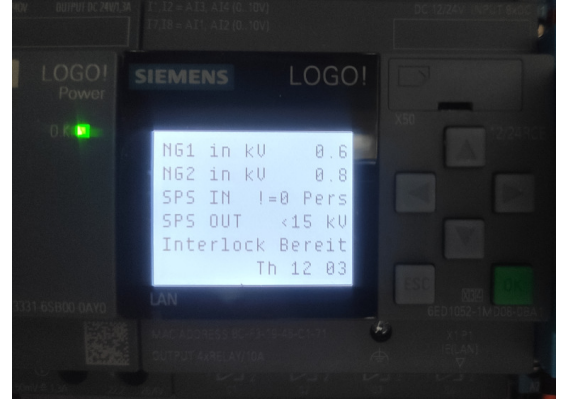


Figure 2: Display of the ExB deflector system, realised using Siemens Logo modules.

The interlock system of the deflector distinguishes between three modes of the system operation depending on the value of high voltages at the exit of the power supplies. In the first mode of operation high voltage at the exit of the power convertes does not exceed 1 kV. In this mode normal access to COSY and MeT areal is granted.

To increase high voltages at the exit of the power

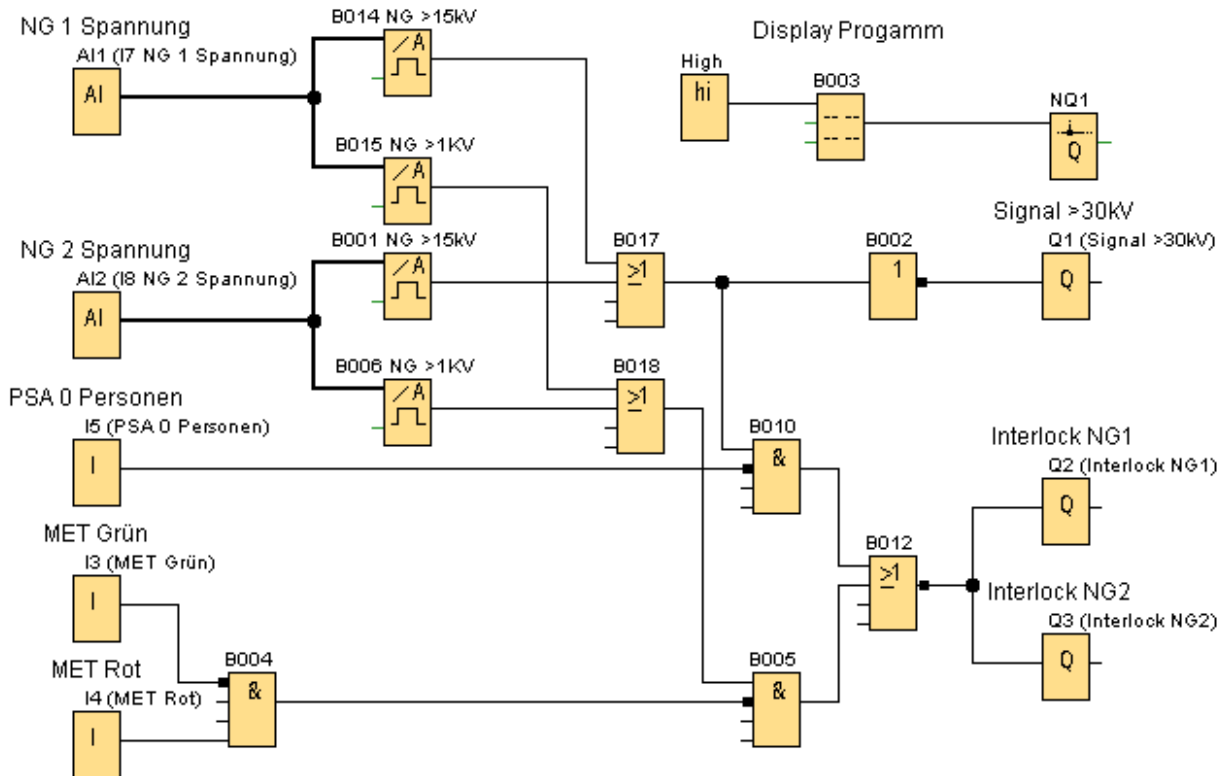


Figure 1: The schematic view of the LOGO program.

supplies from 1–15 kV, the second mode of the interlock system is used. In this case the MeT areal should be secured and status signal "red" has to be present at the input of the Logo interlock module.

To protect personal from the X-rays which might be produced during discharge in the deflector chamber, a third mode of the interlock operation is used. In this mode MeT area has to be sequered and access to the COSY hall is forbidden (PSA signal is "true"), only in this case ExB deflector interlock system will allow power converters to exceed high voltages above 15 kV. In case of unauthorised access to the COSY closed area or a MeT areal ExB deflector interlock system will switch of the voltages of the power converters. The schematic view of the LOGO logic program is presented in Fig. 1.

The power supplies and vacuum status, measured using ion-getter pump, are controlled using LabView based system presented in Fig. 3. The voltages and limiting currents of the power supplies can be set both individually and separately for the each power supply. The voltage and current values are measured using the high resolution ADC NI-9215 from National Instruments connected to the analog outputs of the power converters. The values can be stored with time stamp on the hard disk of the control PC, which is controlled remotely using WinCC.

Interlock and control system developed for the ExB deflector, presented in this contribution, allow safe and reliable operation of the system during the deflector conditioning and experiments [2] necessary for the JEDI experiment.

References

- [1] F. Abusaif, et.al., arXiv:1812.08535 (2019).
- [2] K. Grigoriev et al., Contribution to this Annual Report, 2022.
- [3] User Manual, "Precision High Voltage Power Supplies", V1.8, 2017.

¹ Currently at GSI Helmholtzzentrum für Schwerionenforschung, Darmstadt, Germany

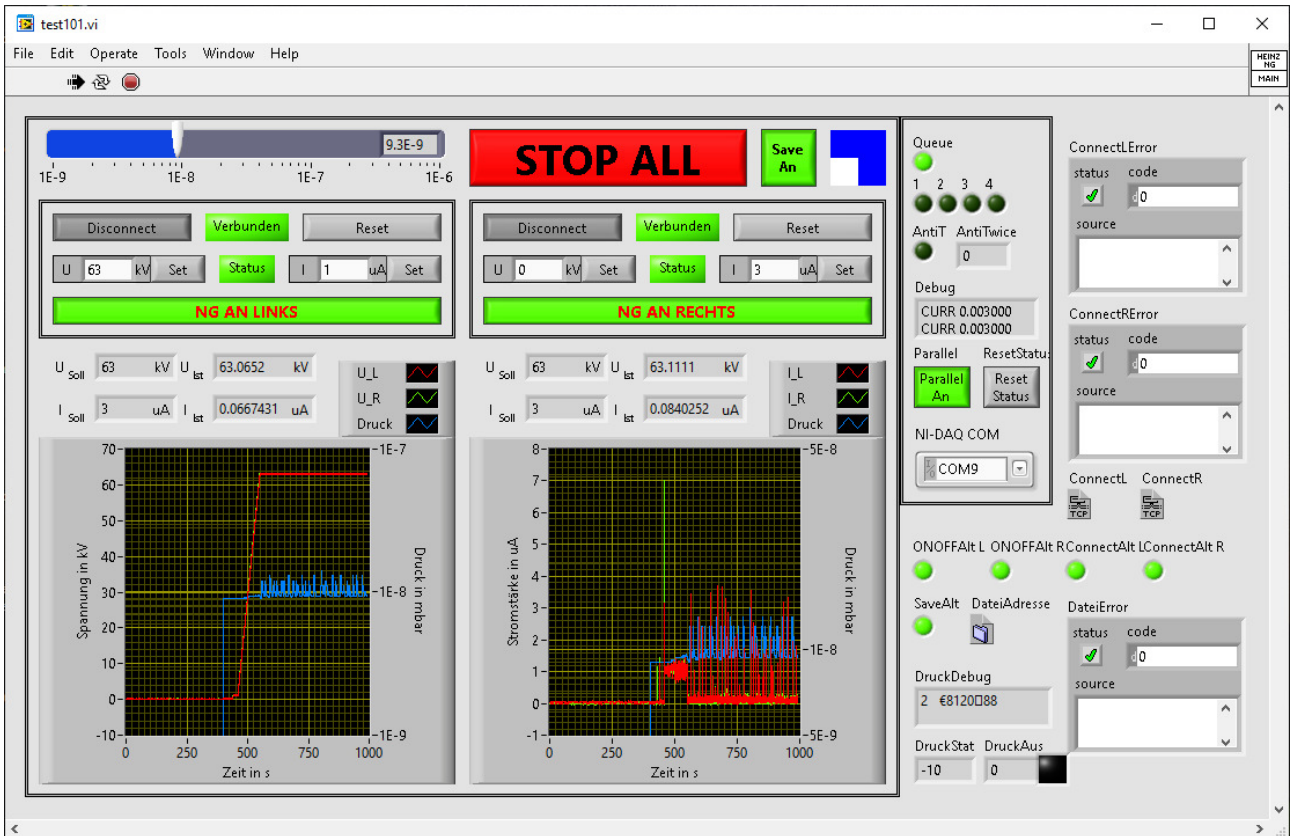


Figure 3: Program to control HV power supplies and interlock signals.

BPM Test Bench Operation for HESR

A. Halama¹, C. Böhme, G. Rupsch¹, K. Reimers

Capacitive Beam Position Monitors (BPM) [1] are essential non-destructive beam diagnostic devices common in most particle accelerators. They utilize a spatial distribution of the beam's image current onto the BPM-electrodes. Pre-amplifiers convert the image current into a voltage signal acting as impedance converters and integrators. The signal balance of opposing electrodes encodes the beam position. Since the difference signal of opposing electrodes normalized by their sum signal is proportional to the beam position. BPMs for the High Energy Storage Ring (HESR)[2] at FAIR are currently characterized at IKP. From the prototype onwards to the series produced BPMs the test bench [3] has been operated to measure the sensitivity and electrical centres. The test bench operation procedure, experiences and results are presented.

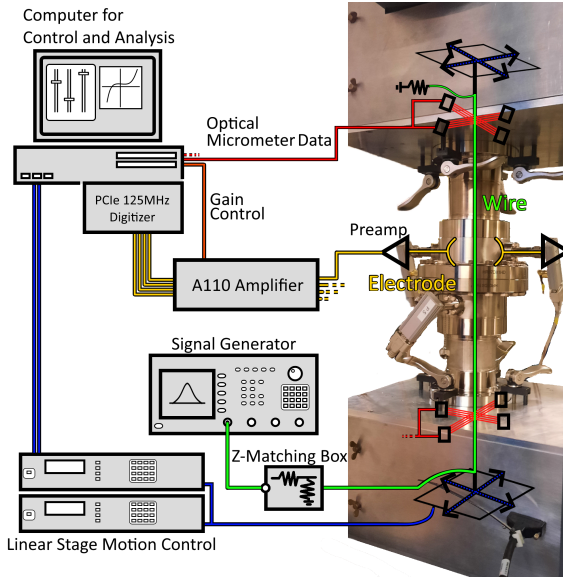


Figure 1: Simplified hardware layout

A pair of BPM electrodes is encapsulated within a certain beam pipe element in its widened end. Two orthogonal measurement planes are realised by combining these beam pipes at their large flange. The electrodes are diagonally cut cylinders, as of the design adoption from COSY BPMs. The diagonal cut ensures a linear response. Due to the scarcity of antiprotons during commissioning runs, the BPM system must meet strict constraints. The requirements include a low noise amplification scheme over several orders of magnitude of amplification as well as attenuation, integrated pre-amplifier gain adjustment as well as precise knowledge of every BPMs characteristic coefficients among others. The desired accuracy and precision per BPM have been proposed to be

100 μm for closed orbit position measurements.

Fig. 1 shows the simplified layout. BPM beam pipe elements are mounted between two almost identical reference boxes. These boxes contain the wire fixture on the linear stages (blue), signal ports (green) and optical micro meters (red). The boxes have low tolerance machined feed to ensure parallelism during assembly. A signal generator feeds 1 V to 4 V Gaussian pulses ($\sigma_t = 0.1 \mu\text{s}$, 500 kHz) to a matching network, which in turn delivers a wire current of $\frac{U_{pulse}}{866 \Omega}$ Amperes. The movable wire acts like a pencil beam. Therefore, the BPM signal picked up is similar to the actual operation case. To get half of the positional relation between the wire position measured at the boxes and the BPM temporary reference pins extend from fitting holes in the flanges into the measurement range of the micrometers. A computer at the test site controls the wire location and collects optical, electrical and miscellaneous data.

Test run progressions are handled by a LabView program. Initial conditions, initial wire alignment, overall progress, latest received signals and data management is handled from a single virtual instrument (VI) window. A run entails the meandering of the wire along 11x11 coordinates in a 20 by 20 mm grid centred around the geometrical BPM centre. Per wire location approx. 1400 pulses are captured per channel in batches of 8192 Samples at 125 MHz sampling frequency. Micrometre data can be averaged and logged between each batch. Each BPM is tested at least for 9 runs on the test bench. A single run takes about one and a half hours, which allowed us to characterize at most two BPMs a week.

The evaluation process consists of two main stages. In a first step all files per individual wire location are processed to calculate the pulse integrals in a bunch-by-bunch basis and obtain the average pulse integral along other statistics. In the second step the condensed data is used to calculate the difference over sum per plane, correct positional offsets picked up via the micrometers, and sieve the data for outliers in a multi staged fashion. The end result is the set of coefficients k_x , k_y , x_0 and y_0 , being the sensitivities and electrical offsets. The linear response allows the characterized by the equation for the beam position x_{beam} , y_{beam} respectively: $x_{beam} = k_x * \Delta / \Sigma + x_0$. In addition, eight statistical parameters are calculated and displayed in a traffic light scheme with tolerance bars to qualify each individual run at a single sight. Based on test bench results, the transverse position of a single bunch of antiprotons at HESR injection conditions ($E = 3 \text{ GeV}$, $N = 10^8$, $\sigma_t \approx 0.1 \mu\text{s}$) can be obtained with an statistical uncertainty of $\sigma_{x,y}$ 2 mm. The proposed accuracy can be achieved by

averaging 400 or more beam positions, with the uncertainty decreasing at a rate of \sqrt{N} per N averaged bunches.

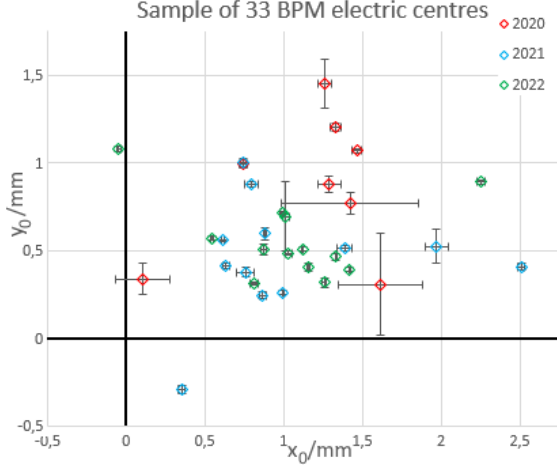


Figure 2: Preliminary electric centre result

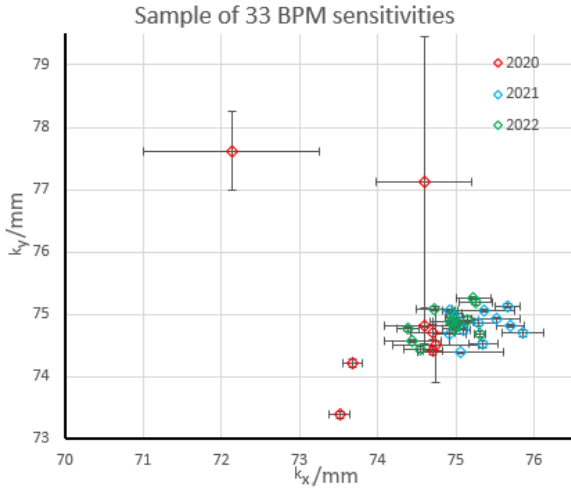


Figure 3: Preliminary sensitivity result

Following up on preliminary results [5] 33 BPM characteristics are shown. Error bars in Figures 2 and 3 are standard deviations within all valid runs per BPM. One can see that later results stray less within runs and compared to other BPM. Preliminary theoretical studies estimated sensitivities about $k_{theo} = 73.5$ mm and electrical offsets about $x, y_{0,theo} = 0.7$ mm [4]. The average BPM with coefficients $k_{x,y} = (74.88 \pm 0.7) \text{ mm}$, $x, y_0 = (0.85 \pm 0.51) \text{ mm}$ lies close to the expected theoretical value.

Measurements of the remaining BPMs and repetitions of early runs are currently in progress. Ongoing optimization of the control software, improvements on the signal port fixtures and sheer experience increased success rate and decreased over all uncertainty. As gain calibration is not implemented at the test bench site matching of similar gain pre-

amplifiers was verified by capturing pulse data while stepwise rotating the pre-amplifiers to all ports and mathematically decouple effects of wire location and individual gains. In order to address uncertainties in the exact geometric centre of the reference boxes, mechanical and software upgrades were implemented to directly couple the reference pins to the wire via the optical micrometers, decoupling the measurement from the reference box layout. Photogrammetric re-evaluation of the geometric centre is pending. This will enable us to compensate systematic errors of former measurement.

References

- [1] P. Fork et al., “Beam Position Monitors”, CERN Accelerator School 2009, GSI, Germany.
- [2] J. Hetzel, “The High Energy Storage Ring (HESR) at FAIR,” ESRW22, Geneva, Switzerland
- [3] S. Srinivasan, “Design and Construction of a stretched wire test bench to characterize Beam Position Monitor for the High Energy Storage Ring,” Master thesis, FH Aachen, 2016.
- [4] A. Halama et. al., “Numerical comparative study of bpm designs for the HESR at FAIR,” IBIC2016, Barcelona, Spain, WEPG01
- [5] C. Böhme et al., “Status Overview of the HESR Beam Instrumentation”, IBIC2022, Kraków, Poland, MOP03

¹ Currently at GSI Helmholtzzentrum für Schwerionenforschung, Darmstadt, Germany

Injection optimization using machine learning at the Cooler Synchrotron COSY

A. Awal^{1,2}

¹RWTH Aachen University

²GSI Helmholtzzentrum für Schwerionenforschung

To achieve a high-intensity, small-emittance particle beam in COSY, it is necessary to efficiently transfer particles from the cyclotron to COSY via the Injection Beam Line (IBL) and inject them successfully. Tuning the IBL requires adjusting various parameters in a complex and non-linear way, which is currently done manually by operators who spend several hours to a few days to optimize the IBL. Machine learning algorithms show promise in addressing this challenge by effectively optimizing the IBL setup, as demonstrated for instance in [2].

Bayesian Optimization is a machine learning method that optimizes an objective function to find the maxima using limited observations. The objective function to be optimized is a black-box continuous function which means it is costly to evaluate and/or is difficult to differentiate. It is therefore seen as a promising method to optimize the complex parameters of the IBL.

During the beam time in March 2022, a framework for executing Bayesian optimization and controlling the IBL has been implemented in Python and supporting libraries [4, 1, 3]. The IBL at COSY has 15 quadrupole magnets and 28 steerers summing up to 43 parameters to optimize. Several optimization experiments were conducted over different parts or magnet types of the IBL. Our experiments concluded that with sufficient time and fair parameters for the exploration-exploitation trade-off, Bayesian optimization typically keeps improving the optimization parameters achieving an experienced level. Figure 1 shows a sample experiment in which Bayesian optimization was executed after manual optimization and it managed to achieve higher density inside COSY. A draft paper on this work exists and is in revision.

Reinforcement Learning (RL) is a type of machine learning in which an agent is trained on making decisions by interacting with its environment and learning from the feedback. RL algorithms learn to map the current observation of the environment at each time step o_t to the best action to take a_t . This mapping is referred to as the agent *policy* and it is expressed as a probability over actions given an observation $\pi(a|o)$. The agent's goal is to maximize the expected future rewards $\mathbb{E}[r]$, which is provided as feedback for its decisions. RL has been successfully

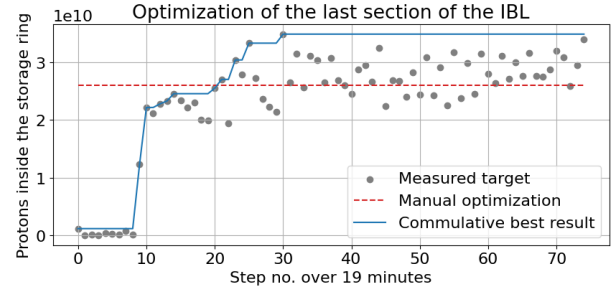


Figure 1: Optimizing the quadrupole and steering magnets of the last section from the IBL via Bayesian optimization. After manual optimization of the IBL there were 2.6×10^{10} protons inside the synchrotron. The objective function objective for Bayesian optimization is the beam current inside COSY and the parameters space is of size 8. The beam intensity after the optimization improved to 3.5×10^{10} protons inside the synchrotron.

applied to a wide range of tasks such as games and robotics and our recent research concerns extending this to optimizing the IBL.

A simulation environment of the IBL for the purpose of training RL agents has been developed with a standard OpenAI Gym interface. Several batches of agents were developed and improved upon to solve the problem of optimizing the IBL in simulation. Recent RL agents were successful to optimize the simulated IBL with a noisy initial beam that may have an angle, offset, and consists of several bunches. The agents managed to optimize the IBL while implicitly keeping the beam β values quite low.

References

- [1] Heidelberg Ion-Beam Therapy Center (HIT). *cpymad: a Cython binding to MAD-X*. 2014-. URL: <https://github.com/hibtc/cpymad>.
- [2] Sabrina Appel et al. “Optimization of Heavy-Ion Synchrotrons Using Nature-Inspired Algorithms and Machine Learning” (2019). DOI: 10.18429/JACOW-ICAP2018-SAPAF02.
- [3] Fernando Nogueira. *Bayesian Optimization: Open source constrained global optimization tool for Python*. 2014-. URL: <https://github.com/fmfn/BayesianOptimization>.
- [4] *PyEpics: Epics Channel Access for Python*. URL: <https://github.com/pyepics/pyepics>.

JULIC Neutron Platform

P. Zakalek, J. Baggemann, I. Pechenizkiy, M. el Barbari, H. Kleines, F. Suxdorf, P. Kämmerling, R. Engels, O. Felden, Y. Valdau, K. Grigoryev, V. Kamerdzhiyev, R. Achten, R. Hanslik, Y. Beßler, M. A. Paulin, F. Ott, E. Mauerhofer, U. Rücker, R. Gebel, T. Gutberlet, Th. Brückel

Neutrons are an essential analytical probe to investigate the structure and dynamics of matter. For the release of neutrons, spallation or fission reactions are used at large research reactors or spallation sources. In recent years a number of research reactors were closed which resulted in a decline in the availability of neutrons in Europe [1]. The High Brilliance neutron Source (HBS) project [2, 3] has been initiated to develop a high-current accelerator-based neutron source (HiCANS) using nuclear reactions at low proton energy to provide a cost-efficient alternative for sustainable provision of neutrons. Due to its scalable design it allows one to establish a network of neutron sources in Europe to ensure a rich neutron landscape. To achieve this goal the development of many key-elements like neutron releasing target or low dimensional finger moderators is required.

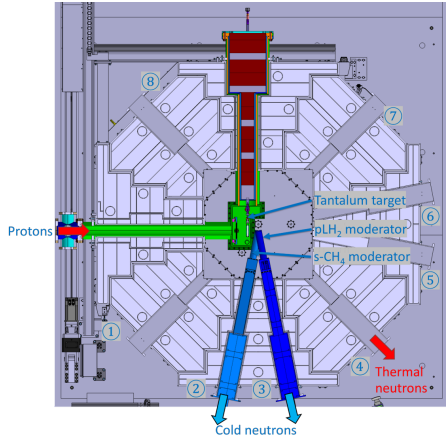


Figure 1: Target test station with indicated neutron extraction as well as numbering of the extraction plugs

A target test station [4] with all major components e.g. target, thermal moderator-reflector assembly, cryogenic moderators and neutron extraction was developed in a collaboration between ZEA-1 and JCNS-HBS (see Figure 1). A proton beamline from the JULIC cyclotron was installed by IKP-4. It provides a 45 MeV proton beam.

The target test station has 8 channels which can be used for neutron beam extraction. The ensemble provides a platform for neutron scattering and analytic experiments as a testbed for the full-fledged HBS. It is named JULIC Neutron Platform. A beam-on-target was realised on December 12, 2022 (Figure 2) producing first neutrons at the JULIC neutron platform at the Forschungszentrum Jülich. The av-

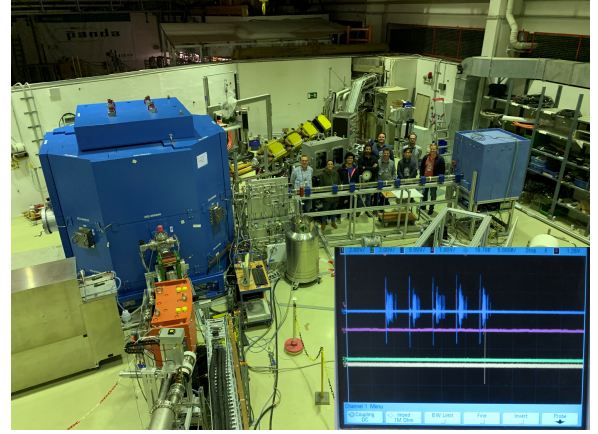


Figure 2: Target-Moderator-Reflector (TMR) test station after beam-on-target with the measured first pulses in the left corner

erage proton beam power on target was around 2 W, sufficient for a proof of principle. This has to be compared to the 100 kW power on target foreseen for the HBS neutron facility. Three neutron beamlines were installed and operational during the beam-on-target tests: a detector test beamline, the time-of-flight reflectometer HERMES provided by LLB / Saclay and a time-of-flight diffractometer.

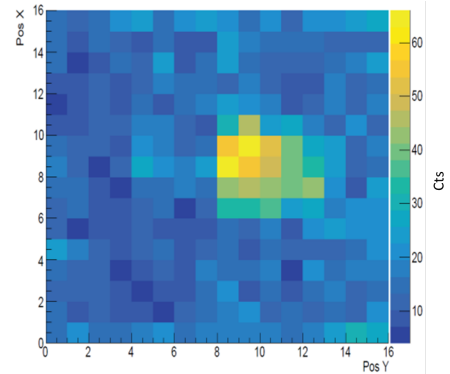


Figure 3: Detector test image

The detector test beamline uses extraction plug no. 4 shown in Figure 1 where a pinhole with a 5 mm diameter is facing the thermal moderator inside the target station. A SONDE detector segment of the SKADI instrument to be installed at the ESS was tested. It utilised a 50 μ s time resolution and a 6 x 6 mm² spatial resolution. In Figure 3 a time-of-flight image at 1.4 ms is shown which corresponds to a wavelength of 2.5 Å. The maximum in the centre

of the image correlates with the thermal extraction channel towards beamline 4.

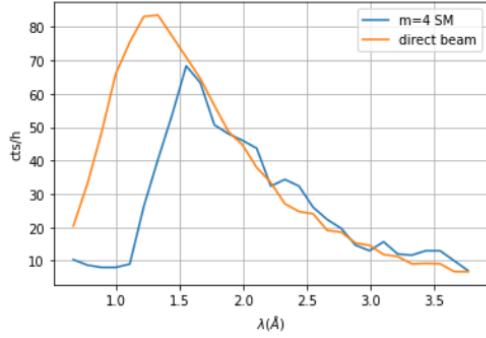


Figure 4: HERMES reflectometry measurement of an $m = 4$ supermirror

The HERMES reflectometer which used to be operated at the ORPHEE reactor in Saclay (F) was installed in collaboration with the Laboratoire Léon Brillouin (LLB). It is placed at the extraction plug no. 3. For future measurements it is planned to equip this extraction channel with a liquid parahydrogen moderator providing cold neutrons. The reflectometer will be used to investigate and characterise neutron guide mirrors. For testing, a $m = 4$ supermirror was measured with thermal neutrons. In Figure 4 the first reflected intensities of the supermirror are shown where the beam is totally reflected by neutrons with wavelengths above 1.5 \AA .

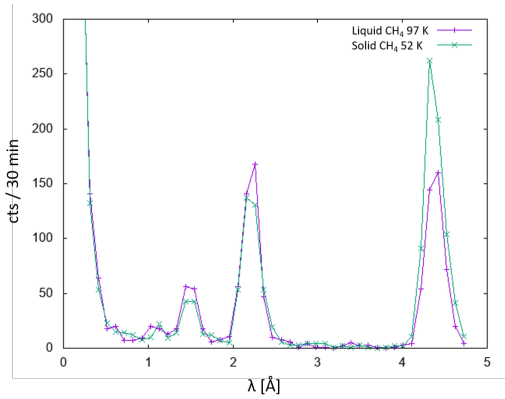


Figure 5: Diffraction experiment of pyrolytic graphite

The third experiment was a diffractometry experiment in time-of-flight mode with a 6.5 m long neutron guide (^{58}Ni) at extraction plug no. 2 equipped with a liquid / solid methane moderator. A pyrolytic graphite sample was measured. The diffraction pattern is shown in Figure 5 where Bragg peaks up to the 4th order are visible for two different temperatures of the methane moderator.

The commissioning of the target test station with its beam-on-target on December 12th was a suc-

cess with the provision of neutrons to three experiments. Nonetheless further optimizations and improvements need to be done. The beam current and the power at the target must be increased to produce more neutrons. The HERMES reflectometer needs a fully functional cryogenic moderator which will be installed in summer 2023. The diffractometer setup will be upgraded with a time-of-flight prompt gamma activation analysis setup. Additional beamlines are planned e.g. for neutron imaging with cold, thermal and fast neutrons.

Furthermore and most important, the target test station will enable the test of all critical components for the HBS project. Different moderators can be investigated with their coupling between neutron release, moderation and extraction. The target handling of an irradiated target and tests of further target designs are planned, such as the investigation of the influence of the target cooling water on the neutron moderation.

References

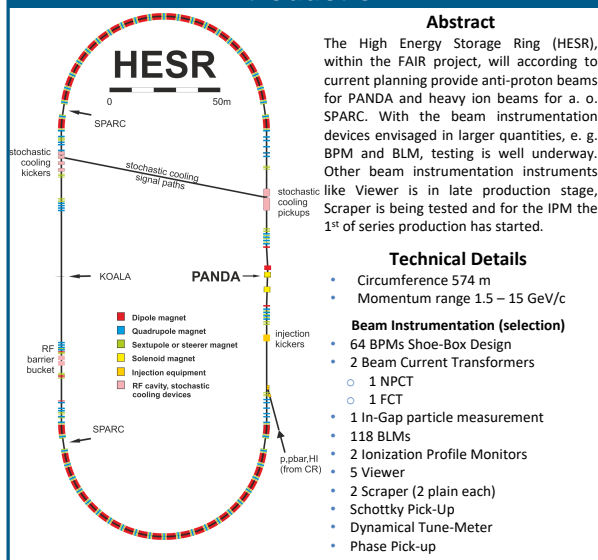
- [1] ESFRI Scripta Volume I; “Neutron scattering facilities in Europe: present status and future perspectives”; ESFRI Physical Sciences and Engineering Strategy Working Group Neutron Landscape Group; June 2016; Editors: Colin Carlile and Caterina Petrillo
- [2] Conceptual Design Report “Jülich High Brilliance Neutron Source (HBS)”; FZJ report (2020)
- [3] P. Zakalek, et al., J. Phys.: Conf. Ser. 1401 012010, 2020
- [4] R. Hanslik, R. Achten, DE 102023200244.2, 2023

Status Overview of the HESR Beam Instrumentation

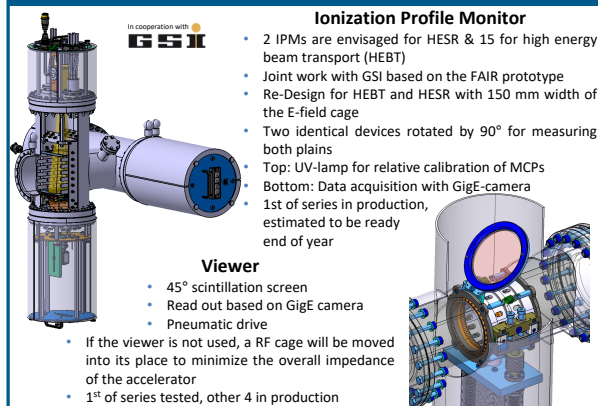
C. Böhme, A. Halama, V. Kamerdzhev, G. Rupsch
IKP, Forschungszentrum Jülich GmbH, Jülich, Germany



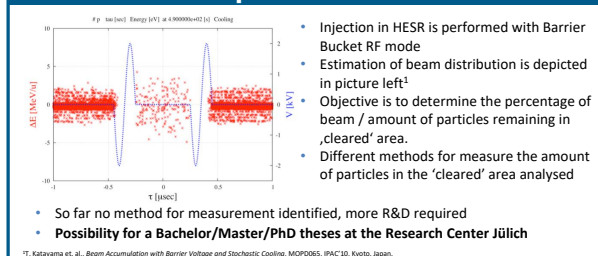
Introduction



Ionization Profile Monitor & Viewer



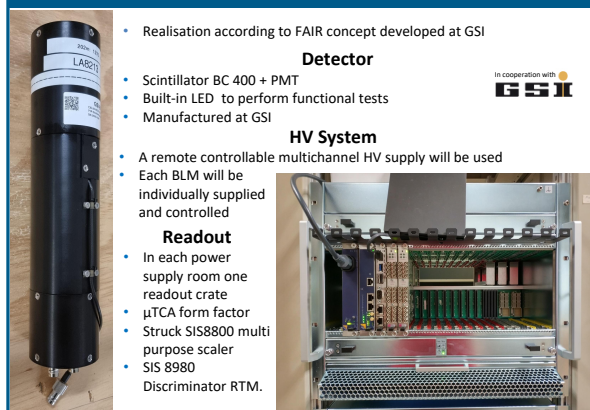
In-Gap measurement



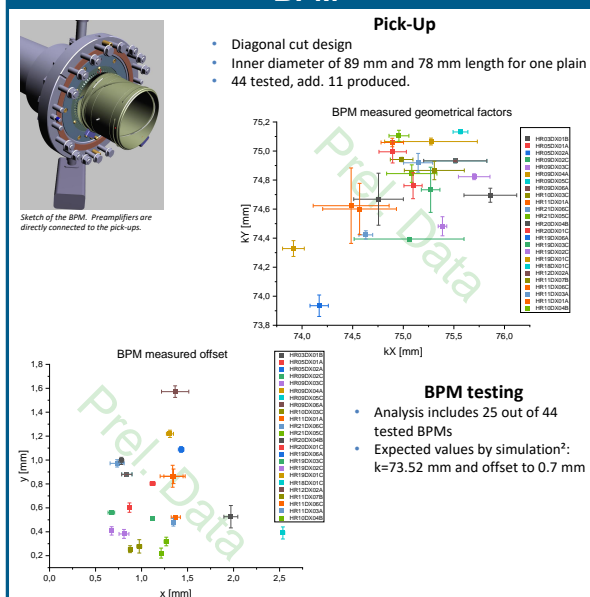
Summary

Significant progress was recently achieved with manufacturing and testing of BI components for the HESR. However, the workpackage requires further attention to complete the manufacturing and testing as well as designing of components like Schottky Pick-Up and In-Gap beam measurement.

BLM



BPM



Signal Amplification

- Head amplifiers mounted on the vacuum feedthrough in addition to iTech's AMPLIFIER 110¹
- AMPLIFIER 110 amplification range +60 dB to -60 dB
- Head amplifier parameters:
 - Amplification: 20 dB
 - Noise: 6 μV at 50 pF input capacitance and 10 MHz BW
 - Bandwidth: 10 MHz by default, configurable up to 70 MHz
 - Input Impedance: 500 kΩ
- Solution adapted at other FAIR machines like HEBT, CR and CRYRING



Beam Position Processor

- Libera Hadron from I-Tech, Slovenia was chosen for FAIR project
- Direct 250 MHz 16 bit signal digitization with all digital signal processing

¹ A. Halama et. al., Numerical comparative study of bpm designs for the HESR at FAIR, IBIC2016, Barcelona, Spain, WEP001

² <https://www.i-tech.si/products/amplifier-110/>

JULIC – driver accelerator for HBS



IKP at Forschungszentrum Jülich

At the Forschungszentrum Jülich (FZJ) the energy variable cyclotron JULIC is used as injector of the Cooler Synchrotron (COSY) and for low to medium current irradiations of different types. At the NESP Target station inside Big Karl Experimental area a Target-Moderator-Reflector-demonstrator (TMR) of the proposed accelerator driven High Brilliance Neutron Source (HBS) was set up.

The TMR-demonstrator gives the possibility to:

- test new target materials,
- different types and concepts of moderators
- handling of irradiated targets and components

Set up in the Big Karl-Experimental Area, it although offers space for complex detector and component setups for nuclear and neutron related experiments.

For beam transport from JULIC to the TMR, the beamline has

- a fast kicker magnet and
 - a three-field permanent magnet
- to guide protons to different target stations, as foreseen in HBS.

For diagnostic purposes measurement tools like

- Beam-Position Monitor (BPM)
 - Fast Current Transformer (FCT)
 - Faraday Cup and
 - Multi Wire Proportional Chamber (MWPC)
- have been installed.

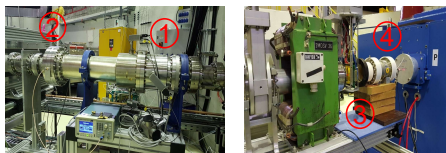


JULIC

Routinely 45 MeV H⁺ and 75 MeV D⁺

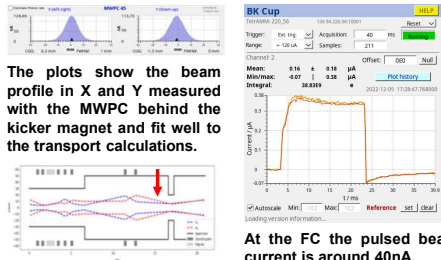
- Pole diameter 3.3 m / 700 t iron
- 20 – 30 MHz (h=3)
- 22.5 – 45 MeV/A
- _{max} = 1.35 T, B_{hull} = 1.97 T
- 2 – 4.5 keV/A injection
- 3 ion sources
 - 2 multicusp
 - pol CBS
- Pre-accelerator of COSY

Beam Diagnostic



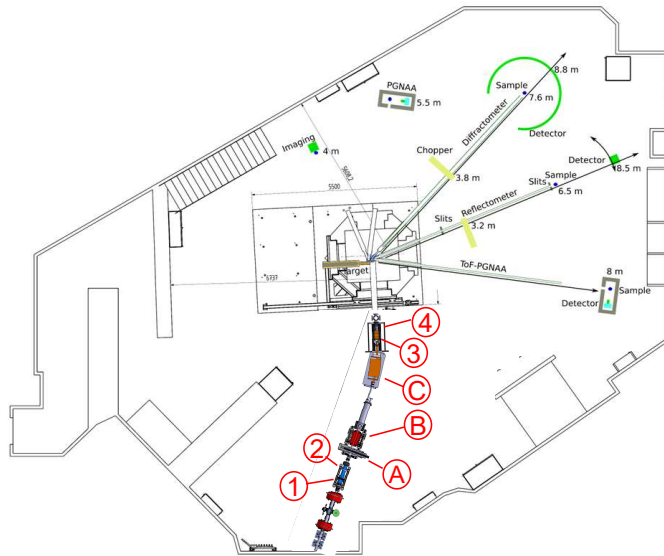
Fast Current Transformer (2) and Beam Position Monitoring System (1) in the beamline in Big Karl area for non-destructive measurement of the beam position and current transported.

In front of the TMR are the Multi Wire Proportional Chamber (3) for beamprofiling and a Farady Cup (4) to measure the current and to calibrate the FCT.



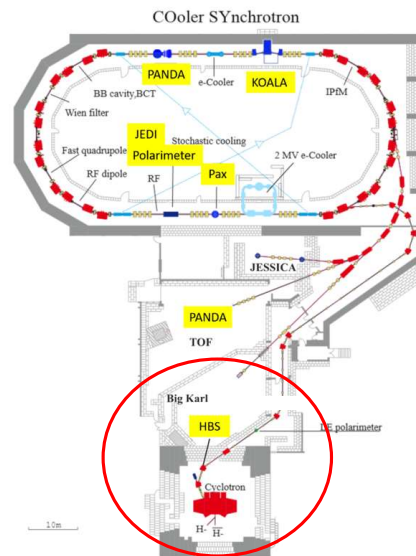
At the FC the pulsed beam current is around 40nA.

HBS JULIC Neutron Platform



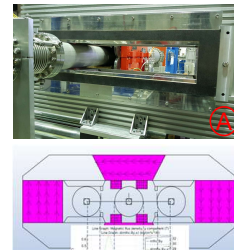
- Development, testing and operation of components of pulsed accelerator based neutron sources
 - targetry and neutron provision,
 - moderator development and optimization of the TMR unit.
- Test of Proton beam transport devices
 - beam control and dynamics,
 - beam multiplexing or beam dump systems
- Design, construction and operation of versatile neutron instruments
 - for neutron scattering purposes,
 - neutron analytics

COSY Facility



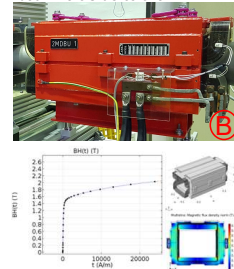
- COoler Synchrotron, 3.7 GeV/c
- Polarized protons and deuterons
- Beam cooling
 - electron cooling
 - stochastic cooling
- Development and Test of FAIR related components
 - accelerator components (BB Cavity, BCT, IPfM...)
 - detectors and modules (PANDA, KOALA, CBM...)

Magnets



Multiplexer system with 3-field permanent magnet (A), fast kicker (B) and bending magnet (C) deflecting the beam up to 40°.

The 3-field permanent magnet is in position to guide the beam left side to the TMR.



Member of the Helmholtz Association

O. Felden, R. Gebel, K.Grigoriev, V. Kamedzhiev, Y. Valdau - Institute for Nuclear Physics, FZ-Jülich IKP-4, Germany, o.felden@fz-juelich.de

THPO005: CYCLOTRONS 2022

Triggering AI and beam-target modeling in the PANDA software

Ralf Kliemt, Klaus Götzen, Peiyong Jiang, Frank Nerling, Klaus Peters for the PANDA collaboration

Beam-Target modeling in the PANDA simulations

In the PANDA experiment it is foreseen to use different targets for the antiproton beam. Due to the geometry of the interaction region, evaporated molecules of the target material, e.g. hydrogen, will enter the beam line. This residual gas will interact with the beam and produce background reactions, which will significantly affect the luminosity measurements. In order to be able to quantify such effects, the overlap of the anticipated beam with the density profile of the residual gas has been integrated with the PandaRoot simulations.

Interaction points are calculated in two steps. First the z coordinate along the beam line is sampled from the gas density profile, which includes the target itself. Secondly the beam envelope shape along the beam line defines the beam spread $\sigma(z)$. The x and y coordinates are sampled from a Gaussian profile with the width of $\sigma(z)$.

The gas density profile is based on realistic GARFIELD simulations [1] that take the outgassing as well as the pumping speeds into account (see Fig. 1).

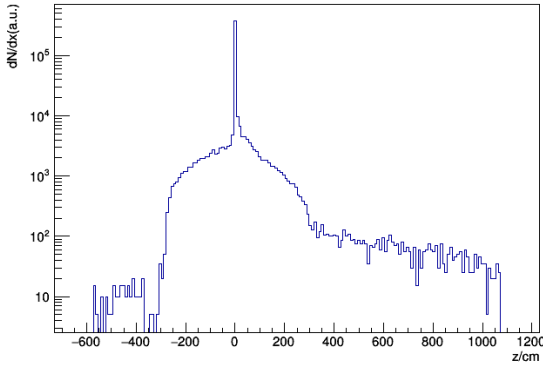


Figure 1: Interaction point distribution with realistic rest gas modeling for a hydrogen cluster jet target.

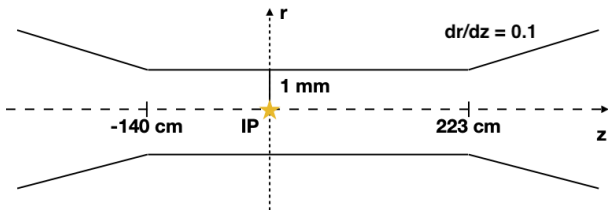


Figure 2: Schematic beam spread envelope.

The beam envelope profile is defined as the Gaussian

1σ surface. Inside the solenoidal field of PANDA the beam is modelled to have a constant width of 1 mm and opening up at the points of half field strength with a slope of $dr/dz = 0.1$ [2], see Fig. 2. A more detailed profile should enter the simulations once the accelerator is set up and commissioning measurements are available.

Triggering with Machine Learning in PANDA

The PANDA experiment at the FAIR facility will measure particle reactions at rates of up to 20 MHz. Physics reactions of interest will feature very small cross sections which are 6 or more orders of magnitude smaller than the continuum background cross section. For an acceptable data volume the aim is to reduce the data stream by a factor of 1000 to an event rate of 20 kHz.

A software trigger scheme has been developed over the last years to filter events of physics interest in an online scenario, featuring physics analysis on free streaming data. Machine learning technologies have been studied [3] to aid the process and to develop a reliable neural network architecture that performs well and robustly.

Ten antiproton induced reactions, covering the main physics interests of PANDA, have been chosen to study the performance of the neural networks at four center-of-mass energies, 2.4, 3.8, 4.5 and 5.5 GeV:

Phys. topic	Reaction	Code	Trigger
EM physics	$\bar{p}p \rightarrow e^+e^-$	<i>ee</i>	$\bar{p}p \rightarrow e^+e^-$
Exotics	$\bar{p}p \rightarrow \phi_{(1)}\phi_{(2)}$	<i>Phi</i>	$\phi \rightarrow K^+K^-$
Charmonium	$\bar{p}p \rightarrow \eta_c\pi^+\pi^-$	<i>Etac</i>	$\eta_c \rightarrow K_S^0 K^- \pi^+$
	$\bar{p}p \rightarrow J/\psi\pi^+\pi^-$	<i>J2e</i>	$J/\psi \rightarrow e^+e^-$
	$\bar{p}p \rightarrow J/\psi\pi^+\pi^-$	<i>J2mu</i>	$J/\psi \rightarrow \mu^+\mu^-$
Open charm	$\bar{p}p \rightarrow D^0\bar{D}^0$	<i>D0</i>	$D^0 \rightarrow K^- \pi^+$
	$\bar{p}p \rightarrow D^+D^-$	<i>Dch</i>	$D^+ \rightarrow K^- \pi^+ \pi^+$
	$\bar{p}p \rightarrow D_s^+D_s^-$	<i>Ds</i>	$D_s^+ \rightarrow K^+ K^- \pi^+$
Baryons	$\bar{p}p \rightarrow \Lambda\bar{\Lambda}$	<i>Lam</i>	$\Lambda \rightarrow p\pi^-$
	$\bar{p}p \rightarrow \Lambda_c\bar{\Lambda}_c$	<i>Lamc</i>	$\Lambda_c \rightarrow pK^- \pi^+$

Two main modes of operating a triggering setup with neural networks are binary and multi-class classification. The former features one neural network per trigger channel, which discriminates signal from background. In the latter approach one neural network is used to classify all channels at once for the complete trigger setup. The first result from the study is that one neural network per trigger channel, performs generally better than the multi-class classification. Additionally, the scalability of the setup improves by using many single networks of smaller capacity and individual training requirements.

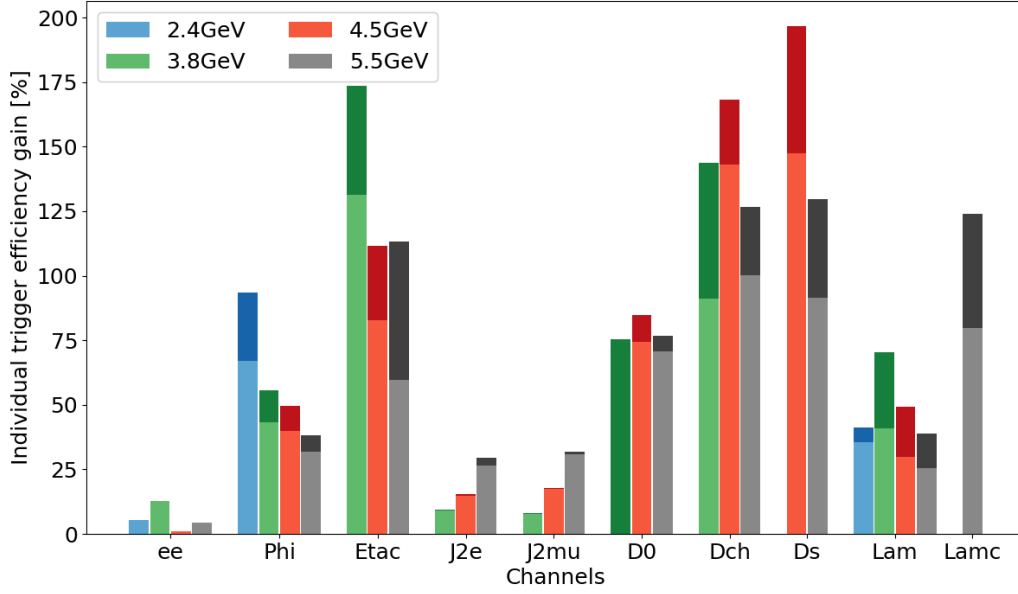


Figure 3: Individual triggering efficiency gains of the neural networks compared to a cut-and-count approach, based on the same set of input observables (light colors), and an extended set of observables (dark colors).

Secondly it was found that from seven network architectures, a coevolution neural network with residual blocks features the generally best performance and robustness under changing the networks depth. It is presumed to adjust the network depth for more complex trigger channels in the future.

Compared to an optimized cut-and-count approach the neural networks are able to improve the triggering efficiency by up to 200% (Fig. 3) while maintaining an overall background reduction factor of 1000. Additionally cross-tagging between the trigger channels is able to increase the performance in channels with similar topology.

An important aspect is the quality of the selected data. For example, when the network is able to extract a resemblance of the invariant mass of the trigger channel resonance, peaking background will appear, which would spoil physics analysis. Also in channels with three decay products the efficiency should be flat over the whole Dalitz plot phase space. A homogeneous efficiency distribution is important e.g. for partial wave analyses. In the future quantifying the data quality and means to ensure it will be subject to further detailed studies.

References

- [1] C. Mannweiler, WWU Münster, private communication (2022)
- [2] "Fair Operation Modes" v.6, internal document (2020)
- [3] P. Jiang, K. Götzen, R. Kliemt, F. Nerling, K. Peters: "Deep Machine Learning for the PANDA Software Trigger", Preprint, arXiv:2211.15390 [physics.ins-det] (2022)

A Partial Wave Analysis Framework for Hadron Physics

A. M. Foda, J. Messchendorp, J. Ritman

The High Acceptance Di-Electron Spectrometer (HADES) experiment located at the heavy ion synchrotron SIS18 is located at GSI Helmholtzzentrum für Schwerionenforschung. The experiment aims to study the structure of nuclear matter. A Partial Wave Amplitude (PWA) analysis is a powerful tool to gain insight to the properties of nuclear reactions. In a PWA analysis, the decay channel is broken down into the contributing resonances taking into account their spin and parity quantum numbers. This allows the identification of contributing intermediate reaction channels to the final state. A fitting process follows to calculate the set of parameter values to describe the reaction. A solution is found when a set of unique amplitudes is able to reproduce the observed distribution. This is usually done by systematically adding higher spin amplitudes to the model & checking if it significantly improves the fit quality. An ambiguity may arise if more than one set of amplitudes produce equally acceptable fits to the data.

Efforts for a PWA analysis using HADES data include the analysis of the two-pion ($\pi^+\pi^-$ and $\pi^-\pi^0$) final state with other world data on single and double pion production in photon, pion and electron induced reactions. The contributions of various final ($\Delta\pi$, $\rho\pi$, $N\sigma$) and initial resonant and non-resonant states were extracted. The HADES data were essential to restrict the ρ production and to extract the branching ratios of $N(1440)$, $N(1520)$ and $N(1535)$ baryon resonances to the ρN channel. These couplings have been used in a Vector Dominance Model to interpret the dielectron production. Fig. 1, shows the $\pi^+\pi^-$ invariant mass distribution measured at HADES in the $\pi^-p \rightarrow \pi^+\pi^-n$ reaction at a mean pion beam momentum of 0.685 GeV/c along with the Bonn-Gatchina (BnGa) PWA solution [1].

PWA analysis studies in HADES have been conducted using BnGa framework which is a FORTRAN based software to perform unbinned maximum likelihood fit using K-Matrix and D-Matrix techniques [2]. The current effort is focused on presenting the analysis framework in a modular setup and user friendly interface. To achieve this, we are collaborating with the BnGa group to implement the K-Matrix and D-Matrix analysis models into AmpTools [3]. AmpTools is a collection of C++ libraries with modular design for unbinned maximum likelihood fitting and a GUI interface for visualization. The first milestone will be to establish a PWA analysis framework for final states

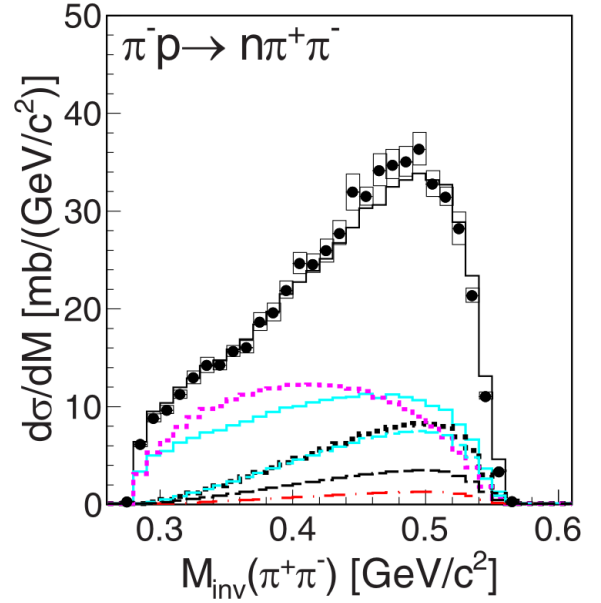


Figure 1: The $\pi^+\pi^-$ invariant mass distribution in the $\pi^-p \rightarrow \pi^+\pi^-n$ reaction for a mean pion incident momentum of 0.685 GeV/c measured at HADES (black circles) compared to the Bonn-Gatchina PWA solution (solid black line). Contributions from the isobar $\Delta\pi$ is shown in cyan, $N\sigma$ in dashed violet and $N\rho$ in violet. Contributions to the ρ are represented by green curves for the s-channels, blue curve for D_{13} partial waves and black curves for the S_{11} partial waves [1].

from pion induced reactions studied with HADES. This will serve as a proof of concept by comparing our results with previous fit results obtained using BnGa and prepare us for PWA analysis efforts for the upcoming π -beam data. Afterwards, we will expand the framework to include more reactions of interest (e.g. proton-beam reactions).

References

- [1] Two-pion production in the second resonance region in π^-p collisions with HADES, HADES Collaboration, Phys. Rev. C, 102, 2, 024001, 2020, 10.1103/PhysRevC.102.024001.
- [2] ‘Bonn-Gatchina’ Webpage <https://pwa.hiskp.uni-bonn.de>
- [3] M. Shepherd *et al.*, ‘AmpTools’ <https://doi.org/10.5281/zenodo.7336113>

Towards a search for the N(1720) double resonance in pion-proton collisions with HADES

J. Gollub, A. Foda, J. Messchendorp, J. Ritman

Mapping out the nucleon excitation spectrum is important for our understanding of the strong interaction. Many experiments search for the so-called "missing" baryon states predicted by different models, such as the quark model. These studies will be able to confirm some of the key predictions.

The Particle Data Group (PDG) [2] lists all the identified states and ranks them from one to four stars. One star indicates that the evidence of this state is poor, whereas four stars imply that the existence is certain and the properties are at least fairly explored. One of those four star states is the N(1720) with the spin-parity assignment $J^P = \frac{3}{2}^+$.

The latest analysis of $\pi^+\pi^-p$ electroproduction and photoproduction data taken by the CLAS collaboration hints to the existence of an additional N'(1720) $\frac{3}{2}^+$ resonance. The comparison of the fits of the electroproduction and photoproduction data solely based on the well-established resonances shows a large deviation by a factor four for the branching fraction of the N(1720) into the ρp final state. This discrepancy can be resolved by including an additional N'(1720) resonance [1]. The fit results are summarized in table 1. To provide evidence for the existence of the N'(1720), complementary data are necessary. In the near future, this may be provided by the HADES collaboration using the pion-beam facility at SIS18.

The HADES (High Acceptance DiElectron Spectrometer) collaboration has a research program dedicated to provide further insights in the field of QCD. Baryon spectroscopy in the third-resonance region using beams of pions impinging on a proton target is part of the program [3]. For the planned pion-beam experiments, it is foreseen to take data at center-of-mass energies in the region of $\sqrt{s} = 1.67 \text{ GeV} - 1.76 \text{ GeV}$. Consequently, with the upcoming data it would be possible to study the production of the N(1720) and N'(1720) resonances.

To eventually demonstrate the feasibility for HADES to identify the production of the N'(1720), the first

steps towards a detailed sensitivity study have been performed. This study uses the Bonn-Gatchina Partial Wave Analysis (BoGa PWA) framework [4]. In a first step, Monte Carlo data with the physical model from the latest fit of the CLAS collaboration have been generated. In figure 1 the $n\pi^-$ invariant mass distribution of the reaction $\pi^-p \rightarrow \pi^+\pi^-n$ at $\sqrt{s} = 1.7 \text{ GeV}$ according to the parameters given in table 1 is presented. The N(1720) (red squares) has a contribution of 32.83% and the N'(1720) (cyan triangles) of 20.42% to the total Monte Carlo data (black circles). A peak of the $\Delta(1232)$ is visible in both channels.

In the following step, the HADES detector acceptance will be applied. In the final step, the BoGa PWA framework will be used to fit the data in two different ways - similar to the approach in [1]. The comparison of these two fits will show whether the HADES data could provide evidence of the N'(1720).

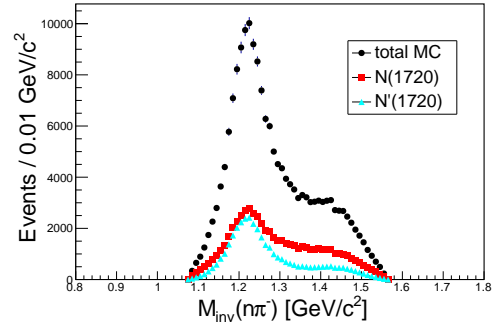


Figure 1: Simulated $n\pi^-$ invariant mass distribution of the reaction $\pi^-p \rightarrow \pi^+\pi^-n$ at $\sqrt{s} = 1.7 \text{ GeV}$ including the N(1720) (red squares) and N'(1720) (cyan triangles) resonances according to the parameters given in table 1. The black circles represent the total Monte Carlo data.

References

- [1] Mokeev, V. I., et al. "Evidence for the N'(1720) $3/2^+$ nucleon resonance from combined studies of CLAS $\pi^+\pi^-p$ photo- and electroproduction data." *Physics Letters B* 805 (2020): 135457.
- [2] R.L. Workman et al. (Particle Data Group), *Prog. Theor. Exp. Phys.* 2022, 083C01 (2022).
- [3] The HADES Collaboration "Baryon couplings to mesons and virtual photons in the third resonance region: vacuum and cold matter studies" internal document (2022).
- [4] Bonn-Gatchina Partial Wave Analysis Web-page: <https://pwa.hiskp.uni-bonn.de>.

Table 1: Masses, widths and branching fractions of the N(1720) and N'(1720) according to [1].

Resonance State	Mass GeV	Width MeV	Branching fraction	
			$\pi\Delta$	ρp
N(1720)	1.743-1.753	114 ± 6	38-53%	31-46%
N'(1720)	1.715-1.735	120 ± 6	47-62%	4-10%

Hyperon-production studies in $p + p \rightarrow \Lambda + K_S^0 + p + \pi^+$ at 4.5 GeV with HADES at GSI

S. Pattnaik, J. Messchendorp, J. Ritman

Proton-induced hyperon production studies can provide valuable insights in the field of baryon spectroscopy [1]. In particular, a study of the coupling strengths of intermediate baryons to hyperon final states will be important to study their internal structure and to search for new baryon resonances. We are analyzing the exclusive process $p + p \rightarrow \Lambda + K_S^0 + p + \pi^+$ using recent data taken with a proton-beam energy of ~ 4.5 GeV at HADES at GSI, Darmstadt [2]. Intermediate kaons and hyperons are reconstructed via their main charged decay channel, i.e. $K_S^0 \rightarrow \pi^+ \pi^-$ and $\Lambda \rightarrow p + \pi^-$.

For the experiment, we used a proton beam with an intensity of 7.5×10^7 particles/s $^{-1}$ bombarding on a liquid-hydrogen target with a length of ~ 4.5 cm. The analysis presented here is based on $\sim 1.5 \times 10^9$ events registered with HADES. Only events containing start time information and a reconstructed global event vertex were retained. We required that all the final-state particles were registered with HADES and reconstructed their momenta by exploiting the magnetic field and drift chamber information of the main detector. This was exploited by imposing momentum conservation thereby optimizing the purity of the event selection. Firstly, the sums of the three (x, y, z) momentum components of all six tracks were required to be within ~ 200 MeV/ c of the initial three-momentum of the beam. Therefore to further improve the selection after the momentum constraints, we required the reconstructed primary vertex to be located in the z (beam)-direction downstream of the target. Time-of-flight information is used for particle identification. The reconstructed masses of the kaon and hyperon are used to identify the reaction channel. Negatively-charged tracks are dominated by pions, therefore, a velocity $\beta > 0.4$ was required. For the particle identification of positively-charged tracks, dominated by pions and protons, we used a relative time-of-flight method to separate the various species. Conventional particle identification methods based on energy-loss information or by making use of timing information of each track with respect to the trigger were not suitable for the high-momentum proton tracks that are present in the reaction of interest.

The time of flight measurement is obtained from the Meta detector in HADES. The start time t_{start} is given by the innerTOF while the stop time t_i^{stop} is given by TOF or the RPC. The expected time of flight for a given mass hypothesis was computed for the measured momentum p and a distance traveled l by a particle candidate. The π^- was chosen as the reference candidate as those were the only negative tracks from the final state particle species. The event

time offset value was calculated from the difference between the measured and expected time of flight for the π^- tracks. The time-of-flight of the positively charged tracks were corrected by subtracting this value, thereby eliminating the event-wise t_{start} offset. The new relative time-of-flight significantly improves the time resolution and, hence, the separation power between pions and proton tracks. For the particle identification of the positively charged tracks, we studied the difference between the corrected time-of-flight measurement and the expected (calculated) time-of-flight based on the mass hypothesis and reconstructed momentum, referred to as ΔT . The difference, ΔT , of all charged-particle combinations for each event was obtained, assuming a mass hypothesis of two positively-charged pions and two proton candidates present in the channel of study. The combination that gave the smallest ΔT sum was used as the joint particle identification hypothesis for the event.

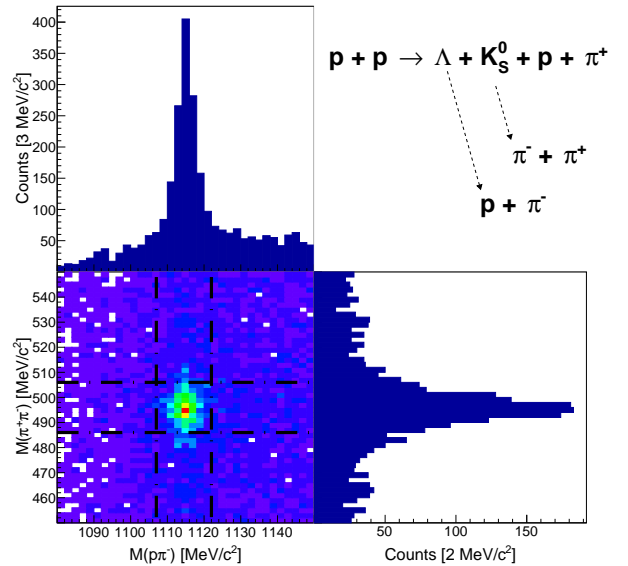


Figure 1: Reconstructed invariant mass distribution of the $\pi^+\pi^-$ versus the $p\pi^-$ final state along with their projections within the dashed lines are shown.

To identify the decay products of the Λ and K_S^0 , we combined all possibilities after particle identification (two for each particle). The proton-pion combination that results in an invariant mass closest to its nominal value of 1115.68 MeV/c^2 was used to identify the best candidates of the Λ decay. Similarly, the best K_S^0 candidate was selected from the combination closest to the invariant mass of 497.61 MeV/c^2 . The primary vertex was reconstructed by calculating the point of closest approach between the remaining

two bachelor candidates (π^+ , proton). The fig.1 depicts the reconstructed invariant-mass distributions of the tracks associated with the decay products of the Λ and K_S^0 candidates. The spectrum reveals a clear observation of a reconstructed Λ decay in coincidence with the decay of a K_S^0 . The top left panel shows the $p\pi^-$ invariant mass distribution obtained from a projection of the two-dimensional spectrum with a constraint on the $\pi^+\pi^-$ invariant mass between $[485-505]$ MeV/ c^2 . The bottom right panels displays the $\pi^+\pi^-$ invariant mass distribution under the condition that the $p\pi^-$ invariant mass is within the range of $[1107-1122]$ MeV/ c^2 . From a fit of the reconstructed Λ (K_S^0) projected mass spectra, we estimated 385 (480) counts and we obtained a reconstructed mass of 1115.0 ± 2.7 MeV/ c^2 (495.7 ± 5.6 MeV/ c^2), whereby the second value corresponds to the resolution (σ). The reconstructed masses are well within the expected values provided by the particle data group [3].

A clean signal of the exclusive reaction $p + p \rightarrow \Lambda + K_S^0 + p + \pi^+$ at 4.5 GeV was extracted using a new relative time-of-flight particle identification technique. To further improve the particle identification, various machine learning-based models will be tested. Lastly, to enable a proper partial wave analysis, it is necessary to enhance the selection of kaons and hyperons, for which a Kinematic Fitter tool will be implemented.

References

- [1] J. Adamczewski-Musch and A. Belyaev *et al.*, Production and electromagnetic decay of hyperons: a feasibility study with HADES as a Phase-0 experiment at FAIR. Eur. Phys. J. A **57**, 138 (2021).
- [2] G. Agakichiev and C. Agodi *et al.*, The High-Acceptance Dielectron Spectrometer HADES. Eur. Phys. J. A **41**, 243–277 (2009).
- [3] P.A. Zyla *et al.*, (Particle Data Group), Prog. Theor. Exp. Phys. **2020**, 083C01 (2020).

Hyperon reconstruction at HADES with kinematic fitting and forward detector upgrades

J. Regina, W. Esmail, A. Illari, J. Messchendorp, J. Rieger, J. Ritman and A. Strach

Following a successful proton-proton run at a beam kinetic energy of 4.5 GeV with the HADES spectrometer in February 2022, the physics analyses are now progressing. For this run, HADES was upgraded with Straw Tracking Stations (STS) covering polar angles below 7° and a forward RPC (fRPC) enabling time-of-flight measurements. The STS consists of eight double-layers of horizontal, vertical and tilted by 45° straw tubes. This new addition is especially important for the hyperon program where many decay products scatter towards the forward direction. After one month of data taking, various activities have been dedicated to the calibration and alignment of the setup.

One summer student project in the group focused on using a neural network with fully connected dense layers for the alignment of the STS detector. The neural network was trained on data sets where various degrees of misalignment in the X-, Y- and Z-directions had been applied. The loss function to be minimized was chosen to be the sum of all residuals between tracks and the tube wires. The neural network was able to predict the degree of misalignment at a level of $100\ \mu\text{m}$ in the Z-direction.

For another alignment procedure, elastically scattered proton pairs are exploited, where one proton is detected in the main HADES detector with fairly well known alignment. The other proton is registered by the forward detector. Different selection criteria are used for the forward tracks and main HADES tracks based on detector resolutions. These conditions follow from momentum conservation of the two-body process. In addition, only the HADES track in a given event that has momentum closest to the theoretical momentum of an elastic scattered proton with the measured polar angle is selected. The expected θ and ϕ of the forward going track is then calculated from the scattering angles of the proton detected by HADES and using momentum conservation.

In order to have a point to extrapolate a track from, the average point of closest approach between the two reconstructed elastic scattered protons is approximated as an event vertex. The mean of a Gaussian fitted to the distribution is used as the one common vertex position for all events. The tracks are extrapolated to the tube layers and the residuals to the tube centers are used to determine the misalignment. Note that the method only uses the forward tracks to select the HADES tracks but the final alignment is independent of the reconstruction in the forward detector. The results for the six horizontal and vertical layers show a sub mm precision for low resolution tracking (*i.e.* tracks are fit to the wire positions, disregarding the isochrone information) in the

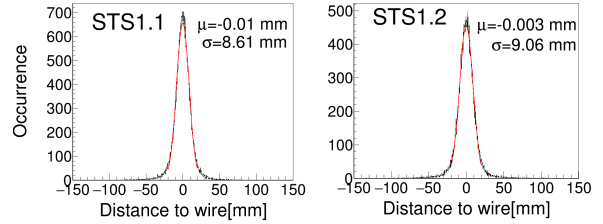


Figure 1: Residuals for the first two STS planes after alignment. The mean (μ) and standard deviation (σ) of the red Gaussian fits are given in the figure.

X- and Y- directions. The track quality (χ^2) is also improved after the alignment. The residuals after alignment are shown in Figure 1.

For the purpose of the hyperon analyses, a kinematic fitting procedure has been developed over the last few years for HADES. This uses several constraints such as a mass constraint, vertex constraint, missing particle constraint, 4-momentum conservation at a decay vertex and 4-momentum conservation of final state particles to the beam-target system. In the context of a summer student project, the performance of the fitter has been investigated by studying how well the kinematic fitting algorithm works for events in HADES with two neutral particles, something that had not been tested before. The results showed that the fitter has promising potential to be used for these events and the studies will continue. The development group has completed a draft manuscript dedicated to a description and benchmark of the software, KinFit.

One analysis focuses on the reaction $pp \rightarrow K^+ K^+ p \Xi^-$, $\Xi^- \rightarrow \pi^- \Lambda$, $\Lambda \rightarrow p \pi^-$. For this analysis, simulations have been tested in order to find optimal parameters for event selection and to understand the decay topology of this complex channel. The particle identification in experimental data is performed by selecting a narrow window on the calculated mass, from the time-of-flight and tracking detectors at HADES, around the nominal values of protons, pions and kaons. The current approach is to reconstruct the Λ hyperon by combining protons and pions and selecting the pair for which the kinematic fitter with a Λ mass constraint gives the best probability. A minimal probability of 0.001 is also applied in order to suppress wrong combinations. Following this step, a pion is combined with the Λ candidate. Further constraints and selections are now needed in order to observe the Ξ^- mass peak which is the focus of the current work. The main HADES detector is currently being used in the analysis and the forward detector will be added in the next step.

A detector consisting of a scintillator and a photomultiplier tube (PMT) can be found in nearly every nuclear physics experiment. Nowadays, PMTs are being replaced more and more by the solid-state alternative, silicon photomultipliers (SiPMs), since they are smaller, less expensive, not sensitive to strong magnetic fields and only need a voltage supply of approx. 30 V. However, there are two disadvantages of SiPMs: They have a higher level of background noise and are more sensitive to radiation damage. While the first can be solved by requesting signals in coincidence with other sensors, the latter case is the subject of our investigations presented here as well as the possible regeneration.

Based on irradiation studies of SiPMs and other silicon-crystal structures (e.g. silicon wafers) the radiation damage is classified into bulk damage and surface damage. While the former is caused by the displacement of crystal atoms, the latter deals with effects in the covering dielectrics and the interface region. In order to check the homogeneity of the irradiation damage a cross table with a pulsed laser diode is used. Through two apertures of 0.2 mm an illuminated region of approx. 0.25 mm is provided which is shifted with steps of 20 μm in the x- and y-direction across the SiPM. Within the sensitivity, which was checked by covering a region of the SiPM with a printed black dot, see Fig. 1, there is no significant difference in the signal homogeneity of an irradiated (11 Gy) and a new SiPM as expected for a homogeneous irradiation damage.

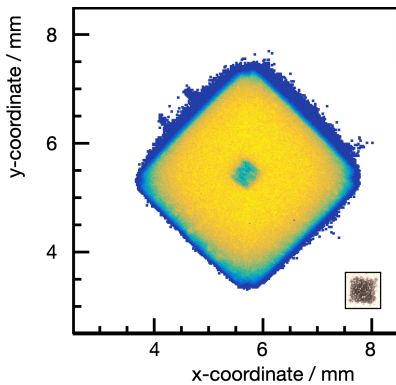


Figure 1: Signal distribution for a scan of a new 3x3 mm² SiPM by a laser LED in 20 μm steps. In the center a foil with a printed black dot with a size of about 0.4 mm was placed to check the method. The box in the lower right corner shows a picture of the dot.

The dark current of a SiPM is a good indicator of the radiation damage. It is well known that an irradiation of SiPMs results in an current increase by orders of magnitude, e.g. with a proton radiation dose of 11 Gy from the Jülich cyclotron a current increase from about 1 μA up to 2.5 mA was measured. A strong current increase was also observed in the proton beam time operation of the ITOF-detector modules in the HADES experiment at GSI. Each ITOF-module, consisting of three scintillators with 12 SiPM's at each scintillator, takes an average current of 1.53 mA, while a not irradiated reference module only consumes 0.26 mA. The performance of the detector modules was essentially not influenced by the higher current as is shown in Fig.2.

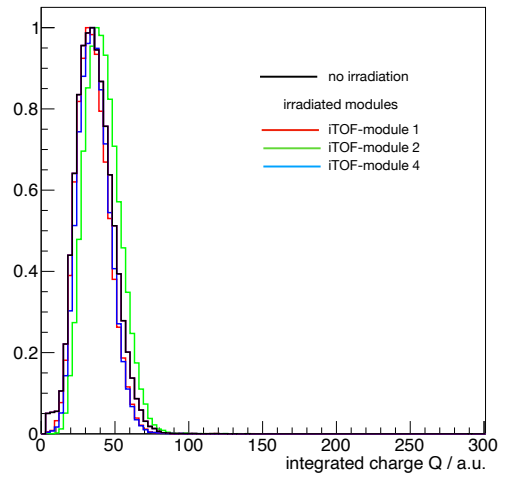


Figure 2: Response of SiPM-sensors of iTOF-detector modules to a ⁹⁰Sr source and multiplicity of signals for a threshold setting of about 2 mV.

The extraction of a correlation between SiPM-performance and dark current is important to have an indication for a required sensor exchange which will be a topic of the further studies.

Another topic is the possible regeneration. By heating a single SiPM which accumulated about 11 Gy of radiation dose up to 175 °C it was possible to reduce the current from 2.3 mA to 0.2 mA (at 29 V).

For a more precise analysis of the radiation effects further proton irradiations at the Jülich cyclotron for a set of SiPMs in a dose range between 1 Gy and 10 000 Gy are planned. At the maximum dose they should completely lose their ability to function as a photo sensor. This SiPM-set will allow a detailed offline analysis of the SiPM-performance as a function of radiation dose.

Integrated Luminosity Determination for the FAIR Phase-0 Beamtime with HADES

G. Perez-Andrade, P. Wintz and J. Ritman

The HADES spectrometer at GSI in Darmstadt, Germany, is part of the new FAIR facility, under construction at GSI. The spectrometer was upgraded by updating existing systems and the integration of new detector systems. Especially important for the FAIR phase-0 physics program is the new Forward Detector (FD) consisting of two new Straw Tracking Stations and a Forward Resistive Plate Chamber for time-of-flight measurements. The FD increases the HADES acceptance to low polar angles ($\theta < 7^\circ$), crucial for hyperon reconstruction [2]. New data on hyperon production was taken with the upgraded HADES spectrometer during February-March 2022. These measurements used a proton beam of 4.5 GeV kinetic energy impinging onto a fixed LH₂ target. Proton-proton elastic scattering is used for calibrating the FD and determining the integrated luminosity for the production run. In the event selection, one proton is detected in the FD ($3^\circ < \theta_{FD} < 6^\circ$) and it is combined with a proton measured in the main HADES acceptance ($70^\circ < \theta_H < 79^\circ$). The kinematic constraints of p-p elastic processes are discussed in [3]. The momentum p_{el} of a proton from an elastic scattering process is calculated with its reconstructed polar angle θ_H and the momentum of the incoming beam proton p_1 as:

$$p_{el} = \frac{p_1}{\cos\theta_H(1 + \tan^2\theta_H \times \gamma_{CM}^2)} \quad (1)$$

The selection criteria are: i) $173^\circ < \Delta\phi < 187^\circ$, ii) $|\tan\theta_H \times \tan\theta_{FD} - 0.29429| < 0.1$ and iii) $|\Delta p| = |p_{el} - p_H| < 500$ MeV/c. If multiple p-p elastic candidates are found within one event, the one with the smallest $\delta \sim \sqrt{\delta_{\Delta p}^2 + \delta_{\Delta\phi}^2 + \delta_{\tan\theta_H \times \tan\theta_{FD}}^2}$ is kept. The different δ factors are weighted according to the corresponding resolution. Figs. 1, 2 and 3, show the Δp , $\Delta\phi$ and $\tan\theta_H \times \tan\theta_{FD}$ distributions for simulation and data for the initial and final selections, together with the selection ranges and a fit to the signal distribution. The yield of elastic pairs N_{el} over the full beamtime period was determined from the

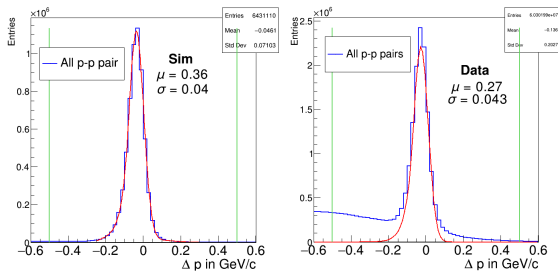


Figure 1: Δp distribution for simulation (left) and data (right). All p-p combinations are shown in blue and the signal in red. The green line shows the selection window.

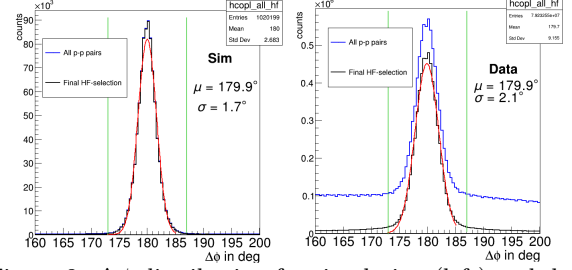


Figure 2: $\Delta\phi$ distribution for simulation (left) and data (right). All p-p combinations are shown in blue and the black histogram shows the final selection, fitted with a Gaussian. The selection range is shown in green.

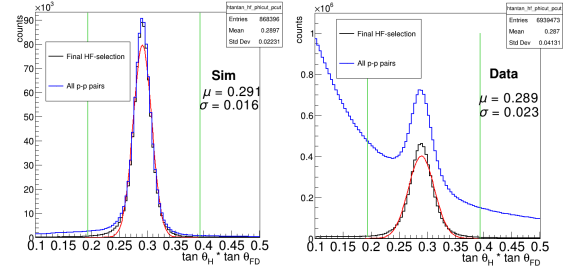


Figure 3: $\tan\theta_H \times \tan\theta_{FD}$ distribution for simulation (left) and data (right). All p-p combinations are shown in blue and the black histogram shows the final selection, fitted with a Gaussian. The selection range is shown in green.

$\Delta\phi$ distribution, and the integrated luminosity $\int \mathcal{L}$ is obtained as:

$$\int \mathcal{L} = \frac{N_{el} \times DS}{\sigma_{el} \times \epsilon_{sim}} \times \eta, \quad (2)$$

where $\sigma_{el} = 4.4^{+0.8}_{-0.3}$ mb is the elastic scattering cross-section in this angular range, that has been interpolated from other experiments, DS is a scaling factor defined for the trigger, ϵ_{sim} the reconstruction efficiency estimated from simulation, and η a correction factor accounting for the reconstruction in the FD, obtained by comparing the simulation and data [4]. With Eq. 2, the preliminary integrated luminosity of the beamtime is determined to (5.6 ± 0.4) pb⁻¹. Currently the effects of using a narrow selection range for Δp is being investigated.

References

- [1] The HADES Collaboration, G. Agakichiev, *et al.*, Eur. Phys. J. A **41**, 243–277 (2009).
- [2] J. Adamczewski-Musch, *et al.*, Eur. Phys. J. A, **21**, (2021) no 4, p. 1-21.
- [3] Anar Rustamov. Doctoral dissertation Technical University of Darmstadt, 2006.
- [4] J. Rieger, Presentation at the HADES XLIII HADES Collaboration Meeting, 2022.

Evaluating the Resolution of Track Candidates Reconstructed by a Language Model Based Track Finder

J. Kannika, T. Stockmanns and J. Ritman

Track finding is the process of identifying groups of hits that belong together. Each hit corresponds to a signal generated in the detector by a charged particle traversing that element of the detector. Many track-finding algorithms are based on intensive numerical calculations. In this work, we use a language model as a hit predictor for the next hit along a track based on the history of the previous hits. Figure 1 shows four Monte Carlo generated training samples containing a series of azimuthal angles connecting two consecutive hits in the track. The angles are recorded in the language model as the word history, and the last angles are recorded as the possible next word. The conditional probabilities of the next words are then calculated based on the number of samples that share the same word history. These sequences of discrete values with their probabilities are called a language model. The language model is used by taking the sequence of azimuthal angles measured in degrees connecting the previous hits in the track, the input used to predict the most probably next step. The example in Figure 1 is a simplified version of the track finding algorithm, in which 90 will be selected in Figure 2 as the next step to extend this track candidate.

Train a language model with the MC data:							prob.
sample #1	30	30	30	90	30	330	25%
sample #2	30	30	30	90	30	30	25%
sample #3	30	30	30	90	30	90	50%
sample #4	30	30	30	90	30	90	
	word history				next word (predicted)		

Predict real data using the language model:

30 30 30 90 30 X

Based on the history from the 4 training samples above the most likely value for X is 90.

Figure 1: Series of angles and probabilities are recorded as a language model, which is used to predict the most likely next step.

Previously, we showed evaluation parameters indicating that our algorithm was able to recognize tracks from the testing samples [1] but to check the qualities of the found tracks one also has to look into the track resolution. We performed track parametrizations to the reconstructed track in both the XY plane and the RZ plane, then compared the obtained results to the MC truth information. On the XY plane, we calculated track parameters ϕ_0 and transverse momentum p_t from the reconstructed

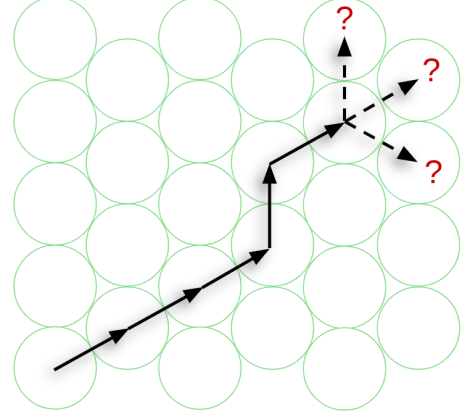


Figure 2: Sequences of angles calculated from positions detected by a straw-tube based detector.

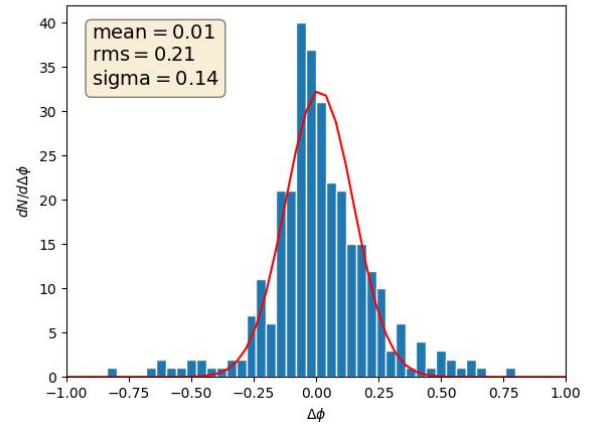


Figure 3: Distribution of the difference between the reconstructed ϕ_0 minus the MC truth value in degrees.

tracks, where ϕ_0 is the angle from the origin tangent to the trajectory of the particle, and p_t is the transverse momentum of the particle. The histogram in Figure 3 shows the distribution of the difference between ϕ_0 of the reconstructed track minus the MC truth value, and Figure 4 shows the distribution of the relative difference between the reconstructed p_t minus the corresponding MC truth value. In the Z direction, we calculated the dip-angle λ ($\lambda = 90^\circ - \theta$). Figure 5 shows the distribution of the difference between the reconstructed $\tan(\lambda)$ minus the corresponding MC truth value. These histograms in the XY plane and the RZ plane tell us that the track resolutions are satisfactory, and the tracking algorithm works as expected.

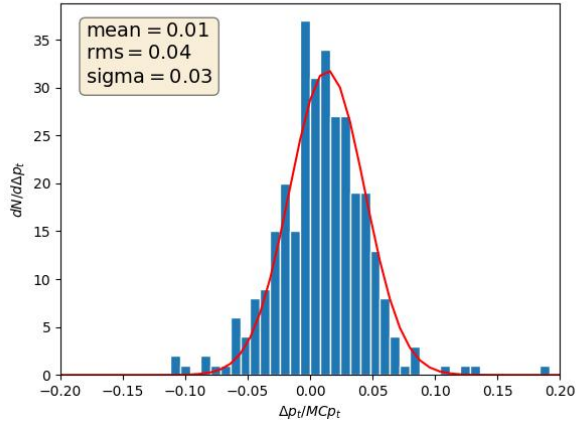


Figure 4: Distribution of the relative difference between the reconstructed p_t minus the MC truth value.

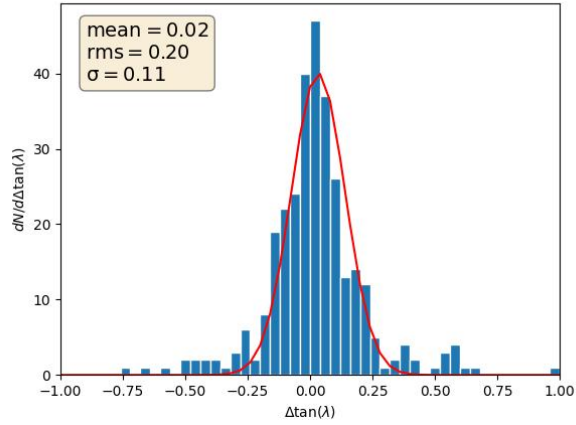


Figure 5: Distribution of the difference between the reconstructed $\tan(\lambda)$ minus the MC truth value.

We are now developing a branching algorithm to improve the efficiency of the tracking algorithm. To select the most probable track from the hit data, the branching algorithm does not only follow the most probable path at each step, but instead creates multiple track candidates that fit the patterns in the language model, then when there are no more hits to add to the track, a track selector chooses the best track candidate.

References

- [1] J.Ritman J.Kannika, T.Stockmanns. Track finding in hexagonal geometry using language models. In *Annual Report 2021*. Institute für Kernphysik/COSY, Forschungszentrum Jülich, 2022.

Acts tracking toolkit for PandaRoot

K. Suzuki, T. Stockmanns, J. Ritman¹

PandaRoot [1] is the official software framework of the PANDA collaboration. It has custom track finders and fitters and employs genfit2 [2] as a Kalman filter. The emphasis for our tracking is high accuracy also for low momentum tracks in an environment with low track multiplicities.

The reconstruction of the charged particle trajectories is one of the key computational challenges for nuclear and particle physics experiments. The increasing demands are associated with the increasing beam energy and hence an increasing number of charged particles, the higher luminosity and the trigger-less data acquisition system. Such a trend is expected to continue in the coming decades. The algorithms currently used by experiments share many common features, such as, track seeding, finding, fitting, and propagation as well as parallel computing using GPU/CPU and empowerment with Machine Learning.

Collaborative efforts are being made to develop tracking software that can be used for multiple experiments. This not only saves time and resources but also improves the overall quality and accuracy of tracking across multiple experiments. We, therefore, test the Acts, A Common Tracking Software [3], that is being offered to the community from the above concern, to integrate into our PandaRoot [1], or to be discarded.

Acts, A Common Tracking Software, is an open-source software framework. It was originally developed by the ATLAS collaboration at LHC, CERN, and its active development continues towards their upgrade to High-Luminosity LHC, which poses much higher computational challenges.

In an attempt to reduce computational overheads, Acts adopts a surface-based material mapping, that is to be compared with a volume-based mapping. In surface-based mapping, particle passage in a material is simplified to take place at a point, rather than along a line in the latter case so that the simulation code doesn't need to track individual particles inside a material volume and thus lower the computational overheads. Fig. 1 depicts this simplification. The detector material is modelled using a dedicated mapping algorithm that remaps the detailed Geant4 material. The surface-based approach also has an advantage for modelling detectors that have thin layers of material, such as micro-strip detectors.

Fig. 1 also shows a comparison of the mapped material with the material used in the full simulation geometry for the Open Data Detector. The geometry of the Open Data Detector is described with a realistic passive material model based on DD4hep, which translates into a Geant4 detector model. The

agreement between the material budget described in Geant4 and by the Acts geometry is within a few per cent. Further improvement can be obtained by adjusting binning granularity of the material maps and/or additional placement of material surfaces.

As we navigate the early phases of our project, we gain the impression that the software has a high potential, is well backed by a solid development team and will be actively maintained.

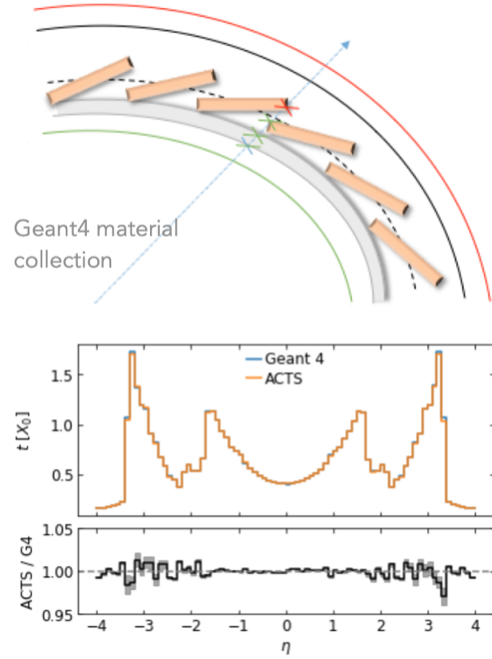


Figure 1: (top) An example of surface-based and volume-based material mapping. The green points are assigned to the current inner layer surface and the red to the next inner layer. (bottom) A comparison of the volume-based material mapping with Geant4 (blue) and the surface-based with Acts (orange). Radiation lengths are calculated as a function of η for the Open Data Pixel Detector (bottom-above) and compared (bottom-below). The agreement is within about 2% [3].

References

- [1] S. Spataro for the PANDA Collaboration, 2011 J. Phys.: Conf. Ser. 331 032031.
- [2] J. Rauch and T. Schlüter, arXiv:1410.3698 [physics.ins-det].
- [3] Xiacong Ai *et al.* A Common Tracking Software Project *Computing and Software for Big Science* (2022)6:8

Deep Learning for Particle Identification at HADES

Waleed Esmail

One of the main steps in all physics analysis at HADES is particle identification (PID). The main purpose of a PID algorithm is to provide a high purity sample of particle species needed by the analyzer to conduct the analysis. The conventional approach used in HADES is to apply the so-called “graphical cuts” around the theoretical Bethe-Bloch curves of the energy loss as a function of momentum. However, the distributions associated with the particle species begin to overlap at some point, and this approach becomes sub-optimal. An alternative and better approach is based on deep learning algorithms.

The neural network developed for this work has been trained to classify particle tracks into three classes or categories; protons p , kaons K^+ and pions π^+ . As a multi-class classification problem, the training data should be labeled, in other words, the network should be trained with simulated events. However, the simulations do not model real data perfectly. As a result, a neural network trained on simulation might not perform well on real data. To address this problem an architecture known as Domain Adversarial Neural Network (DANN) is trained simultaneously on real and simulated events in a semi-supervised way. The main idea behind DANN is to build a system composed of three neural networks. The goal of the *feature extraction network* is to map the original input into domain invariant features. Those features serve as an input to a *classifier network* that classifies the particle track given the domain invariant features. Additionally, the last model, known as *domain classifier*, enforces domain invariance of extracted features through adversarial training procedure. The training of the model is divided into two steps. First, on top of current features from the feature extraction network, the domain classifier is trained independently to classify domain labels whether data come from a real or a simulated events. Then, the domain classifier is frozen so that the particle classifier and the feature extractor can be trained jointly to predict accurate particle types while fouling the domain classifier at the same time. With this approach, the feature mapper’s weights are updated with a gradient from the particle classifier and reversed gradient from the domain classifier.

The training samples for the DANN consists of about 15 million events from 41 simulated channels and about 13 million real events. The number of events from each simulated channel is selected according to the estimated cross section at 4.5 GeV beam energy, while a random sample of real events is selected in such way that each day during the beamtime is

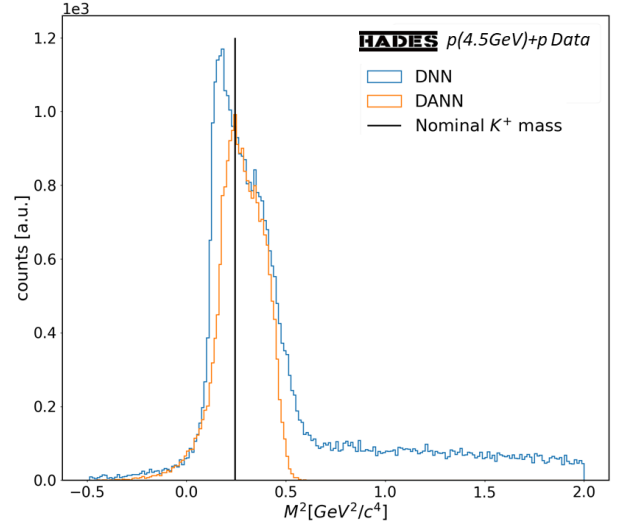


Figure 1: Distribution of the squared mass of the K^+ candidates as predicted by a simple neural network trained only on simulations (blue histogram) and a predicted by a DANN model trained both on simulations and real data (orange histogram).

equally represented in the sample. The input features are the momentum p , the polar angle θ , the azimuthal angle ϕ the energy loss dE/dx in the MDC system, the time-of-flight tof and the distance from the target to the tof hit.

The performance of the DANN is evaluated on a hold-out dataset from the target domain (real data). However, it is not possible to calculate the classification accuracy in this case since the target domain is unlabeled. Instead the squared mass observable (M^2) of the tracks is used to judge the performance of the network. The output layer of the *classifier network* consist of 3 nodes corresponding to the three particles species p , K^+ and π^+ . Fig. 1 shows an example of the DANN prediction for the K^+ node compared to a simple deep neural network (DNN) trained only on simulations using the same training features. As can be clearly seen there is a contamination from protons in the case of the DNN trained only on simulations. In addition, the DANN prediction of the K^+ mass peak is at the correct position, while the DNN prediction is biased and the peak location is shifted to the left.

In our preliminary studies with the $p(4.5\text{GeV})+p$ data, we were able to improve the separation power of the particle species. In the future, the proposed algorithm will be extended to include leptons.

A new method to polarize atoms, molecules, and their ions

C. S. Kannis^a, M. Büscher^{b,c}, R. Engels, N. Faatz^{a,d} and A. Lehrach^a

The polarization of nuclei and electrons in atomic, molecular, and ionic systems has many applications in a wide variety of scientific fields, such as physics, chemistry, and medicine. Various polarization techniques have been developed over the years, e.g., Stern-Gerlach spin-separation, spin exchange optical pumping, brute-force polarization, etc.

Recently, we studied a polarization method, introduced by P. G. Sona [1], for the BoB project [2], which investigates the neutron bound beta decay. Its concept is realized by a device, often called “Sona transition unit”, which provides a static magnetic field whose direction is reversed along the polarization axis. The particle beam moves through the device, so that its velocity is always parallel to the spin quantization axis. The reversal of the longitudinal component (B_z) produces a radial component $B_r = -\frac{r}{2} \frac{dB_z}{dz}$, where r is the radial distance from the z -axis. Employing a semi-classical approach, P. G. Sona derived the conditions for a successful “Sona transition”. For a beam with a defined velocity and size, the Sona conditions determine the limits of the magnetic field gradient. However, experiments with ground-state and metastable H atoms revealed an unexpected behavior.

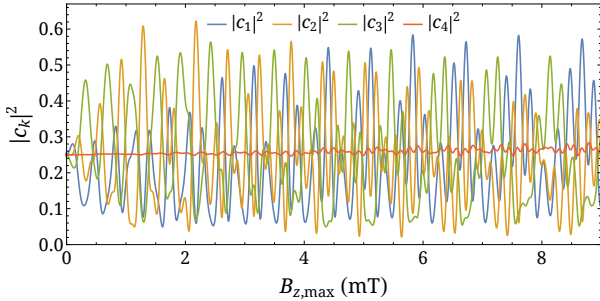


Figure 1: Probabilities of the hyperfine states of metastable H ($2S_{1/2}$) as a function of the maximum longitudinal field. The kinetic energy of the beam is 1 keV and its diameter is 1.5 cm. The probabilities are calculated at the exit point of the Sona unit for an initially unpolarized beam.

As shown in Ref. [3], the observed effect does not only depend on the gradient of the longitudinal component, but on the shape of the magnetic field in general. In particular, the radial field B_r induces transitions between the different energy levels that are associated with the atomic spin states. These transitions can be described by means of time-dependent perturbation theory applied in the rest frame of the beam [4]. A new coil for the Sona unit was developed with a longitudinal component equal to a single sine wave with respect to the z -axis. During some experimental runs, intrabeam collisions caused a partial

deexcitation of the initial state. Therefore, the numerical simulations were altered accordingly to describe this effect. Figure 1 shows the probabilities of the hyperfine states of metastable H for an initially unpolarized beam.

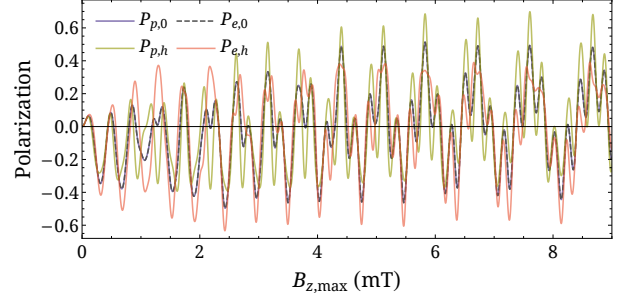


Figure 2: Nuclear (P_p) and electron (P_e) polarizations as a function of the maximum longitudinal field. The polarization values are evaluated at the zero (index 0) and high (index h) field limits.

The magnetic field in the device creates spin-polarization. This is clearly illustrated in Fig. 2, where the nuclear and electron polarizations are plotted at the zero and high field limits. The difference in the two limits is produced by the magnetic field dependent polarization of the mixed hyperfine states. Therefore, the proton and electron polarizations are equal in the zero field limit (only pure states contribute) and differ in the high field limit. The extreme values of polarization are $P_{(p,e),0} \sim \pm 50\%$ (at 5.8 mT and 2.4 mT, respectively), $P_{p,h} \sim 70\%$ (at 7.6 mT), $P_{p,h} \sim -40\%$ (at 1.6 mT), $P_{e,h} \sim 40\%$ (at 8.6 mT), and $P_{e,h} \sim -63\%$ (at 2.4 mT).

The described technique can produce spin-polarization in atoms, molecules, and ions. High values can be achieved for systems with simple hyperfine structure, i.e., low rotational levels of molecules or low atomic orbitals. Focusing the beam in a position with high B_r can further increase the maximum polarization.

References

- [1] P. G. Sona, *Energ. Nucl.* **14** (1967) 295.
- [2] J. Schön *et al.*, *AIP Conf. Proc.* **1441** (2012) 432.
- [3] R. Engels *et al.*, *Eur. Phys. J. D* **75** (2021) 257.
- [4] C. Kannis, PhD thesis (RWTH Aachen University, 2023).

^a III. Physikalisches Institut B, RWTH Aachen University, Germany

^b Peter Grünberg Institut, FZ Jülich, Germany

^c Laser and Plasma Physics Institute, HHU Düsseldorf, Germany

^d GSI Helmholtzzentrum für Schwerionenforschung, Germany

Actual Measurements with the Sona Transition Unit

L. Kunkel ^{a,b}, R. Engels ^a

Since P.G. Sona introduced a new method back in 1967 it got used to invert population of pure states [1]. Experiments have shown that in several cases oscillations can occur during the change of magnetic flux or the particle velocity. To explain the oscillations, the radial magnetic fields must act like photons for the moving particles. These photons can induce transitions which explain the oscillations at an odd multiple of the photon energy. To measure these transitions induced by the radial field component of the Sona magnetic field, a Lamb-shift polarimeter (LSP) in combination with a second spin filter is used [2]. After the LSP, there are only atoms in the ground state or an excited state present in the beam. They pass through a Sona region, where a standing magnetic wave emits photons with corresponding energy in the rest system of the atoms. The relative velocity of the photons in the inertial system of the atoms corresponds to the relative velocity of the atoms in the laboratory system. The atoms are excited by the photons and can carry out transitions between the states. In addition, the $\alpha 1$ - and the first β - state ($\beta 3$ for hydrogen and $\beta 4$ for deuterium) of the $2S_{1/2}$ orbit are exchanged at the zero crossing. The precession motion of the coupled nuclear and electron spins around the external magnetic field can not follow the rapid change in polarity of the magnetic field, resulting in a parallel spin alignment ($\alpha 1$) is transformed into an anti-parallel one ($\beta 3$) and vice versa. In a subsequent spin filter, the states can be filtered so that only atoms in one state remain in the beam. These excited atoms are transferred to the ground state in the quenching chamber by a static electric field. The produced Lyman-alpha photons represent the amount of excited atoms entering the quenching area. An example of such measurements where only atoms in the state $\alpha 1$ can pass the spinfilter is shown in Fig. 1. With this settings excited atoms can only reach the quenching chamber if they are in $\alpha 2$ before the Sona transition happens and afterwards go back to $\alpha 1$. Thus the shown signal requires two transitions, one before and one after the zero crossing. The small dips in the resonance signal of Fig. 1 are produced by losses of atoms in the state $\alpha 2$ due to the parallel transition into the state $\beta 3$. Important for the oscillations to occur is that the states are populated to different degrees. The LSP ideally generates a beam in which only atoms are present in the ground state and a selected excited state. Therefore, the imbalance between the occupation numbers of the states is greatest after the first spin filtering. When the ground state atoms collide with other particles, this can again result in excited states. Changing the initial population leads to strong changes in

the interference behavior. This is noticeable when the pressure upstream of the quenching chamber is increased. Under normal conditions, the increasing pressure reduces the number of excited atoms reaching the quench chamber due to the deexciting collisions. In the measurement shown in Fig. 2, this is not the case, since the signal amplitude increases. This could be due to a higher number of metastable atoms being created in the LSP. It is also possible that collision reactions between atoms in the ground state cause the amplitude to become stronger as new excited states are created. However, this cannot be determined from this measurement and therefore needs to be investigated further.

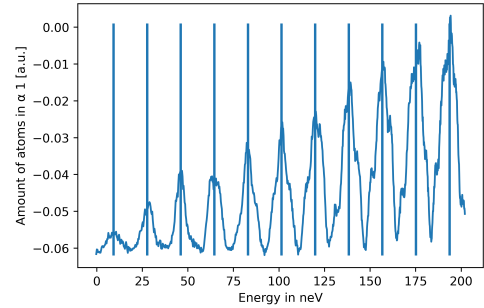


Figure 1: Relative occupation number of the hyperfine substate $\alpha 1$ as function of the energy difference between the states $\alpha 1$ and $\alpha 2$; the basic photon energy is 9.2 neV.

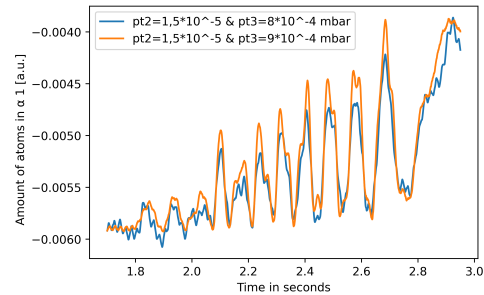


Figure 2: Signal of two measurements with same settings except the pressure near the quenching chamber.

References

- [1] P. G. Sona; *Energ. Nucl.* **14**, 295 (1967).
- [2] R. Engels et al.; *Eur. Phys. J D* **75**, 257 (2021).

^a Forschungszentrum Jülich GmbH, Institut für Kernphysik, Germany

^b FH Aachen Campus Jülich, Germany

Remote Control of the Lamb-Shift Polarimeter at the pulsed \vec{H}^-/\vec{D}^- Ion Source

S. Pütz^{a,b}, R. Engels^a, R. Gebel^a, K. Grigoryev^a, Y. Valdau^a

The polarized ion source produces a 2 keV pulsed beam of nuclear spin polarized H^- or D^- ions for stripping injection into the storage ring COSY. Before injection, the nuclear polarization needs to be determined and optimized. Usually, this was done with the Low Energy Polarimeter (LEP), which is based on the polarization dependent elastic scattering of protons on a carbon foil. Since this procedure requires a pre-accelerated beam of 45 MeV from the cyclotron JULIC, it is very energy and time consuming. Alternatively, the polarization measurement can be performed with a Lamb-shift Polarimeter (LSP) directly at the source. Typically, LSP measurements are performed with protons or deuterons but it was shown that measurements are also possible with H_2^+ , D_2^+ and HD^+ molecular ions [1, 2]. In 2020 it was shown that the nuclear polarization of H^- or D^- can be measured with an LSP. Figure 1 shows the

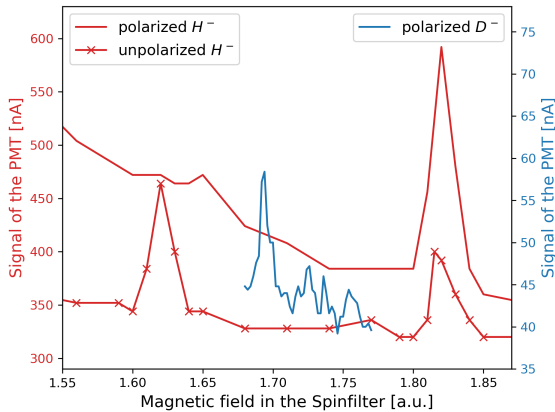


Figure 1: Spectra of H^- and D^- ion beams. Equal population of the two hyperfine substates with an equal nuclear spin is visible for the unpolarized H^- beam. For the polarized H^- beam the atoms with spin down dominate. The spectrum of the polarized D^- beam (blue line) shows that $m_s = +1$ dominates.

Lyman- α intensity of a polarized and unpolarized H^- and D^- ion beams. The signal-to-background ratio is about 1:3 and the background is dominated by residual ions. In addition, it is visible that the background is influenced by the longitudinal magnetic field in the spinfilter. Larger fields help to better focus the ions through the device so the background signal is reduced and less ions scatter with the walls in the spinfilter to produce light which is manipulating the photomultiplier signal. It is possible to calculate the nuclear polarization of these spectra, but poor statistics do not allow a good precision. To im-

prove this, a remote control of the measurement was installed that automatically ramps the longitudinal magnetic field of the spinfilter in certain steps and does the data readout in parallel. For the spectra

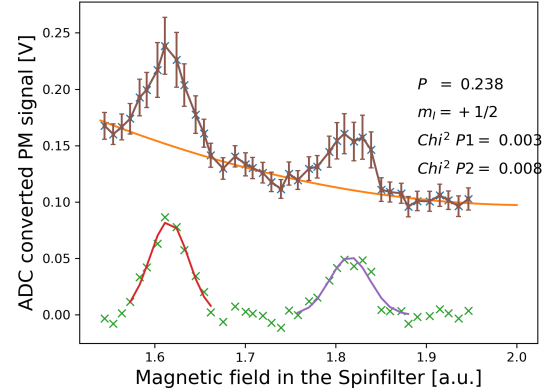


Figure 2: Lyman- α spectrum for positive polarization. The upper graph shows the averaged data whereas the lower graph shows the background-subtracted signal.

shown in figure 2, the new data taking method was used. The setup for this data acquisition consists of an additional computer with a software that runs a loop for the data taking and also stores the data. First, the start and end values of the magnetic field were manually specified, and with a certain step size, the software automatically ramps the magnetic field while recording multiple data points at each individual step (In this case 30 data points per step). This allows for better reproducibility and better statistics of the measurement. The current status of the measurement setup allows a relative tuning of the polarization. To improve statistics the temperature of the cesium cell of the LSP must be further optimized. Another open question that only further experiments can answer is the necessary magnetic field strength in the cesium cell to avoid polarization losses during the charge exchange into metastable atoms.

References

- [1] R. Engels *et al.*; Phys. Rev. Lett. **124** (2020) 113003.
- [2] R. Engels *et al.*; Phys. Rev. Lett. **115** (2015) 113007.

^a GSI Helmholtzzentrum für Schwerionenforschung, Planckstraße 1, 64291 Darmstadt, Germany

^b University of Cologne, Zùlpicher Straße 77, 50937 Cologne, Germany

Concept of a polarized $^3\text{He}^+$ ion source

N. Faatz^{a,b}, M. Büscher^{c,d}, R. Engels, O. Felden, R. Gebel^b, K. Grigoryev^b,
C. Kannis, A. Lehrach^{a,e}, S. Pütz^{b,f}, Y. Valdau^b, C. Zheng^c

Since a long time the study of polarized neutrons is a topic of great importance. A major challenge is that neutrons are difficult to handle as they are not or just very weakly influenced by external fields. For example, inside an accelerator or storage ring like COSY it is not possible to guide them. Therefore, the neutron study needs to be done indirectly through nuclei which have a configuration such that one neutron spin stays uncoupled from the others inside the core. The best example for this is the ^3He isotope. Here, the two protons are strongly coupled to each other due to the Pauli principal such that the neutron spin stays mostly free and can couple to external fields. This has been recently proven and measured with high precision in [1]. Subsequently, to study polarized neutrons it is necessary to be able to polarize the ^3He isotope and its ions in large numbers. At this point, a new method based on radio-frequency pumping with monochromatic and coherent single pulses comes into play. With this it is possible to polarize any kind of atoms and ions, as long as their states can be separated by the hyperfine splitting, when passing as a beam through the specific arrangement of static magnetic fields. The problem occurs in the detection of the polarization of the $^3\text{He}^+$ ions. One option is the asymmetrical elastic scattering of polarized $^3\text{He}^+$ ions on protons at about 100 MeV where the corresponding analysis powers are recently published [2]. With the cyclotron JULIC, the positive ions can be accelerated to the necessary energy and the existing low-energy polarimeter can be used to measure the nuclear polarization.

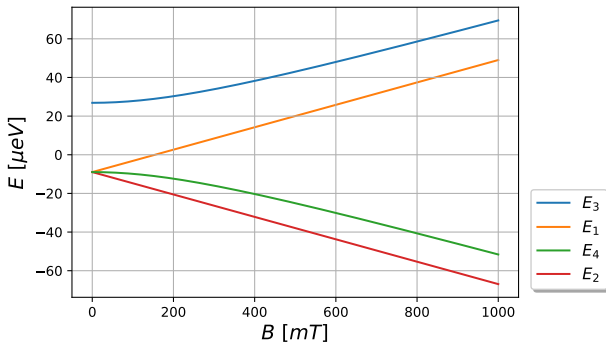


Figure 1: The Breit-Rabi diagram shows the energy dependence on the magnetic field of the four hyperfine states from the $1S_{1/2}$ ground state of the $^3\text{He}^+$ -ion.

Since the new method, based on a Sona transition unit, makes usage of the hyperfine splitting to produce polarization, the experiment needs to run for $^3\text{He}^+$ ions, which have such a splitting as illustrated

in Fig. 1. Before such an experiment can be conducted, some simulations need to be done. Therefore, using time dependent perturbation theory, the Schrödinger equation for the occupation numbers of the four hyperfine ground states of the $^3\text{He}^+$ ions is solved [3]. The result is shown in Fig. 2.

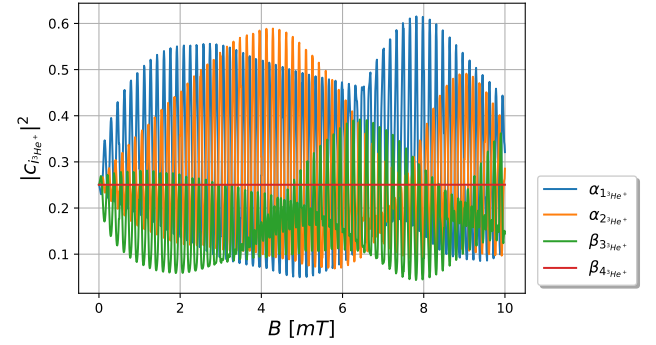


Figure 2: Probabilities to find the four different hyperfine states of the $^3\text{He}^+$ -ion $1S_{1/2}$ ground state for different magnetic field amplitudes applied onto the Sona unit.

The Sona system consists of two coils with opposite field direction to produce a stationary sinusoidal field in the beam direction. By ramping this external magnetic field transitions between the single hyperfine states appear, which are illustrated in Fig. 2. In this figure, the y -axis shows the probability to find the specific state at the end of the time of flight through the Sona unit as function of the applied magnetic field. As for the elastic scattering experiment only the nuclear spin is important, the states 4 and 1 have in a high field regime both nuclear spin aligned. Therefore, one can expect to have a polarization of about 85% for example at an applied field of $B = 8$ mT.

References

- [1] A. Schneider *et al.*, Nature **606** (2022) 878.
- [2] A. Watanabe, PhD thesis, springer thesis.
- [3] N. Faatz, Mastersthesi RWTH Aachen (2023).

^a III. Physikalisches Institut B, RWTH Aachen, Germany

^b GSI Helmholtzzentrum für Schwerionenforschung, Darmstadt, Germany

^c Peter Grünberg Institut, FZ Jülich, Germany

^d Laser and Plasma Physics Institute, HHU Düsseldorf, Germany

^e JARA-FAME, FZ Jülich, Germany

^f University of Cologne, Köln, Germany

Preparation of Storage Cell Tests for the Polarized Target at LHCb@CERN

T. El-Kordy^{a,b}, R. Engels^a, K. Grigoryev^a, M. Westphal^{a,b}

Currently, the Atomic Beam Source (ABS) of the former ANKE spectrometer at COSY is employed in combination with an interaction chamber and a Lamb Shift Polarimeter (LSP). The setup allows us to produce and measure polarized atoms and molecules. A storage cell, cooled down to 100 K inside the interaction chamber, can enhance or prevent the recombination process and the loss of polarization, depending on the inner surface coating.

At CERN, the LHCb experiment will use polarized gas targets. Thus, carbon coated storage cells have been proposed to prevent the target atoms from recombining and losing polarization. A 200 nm amorphous carbon coating was applied at CERN. The recombination rate and polarization preservation will be measured at the Nuclear Physics Institute (IKP) in Jülich. Hence, necessary preparations of the LSP had to be made. Specifically, the repair and reassembly of a spin filter had to be carried out. Additionally, an extension for the supportive frame of the LSP had to be constructed.

The dissociator of the ABS is able to dissociate the gas molecules being injected, before a Stern-Gerlach setup and following transition units bring the atoms into a desired hyperfine substate. When they enter the storage cell, wall collisions lead to recombinations and also to a loss of polarization. The ratio between the critical magnetic field B_c of the molecules and the external magnetic field B , applied over the storage cell, determines the loss of polarization after n wall collisions:

$$P_m(B) = P_{m_0} e^{-n(B_c/B)^2}$$

where P_{m_0} is the initial polarization, while $P_m(B)$ is the polarization after the wall collisions [1]. Prevention of recombination on the other hand, depend on the storage cell coating. Previous tests of carbon coated storage cells manufactured by IKP have shown a recombination rate between 80 and 90% [2]. It was thought that the recombination on the carbon surface might be facilitated by Lyman- α photons originating from the dissociator. Thus, a beam chopper was implemented into the ABS, enabling us to stop 80% of the radiation. However, no effect on the recombination rate could be observed. Estimates of the generated radiation energy lead us to the conclusion that an improved beam chopper is required to reach the threshold where the number of atoms exceeds the number of available photons in the storage cell.

We constructed an extension to the existing frame of the LSP. As can be seen in figure 1, this will enable us to add supplementary components to the current LSP setup.

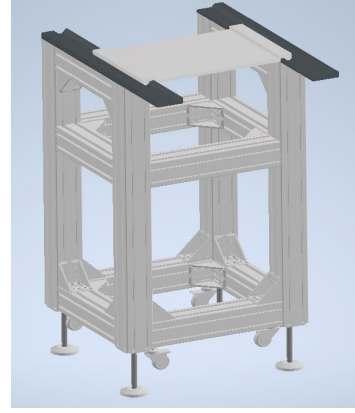


Figure 1: CAD model of the frame extension. The rack, consisting of aluminum profiles, holds two steel rails, which reach over the body on one side to connect to the main frame.

A spin filter uses several coils to build a homogeneous magnetic field inside of its cavity. Due to apparent non-uniformity in the magnetic field of the LSP spin filter, it was disassembled and four secondary coils were rewound. Measurements of the improved magnetic field B_z in longitudinal direction are shown in figure 2.

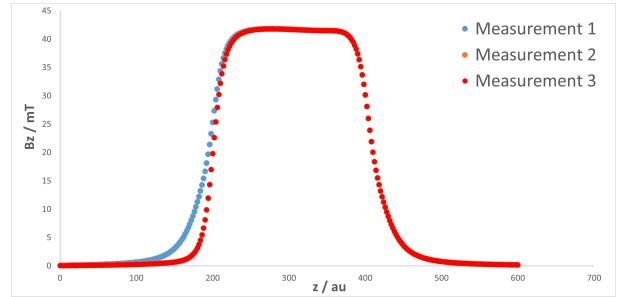


Figure 2: B-field of the LSP spin filter. During measurement 1 a single end coil was deactivated, throughout measurement 2 two coils were deactivated. All coils were active during measurement 3.

In March 2023 the storage cells coated at CERN should be delivered. They will be implemented into the interaction chamber to be tested together with an improved chopper inside the ABS. Following that, the setup may be used to study Sona transitions in H_2^+ , D_2^+ , HD^+ , or H_3^+ .

References

- [1] R. Engels *et al.*; Phys. Rev. Lett. **115** (2015) 113007.
- [2] O. Bilen; Master thesis at HHU Düsseldorf (2022).

^a GSI Helmholtzzentrum für Schwerionenforschung

^b FH Aachen - University of Applied Sciences

A Transition Unit for the Bound-Beta Decay Experiment

M. Westphal^{a,b}, R. Engels, N. Faatz^{a,c}, C. S. Kannis^c, B. Klimczok, A. Mandiwal^b,
M. Maubach^a, H. Soltner^d

For many experiments a separation of the hyperfine states (HFS) of hydrogen is needed. One possible device to do that is the spin filter, which is able to separate one of the two $2S_{1/2}$ α states. But unfortunately for experiments like the Bound-Beta-Decay (BoB), [1] experiment in Munich, a separation of the $2S_{1/2}$ β_3 state is needed. A new spin filter has been designed for this task, after the Sona transition unit [2] had been found inappropriate for it. This new filter features a rectangular cavity for the application of two different radio frequencies. In dependence of the magnetic field, these radio frequencies should couple three of the four $2S_{1/2}$ states weakly to the corresponding $2P_{1/2}$ states resulting in a deexcitation into the $2P_{1/2}$ states. Simultaneously, the fourth state is coupled strongly to the remaining $2P_{1/2}$ state, inducing an oscillation which allows this $2S_{1/2}$ state to survive. To ensure that this principle works, it was tested with one of the old spin filters by turning off the electric field. Unfortunately, the results showed a large background with very low population of both α states leading to a insufficient separation.

Therefore, a new idea was needed to separate metastable atoms in the HFS from the others. This should be solved with a new medium field transition unit similar to those used in the ANKE ABS [3] but for excited and not for ground state atoms. Those transition units consist of a magnetic gradient field and a magnetic holding field perpendicular to the beam axis and an induced radio frequency. With this concept incoming atoms in the $2S_{1/2}$ α states can be transitioned into the $2S_{1/2}$ β_3 state and vice versa.

For the case of the $2S_{1/2}$ α_1 state there is a photon transition first into the $2S_{1/2}$ α_2 state and then another one into the $2S_{1/2}$ β_3 state. The magnetic field provides the necessary energy splitting while the radio frequency delivers the energy to induce the transitions. This can be observed in Fig. 1. The gradient of the magnetic field ensures, that the en-

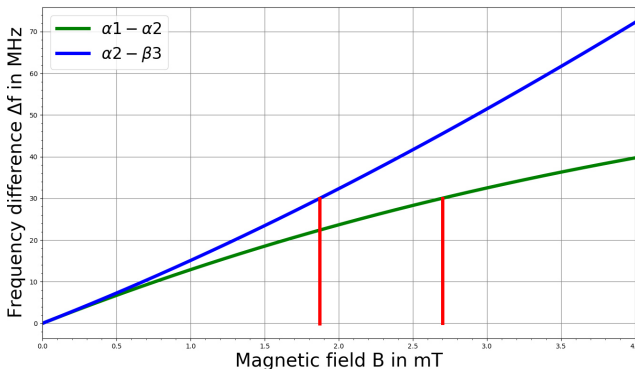


Figure 1: Energy differences between the HFS α_1 and α_2 as well as α_2 and β_3 .

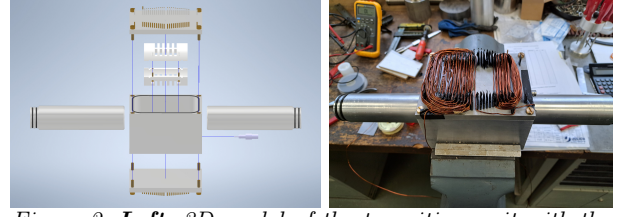


Figure 2: **Left:** 3D-model of the transition unit with the radio frequency coil holder (white) and the gradient coil holder on the top and bottom.

Right: Winding process of the magnetic gradient coil half embedded in epoxy glue.

ergy of the radio frequency matches the energy difference between the states only at one discrete point in the transition unit. This principle creates an environment where the atoms only change once, thereby preventing oscillations.

The transition unit was designed and built similar to the one at the ANKE ABS [3]. The design as well as the manufacturing process of the gradient coil are shown in Fig. 2. The achieved magnetic field of the gradient coil and the holding field as well as the combined field (Fig. 3) are as expected from the simulations. The next step is the test of the apparatus which will be done in beginning of 2023

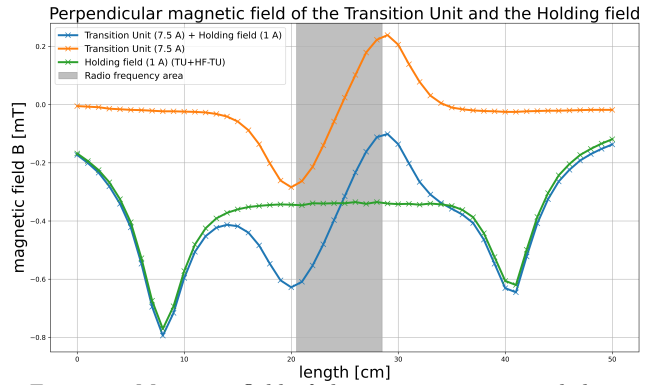


Figure 3: Magnetic field of the transition unit and the holding field along with the combined field.

References

- [1] J. McAndrew *et al.*, Hyperfine interact. **210** (2012) 3.
- [2] R. Engels *et al.*, Eur. Phys. J. D **75** (2021) 257.
- [3] S. Lorenz, PhD Thesis, Univ. Erlangen-Nürnberg, (1999).

^a GSI Helmholtzzentrum für Schwerionenforschung GmbH, Darmstadt, Germany.

^b FH Aachen University of Applied Sciences, Campus Jülich, Germany.

^c Rheinisch-Westfälische Technische Hochschule (RWTH), Aachen, Germany.

^d ZEA 2, Central Institute of Engineering, Electronics and Analytics, Research Center Jülich, Germany.

Precision Physics with a Sona Transition Unit

H. Sharma^{a,g}, R. Engels^g, C.S. Kannis^{b,g}, N. Faatz^{c,g}, S. Krieg^d, M. Büscher^{e,f}

At Forschungszentrum Jülich, an experimental set-up with the components of a Lamb-shift polarimeter and a Sona transition unit was used to study the effects of polarization in different kinds of ground-state and metastable sources (H, D). The basis of this work is the method proposed by P. G. Sona in 1967[1] to increase the nuclear polarization of polarized hydrogen and deuterium negative ion sources by applying a static magnetic field induced by two opposing coils. To produce this effect, the rotation of the quantized axis must be faster than the Larmor precession. Experimental realizations of Sona transitions showed oscillatory effects that were neither explained nor expected in Sona's original work. The observation of transitions between hyperfine substates of metastable hydrogen atoms in the metastable $^2S_{1/2}$ at the neV level using the Sona transition unit provided the foundation for measurements and tests of QED corrections in the $\Delta E/E \sim 10^{-4} \rightarrow \Delta E \sim 0.1$ peV energy regime.

A classical approach was committed to comprehend the effect using the photon model, but the interference of transitions between the $\alpha_1 \leftrightarrow \alpha_2$ and $\alpha_2 \leftrightarrow \beta_3$ substates limits this to uncertainty of $\Delta E/E \sim 10^{-2}$. In parallel, it is observed that the presence of even a small electric field leads to distortion of the spectral resonance peaks. Nevertheless, these disturbances are very sensitive to external parameters and can be used to advantage.

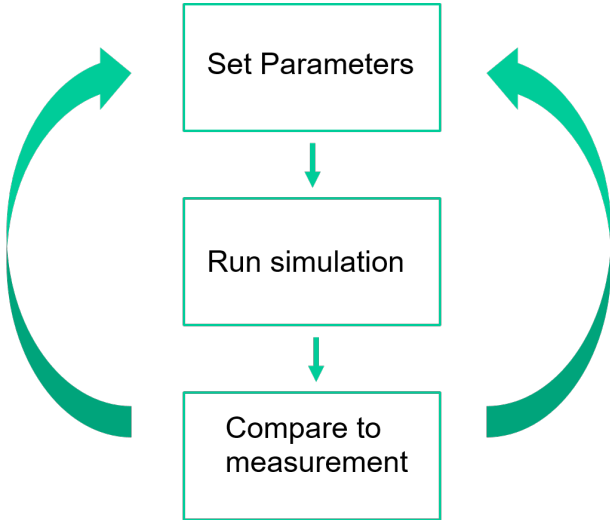


Figure 1: Flow chart for the Hartee-Fock Approximation Method.

In addition to experimental measurements, differential equations for the interaction of hyperfine structures with external magnetic fields are derived and

numerically analyzed. The quantum mechanical dynamics involved in these transitions are theorized by Schrödinger's first-order perturbation theory. The system is studied in the rest frame to focus on spin dynamics and avoid motion-related terminology.

The complexity of measuring initial conditions and obtaining spectra comparable to experimental values requires a Hartee-Fock like approximation method. In 1927 D.R. Hartee introduced a procedure commonly used to solve the time-independent Schrödinger equation for multi-electron atoms or molecules. Using this technique, various parameters defining the spin dynamics of metastable hydrogen atom such as the magnetic field ($B(r,t)$), the hyperfine splitting energy (A_{HFS}), the g-factor of bound the electron and the proton (g_e, g_p) can be determined. These parameters are variables of the Hamiltonian operator that describe the interaction of atoms with an external magnetic field. Due to the fact that the magnetic field does not change with the measurement, it may be necessary to allow the g-factor to be changed. The method steps include outlining a set of initial parameters and obtaining predictions from simulations. Additionally, the results can be compared to experimental measurements and the initial parameters can be manipulated until the desired configuration of the data is obtained. This method is expected to achieve QED correction of the g-factor and hyperfine splitting energy, but requires supercomputer power.

References

- [1] P. G. Sona, *Energ. Nucl.* **14**, 295 (1967).
- [2] R. Engels et al.; *Eur. Phys. J. D* **75**:257 (2021).
- [3] C. Kannis, PhD Thesis (2023).

^a FH University of Applied Sciences, Jülich, Germany

^b JARA-Fame and RWTH Aachen University, Aachen, Germany

^c RWTH Aachen University, Aachen, Germany

^d Jülich Supercomputer, Forschungszentrum Jülich, Jülich, Germany

^e Peter-Grünberg Institut, Forschungszentrum Jülich, Jülich, Germany

^f Heinrich-Heine University Düsseldorf, Düsseldorf, Germany

^g GSI Darmstadt, Darmstadt, Germany

Progress towards a direct measurement of the deuteron Electric Dipole Moment at COSY

A. Andres for the JEDI Collaboration

The Standard Model of elementary particle physics cannot explain the observed matter-antimatter asymmetry in the universe. Additional CP violating phenomena are needed to understand the matter-antimatter asymmetry. Permanent Electric Dipole Moments (EDM) of subatomic elementary particles violate both time reversal and parity asymmetries and therefore also violate CP if the CPT-theorem holds. This report covers the current progress of the analysis of the Precursor I (2018) & II (2021) experiments of measuring the deuteron EDM at COSY. The spin motion inside a storage ring can be characterized by the so-called invariant spin axis \vec{n} . It is defined by the rotation axis around which the radial component of the spin vector precesses. The number of spin rotations around the invariant spin axis per revolution around the accelerator is defined as the spin tune ν_s . The invariant spin axis is tilted in radial direction (\vec{n}_x) in the presence of a non-zero EDM inside an ideal storage ring. The goal of the experiment is to measure the direction of the invariant spin axis. However, magnetic misalignments lead to additional tilts in the longitudinal and radial directions. Therefore, the results need to be compared to a full simulation model of COSY in order to disentangle the true EDM signal from misalignments. In previous reports [1], methods to extract \vec{n}_x and \vec{n}_z using an rf Wien Filter were discussed. The results are summarized in Table 1. This report focuses on the determination of the longitudinal component of the invariant spin axis (\vec{n}_z) at the location of the two static solenoids (2MV Solenoid and Siberian Snake). By ramping the solenoids, the spins encounter an additional spin kick, which modifies the spin tune. The change of spin tune as a function of the 2MV Solenoid current (I_1) and Siberian Snake current (I_2) is given by [2]

$$\Delta\nu_s = \frac{1}{-\pi} \left[\cot(\pi\nu_s) \left(\cos\left(\frac{k_1 I_1}{2}\right) \cos\left(\frac{k_2 I_2}{2}\right) - 1 \right) - \vec{n}_{z,\text{sol}} \sin\left(\frac{k_1 I_1}{2}\right) \cos\left(\frac{k_2 I_2}{2}\right) - \vec{n}_{z,\text{snake}} \sin\left(\frac{k_2 I_2}{2}\right) \cos\left(\frac{k_1 I_1}{2}\right) - \frac{1}{\sin \pi\nu_s} \sin\left(\frac{k_1 I_1}{2}\right) \sin\left(\frac{k_2 I_2}{2}\right) \right], \quad (1)$$

where ν_s denotes the unperturbed spin tune. The longitudinal orientation of the invariant spin axis at the solenoids are given by $\vec{n}_{z,X}$. The calibration parameters k_1 and k_2 translate the applied solenoid current to a corresponding spin flip. The measured change of spin tune as a function of the solenoid cur-

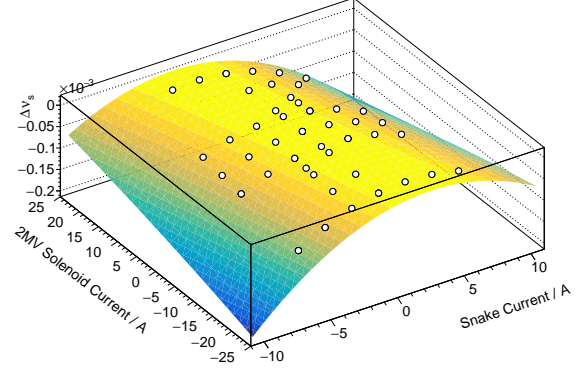


Figure 1: Fit to the change of spin tune $\Delta\nu_s$ as a function of the 2MV Solenoid (I_1) and Snake (I_2) current using Equation 1.

Table 1: Summary of experimental results.

Device	Obs.	Prec. 1	Prec. 2
rf WF	\vec{n}_x/mrad	-2.47(8)	-2.91(8)
	\vec{n}_z/mrad	4.46(8)	-5.22(8)
Sib. Snake	\vec{n}_z/mrad	0.54(5)	-0.0612(9)
2 MV Sol.	\vec{n}_z/mrad		-0.0585(5)

rents is shown in Figure 1. The results of the fit are given in Table 1. During Precursor 1, only the Siberian Snake was used. Therefore no result for $\vec{n}_{z,\text{sol}}$ is available. Current investigations focus on understanding the results. In an ideal world, the longitudinal component $\vec{n}_z = 0$ all along the ring. Alignment campaigns between the two experiments improved the results at the Siberian Snake by an order of magnitude. While the order of magnitude of \vec{n}_z at the 2MV Solenoid and the Siberian Snake is the same during Precursor 2, the corresponding value is two orders of magnitude larger at the rf Wien filter. From our understanding, this difference is not possible as the two devices are only nine meters apart. A possible solution is to check the beam direction inside the rf Wien filter, as the invariant spin axis is measured with respect to the magnetic field axis.

References

- [1] A. Andres, The Search for Electric Dipole Moments of Charged Particles in Storage Rings, 20th Conference on Flavor Physics and CP Violation, Oxford, MS, (2022).
- [2] A. Saleev, N. N. Nikolaev, F. Rathmann, Spin tune mapping as a novel tool to probe the spin dynamics in storage rings, Physical Review Accelerators and Beams, 20 (2017).

Analysis of the second precursor experiment

V. Shmakova on behalf of the JEDI collaboration

In 2020, the second precursor experiment for measuring the electric dipole moment of the deuteron was obtained at COSY. To utilize a new measurement method, fast RF switches were installed on the Wien filter (WF) [1]. These switches have the ability to turn the RF of the WF on and off for each of the two bunches in the ring. This way, one of the bunches in the ring can be shielded from the WF field and used to lock the phase with the feedback system, while the other bunch experiences the full field, and its asymmetry oscillation can be measured.

During the experiment, data for both vertical and horizontal asymmetries was collected and conducting simultaneous fit of both enables a more accurate analysis. The formalism that was used for the data fitting accounts for the effect of momentum spread in the bunch causes decoherence of the horizontal polarization, while it has no impact on the vertical one.

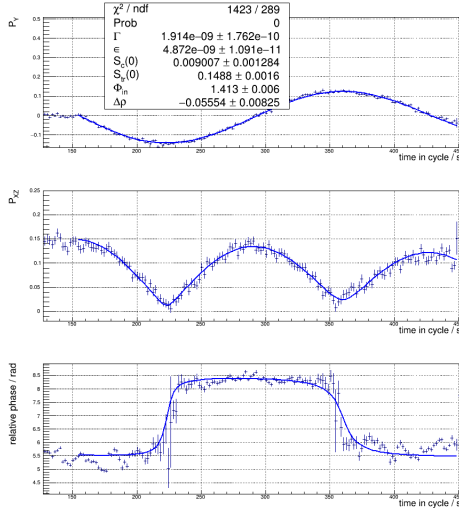


Figure 1: Combined fit for the vertical and in-plane polarization as well as the phase dependencies for run 6006, cycle 3. The $\Delta\rho$ parameter shows the distance from resonance. $\Delta\rho$ of -0.05 corresponds to deviation of around 0.2 mHz from resonance frequency.

It was also necessary to include the impact of detuning of the WF RF from its resonance frequency, as the phase locking was achieved using the pilot bunch and the spin tune of the signal bunch may differ. Fig.1 shows an example of the combined analysis performed for one cycle, which includes vertical and in-plane polarizations, as well as the phase. Having all three increases the accuracy of the fit results. It is particularly crucial to include phase dependencies for points on small angles of the WF and snake, as in these cases, a full rotation of polarization is not

observed during the cycle time, limiting the ability of a polarization fit alone. Fig.3 demonstrates the impact of excluding phases from the analysis. This results in large residuals near the minimum points in the fit of the resonance strength map.

Fig.2 demonstrates a scenario where detuning becomes visible. The $\Delta\rho$ parameter reflects the distance from resonance, with a value of zero representing the resonant condition. In this case the $\Delta\rho$ of 0.2 corresponds to approximately a 1.2 mHz off-resonance case. To maintain the quality of the analysis, detuning of this magnitude has to be taken into account.

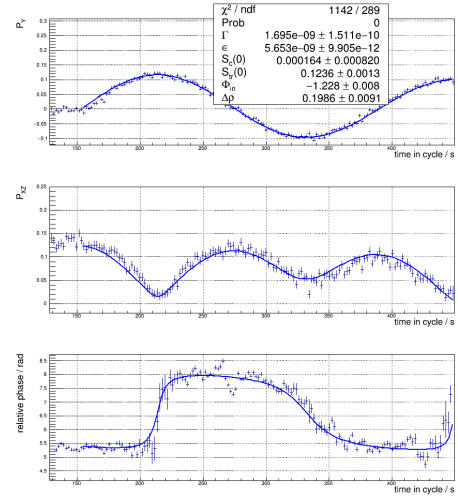


Figure 2: Combined fit for the vertical and in-plane polarization and the phase dependencies for run 6030, cycle 2. $\Delta\rho$ of 0.2 corresponds to deviation of around 1.2 mHz from resonance frequency.

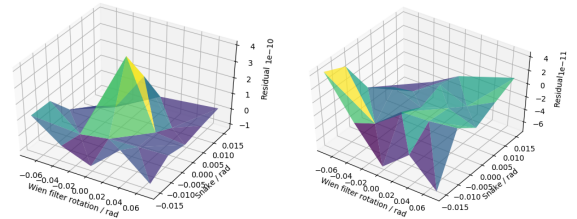


Figure 3: Residuals for the resonance strength maps. Left: phase dependencies were not included in the analysis. Right: Residuals after combined analysis including the phases.

References

- [1] A. Andres *et al.*, Proposal: First electric dipole moment measurement of the deuteron with the waveguide RF Wien Filter (2020)

Proton spin coherence time from March'22 measurement

S. Dymov for the JEDI collaboration

The strategic approach to the study of EDM in storage rings, developed by JEDI collaboration, involves measurement with an all-electric ring with counter-rotating proton beams. A long Spin Coherence Time (SCT) of the rotating or frozen beam spin is a necessary precondition for any such experiment. Prior to 2022, the JEDI experimental program was concentrated on optimization of the deuteron beam SCT. In these studies, the sextupole configurations minimizing the chromaticities in the horizontal and vertical planes were found to produce a long SCT ~ 1000 s. A first such measurement with the proton beam was undertaken during the COSY beam time of March 2022 [1].

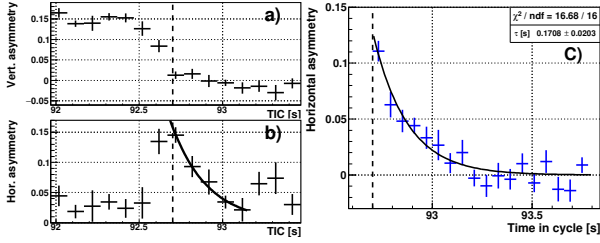


Figure 1: **a)** vertical, **b)** horizontal asymmetries for a single cycle. **c)** Common fit for run 6303.

In order to compare the experimental results for the protons and deuterons, the measurements started with the setting with the longest deuteron SCT achieved, i.e. with minimized dispersion in the straights and zero chromaticity. It was expected for the proton SCT to be small $\tau < 1$ s in these conditions. This was confirmed by the data, as shown in Figs. 1a), b), where the horizontal and vertical asymmetries are presented as functions of time in the cycle. The spin is completely rotated into the horizontal plane at $t = 92.7$ s and undergoes idle precession after that. The much shorter SCT value for protons is due to a higher anomalous moment compared to deuterons, as well as a greater number of intrinsic and imperfection spin resonances. This requires using substantially higher detector rates of $10^5 - 10^6$ /s in order to reach the sufficient statistical accuracy with finer time binning. It has been achieved with the JEPO LYSO crystal polarimeter [2] and a dedicated analysis.

The horizontal asymmetry shown in Fig. 1b) is obtained, as described in [3], in each time bin with a sine wave fit of an asymmetry distribution as a function of the spin phase, with the latter calculated from the recorded event time under a fixed spin tune value. A low statistics results in an increased systematic overestimation of the positively defined amplitude parameter, caused by the vicinity of its phys-

ical boundary of 0. One way to fight this effect, that was employed here, is to parameterize the phase offset dependence on time and fit the whole cycle data at once. The amplitude then becomes a signed parameter thus removing the cause of the effect. A more general approach based on Bayesian statistics was developed in [4].

In the case of limited statistics it is desirable to combine the data from several cycles collected under the same conditions. This can be done in a common minimization procedure with the relative phase offset for each cycle included as additional fit parameters. This way, the iterative spin correction described in [3] can be done coherently for all cycles. Fig. 1c) demonstrates results of such a combined fit for all cycles in run 6303.

The effect of the sextupole correction was studied by varying the MXS, MXG and MXL sextupole families settings. The scanning was done along the line of zero chromaticity as well as two MXG-MXS scans at fixed MXL values. The result of zero chromaticity scan is shown in Fig. 2 as a function of MXS. The fixed MXL scans, not shown here, also have not demonstrated any clear dependence. As it was expected from the simulation, the effect of the sextupole correction in the zero chromaticity region is much weaker for protons than the one observed for deuterons. To compensate the effects of intrinsic resonances, one probably needs to explore the large positive values of vertical chromaticity.

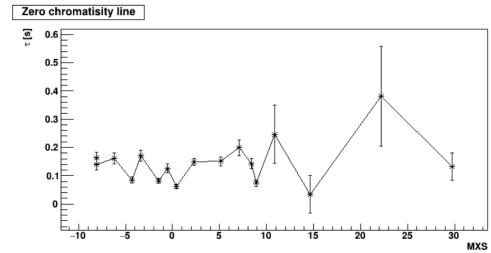


Figure 2: Proton SCT along the 0 chromaticity line.

References

- [1] Measurement and Optimization of the Spin Coherence Time for Protons in COSY. COSY CBAC proposal. July 15, 2021
- [2] F. Muller *et al.*. Journal of Instrumentation, 15(12), P12005 (2020).
- [3] D. Eversmann *et al.* Phys. Rev. Lett. 115, 094801 (2015).
- [4] D. Eversmann, J. Pretz, M. Rosenthal. Journal of Instrumentation, 11(5), P05003 (2016).

Optimization of the COSY Simulation Model Using Orbit Matching Algorithm in Bmad

M. Manerova on behalf of the JEDI Collaboration

This report presents the orbit matching algorithm used to optimize the simulation model of the COSY orbit as well as the results of its implementation.

Various systematic effects limit our ability to build a perfect accelerator, which therefore necessitates an implementation of an orbit correction system. To provide an orbit resembling the desired target orbit, additional dipoles are used to guide the beam in the vertical and horizontal directions. The orbit's response to these dipoles' influence is measured using beam position monitors (BPM). The connection between the changes in dipole magnet strengths, $\Delta\vec{k}$, and the motion of the beam particle at the BPM, $\Delta\vec{x}$, is established by the $m \times n$ -dimensional orbit response matrix (ORM) \mathbf{R} :

$$\Delta\vec{x} = \mathbf{R}\Delta\vec{k}, \quad (1)$$

Based on Equation (1), the magnet strengths $\Delta\vec{k}$ are calculated using the general formula:

$$\Delta\vec{k} = -\mathbf{R}^{-1}\Delta\vec{x}. \quad (2)$$

Since the number of BPMs at COSY does not match the number of corrector magnets, the inverse of the ORM is calculated via singular value decomposition. The magnet strengths \vec{k} are therefore expressed by

$$\Delta\vec{k} = \mathbf{V}\mathbf{S}^{-1}\mathbf{U}^T\Delta\vec{x}. \quad (3)$$

The orbit matching algorithm calculates the difference between the values of the target and simulated orbits, $\Delta\vec{x} = \vec{x}_{tar} - \vec{x}$, and magnet corrections $\Delta\vec{k}$ according to Equation (3). The corrections $\Delta\vec{k}$ stored after each iteration are added up to a final setting of a steerer magnet. The progress

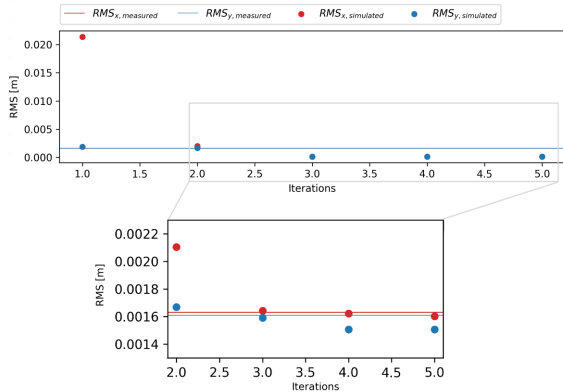


Figure 1: RMS values trend of the horizontal and vertical orbits after each iteration of the orbit matching algorithm.

is represented by the root mean square (RMS) trend of the closed orbits. The simulated orbits including the systematic effects do not correspond to the measured orbits. As seen in Figure 1 the RMS of the horizontal and vertical closed orbits differ strongly from the measurement and therefore both approach the desired values only after the 3rd iteration. The orbits obtained after three iterations, as well as the measured orbits for comparison, are displayed in Figure 2. The changed values of the

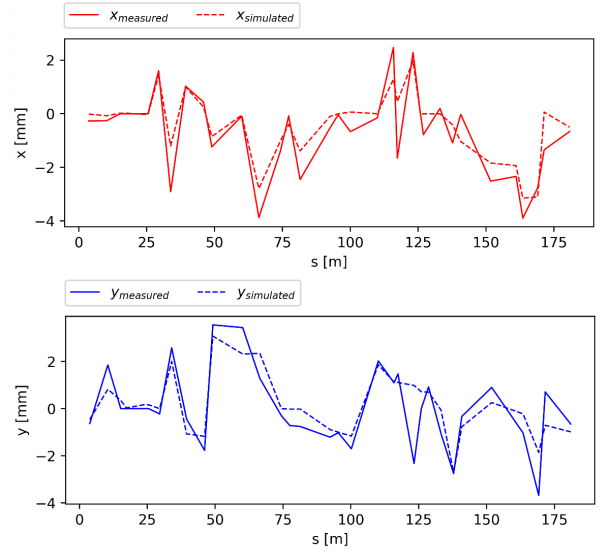


Figure 2: Results of the orbit matching procedure. The simulated horizontal and vertical orbits resemble the measured ones already after the 3rd iteration.

corrector magnets have a strong impact on the orbits, which allows the simulation to describe measured orbits significantly better. However, the adjusted steerer strengths do not eliminate the discrepancies between the orbits. In principle, a perfect match is not to be expected as this cannot be achieved with a different number of BPMs and steerers. Despite the success of the presented matching algorithm, there are various systematic effects neglected this time, which will improve the model accuracy and thereby help optimise the data analysis.

References

- [1] Hoffstaetter, G.H., Keil, J. and Xiao, A., *Orbit-response matrix analysis at HERA*, 8th European Particle Accelerator Conference, 2002.
- [2] W. Press, S. Teukolsky, W. Vetterling, and B. Flannery, *Numerical Recipes 3rd Edition: The Art of Scientific Computing*, Cambridge University Press, 2007.

SCT optimization and determination of the Invariant Spin Axis in a COSY model using Bmad

M. Vitz on behalf of the JEDI Collaboration

This report covers the optimization of the Spin Coherence Time (SCT) by minimizing the spin tune spread and the analysis of the impact of systematic effects on the Invariant Spin Axis (ISA) in a Bmad COSY model for deuterons. The lattice settings used for this investigation were directly obtained from the precursor 2 run performed in 2021.

Within the last year a routine was established, which is able to determine the sextupole settings, needed to minimize the spin tune spread. Adjusting the sextupoles to the determined settings results in very long SCTs as the spin rotation for a particle bunch gets coherent. This routine operates independent of the initial machine settings and can be used for any particle species. By giving initial offsets in every phase space coordinate and starting to variate the strengths of the three main sextupole groups in COSY (MXS, MXL, MXG), a system of linear equations can be derived and solved. The solution of the system of linear equation will reveal the sextupole settings needed for a coherent spin rotation and therefore long SCTs. This is shown in the equations below and figure 1.

$$\begin{aligned}\Delta\nu_{x,0} &= a_{mxs,x} \cdot k_{2,mxs} + a_{mxl,x} \cdot k_{2,mxl} + a_{mxg,x} \cdot k_{2,mxg} \\ \Delta\nu_{y,0} &= a_{mxs,y} \cdot k_{2,mxs} + a_{mxl,y} \cdot k_{2,mxl} + a_{mxg,y} \cdot k_{2,mxg} \\ \Delta\nu_{p,0} &= a_{mxs,p} \cdot k_{2,mxs} + a_{mxl,p} \cdot k_{2,mxl} + a_{mxg,p} \cdot k_{2,mxg}\end{aligned}$$

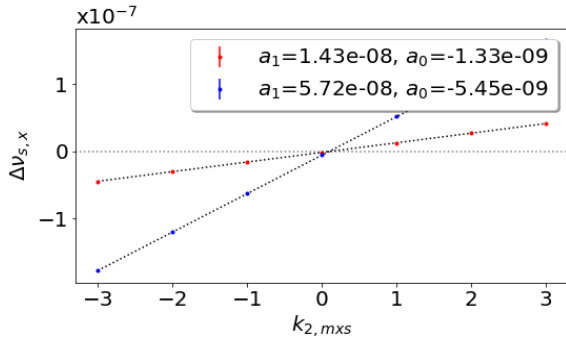


Figure 1: Sketch showing the typical impact of the sextupole group MXS on the spin tune spread $\Delta\nu_s$. In this case it assumes an initial radial offset of 1 mm (red graph) and 2 mm (blue graph) of the tracked particle.

Even though the algorithm optimizes the SCT successfully, the results do not coincide with the settings for long SCTs, achieved within the precursor run 2. There is evidence that fringe fields contribute significantly to the optimal settings and therefore

have to be implemented correctly for quadrupoles and dipoles. This is under further investigation. Another project, which was further developed within 2022, was the investigation of the ISA under the impact of systematic effects and the comparison with the data from precursor run 1 and 2. A direct implementation of all measured systematic effects in the simulation model revealed a tilt of the ISA by one order of magnitude less than the measured values in the radial and longitudinal direction. As it is very unlikely that this large deviation in the radial direction comes from an EDM, another way of explaining this tilt has to be found. Recently this was investigated by inspecting the distribution of the ISA under a set of Gaussian distributed quadrupole misalignments. The outcome of this approach is shown in figure 2.

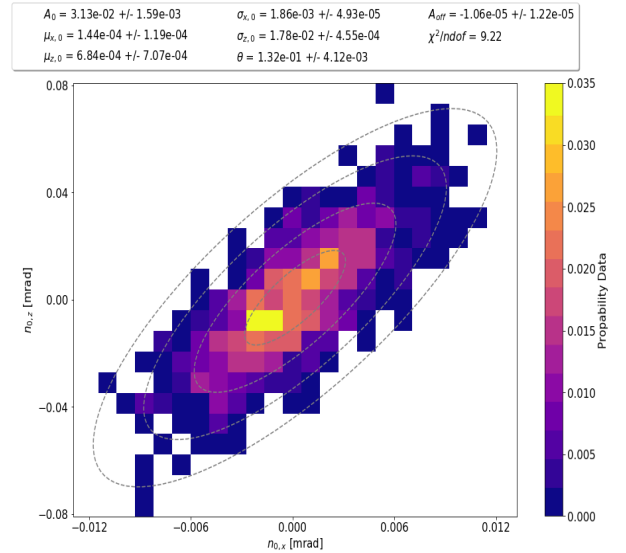


Figure 2: Distribution of the ISA (radial on the x-axis, long. on the y-axis) by assuming Gaussian distributed quadrupole offsets. A two-dimensional Gaussian fit was applied to the data and is indicated via the grey lines.

This approach is under further development since it gives a more detailed look on the possible tilt angles for the ISA and their probability. So far only shifted quadrupoles were considered. For a full picture of the distribution of the ISA under the effect of misalignments, also rotations of the quadrupoles as well as the shifts and rotations of the dipoles have to be considered. In addition, it is also necessary to have a look at other systematic effects. This should finally result in a similar plot as shown in figure 2, which indicates confidence levels with which the ISA is to be expected when performing a direct measurement of the ISA in COSY.

Optimization of spin coherence time of protons with BMAD

Daoning Gu on behalf of the JEDI Collaboration

In this report, a COSY model without misalignments or field errors is implemented in the software library Bmad. A method based on a fast Fourier transform (FFT) is used which removes the modulation of synchrotron oscillations to obtain accurate spin tunes and saves a lot of computing time. Three families of sextupoles (MXG, MXS, MXL) located in the arc section were varied to investigate the relationship between chromaticities and the spin coherence time (SCT).

Searches were performed using a scanning program together with spin tracking simulations to find a sextupoles setting where spin tune spread $\Delta\nu_s$ is minimal. The SCT has reached (7.009 ± 0.352) s.

In previous deuteron experiments, G. Guidoboni *et al.* suggested that $\Delta\nu_s$ has a linear relationship with the sextupole magnet currents (I_s , I_L and I_G) [3]. Assuming a similar dependency for the contribution of momentum deviation $\Delta p/p$, the $\Delta\nu_s$ can be written as [1] [2]:

$$\begin{aligned} \Delta\nu_s = & |A + a_1 I_s + a_2 I_L + a_3 I_G| \cdot \langle (\Delta x)^2 \rangle \\ & + |B + b_1 I_s + b_2 I_L + b_3 I_G| \cdot \langle (\Delta y)^2 \rangle \\ & + |C + c_1 I_s + c_2 I_L + c_3 I_G| \cdot \left(\frac{\Delta p}{p_0} \right)^2 \end{aligned} \quad (1)$$

here Δx and Δy represent the deviations in the horizontal and vertical directions. A and B are the chromaticities without sextupole correction. a_i and b_i denote the coefficients of the sextupole magnet currents, respectively.

In order to minimize the $\Delta\nu_s$ in all phase space coordinates, the linear system of equations for the coefficients can be solved by the spin tracking simulations. This leads to an optimized setup for the three sextupole families of COSY. One can use a Bmad program to adjust sextupoles to the desired value, simulations were performed for three separate beams with x, y and momentum offsets. Seven different values were chosen for each sextupole family, and the output data were analysed by linear fitting. The optimal normalized sextupole strengths obtained from the simulations are as follows:

$$\begin{aligned} k2_{mxs} &= 0.09701016 \text{ } 1/m^3 \\ k2_{mxl} &= 0.07542403 \text{ } 1/m^3 \\ k2_{mxg} &= 0.00589589 \text{ } 1/m^3. \end{aligned}$$

Using these settings, one can find that spin tune spread $\Delta\nu_s$ was suppressed to -6×10^{-12} . After a 12 million turns spin tracking simulation (see Figure 1), the total polarization remains above 0.9. For the ideal COSY lattice, the optimal sextupole settings

with the longest SCT of a proton beam was found. The results obtained by scanning and fitting methods are listed in Table 1.

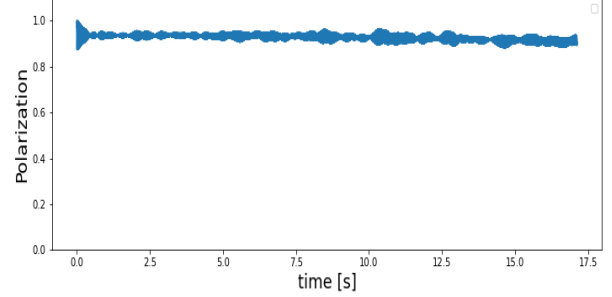


Figure 1: Spin coherence time for a polarized proton beam with optimal sextupole settings. The x-axis is the time and the y-axis is the total polarization.

Table 1: Spin tracking results of the optimization. The α_1 is the 2nd-order momentum compaction factor. ξ_x and ξ_y refer to the horizontal and vertical chromaticities, respectively.

	α_1	ξ_x	ξ_y	SCT(s)
Scan	0.005	-3.8676	-5.2498	7.009 ± 0.352
Fitting	0.016	-3.7187	-5.1487	> 17

The values of chromaticity are very close to those obtained earlier using the scanning method, both being negative. It is known that if all chromaticities are zero, there would be zero contribution from orbit-lengthening caused by betatron motion. One possible explanation is due to the ideal model we used. Recent studies using different software have suggested that the optimal settings will coincide with the zero chromaticities when the fringe fields are taken into account, which requires further simulations with Bmad to cross-check. In addition, the simulations show that the SCT is very sensitive to the beam parameters. This raises the requirement for a more accurate manipulation of chromaticity in future real experiments, and it is also very challenging to perform measurements for the 2nd-order momentum compaction factor α_1 .

References

- [1] M. Rosenthal. PhD thesis, RWTH Aachen University, 2016.
- [2] M. Vitz. Private Communication. Forschungszentrum Jülich, 2022.
- [3] G. Guidoboni *et al.*, Phys. Rev. Accelerators and Beams 22 (2018) 024201.

Optimization of Spin Coherence Time at the Prototype Storage Ring

Rahul Shankar, on behalf of the JEDI collaboration

In this report, the recent progress in the optimization of spin coherence time in simulations at the prototype storage ring is discussed. These simulations were conducted on a proton beam of mean momentum of 294 MeV, in frozen-spin mode. In this mode the spin coherence time τ is given by the solution of $|\vec{P}(\tau)| = \frac{1}{e}$, where...

$$\vec{P}(t) = \frac{1}{n} \sum_{i=1}^n \hat{s}_i(t) \quad (1)$$

...and $|\vec{P}(0)| = 1$ by definition. Thus, the decoherence can be observed by tracking the magnitude of the polarisation vector $\vec{P}(t)$.

The horizontal spin tune spread $\Delta\theta_x(t)$ defined as the angle of deviation of the polarisation vector at time t from its initial direction $\vec{P}(0)$, is also tracked in each simulation. Its rate of change gives the error in the spin tune $\Delta\nu_s$, since in frozen-spin mode, the spin tune $\nu_s = 0$ by definition.

To optimize the SCT, at fixed quadrupole settings, these quantities were measured at various values of the second order optical settings ξ_x (horizontal chromaticity), ξ_y (vertical chromaticity), and α_1 (second order momentum compaction factor), which are linearly determined by the field strengths of the three available sextupole families.

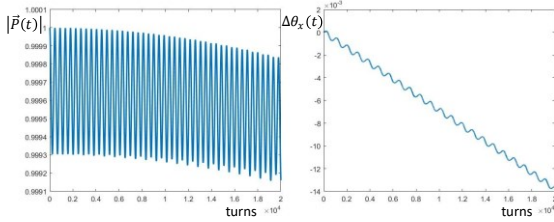


Figure 1: (left) A plot showing the decoherence of 1000 particles as a function of number of turns. (right) A plot showing the spin tune spread of the polarisation vector measured simultaneously.

The SCT was measured by fitting the gradual downtrend of the data in Figure 1 (left) and using the expression to solve $|\vec{P}(\tau)| = \frac{1}{e}$. It was observed that for the prototype ring, the variation of $1/\tau^2$ across the space of the second order optical settings follows the distribution of a three-dimensional paraboloid, specifically a family of concentric ellipsoids. This was also confirmed by fitting data points lying on a single plane with a two-dimensional paraboloid representing a family of concentric ellipses as shown in Figure 2 (a).

The variation of the momentum offset δ of the particles due to the longitudinal synchrotron oscillations manifest as vibrations in the magnitude of the polarisation vector seen in Figure 1 (left). The effect of path lengthening on the other hand manifests as vibrations in the directional shift of the polarisation vector, seen in Figure 1 (right). This path lengthening was modelled by [1] and [2] as:

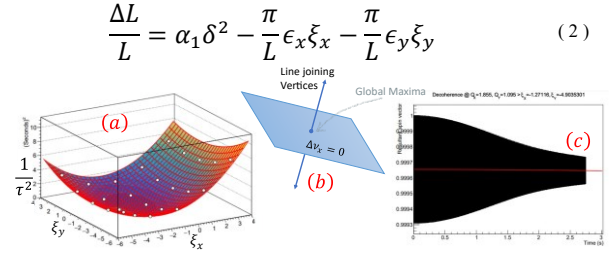


Figure 2: (a) Inverse-square of spin-coherence time almost exactly varies as a 2D paraboloid (or a family of concentric ellipses). The vertex of the paraboloid represents the optimized field setting in the chosen 2D slice. (b) A diagram showing a possible method to estimate the SCT maxima as the intersection point between the $\Delta\nu_s = 0$ plane and the line joining the vertices of many 2D paraboloid fits. (c) A decoherence plot of the polarisation vector measured at the optimized point, showing almost no decoherence.

When measured across the parameter space by tracking the amplitude of the vibrations, the path lengthening varies according to a plane, confirming the validity of the model on the prototype ring. Interestingly, the spin-tune error $\Delta\nu_s$ was also observed to vary as a plane parallel to the one representing path lengthening. Thus, a rough model of the spin tune error can be surmised as:

$$\Delta\nu_s = A\delta + B\delta^2 + C\left(\frac{\Delta L}{L}\right) \quad (3)$$

Here, $A\delta + B\delta^2$ is the “default” spin tune error at the origin ($\xi_x = 0$, $\xi_y = 0$, $\alpha_1 = 0$), and A and B are constants which depend solely on the Lorentz factor γ , and the G -factor of the proton. The set of all points with $\Delta\nu_s = 0$ thus forms a plane in this space, which represents the second order optical configurations where the path-lengthening effect cancels out the original spin tune error. From the fits of the SCT of all data points, it was observed that the point with highest SCT always lies on the plane $\Delta\nu_s = 0$. Thus, while optimizing a large set of quadrupole settings, this fact was used to narrow down the optimization.

Using this optimization method, several points with SCT above 1000 s, like Figure 2 (c), were found, which enables the target precision for the EDM experiment as discussed in the feasibility study [3].

References

- [1] Yoshihiko Shoji, “Dependence of average path length betatron motion in a storage ring,” *Physical Review Special Topics - Accelerators and Beams*, vol. 8, p. 094001, 2005.
- [2] Marcel Stephan Rosenthal, “Experimental Benchmarking of Spin Tracking Algorithms for Electric Dipole Moment Searches at the Cooler Synchrotron COSY,” PhD Thesis, RWTH Aachen University, Aachen, 2016.
- [3] CPEDM Collaboration, “Storage ring to search for electric dipole moments for charged particles: Feasibility study,” CERN Yellow Reports: Monographs, Geneva, 2021.

Study of Beam dynamics of a Prototype Electric Dipole Moment Storage Ring

S.Siddique for the JEDI and CPEDM Collaboration

This report covers beam simulations of a prototype EDM storage ring for proton with $T = 30$ MeV. Four different lattices with different focusing strengths ($\beta_y[m] = 33, 100, 200, 300$) were generated by MADX and studied in the context of beam losses. The objective of these calculations is to find an optimized lattice with minimum systematic effects and maximum beam lifetime. Initially, four major effects which cause immediate beam loss in a storage ring named Hadronic interactions, Coulomb scatterings, Energy loss straggling, and Touschek effect, were studied and applied analytically.

After getting results from rough analytical formulas which were performed by using Wolfram Mathematica, another software BetaCool was used to perform beam loss calculations. BetaCool is used because it enables a more realistic description of the storage ring. A very good agreement between analytical calculations and Betacool results was observed, which can be seen in figure 1.

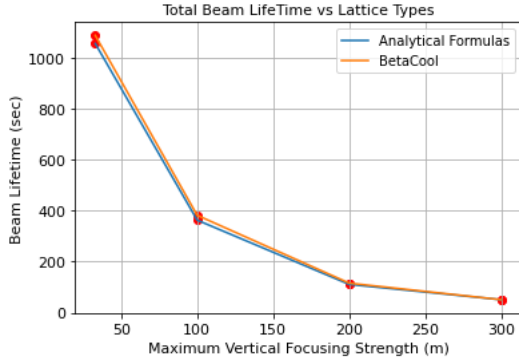


Figure 1: This plot shows a comparison of analytical formulas and BetaCool results in the form of beam lifetime vs lattice types (in terms of their maximum vertical focusing strength β_{y-max}).

These calculations show that a lattice with a vertical focusing strength $\beta_y - max < 100$ m is considerable to store the beam for a longer time however, further optimization is required[1]. Besides, there are some other effects that contribute slowly to beam blow-up i.e. emittance growth due to intra-beam collisions and multiple Coulomb scatterings with residual gas and with the target material. These calculations were performed by using BetaCool, which showed that intra-beam collisions and multiple Coulomb scatterings with residual gas are satisfactory and do not significantly influence beam losses because of very small emittance growth rate. This behavior can be seen for the lattice with $\beta_{y-max} = 33m$ with only residual gas and intra-beam collisions. The horizontal and vertical emittance growth can both be seen within the same figure 2.

Next, a carbon pellet with a diameter of $30\mu m$ is also introduced in the beam to scatter it toward the p404

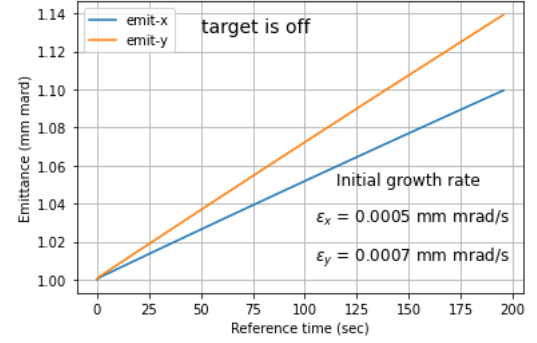


Figure 2: Emittance growth for a lattice with $\beta_{y-max} = 33$ m vs time and without target inclusion: Horizontal and Vertical emittance growth rates (ϵ_x, ϵ_y) are also shown within the plot.

larimeter for beam polarization measurements. One pellet traverses the beam at any one time and it causes a massive beam blow-up due to the high target density, which can be seen below in figure 3.

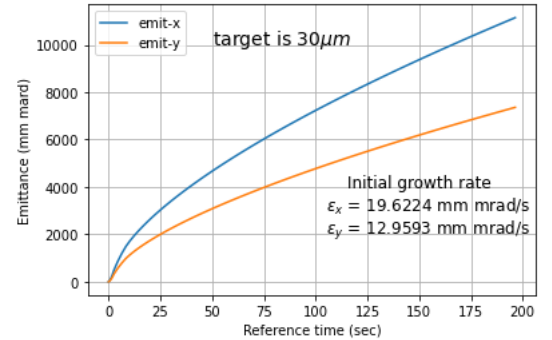


Figure 3: Emittance growth for a lattice of $\beta_{y-max} = 33$ m vs time. The beam also interacts with a target of diameter $30\mu m$: Horizontal and Vertical emittance growth rates (ϵ_x, ϵ_y) are shown within a carbon target plot.

In conclusion, Beam-Target interaction causes significantly more beam loss and a higher beam emittance growth rate. As the beam passes through the target, not all particles suffer the same interaction with the target. This inhomogeneous influence on the beam by the target scatters the beam particles to different angles and momentum. Therefore, the purpose of extracting the beam at a specific angle needs a deeper study of this interaction. For this purpose, beam tracking is being performed including the interaction with the target.

References

- [1] CERN Yellow Reports, *Storage ring to search for electric dipole moments of charged particles: Feasibility study*, 2021.

Measurement of second-order momentum compaction factor at COSY

A. Saleev for the JEDI Collaboration

Suppressing the decoherence of spins in the bunch of particles to increase polarization lifetime is an important milestone towards the measurement of the proton EDM in an all-electric storage ring. Decoherence reduces the available observation time for the polarization build-up as an EDM signature. To study the polarization lifetime at the all-magnetic ring COSY, the JEDI Collaboration developed a special method [1]. After injection and acceleration of the beam, the originally vertical polarization is rotated to the horizontal plane by means of a resonant RF solenoid. The survival of the in-plane polarization depends on the spin tune spread. The conditions under which the spin tune spread is minimized lead to the same rate of spin phase accumulation for all particles (and thus the lifetime of polarization is longest). For deuterons, the results with the longest in-plane polarization lifetime were obtained when both the vertical and horizontal chromaticities vanish [2].

In theory, correcting the chromaticities and second-order momentum compaction factor reduces the increase of the path length for particles that do not have the same momentum as the reference particle [3]. This effectively brings all particles to the same orbital length and spin tune. To suppress the spin-tune spread, three families of chromatic sextupoles are used. The influence of the sextupoles on the chromaticity and connection to the polarization lifetime was studied with deuterons [2], but the role of the second-order momentum compaction factor remained unclear. The available method to measure the momentum compaction factor by ramping the dipole field did not allow to probe the second-order effects, because the beam was lost when the required momentum offset (via B-jump) pushed the coasting beam out of the COSY acceptance.

In the JEDI beamtime in Spring 2022 that was dedicated to optimization of spin coherence time of proton beam, we applied a new method to measure

the second-order momentum compaction factor, α_1 . The method was originally developed for synchrotron light sources [4] and was implemented for the first time ever at COSY to measure α_1 . However, it became possible thanks to the recent upgrades at COSY Control System [5], such as Schottky diagnostics, which allowed to measure the slip factor precisely by observing the synchrotron side bands. The dependence of the synchrotron tune Q_s on the slip factor η is given by:

$$Q_s = \sqrt{\frac{heU}{2\pi p L f} |\eta_0 \cos \phi_s|}, \quad (1)$$

where $\eta \rightarrow \eta_0 = \alpha_0 - 1/\gamma^2$.

If the cavity voltage U is ramped it will shift the synchrotron sidebands that we can observe near the beam revolution frequency with the Schottky pickup. This allows to determine η_0 after one beam storage cycle by relating the frequency of the sideband and the time duration of the voltage ramp-up as $\propto \sqrt{U}$. We assume synchronous reference particle $\phi_s = 0$, however the bunch was excited longitudinally by overlapping the electron cooling and the bunching processes. This increased the amplitudes of the Schottky signals making them prominent over the noise. The timing at the experimental flattop of the cycle is shown in Fig. 1, where the voltage ramp takes $\Delta t = 70$ seconds, and on the measured Schottky spectrum (Fig. 2), it starts at the “15:11:40” time mark.

Right before the start of the voltage ramp on Figs. 1 and 2, the frequency jump takes place. It brings the beam to another momentum,

$$\frac{\Delta p}{p} = \frac{1}{\eta_0} \frac{\Delta f}{f} \quad (2)$$

We explored dependence of the synchrotron tune on higher orders of momentum compaction. Effectively, Q_s is modified by Δf , α_1 through the slip factor $\eta \rightarrow \eta_s$ as

$$\eta_s(\Delta f, \alpha_1) = |\eta_0| + (\alpha_0 - \frac{2}{\eta_0}(\alpha_1 - \frac{\eta_0}{\gamma^2} + \frac{3\beta^2}{2\gamma^2})) \frac{\Delta f}{f}. \quad (3)$$

The COSY lattice model predicts linear dependence of α_1 on the MXG sextupoles field strength. Therefore, several measurements of η_s were done with variation of MXG sextupoles strength s_{MXG} and Δf -jumps.

Fig. 3 shows a fit of the deduced η_s -factors with Eq. 3 to determine the value of α_1 . At $s_{MXG} = 0$ %, as predicted by global fit to all points, $\alpha_1 = 3.98 \pm 0.51$. At $s_{MXG} = 5.29 \pm 0.57$ %, for any off-momentum particle, $\eta_s(\Delta f, \alpha_1) = \eta_0$. The synchrotron tune does not

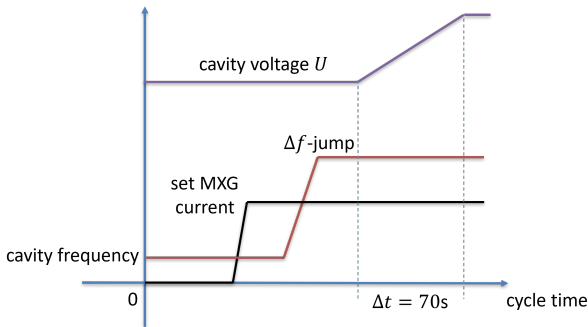


Figure 1: Timing at the flattop of the experiment cycle.

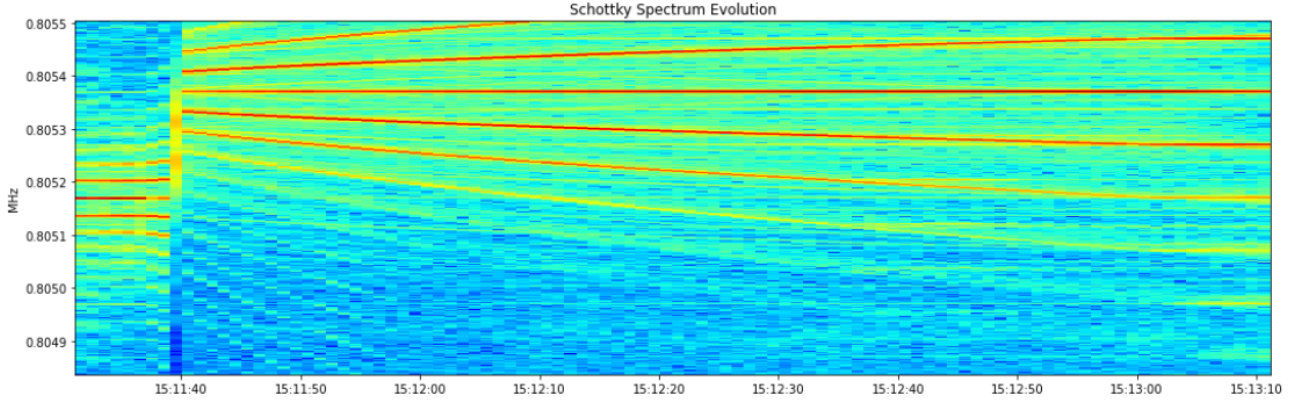


Figure 2: Schottky measurement. Note the frequency jump at the beginning, at “15:11:40”, and the spread of the sidebands towards the end of cycle, at “15:13:10”.

depend on the momentum in this case - correction of “longitudinal chromaticity” was achieved.

References

- [1] Eversmann, D., *et al.*: New method for a continuous determination of the spin tune in storage rings and implications for precision experiments. *Phys. Rev. Lett.* **115**, 094801 (2015).
- [2] Guidoboni, G., *et al.*: Connection between zero chromaticity and long in-plane polarization lifetime in a magnetic storage ring. *Phys. Rev. Accel. Beams* **21**, 024201 (2018).
- [3] Senichev, Yu., *et al.*: Spin tune decoherence effects in electro- and magnetostatic structures. Proceedings of IPAC2013, Shanghai, China. <https://accelconf.web.cern.ch/ipac2013/papers/wepea036.pdf>
- [4] Nadji, A.: Quasi-isochronous experiments with the Super-ACO storage ring, *Nucl. Inst. Meth.* **A378**, 376 (1996).
- [5] Control System Upgrade, In: Accelerator Research, Annual Report 2019, Institut für Kernphysik COSY, Jülich, 2019 https://www.fz-juelich.de/en/ikp/downloads/annual_report_2019
- [6] Ng, K.Y.: Momentum compaction and phase slip factor. <https://lss.fnal.gov/archive/test-fn/0000/fermilab-fn-0900-apc.pdf>

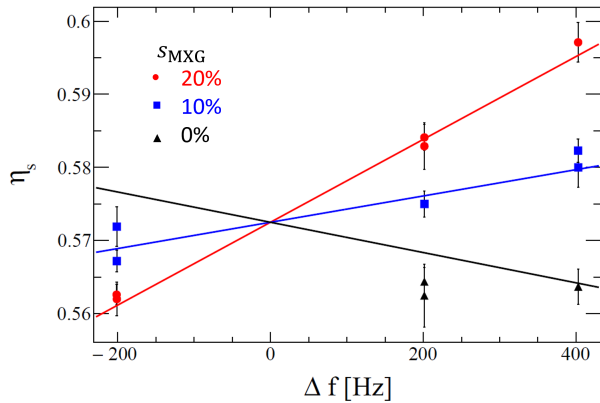


Figure 3: Fit of the measured $\eta_s(\Delta f, \alpha_1)$ with Eq. 3. The color code represents three settings of the MXG sextupoles.

Rogowski Beam Position Monitor – Signal-to-Noise Ratio Investigation

R. Suvarna on behalf of the JEDI Collaboration

This report summarizes the work undertaken on the Rogowski Beam Position Monitor (BPM) system in 2022. A systematic study of the noise profile of the Rogowski BPM system was conducted in a laboratory setting, which produced results comparing the signal-to-noise ratio (SNR) of a Rogowski BPM experimentally and theoretically.

Initial work included designing and conducting specific experiments investigating the noise contribution from the various components that make up the Rogowski BPM setup. The experiments were conducted using a lock-in amplifier. Table 1 describes the results individually, i.e., the noise values of the various components at the 1 V input range of the lock-in amplifier.

component	input noise [$\frac{\text{nV}}{\sqrt{\text{Hz}}}$]
lock-in amplifier	42.91 ± 0.09
cable	1.44 ± 0.12
pre-amplifier	1.84 ± 0.02

Table 1: The values of the input noise of the different components, measured using a lock-in amplifier.

Figure 1 describes the coil segment noise profile, where the red curve represents the circuit with the pre-amplifier, and the blue curve represents the circuit without the pre-amplifier. Both these curves show a resonant circuit-like profile, with resonance peaks at different frequencies. This difference is accounted for by the pre-amplifier; when the pre-amplifier is present in the circuit, the capacitive contribution of the cable, which is around 200 pF, is suppressed. The capacitance of the cable was measured using an LCR meter.

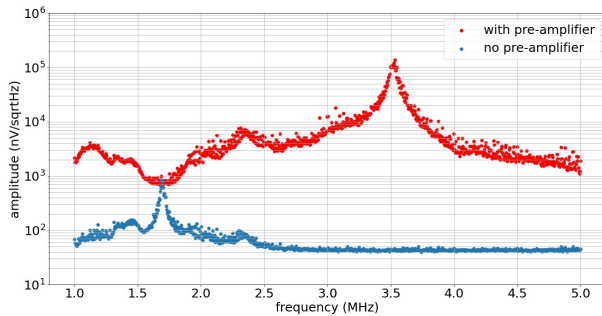


Figure 1: A comparison of the noise profile of the coil segment, with and without the pre-amplifier connected to the circuit under investigation.

The next experiment involved the determination of

the coil parameters R , L and C by performing the impedance measurement of the coil segment. These parameters are used to model the resonant behaviour of the coil segment in the noise model by substituting them into the following equation:

$$F(\omega) = \frac{1}{\sqrt{\left(1 - \omega^2 LC + \frac{R}{R_{\text{out}}}\right)^2 + \left(\frac{\omega L}{R_{\text{out}}} + \omega RC\right)^2}}$$

The result from the above resonant function was fed to the noise model, which is seen in Figure 2. The experimental determination of the SNR was completed by measuring the signal response of the coil segment and combining the data with the previously measured noise data. The top plot in Figure 2 is the average SNR of the four coil segments at various frequencies.

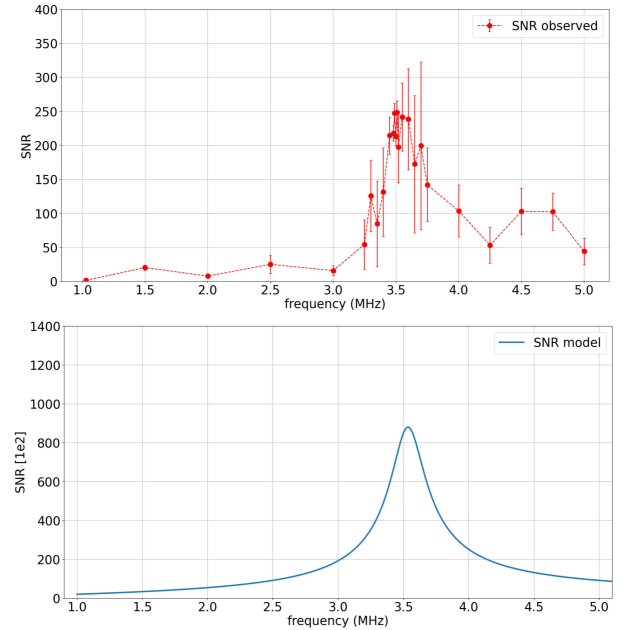


Figure 2: SNR experimental (top) and SNR theoretical (bottom).

The results from the experiment and the theory show similar resonance profiles and have resonance peaks at approximately 3.6 MHz. The measured SNR profile is lower than the predicted theoretical SNR profile. One explanation for this would be the impedance mismatch between the coil segment and the pre-amplifier. A possible solution would be to commission a pre-amplifier purpose-built for the Rogowski BPM system. A possible path for future studies would be to investigate the beam position-based SNR of the Rogowski BPM system.

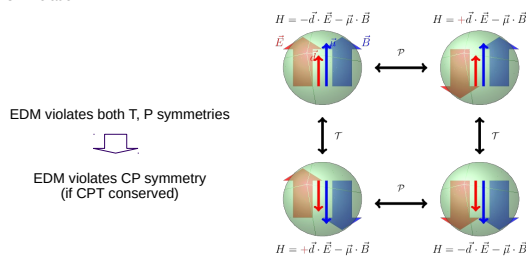
THE SEARCH FOR ELECTRIC DIPOLE MOMENTS OF CHARGED PARTICLES USING STORAGE RINGS

VERA SHMAKOVA FOR THE JEDI COLLABORATION

MATTER – ANTIMATTER ASYMMETRY

Why is our universe is matter dominated?

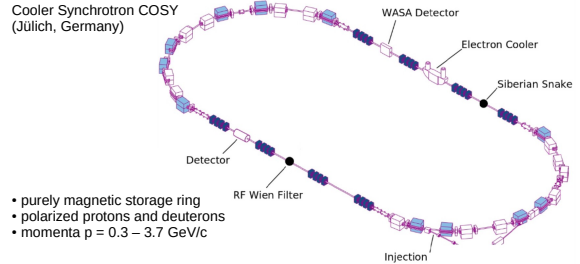
- Experiment predicts^[2] $\frac{n_b - n_{\bar{b}}}{n_\gamma} \sim 10^{-10}$
- Expectations from SCM^[3,4] $\frac{n_b - n_{\bar{b}}}{n_\gamma} \sim 10^{-18}$
- Criteria for preference of matter, A. Sakharov^[5] (1967):
 - CP violation



EDM may possibly contain the missing piece of the puzzle to explain the matter-antimatter asymmetry

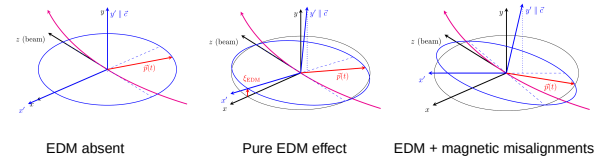
COSY

Cooler Synchrotron COSY (Jülich, Germany)



- purely magnetic storage ring
- polarized protons and deuterons
- momenta p = 0.3 – 3.7 GeV/c

INVARIANT SPIN AXIS



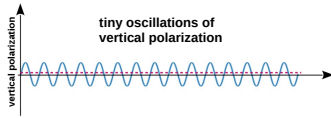
SPIN MOTION IN MAGNETIC STORAGE RING

$$\frac{d\vec{S}}{dt} = [\vec{\Omega}_{MDM} - \vec{\Omega}_{cycl} + \vec{\Omega}_{EDM}] \times \vec{S}$$

$$\vec{\Omega}_{MDM} - \vec{\Omega}_{cycl} = -\frac{q}{m} \left(G\vec{B} - \left(G - \frac{1}{\gamma^2 - 1} \right) \frac{\vec{\beta} \times \vec{E}}{c} \right)$$

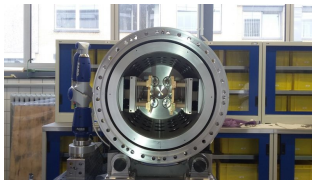
$$\vec{\Omega}_{EDM} = -\frac{\eta q}{2mc} (\vec{E} + \vec{c} \times \vec{\beta} \times \vec{B})$$

access to EDM



In the magnetic ring momentum ↑ spin → spin kicked up momentum ↓ spin → spin kicked down

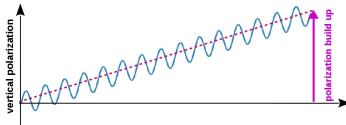
no accumulation of vertical asymmetry



RF Wien filter^[6,7]:

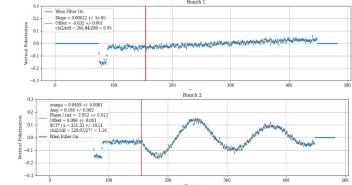
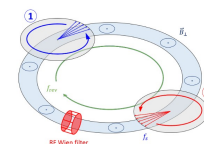
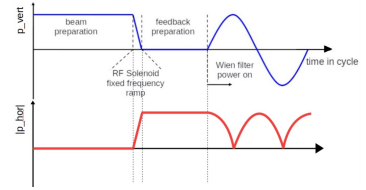
- Lorentz force $\vec{F}_L = q(\vec{E} + \vec{v} \times \vec{B}) = 0$
- $\vec{B} = (0, B_y, 0)$ $\vec{E} = (E_x, 0, 0)$
- phase lock between spin precession and RF Wien filter

polarization build-up

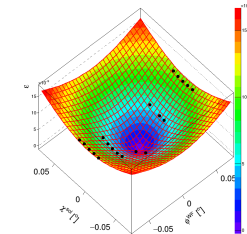


EXPERIMENT AND RESULTS

- Coherent ensembles in ring plane
spin coherence time has to be longer than a measurement
- Feedback monitors spin precession phase and adjust WF frequency to maintain the relative phase between spin precession and Wien filter RF
- 8 high-speed RF switches to gate the WF power for one of two bunches



- Capable of short switch time ~ few ns
- Bunch ② sees the full power of the RF Wien filter and oscillate
- Bunch ① is used for the feedback system to lock the phase between spin precession and Wien filter RF
- Minimum of the surface shows orientation of invariant spin axis:
- Orientation of precession axis without EDM effect will come out of spin tracking calculations



REFERENCES

- 1) F. Abusail *et al.*, Storage Ring Search for Electric Dipole Moments of Charged Particles - Feasibility Study, CERN Yellow Report **257** (2021), <https://doi.org/10.23731/CYRM-2021-003>.
- 2) V. Barger, J. P. Kneller, H.-S. Lee, D. Marfatia and G. Steigman, Phys. Lett. **B566**, 8 (2003).
- 3) W. Bernreuther, Lect. Notes Phys. **591**, 237 (2002).
- 4) WMAP collaboration, Astrophys. J. Suppl. **148**, 1 (2003).
- 5) A. D. Sakharov, Pisma Zh. Eksp. Teor. Fiz. **5**, 32 (1967).
- 6) J. Slim *et al.*, Nucl. Instrum. Methods Phys. Res. A **828**, 166 (2016).
- 7) J. Slim *et al.*, Phys. Rev. Accelerators and Beams **24**, 124601 (2021).
- 8) A. Saleev, N. Nikolaev, F. Rathmann *et al.*, Phys. Rev. ST Accel. Beams **20**, 072801 (2017).
- 9) D. Eversmann *et al.*, Phys. Rev. Lett. **115**, 094801 (2015).
- 10) N. Hempelmann *et al.*, Phys. Rev. Lett. **119**, 014801 (2017).

SUMMARY

- Charged hadron EDMs: Possibility to find sources of CP violation and to explain matter-antimatter asymmetry in the universe.
- Precursor experiments performed as a proof of principle of EDM measurement at storage rings. Analysis of data ongoing.
- New method of manipulating the polarization for one of two bunches in the ring was developed and performed
- CERN Yellow Report prepared by CPEDM collaboration^[1].
- COSY remains a unique facility for such studies.

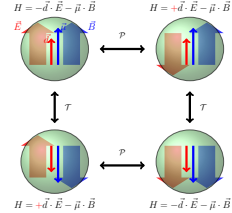
Spin-Tracking simulations in an idealized COSY model using Bmad

M. Vitz, Institut für Kernphysik 4, Forschungszentrum Jülich, 52425 Jülich, Germany,
also at III. Physikalisches Institut B, RWTH Aachen University, 52056 Aachen, Germany
on behalf of the JEDI Collaboration

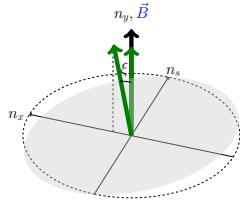
Motivation

- Electric Dipole Moment (EDM) is a fundamental property of a subatomic particle, similar to the Magnetic Dipole Moment (MDM).

$$H = -\vec{d} \cdot \vec{E} - \vec{\mu} \cdot \vec{B}$$

$$H = +\vec{d} \cdot \vec{E} - \vec{\mu} \cdot \vec{B}$$

- Source of \mathcal{P} and \mathcal{T} violation ($\stackrel{CPT}{=} C\mathcal{P}$ violation) and therefore closely connected to matter antimatter asymmetry.
- EDM of charged particles can be measured in a storage ring as spin rotation is defined by EDM and MDM contribution [1].
- Vertical spin build-up is used to estimate the EDMs magnitude but also EDM-like systematic effects occur.
- Spin tracking simulations with Bmad Software Library are used to disentangle systematic effects from a real EDM signal [2].

Invariant Spin Axis

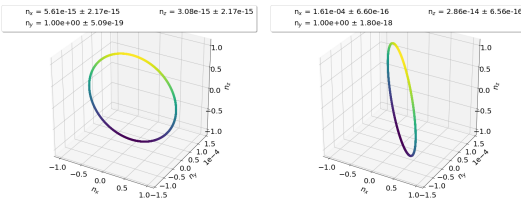


- Expected horizontal tilt n_x due to the EDM strength η is described via:

$$\tan \xi_{EDM} = \frac{\eta\beta}{2G}$$

- Proof of principle was performed using the Bmad COSY model and tracking the reference particle for some thousand turns.

$$\langle \vec{n} \rangle = \frac{1}{n-1} \sum_{i=1}^{n-1} \left(\frac{\vec{S}_i \times \vec{S}_{i+1}}{|\vec{S}_i \times \vec{S}_{i+1}|} \right)$$



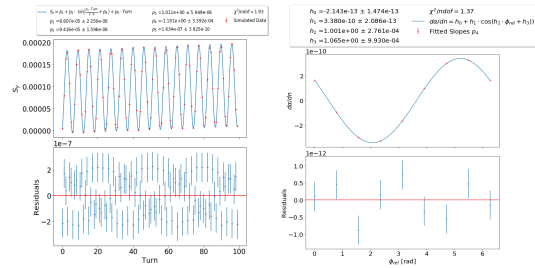
- Simulation result n_x in an idealized COSY model is in agreement with the expected tilt of the invariant spin axis ξ_{EDM} .
- As one cannot apply this method to an experiment a different approach to measure the EDM signal has to be used.

Experiment at COSY

- The experiment measures the EDM using a Wien-Filter and a solenoid \Rightarrow **Resonant Wien Filter Method**
- Wien Filter gives the beam a phase dependent kick for vertical spin build-up:

$$E_x = E_0 \cdot \cos(2\pi f_{rev}|k + \nu_s| + \phi_{rel})$$

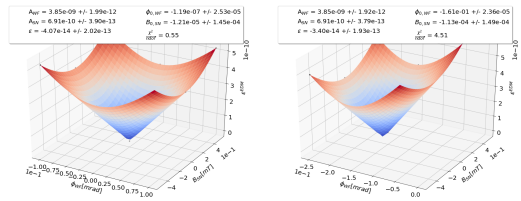
$$B_y = B_0 \cdot \cos(2\pi f_{rev}|k + \nu_s| + \phi_{rel})$$



- Amplitude of oscillation displays the EDM resonance strength [3].

$$\epsilon_{EDM} = \left(A_{WF}^2 (\phi_{WF} - \phi_{WF,0})^2 + A_{SN}^2 \left(\frac{\xi_{SN} - \xi_{SN,0}}{2 \sin(\pi \nu_{s,0})} \right)^2 \right)^{1/2} + \epsilon_0$$

- Find the fit point of **minimal resonance strength**
 $(\phi_{WF,0}, \xi_{SN,0}) \Rightarrow \phi_{WF,0}$ is measured EDM plus systematic effects.



- Shift in $\phi_{WF,0}$ is observed as soon as an EDM signal is included in the simulation $\Rightarrow \phi_{WF,0}$ in an idealized COSY lattice with EDM signal simulated fits the expectation.

- Ring imperfections as magnet misalignments, higher order multipole components etc. are influencing the map minimum \Rightarrow Their effect must be systematically build in and understood!

References

- [1] T. Fukuyama and A. J. Silenko, Derivation of Generalized Thomas-Bargmann-Michel-Telegdi Equation for a Particle with Electric Dipole Moment, Int. J. Mod. Phys A28, 1350147, 2013.
- [2] D. C. Sagan, Bmad: A relativistic charged particle simulation library, Nuclear Instruments and Methods in Physics Research A, vol.558, pp.356-359, 2006.
- [3] F. Rathmann, N. N. Nikolaev and J. Slim, Spin dynamics investigations for the electric dipole moment experiment, Physical Review Accelerators and Beams 23, 024601, 2020.

Contact: Maximilian Vitz - m.vitz@fz-juelich.de

Member of the Helmholtz Association

Optimization of Spin Coherence Time for Electric Dipole Moment measurements in a Storage Ring

Rahul Shankar^{1,2}

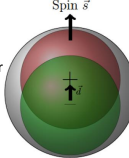
¹University of Ferrara, Ferrara, Italy

²Istituto Nazionale di Fisica Nucleare, Ferrara, Italy

On behalf of the JEDI collaboration.

Motivation

- Electric Dipole Moment is a permanent separation of the positive and negative charge in a fundamental particle → possible via CP violation.
- EDM magnitude closely correlated with matter-antimatter asymmetry in the universe.
- JEDI aims to measure the EDM of charged particles using storage rings in a three-stage experiment. Current work focusses on second stage.



COSY Storage Ring

- Uses only magnetic fields to confine ions
- Spin Precession w.r.t ion momentum
- RF Wien filter to increment planar angle proportional to EDM

PTEDM Storage Ring

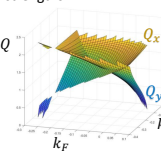
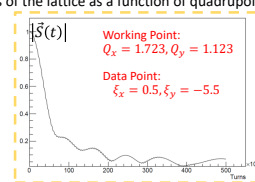
- Combines electrostatic and magnetic confinement
- "Frozen" spin through fine-tuning of E and B fields
- Natural increment via E field

Pure Electrostatic Ring

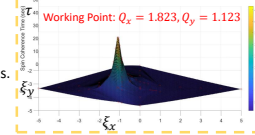
- Uses only Electrostatic confinement
- "Frozen" spin through fine-tuning of E field, momentum and radius.
- Natural increment via E field

- BMAD library used to simulate spin decoherence in PTEDM ring model with two families of quadrupoles and sextupoles.
- Spin Coherence Time (τ): time taken for resultant spin vector to reduce to $\frac{1}{2}$ times its initial value.
- Maximum SCT indicates precision of the EDM measurement at lattice running optimized field parameters.

Optical Properties and Decoherence

- This set of optical parameters are optimized to find maximum SCT:
 - Choice of Lattice
 - Quadrupole Settings (k_F, k_D)
 - Sextupole Settings (s_F, s_D)
- A plot of all accessible betatron tunes of the lattice as a function of quadrupole field strengths:
 

- SCT is measured from the time development of

$$\tilde{S}(t) = \frac{1}{n} \sum_{i=0}^n \tilde{S}_i(t)$$
 of a bunch of 1000 simulated particles. SCT is τ when

$$|\tilde{S}(\tau)| = \frac{1}{e} |\tilde{S}(0)|$$

- Scan of decoherence of multiple data points at a single working point → local SCT maxima. Scan of local maxima over all accessible working points → global SCT maxima.

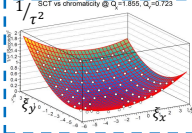
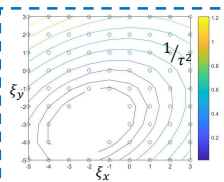
Using STS zero-line and fitting functions to optimize SCT

- Maximum spin-coherence time is likely to coincide with minimum spin tune spread (v_x).

$$v_x = \frac{d}{dt} \left[\sin^{-1} \left(\frac{\tilde{S}(t) \cdot \hat{i}}{|\tilde{S}(t)|} \right) \right]$$
- v_x varies linearly with chromaticity in both transverse directions ⇒ there is a straight line of vanishing v_x on the ξ -space.
- ∴ optimized data point can be found from a search along the "zero-line".
- Maximum SCT in good agreement with earlier brute force searches.
- Contour lines of SCT form concentric ellipses over the ξ -space, regularly scaled at $1/\tau^2$.
- Thus, SCT shown to vary with chromaticity as:

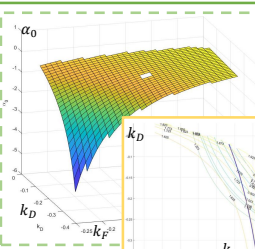
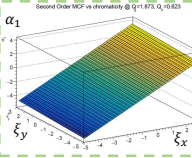
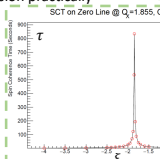
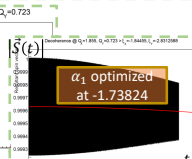
$$\frac{1}{\tau^2} = \frac{1}{\tau_0^2} + L(\xi_x - h)^2 + M(\xi_y - k)^2 + N(\xi_x - h)(\xi_y - k)$$

Free parameters:
Maximum SCT → τ_0
location of maxima → $(\xi_x, \xi_y) = (h, k)$
 L, M and N → size, shape and rotation of ellipse.

Results

- Negative values of first order momentum compaction factor (α_0) indicate the inaccessibility of the working points at the current phase ($\cos \varphi_s = -0.5$) of the RF cavity (synchrotron frequency becomes imaginary):

$$f_s = f_{rf} \sqrt{-\frac{\alpha_0 e U_0}{2\pi \beta_0 E_0 h} \cos \varphi_s}$$
 limiting the search to positive points.
 
- Second order momentum compaction factor (α_1) varies linearly with chromaticities.
 
- Global SCT maxima, upwards of 1000s, was found for optimized second order optics ($\xi_x = -1.845, \xi_y = -2.831, \alpha_1 = -1.735$) at working point $Q_x = 1.855, Q_y = 0.723$.
- SCT highly sensitive to chromaticity possibly due to simultaneous change of at least two parameters → is precision practically achievable?
 
- Sharpness of such peaks may reduce with additional family of sextupoles.
 

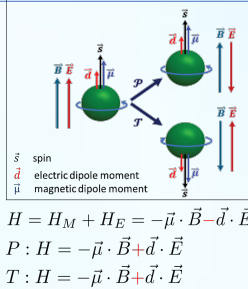
Simulations of Beam Dynamics of Prototype EDM Storage Ring

Saad Siddique, on behalf of the JEDI Collaboration
Institut für Kernphysik, Forschungszentrum Jülich, Germany
III. Physikalisches Institut B, RWTH Aachen University, Germany
GSI Helmholtzzentrum für Schwerionenforschung GmbH Darmstadt, Germany
saad.siddique@rwth-aachen.de

Physics Case:

- Matter antimatter asymmetry can be explained by CP- violation
- Permanent electric dipole moment (EDM) is fundamental property of particles (like mass, charge, magnetic moment)
- Existence of EDM only possible if violation of time reversal and parity symmetry.

$$\eta = \frac{N_B - N_{\bar{B}}}{N_B}$$



Methodology :

- Inject longitudinally polarized beam in storage ring
- Radial electric field interacting with EDM (torque)
- Observe vertical polarization with time

BMT-Equation:

$$\frac{d\vec{s}}{dt} = (\vec{\Omega}_{MDM} + \vec{\Omega}_{EDM}) \times \vec{s}$$

$$\vec{\Omega} = \frac{q}{m} \left\{ G\vec{B} + \left(G - \frac{1}{\gamma^2 - 1} \right) \frac{\vec{\beta} \times \vec{E}}{c} + \frac{\eta}{2} \left(\frac{\vec{E}}{c} + \vec{\beta} \times \vec{B} \right) \right\}$$

$$\left(G - \frac{1}{\gamma^2 - 1} \right) \equiv 0! \rightarrow \text{Magic momentum}$$

If $G > 0 \rightarrow$ pure electric ring
If $G < 0 \rightarrow$ combination of E-B

Strategy :

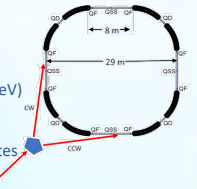
- Precursor Experiment @ COSY Storage Ring Forschungszentrum Jülich Germany
- Prototype proton EDM Storage Ring (PTR)
- All electric Storage ring

Prototype EDM Storage Ring:

- Ring will be operated in two modes:
- Electrostatic bendings (at T=30 MeV)
 - Electromagnetic bendings (at T=45 MeV)

Goals

- Beam injection with multiple polarization states and for longer time. (> 1000 sec)
- Develop key technologies beam cooling, deflector, beam position monitors, magnetic shielding....
- Perform EDM measurement



Simulations :

- Four Lattice with different focusing strength generated by MADX.

Estimation of Beam Loss Rates:

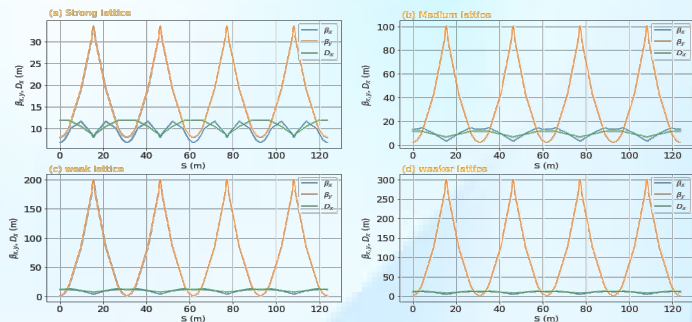
- Hadronic Interactions (HI)
- Coulomb Scatterings (CS)
- Energy Loss straggling (ELS)
- Intrabeam Scatterings (IBS)

$$\tau^{-1} = n\sigma_{tot}f_0$$

Residual Gas & Target:

- Gases composition $H_2 : N_2$ with 80:20
- Nitrogen equivalent pressure $P_{eq} = 2.8 \times 10^{-11}$ torr

- Rest Gas density $n_{rg} = 5.30 \times 10^5$ atoms/cm³
- Carbon target density $n_t \sim 2 \times 10^{12}$ atoms/cm²



Results :

$$\text{Total beam loss rates } \left(\frac{1}{\tau} \right)_{\text{Tot}} = \left(\frac{1}{\tau} \right)_{HI} + \left(\frac{1}{\tau} \right)_{CS} + \left(\frac{1}{\tau} \right)_{ES} + \left(\frac{1}{\tau} \right)_{IBS}$$

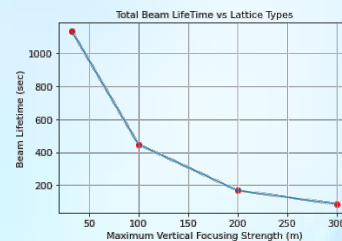
Beam loss rates for residual and target for all four lattices

Lattice	HI (10 ⁻⁶ s ⁻¹)	CS (10 ⁻⁴ s ⁻¹)	IBS (10 ⁻⁴ s ⁻¹)	(1/τ) _{tot} (10 ⁻⁴ s ⁻¹)	τ _{tot} (s)
Strong	2.14	6.46	2.34	8.82	1133
Medium		20.21	2.10	22.34	447
Weak		57.48	1.99	59.49	168
Weaker		115.87	1.90	117.79	85

Summary:

- Preliminary design of prototype EDM ring
- Most dominating effect is Single Coulomb Scatterings
- Lattice with $\beta_{y-max} \leq 100$ m is preferable for longer beam lifetime.

Energy loss straggling isn't contributing theoretically in beam loss rates



References:

- F. Hinterberger, Beam-Target Interaction and Intrabeam Scattering in the HESR Ring, Technical Report JUEL- 4206, Forschungszentrum Jülich GmbH (Germany), Feb 2006.
- F. Abusaif et al., Storage ring to search for electric dipole moments of charged particles. Feasibility Study. CERN Yellow Reports: Monographs, Geneva. Geneva: CERN. CERN, Jan 2019

Source Insertion Calibration System of OSIRIS

Runxuan Liu

The OSIRIS (Online Scintillator Internal Radioactivity Investigation System) detector is a pre-detector of JUNO. It is designed to monitor the radiopurity of the liquid scintillator (LS) after a chain of purification and mixing of the LS, during several months of the filling of the JUNO central detector. OSIRIS will search for the fast coincidence decays of ^{214}Bi - ^{214}Po and ^{212}Bi - ^{212}Po in the decay chains of ^{238}U and ^{232}Th , respectively. The required sensitivity levels from JUNO are: 10^{-15} g/g (mass of ^{238}U or ^{232}Th to mass of LS) for neutrino mass ordering detection and 10^{-16} g/g for solar neutrino detection [1].

The source insertion system of the OSIRIS detector is placed at the top of the detector in the clean room. It is a fully automated and sealed system, based on an Automated Calibration Unit (ACU), provided by the Daya Bay collaboration. Different functional components of the ACU are sealed in a bell jar. After the clean room was ready, the ACU bell jar was opened to allow installation and refurbishment of some of the small parts inside. Cleaning with pure water was also performed on the surface of different parts inside. Figure 1 shows the different parts inside. There are three capsules that contain different radioactive sources or blue LED light source. During the calibration, the capsules will be lowered down from three wheels into the LS. The three different sources, together with their functions, are discussed in the following.

For OSIRIS, the energy region of interest is about 0.6 MeV to 3.5 MeV. To cover this range, isotopes of ^{137}Cs (0.66 MeV), ^{65}Zn (1.12 MeV), and ^{60}Co (2.43 MeV) are selected for the multi-gamma source capsule. The sources are already ordered, with the combined activity of 11.6 kBq. The second capsule will hold a ^{40}K source, which emits photons of 1.46 MeV. The activity will be ≤ 1 Bq. So that this source can serve continuously inside the LS during the 6 months of filling of the LS and has minimal disturbances to

the analysis. Meanwhile, it is possible to monitor the change of the light yield at the 1% level in a few hours. To provide time and charge calibration for the PMTs, we have installed a blue LED as the third capsule. It is also equipped with turnable intensity to investigate the PMT response to higher p.e. occupancy.

Many parts inside the ACU need power and control, including load cells, motors of the wheels and turntable, limit switched, CCD, and LED driver. They are connected by 2 I/O cables via a vacuum feedthrough flange on the bell jar and connected to the control box of the ACU, which is mounted inside the cabinet of OSIRIS outside of the clean room.

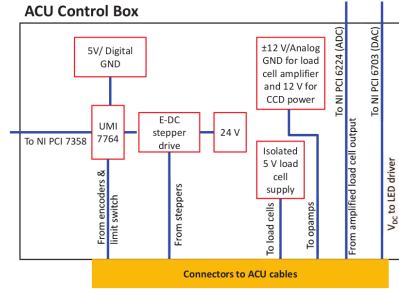


Figure 2: Schematics of the ACU control box [3].

As shown in the simplified schematic diagram of the ACU control box in Figure 2, all stepper motors are first connected to their driver. The output current range on this drive is customized to limit the output torque from the stepper motors. An interface board UMI 7764 collects all the motion I/O signals and then connect to the the NI PCI 7358 motion control card. The ACU control box also holds three independent power supplies for different load cells and the ACU CCD, which will provide video livestream during calibration operation. Furthermore, the load cell signals are amplified and pass through the control box, then entering into the ADC (NI PCI 6224), whereas a DAC (NI PCI 6703) passes a DC voltage through the ACU control box to the LED driver. Those three NI PCI boards are installed in a Magma extension crate, which is mounted by the side of the ACU control box.

All the electronics of the ACU have been setup and tested. Further tests of the software is ongoing.

References

- [1] JUNO collaboration, The European Physical Journal C 81.11 (2021): 973.
- [2] C. Genster, RWTH-2019-11430.
- [3] J. Liu, *et al.*, Nuclear Instruments and Methods in Physics Research Section A 750 (2014): 19-37.

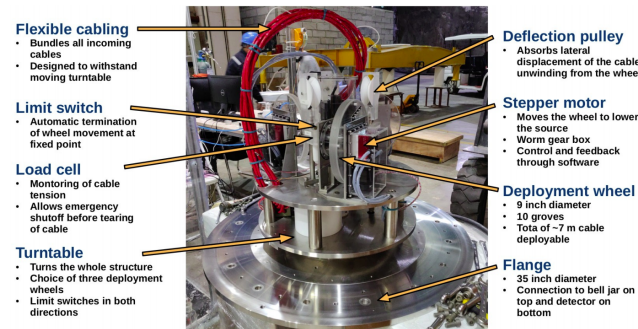


Figure 1: Opened ACU with detailed description of different parts [2].



Geoneutrinos and NMO sensitivity: an approach based on full Monte Carlo simulations



WP 1

WP 2

Anita Meraviglia^{1,2} and Nikhil Mohan^{1,2}

¹GSi Helmholtz Centre for Heavy Ion Research

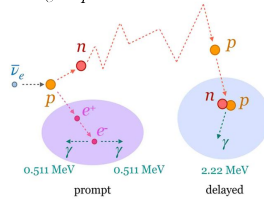
²RWTH Aachen University

WP 4

Signals and backgrounds

Inverse Beta Decay reaction

$$\bar{\nu}_e + p \rightarrow e^+ + n$$



Signals: reactor antineutrinos (47 events/day), from the two adjacent nuclear power plants at a baseline of 53 km each, and geoneutrinos (1.2 events/day), from the decays of long-lived radioactive elements inside the Earth

Prompt signal (e^+)

e^+ scintillation + annihilation (2γ)

$$E_{\text{prompt}} \approx E_{\bar{\nu}} - 0.782 \text{ MeV}$$

Delayed signal (n capture on p)

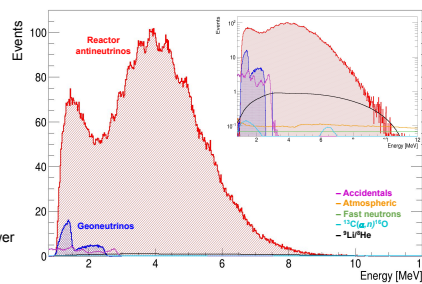
$$E_{\text{delayed}} \approx 2.2 \text{ MeV}$$

$$\Delta t_{\text{prompt-delayed}} \approx 250 \mu\text{s}$$

$$E(\bar{\nu}_e) \approx K(e^+) + 1.8 \text{ MeV}$$

Coincidence in time, space and energy between prompt and delayed guarantees a very high signal/background ratio

Number of events expected for 1 year of data-taking as a function of the antineutrino energy



Backgrounds after cuts

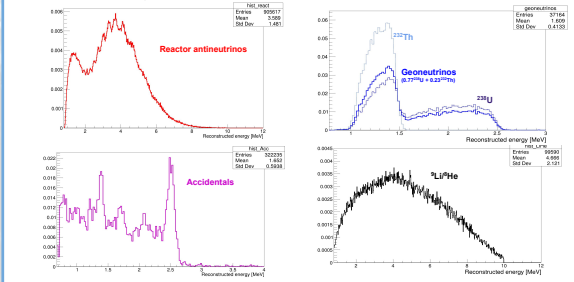
- **Accidentals** (0.8 events/day) are random energy depositions in the liquid scintillator (LS)
- **Atmospheric neutrinos** (0.16 events/day) interact via neutral current with the ^{12}C nuclei in the LS
- **Fast neutrons** (0.1 events/day), produced by cosmic muons, scatter off protons in the LS
- $^{13}\text{C}(\alpha, n)^{16}\text{O}$ (0.05 events/day): the α particles from the ^{238}U and ^{232}Th chains react with the ^{13}C in the LS
- $^9\text{Li}/^8\text{He}$ (0.8 events/day), the most relevant cosmogenic background, decay $\beta+n$

Analysis strategy



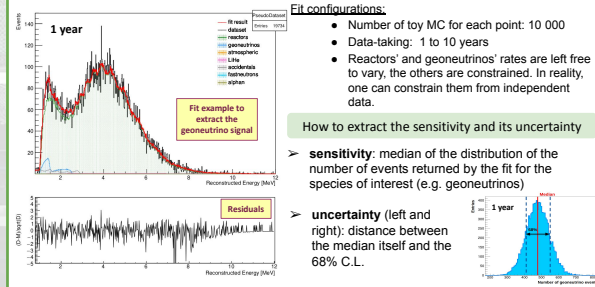
Monte Carlo spectral shapes: some examples

Probability density functions (PDF) spectral shapes from the Monte Carlo simulations with full detector response.



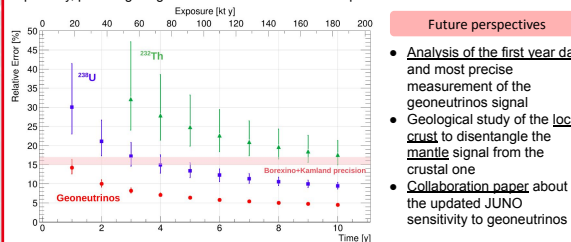
Toy data sampling and fitting with JUST

Jülich nUsoL Sensitivity Tool (JUST) is a software tool for neutrinos sensitivity and analysis, based on a binned poisson likelihood optimization.



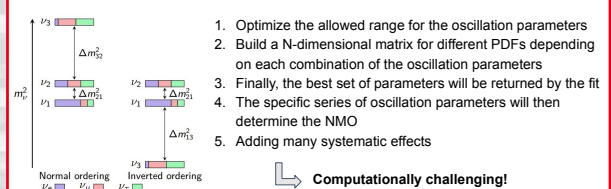
Geoneutrinos

Sensitivity studies: JUNO has a potential to measure geoneutrinos (with a fixed $^{238}\text{U}/^{232}\text{Th}$ ratio) with a precision of $\sim 14\%$ even after only 1 year of data-taking, thus improving the current best results from Borexino [3] and KamLAND [4]. The main final goal is to estimate the Earth radiogenic heat. Additionally, JUNO will be able to measure for the first time the contribution of ^{238}U and ^{232}Th separately, providing insights about the Earth's formation processes.



Neutrino Mass Ordering (NMO) sensitivity

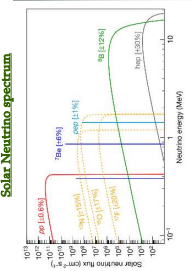
In order to perform NMO sensitivity studies, we plan to further develop JUST and make it fit not only the number of events but also the oscillation parameters.



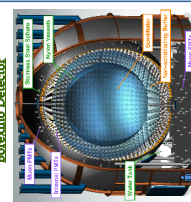
References

- [1] JUNO Collaboration, *Neutrino Physics with JUNO*, J. Phys. G43, 3, 2016
- [2] Han R. et al., *Potential of Geo-neutrino Measurements at JUNO*, Chin. Phys. C, 40, 3, 2016
- [3] Borexino Collaboration, *Comprehensive geoneutrino analysis with Borexino*, Phys. Rev. D101, 012009, 2020
- [4] KamLAND Collaboration, *Abundances of Uranium and Thorium Elements in Earth Estimated by Geoneutrino Spectroscopy*, Geophysical Research Letters 49, 16, 2022

INTRODUCTION



Solar Neutrino spectrum



Borexino Detector

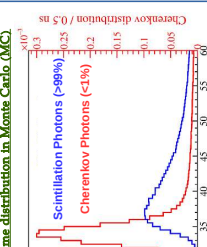
Neutrinos detected via elastic scattering of electrons

$\nu_e + e^- \rightarrow \nu_e + e^-$

Features of the Detector

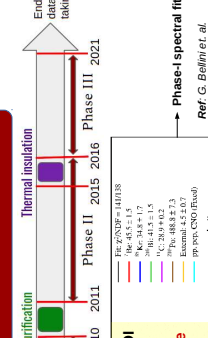
- ~280 tons liquid scintillator (LS)
- The most radio-pure LS detector
- Effective light yield = 500 p.e/MeV
- Energy resolution: 5% @ 1 MeV
- Position resolution: 10 cm @ 1 MeV

PMT hit time distribution in Monte Carlo (MC)



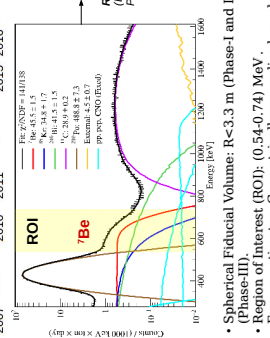
- Cherenkov photons are emitted by electrons with energy threshold of 0.16 MeV.
- Most of the Cherenkov photons emitted earlier than scintillation photons.

DATA SELECTION



calibration purification Thermal insulation End of data taking

Phase I 2010-2011 Phase II 2015-2016 Phase III 2021



ROI

Phase-I spectral fit
Ref: G. Bellini et al. (Borexino Collaboration) Phys. Rev. D 89, 112007

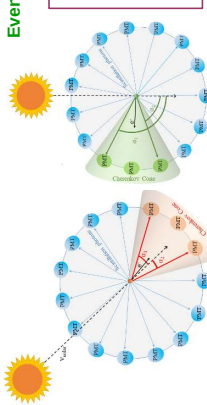
- Spherical Fiducial Volume: $R < 3.3$ m (Phase-I and II), $R < 3.0$ m (Phase-III).
- Region of Interest (ROI): (0.54 ± 0.74) MeV.
- Energy estimator: Geometrically normalised number of hits (N_{geo}) .
- α/β pulse shape discrimination cut to remove ^{210}Po events with 99% efficiency.
- Signal: ^{10}Be (89% of solar neutrinos in ROI) + CNO + pep neutrinos
- Background: ^{210}Bi + ^{210}Kt

CORRELATED AND INTEGRATED DIRECTIONALITY

Event by Event Directional Reconstruction Not Possible

Correlating the first two hits of an event with the known position of the Sun

α : angle between the solar direction and direction of hit PMT with respect to the reconstructed event position.

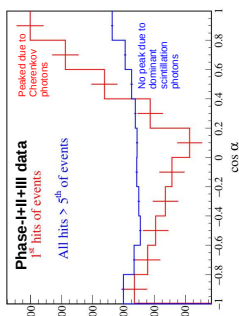


Background Event

N^{th} hit Analysis Strategy

- Systematics differences in Time of Flight (ToF) corrected hit time distribution of data and MC at early times.
- Photons are sorted in time after subtracting ToF for each event.
- Look at relative ordering of hits in time.
- N is chosen to maximise ratio of Cherenkov photons with highest sensitivity to directional differences between signal and background MC. The best value of N is 2.

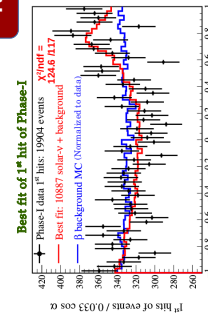
Phase-I+II+III data



Peaked due to 1st hits of events
All hits > 5th of events
No peak due to dominant scintillation photons

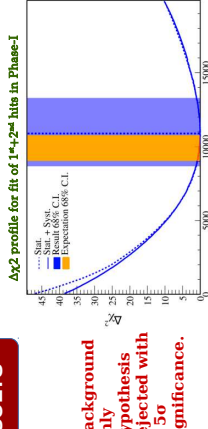
RESULTS

Best fit of 1st hit of Phase-I



Best fit: 10887 solar + background 124.6 ± 11.7
Best fit: 10887 solar + background 124.6 ± 11.7
Background only hypothesis rejected with > 5 σ significance.

$\Delta\alpha^2$ profile for fit of 1st, 2nd hits in Phase-I



Number of solar neutrinos $N_{solar-\nu}$

Measured number of solar neutrinos

10887 $^{+2808}_{-2400}$ (stat.) ± 947 (syst.)

Extracted ^{10}Be rate (fixing CNO, pep + rate to SSM predictions):

51.6 $^{+3.9}_{-3.5}$ (stat.+syst.) counts per day 100 tons.

Fit Strategy:

$$\chi^2(N_{solar-\nu}) = \sum_{i=1}^N \left[\frac{(\cos \alpha_i^D - (\cos \alpha_i^M (N_{solar-\nu} \Delta_{dir}^{solar-\nu}) + \Delta_{dir}^{CNO}))^2}{(\sigma_i^D)^2 + (\sigma_i^M)^2} + \frac{(g_{\nu}^{corr} - 0.108 \text{ ns m}^{-1})^2}{(0.039 \text{ ns m}^{-1})^2} \right]$$

True Position \vec{r}_{true}
Reco. Position \vec{r}_{reco}
Event Direction \vec{r}_{event}

Large uncertainties due to g_{ν}^{corr} and Δ_{dir} : e- Cherenkov calibration essential

- $(\cos \alpha)^D$ and $(\cos \alpha)^M$: cos α distributions of data and MC respectively.
- $N_{solar-\nu}$: Number of solar neutrino events; free parameter.
- g_{ν}^{corr} : group velocity correction from y radiative sources = (0.108 ± 0.039) ns/m; a pull-term.
- Δ_{dir} : misreconstruction of e-; nuisance free parameter; cannot be corrected without a e- Cherenkov calibration.
- A bigger misreconstruction increases the slope at $\cos \alpha < 0$ and decreases the actual Cherenkov peak around $\cos \alpha \approx 1$.

CALIBRATION

Effective Correction on Refractive Index for Cherenkov Photons:

- Essential to calibrate relative time difference between Cherenkov and scintillation photons in MC.
- No dedicated e- Cherenkov source. Use γ radioactive sources (^{54}Mn , ^{40}K).
- Fitting of cos δ distribution of calibration data and MC PDFs with different group velocity corrections (and hence, refractive index) for Cherenkov photons.
- Systematic correction of direction misreconstruction is applied using ^{54}Mn on ^{40}K \rightarrow 36% systematic error (0.039 ns/m).
- Best value of group velocity correction (g_{ν}^{corr}) is (0.108 ± 0.006) (stat.) ± 0.039 (syst.) ns/m.** (2% correction on refractive index @ 400 nm).
- Treated as **Gaussian pull term** in the final fit.

Cherenkov group velocity corr.

New PMT hit time of Cherenkov photons

Old PMT hit time of Cherenkov photons

Effective correction on refractive index

Track length of photons

Cherenkov cone

reco position

scintillation

event

Y source

$t_{ch-new} = t_{ch-old} - (g_{\nu}^{corr} \cdot L_{true})$

$t_{ch-old} = t_{ch} - \frac{\Delta t_{ch}}{c} \cdot L_{true}$

SYSTEMATIC ERRORS

Contributing sources of systematic error

Source	Uncertainty [%]
Choice of N^{th} Hit	4.8
Selection of PMTs	5.9
Choice of histogram binning	4.2
Total for $N_{solar-\nu}$	8.7
Exposure	4.6
MLP variable	1.0
CNO and pep rates	$^{+3.3}_{-3.3}$
Total for $N(^{10}\text{Be})$	$^{+10.1}_{-10.0}$

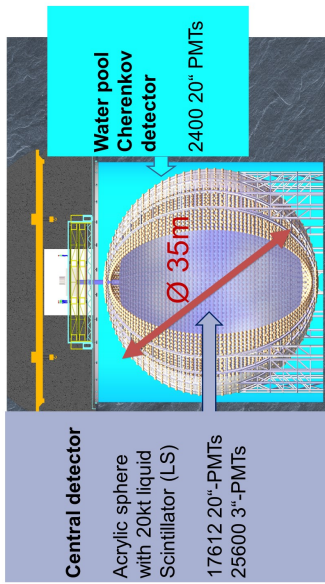
- Due to finite number of PMTs and their non-uniform distribution in the detector \rightarrow Highly dependent. MC follows distribution of live channels same as of distribution of events \rightarrow negligible for non-uniformity at the level of Phase-I data.
- Negligible difference in cos α distribution shape of ^{10}Be , pep and CNO solar neutrinos.

CONCLUSIONS

- > 5 σ detection of sub-MeV solar neutrinos using their directional Cherenkov photons.
- Measurement of ^{10}Be neutrinos rate in agreement with SSM predictions and Borexino Phase-I spectral fit results.
- Can help boost sensitivity for rare processes like CNO solar neutrinos.
- Readily applicable to other LS detectors without need of any specialized hardware.
- For future large volume liquid scintillator detectors: dedicated e- Cherenkov calibration essential.

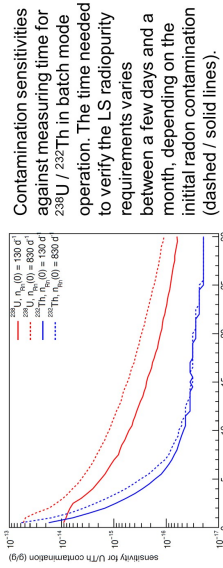
The JUNO experiment

- Main goal: measure neutrino mass hierarchy with $\sim 3\sigma$ (6 years) via reactor antineutrino oscillation patterns with 53 km baseline
- Huge potential for other topics in (astro-)particle physics
- Excellent energy resolution of 3% at 1 MeV
- ~ 700 m overburden
- Construction ongoing in Southern China, first data taking in 2023



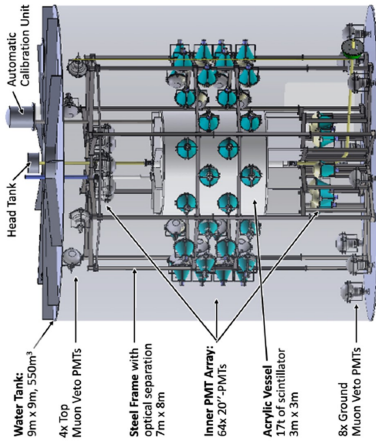
Sensitivity of OSIRIS

- JUNO requirements for both $^{238}\text{U}/^{232}\text{Th}$: 10^{-15} g/g for reactor measurements, 10^{-16} g/g for solar neutrino measurements
- Time needed to determine radiopurity levels strongly depending on Radon contamination in LS
- ^{222}Rn / ^{220}Rn emanating from surfaces of JUNO purification and filling systems in direct contact with LS
- Additional low radon contamination from ambient air via gas leaks in valves and connections



^[1] Forschungszentrum Jülich GmbH, Institut für Experimentelle Kernphysik (IEK-6), RWTH Aachen University, Aachen

The OSIRIS detector



- LS radiopurity monitoring during months-long filling of JUNO
- Optimised for detecting ^{214}Bi - ^{214}Po / ^{212}Bi - ^{212}Po fast coincidence decays in $^{238}\text{U}/^{232}\text{Th}$ decay chains
- Detection of air leaks and malfunctions in LS purification process
- Additional measurement of ^{210}Po , ^{14}C , ^{85}Kr levels in LS
- Two calibration systems for energy & vertex recoils / iPMT charge & timing → see poster „The Calibration of the OSIRIS Subdetector of JUNO“ by Tobias Sterr

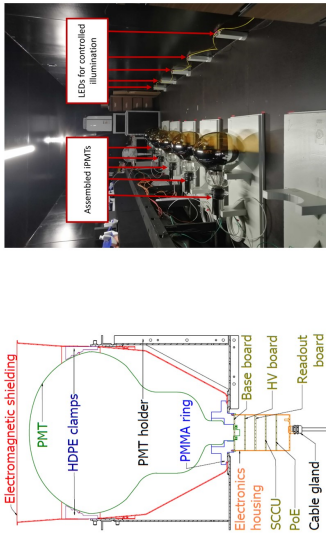
Construction status

- Experimental hall ready, installation of OSIRIS ongoing
- Water tank and acrylic vessel in place
- Detector commissioning phase: July 2022 until end of 2022



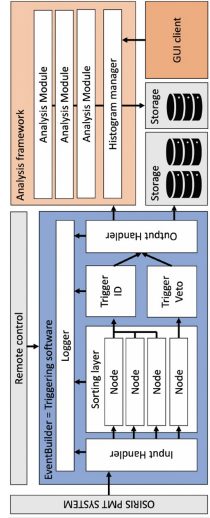
Intelligent PMTs

- Novel design combining 20''-PMT with readout electronics
- Digitization and waveform reconstruction directly on intelligent PMT (iPMT)
- Single Cat5e cable for data and power transfer
- Readout chip: VULCAN of ZEA-2, Forschungszentrum Jülich
- Highly configurable electronics, also after assembly
- Self-triggering during normal operation



Online data acquisition

- iPMT data digitized directly on iPMT → no detector-wide analog trigger possible, online trigger needed
- Single computer („EventBuilder“) as online trigger, combines iPMT data stream into events for further analysis
- Online analysis of detector data („Online Monitor“)
 - Needed for live Bi-Po rate monitoring, sudden rate rises indicate problems in JUNO filling line
 - Also used for calibration, event reconstruction and more
 - Online analysis framework based on RootSorter toolkit
- Detector operation controlled via EPICS
- Several servers for communication infrastructure
- Redundant data storage on-site and on JUNO clusters



Luca Pelicci^{1,2} for the JUNO collaboration

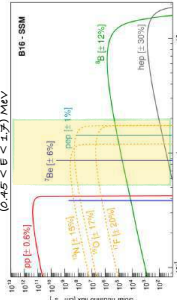
¹RWTH Aachen University - Physics Institute III B, Aachen, Germany
²Institut für Kernphysik, Forschungszentrum Jülich, Germany

Solar neutrino physics with JUNO: analysis strategy and sensitivity studies for ⁷Be, pep, and CNO neutrinos



1. Solar neutrinos

- ★ The only real-time messengers from the Sun core
- ★ Produced in the two nuclear fusion sequences fueling our Sun: the dominant pp-chain ($\approx 0.99 \cdot L_\odot$) and the sub-dominant CNO cycle ($\approx 0.01 \cdot L_\odot$)
- ★ Can be used to tackle the long-standing solar metallicity problem [1]



Intermediate energy solar neutrinos: ⁷Be, pep, and CNO

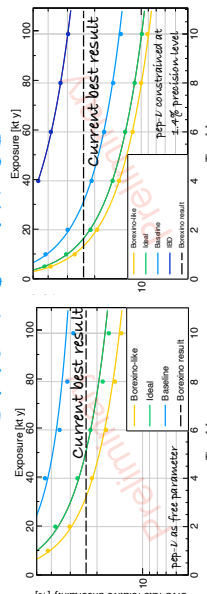
The Solar Standard model (SSM) predicts solar neutrino fluxes (Φ^{SSM}) [1]:

Solar r	Flux B16-BGS16 (10 ¹⁰ cm ⁻² s ⁻¹)	Flux B16-AGSS16 (1.22) (cm ⁻² s ⁻¹)	% diff
⁷ Be	5.8(1) ± 0.06(1) · 10 ¹⁰	6.0(1) ± 0.06(1) · 10 ¹⁰	0.8%
pep	5.4(1) ± 0.1(1) · 10 ¹⁰	5.4(1) ± 0.1(1) · 10 ¹⁰	0.0%
¹¹ B	1.4(1) ± 0.1(1) · 10 ¹⁰	1.4(1) ± 0.1(1) · 10 ¹⁰	0.0%
¹³ C	5.6(1) ± 0.1(1) · 10 ⁹	5.6(1) ± 0.1(1) · 10 ⁹	0.0%
¹⁴ N	2.2(1) ± 0.1(1) · 10 ⁹	2.2(1) ± 0.1(1) · 10 ⁹	0.0%
¹⁵ N	2.6(1) ± 0.1(1) · 10 ⁹	2.6(1) ± 0.1(1) · 10 ⁹	0.0%
¹⁶ O	2.9(1) ± 0.1(1) · 10 ⁹	2.9(1) ± 0.1(1) · 10 ⁹	0.0%
All CNO	2.4(1) ± 0.1(1) · 10 ⁹	2.4(1) ± 0.1(1) · 10 ⁹	0.0%

Solar neutrinos are the perfect candidates to solve the metallicity puzzle!

4. Sensitivity studies

CNO neutrinos



Constraint on pep-ν is crucial for CNO detection. CNO rate can be identified with precision better than 20% (except for IBD scenario)

Most critical backgrounds: ²¹⁰Pb, pep-ν (and ¹¹C)

CNO spectral shape degeneracy with pep-ν and ²¹⁰Pb translates in a strong anti-correlation that affect the sensitivity:

- Constraint on pep-ν is crucial
- Constraint on ²¹⁰Pb is foreseen

References

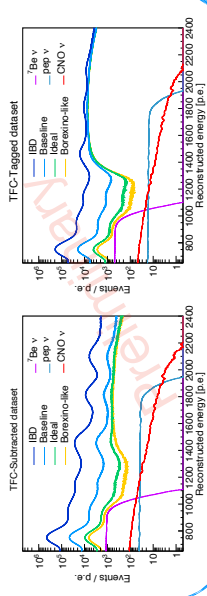
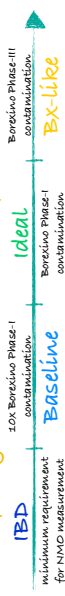
[1] N. Vignati et al., "A new Generation of Standard Solar Models", in: *Astrophys. J.*, 855, 2017, 1611, 08677 (astro-ph.SR)
 [2] A. Avasthi et al., "JUNO physics and detector", in: *Progress in Particle and Nuclear Physics*, 123, 2020, 102401
 [3] S. et al., "Production of radioactive isotopes through cosmic muon spallation in KamLAND", in: *Phys. Rev. C*, 81, 025807, Feb 2010
 [4] M. M. M. et al., "Identification of the cosmogenic ¹¹C background in large volumes of liquid scintillators with Boron-10", in: *Eur. Phys. J.*, C 41 (1995), 2021

2. Signal and backgrounds in Juno [2]

Detection channel: neutrino-electron elastic scattering

Internal backgrounds: intrinsic radioactive decays from ²¹⁰Pb, ²¹⁰Po, ⁸⁵Kr, ²²⁶Ra, ²³²Th chain, and ²³⁸U chain
 cosmogenic backgrounds: mainly ¹¹C produced by cosmic muons spallations, estimated scaling measurements from previous experiments [3]
 External backgrounds: γs from materials surrounding the LS, mainly from PMT glass (suppressed via FV cut)

Radio-purity scenarios considered (from worst to best):



3. Statistical tools

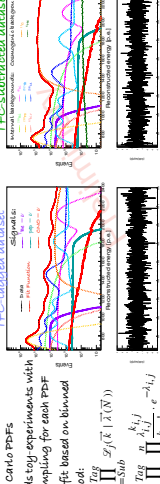
Three fold coincidence (TFC) algorithm [4]:

Identify cosmogenic backgrounds finding the space-time correlations between t_1 , t_2 decay, n capture, and parent muon:
 $t_1 \rightarrow t_2 \rightarrow t_3 \rightarrow t_4 \rightarrow t_5$
 Relevant parameters:
 Tagging power (TP): percentage of correctly identified cosmogenic events
 Subtracted background (SB): remaining exposure in the TFC-subtracted dataset

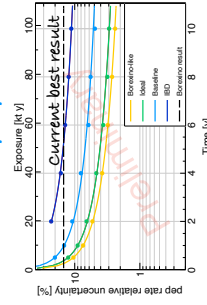
Sensitivity Tools:

β/γ backgrounds are indistinguishable from neutrino signal on an event by event basis
 Two independent spectral fit (JUST & MUST) are used to extract signals (agreement at $\sim 10^{-4}$ level)

Estimate JUNO's sensitivity:



pep neutrinos



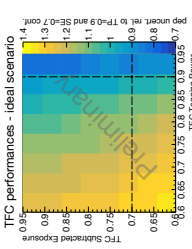
After 2 year of data-taking (except for IBD scenario) JUNO can reach and overcome current best result (14.8%).

Most critical background: ¹¹C

Impact of TFC performances:

$$0.6 < i < 0.95 \text{ with } i = TP, SE$$

- TFC performances are more important in most radiopure scenarios
- Efficient identification of ¹¹C (TP) is more relevant than high fraction of events in the TFC-Sub spectrum (SE)



Outlook and perspectives

- Possible sources of systematic error
- Sensitivity to ¹³N-ν and ¹⁵O-ν
- Low energy analysis (pp neutrinos)
- Day/Night asymmetry with ⁷Be - ν

Conclusions

JUNO has the potential to detect ⁷Be, pep, and CNO neutrinos with highly improved accuracy with respect to current state-of-the-art in the solar neutrino field.



WP 2
WP 3
WP 4

Solar neutrino physics with JUNO: sensitivity studies for Be7, pep, and CNO neutrinos

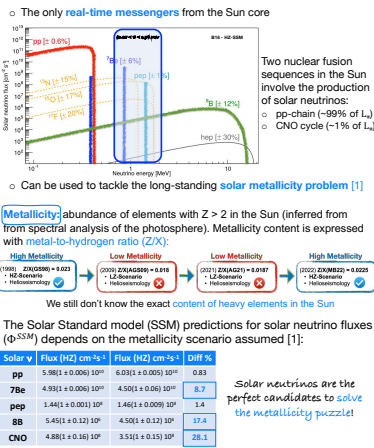
Luca Pelicci^{1,2}

1. RWTH Aachen University - Physics Institute III B, Aachen, Germany
2. Institut für Kernphysik, Forschungszentrum Jülich, Germany

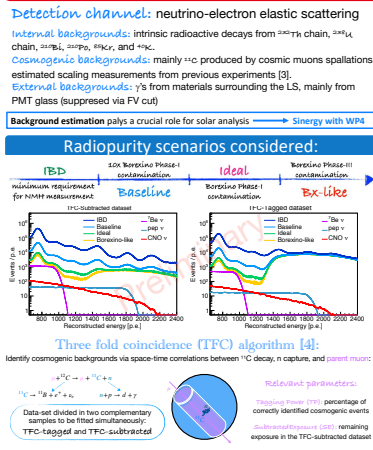


WP 2
WP 3
WP 4

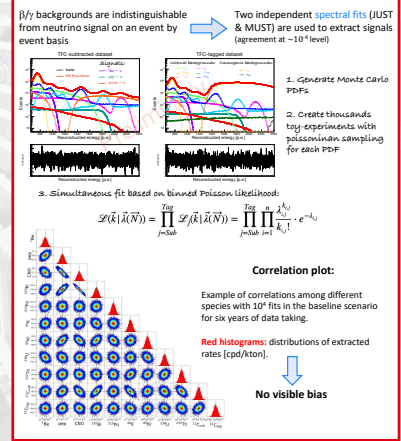
Solar neutrinos



Signal and backgrounds [2]

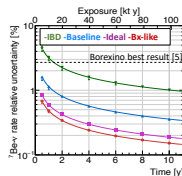


Estimate JUNO's sensitivity



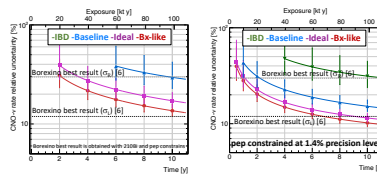
Sensitivity studies

Be7 neutrinos



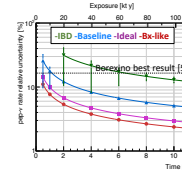
- After 1 year of data-taking JUNO can **reach current best result** (2.7%) [5].
- Most critical backgrounds: ^{86}Kr , ^{210}Po , ^{226}Ra . Eventual additional contaminations (in different realistic scenarios analysed) do not spoil the potential measurement.

CNO neutrinos



- JUNO will be able to **measure CNO without ^{210}Bi constraint** (as it was applied in [6])
- pep constraint** plays a crucial role in high precision CNO determination
- JUNO can match current best precision** [6] for all radiopurity scenarios, except IBD
- Potential for **first detection of ^{15}N and ^{14}O neutrinos**

pep neutrinos



- After 2 year of data-taking (except for IBD scenario) JUNO can **reach current best result** (14.8%).
- Most critical backgrounds: ^{11}C and TFC parameters

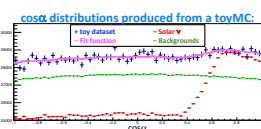
JUNO has the potential to detect ^7Be , pep, and CNO neutrinos with **improved accuracy** with respect to current state-of-the-art in the solar neutrino field.

Correlated and Integrated Directionality (CID)

Novel method developed by Borexino [7]:

Directionality measurement of sub-MeV solar neutrinos: exploit the correlation between detected photons in each event and the known position of the Sun using sub-dominant, fast Cherenkov light emission

Statistical separation of solar neutrinos and background with measured $\cos\theta$ distribution



- Region of Interest (ROI): $0.8 - 1.4$ MeV in TFC-subtracted spectrum
- TFS correction and noise bins included (Full Monte Carlo)
- Extract N_{true} (number of solar neutrino events in the ROI)



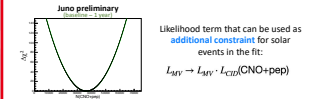
Main systematic effects [7]:

1. Bias in position reconstruction: Systematic shift in true position of the event and its reconstructed position. Value in data unknown without Cherenkov calibration
2. Effective correction on refractive index for Cherenkov photons: tuned with γ radioactive sources due to lack of dedicated Cherenkov source [7].

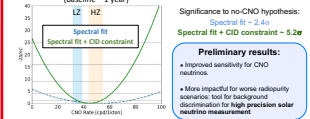
Importance of a dedicated calibration in JUNO!

Combined analysis for CNO neutrinos

$N(\text{Solar } \nu)$ profile with simultaneous fit for each 5th to 30th hit:



Apply CID constraint in the Spectral Fit:



Significance to no-CNO hypothesis: Spectral fit $\sim 2.4\sigma$, Spectral fit + CID constraint $\sim 5.2\sigma$

Preliminary results:

- Improved sensitivity for CNO neutrinos
- More impactful for worse radiopurity scenarios: test for background discrimination for high precision solar neutrino measurement

Future steps

- Study **systematic effects** of CID method
- Exploit spectral features to understand **background levels** with the first weeks of real data
- Calibration campaign:**
 - Low energy γ calibration sources
 - Dedicated Cherenkov source
- Further investigations in **CID applications** for other solar neutrinos
- Sensitivity to intermediate energy neutrinos with the **first data**

References

- [1] N. H. Avignone et al., "A New Generation of Standard Solar Models," in: *Neutrino Physics*, vol. 1, pp. 1-10, 2007.
- [2] L. Pelicci et al., "Production of radioactive isotopes through cosmic muon spallation in JUNO," in: *Phys. Rev. C*, vol. 81, no. 5, p. 054607, 2010.
- [3] M. Agostini et al., "Measurement of the cosmogenic ^{11}C background in the JUNO detector," in: *Phys. Rev. C*, vol. 81, no. 5, p. 054607, 2010.
- [4] M. Agostini et al., "Comprehensive measurement of the ^{11}C background in the JUNO detector," in: *Phys. Rev. C*, vol. 81, no. 5, p. 054607, 2010.
- [5] M. Agostini et al., "Experimental evidence of neutrino production in the CNO fusion cycle in the Sun," in: *Nature*, vol. 462, no. 7285, pp. 455-458, 2009.
- [6] M. Agostini et al., "Combined and Integrated Directionality for sub-MeV solar neutrinos in Borexino," in: *Phys. Rev. D*, vol. 79, no. 1, p. 012001, 2009.

Atmospheric neutrino physics in JUNO: reconstruction of GeV interactions

Mariam Rifai^{1,2}, Marta Molla Colomer³ and Rosmarie Wirth⁴, on behalf of the JUNO collaboration

1.Forschungszentrum Juelich, IKP-2, 2.RWTH Aachen University, Germany 3.Université Libre de Bruxelles, Belgium 4. Hamburg University, Germany

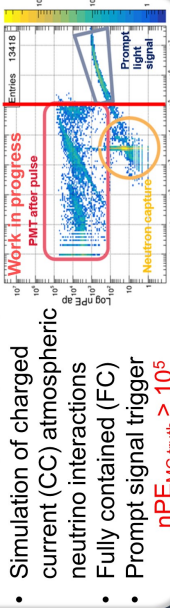


Why atmospheric neutrino reconstruction ?

-> Enhance JUNO sensitivity to neutrino mass ordering (NMO) via combined analysis with reactor anti-neutrinos

See also Poster 231 by Hongyue Duiyang

Atmospheric neutrinos in JUNO: MC simulation



- Simulation of charged current (CC) atmospheric neutrino interactions
- Fully contained (FC)
- Prompt signal trigger
- $nPE_{MC \text{ truth}} > 10^5$

Novel technique: Topological reconstruction (directionality) [1]

Basic idea: Use the PMT detection probability to infer the reconstructed light emission topology

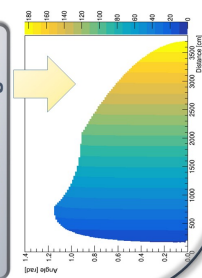
$$\hat{\mathbf{r}}(x) = t_{ref} \pm \frac{|\mathbf{r} - \mathbf{r}_{ref}|}{c_0} + \frac{|\mathbf{r} - \mathbf{r}|}{v_g}$$

ref: point (any point in the track)
[1] H. Rebber et al/2021 JINST16 P01016

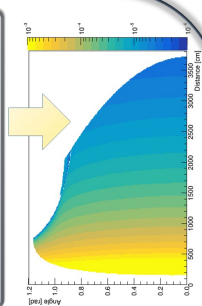
Analytical probability density functions:

Based on the scintillation average wavelength (436 nm)
Removing total reflection and re-emitted light

1. Mean propagation time of direct light:

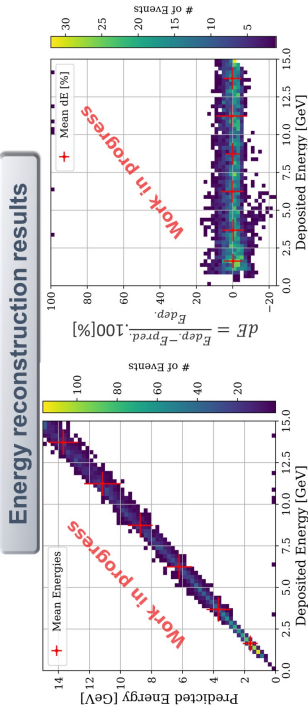
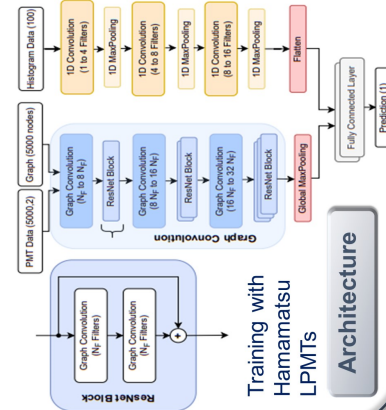


2. Detection probability



Conclusion:
JUNO will have potential to reconstruct energy and direction of atmospheric neutrinos

Neutrino energy reconstruction: Graph Convolutional Neural Network (GCN)



- PMT data: first hit time and total charge in selected trigger windows
- Event selection ensures good linearity between $E_{visible}$ and E_ν
- Energy resolution after bias correction remains $\sim 6\%$

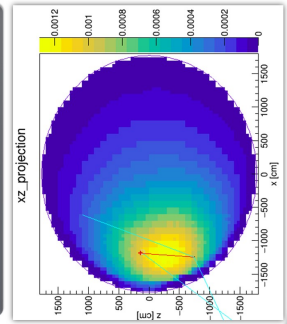
Neutrino direction reconstruction: topological reconstruction

PMT data (17612 LPMTs): charge and hit time per PMT (400 ns event window)

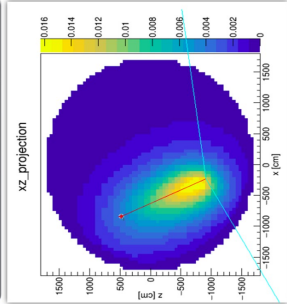
Ref point: MC truth vertex smeared with 25 cm uncertainty + PMT time resolution

Direction reconstruction results: ν_μ atm CC (3 GeV)

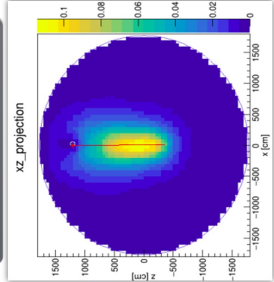
($E_{hadrons}$ non negligible)



($E_{hadrons}$ is negligible)



Muon with E = 3 GeV



Red: primary track (MC truth) /// Blue: neutrinos
Results: 6 iterations with different mesh size

Physics Prospects of The JUNO Experiment

Mariam Rifai on behalf of the JUNO collaboration

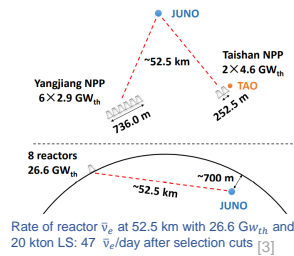
Forschungszentrum Juelich, IKP-2 and RWTH Aachen University, Germany



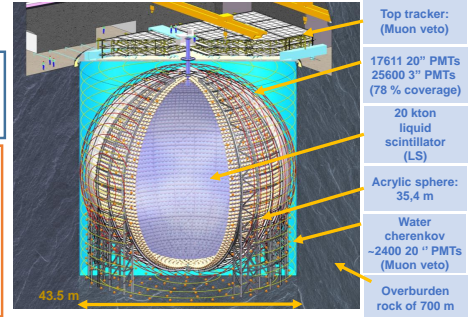
Jiangmen Underground Neutrino Observatory Experiment:

Construction in south China to be completed by the end of 2023.

JUNO is the first multi-kton liquid scintillator (LS) detector ever built.
Main goal: determination of the Neutrino Mass Ordering (NMO) [1,2]



- Excellent energy resolution: $3\%/\sqrt{E(\text{MeV})}$
- 1% energy scale uncertainty, controlled by several calibration sources: $\gamma/\alpha/\beta$, UV-laser, and light pulses sources.
- High photon yield (10^4 photons/MeV)
- Other detectors related to JUNO under construction:
 - The OSIRIS detector: [4]
 - Monitors radiopurity of the liquid scintillator during filling.
 - Satellite detector TAO (Taishan Antineutrino Observatory):
 - 2.8 ton Gd-loaded liquid scintillator detector at ~30 m baseline from the Taishan (1 reactor core).
 - Energy resolution < 2% at 1 MeV.
 - Reference reactor spectrum for JUNO.



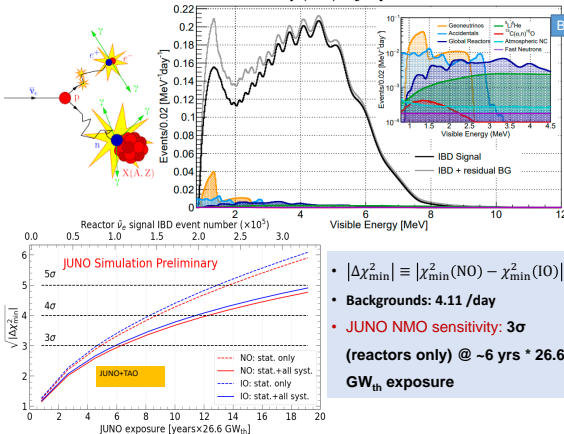
Reactor $\bar{\nu}_e$ oscillations: [1,2]

- Determination of the Neutrino Mass Ordering via vacuum oscillation of reactor $\bar{\nu}_e$: Normal or Inverted Ordering (N/IO)
 - Used only by JUNO and independent of θ_{23} and δ_{cp}

$$P_{\bar{\nu}_e \rightarrow \bar{\nu}_e} = 1 - \cos^4 \theta_{13} \sin^2 2\theta_{12} \sin^2 \frac{\Delta m_{21}^2 L}{4E} - \sin^2 2\theta_{13} \left(\cos^2 \theta_{12} \sin^2 \frac{\Delta m_{21}^2 L}{4E} + \sin^2 \theta_{12} \sin^2 \frac{\Delta m_{31}^2 L}{4E} \right)$$

Solar parameters

Atmospheric parameters
- Complementary to other experiments measuring NMO via matter effects on neutrinos oscillations (DUNE, PINGU ..) [5]
 - NO: $m_3 > m_2 > m_1$
 - IO: $m_3 < m_1 < m_2$
- Detection channel: Inverse Beta Decay (IBD): $\bar{\nu}_e + p \rightarrow e^+ + n$



Geo-neutrinos: [6]

Main goal: understanding the radiogenic heat in the Earth

- Geo-neutrinos from ^{238}U and ^{232}Th decay chains in the Earth: 400/year
- Detected channel: Inverse Beta Decay (IBD)
- JUNO will be sensitive to U/Th ratio
- Ongoing geological study of the local crust

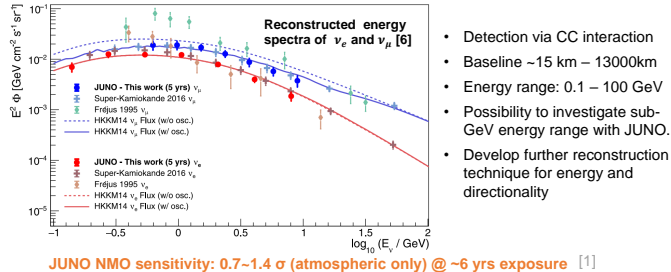
JUNO can reach 17% precision within the first year and 6% after 10 years -> outnumbers the current precision of Borexino and KamLAND

Atmospheric neutrinos: [1,7]

First measurement with liquid scintillator

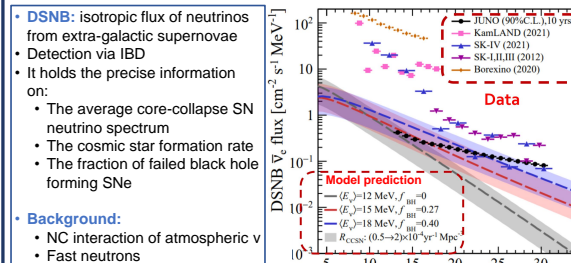
Complementary NMO measurement via matter effects on the oscillation

Applied an unfolding method to extract the energy spectrum: 25% precision after 5 years



Diffuse Supernova Neutrino Background [1]

DSNB discovery potential: 3 σ in 3 years with nominal models



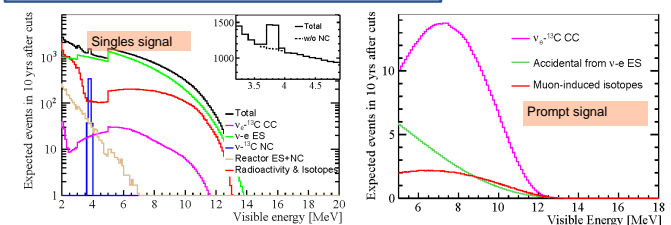
References

- JUNO physics and detector, Progr. Part. Nucl. Phys. 123 (2022) 103927
- Yellow Book, J. Phys. G: Nucl. Part. Phys. 43 (2016) 030401
- Sub-percent Precision Measurement of Neutrino Oscillation Parameters with JUNO, arXiv:2204.13249
- OSIRIS, Eur. Phys. J. C 81 (2021) 973.
- Combined sensitivity to the neutrino mass ordering with JUNO, the IceCube Upgrade, and PINGU, Physical Review D 101 (2020) 032006
- Geo-neutrinos, Chin. Phys. C 40,3 (2016) 033003
- JUNO sensitivity to low energy atmospheric neutrino spectra, Eur. Phys. J. C 81 (2021) 887

^8B solar neutrinos

publication is coming soon!

- Model independent of ^8B neutrino flux measurement via Elastic Scattering (ES), Charge-Current (CC), and Neutral Current (NC)
- ^8B neutrino flux will reach 5% precision in 10 years, $\sin^2 \theta_{12} \sim 9\%$, and $\Delta m_{21}^2 \sim 25\%$ without SNO constraint
- Measuring MSW-transition region
- Detection via CC and NC interaction 13C (0.2 kt 13C)
- Low threshold of 2 MeV for ES



JUNO sensitivity to intermediate energy solar neutrinos

publication is coming soon!

- ^7Be : in 1-2 years time < 2.7% for all radiopurity scenarios
 - ^8B : in 1-2 years time < 17% for most of the radiopurity scenario
 - CNO: constraining pep solar neutrino rate is crucial
 - Independent measurement ^{13}N and ^{15}O and 20% precision without constraint on ^{210}Bi internal background might be feasible for the first time
- JUNO will improve the precision of the existing Borexino measurements



Atmospheric Neutrinos Reconstructions

Mariam Rifai^{1,2} and Rosmarie Wirth³

WP 3

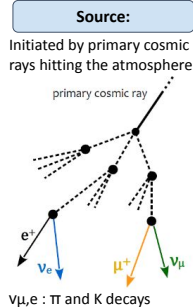
1. Forschungszentrum Jülich GmbH, Nuclear Physics Institute IKP-2, Jülich
2. III. Physikalisches Institut B, RWTH Aachen University, Aachen
3. Institute of Experimental Physics, University of Hamburg, Hamburg

WP 1

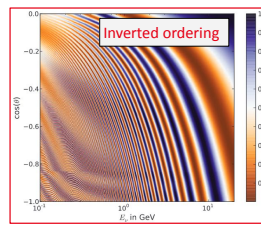
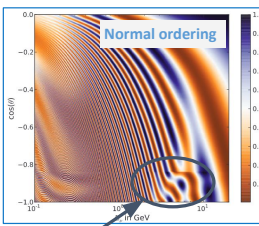
Why Atmospheric Neutrinos in JUNO?

- To enhance JUNO sensitivity to neutrino mass ordering (NMO) via combined analysis with reactor anti-neutrinos.
- To provide the first measurement with a large liquid scintillator detector and in the sub-GeV energy region.
- To measure neutrino oscillation parameters θ_{23} and eventually CP violating phase.
- Accessible from the first year of data taking, with ~15 events/day.

Atmospheric Neutrinos in Nutshell



Oscillations of atmospheric neutrinos: $P_{\nu_\mu \rightarrow \nu_\mu}$ Normal (NO) vs Inverted (IO) ordering



Oscillation probability depends on energy and the zenith angle (direction) of atmospheric neutrinos

Matter effects arise in neutrino oscillations for NO, anti-neutrino for IO -> More details see poster #4
Neutrinos propagate through the Earth and modify the vacuum oscillation pattern

Novel Technique: Topological Reconstruction (Directionality)

Idea: Reconstruct the voxelized probability distribution of optical photon emissions in the detector, based on the charges and times of hits detected per PMT^[1].

Approach - Topological Track Reconstruction: [1] H. Rebber et al 2021 JINST 16 P01016

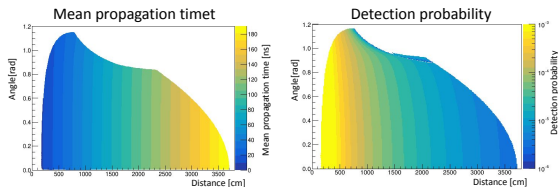
$$\hat{x}(x) = t_{ref} \pm \frac{|\hat{x} - \hat{r}_{ref}|}{c_0} + \frac{|\hat{r}_j - \hat{x}|}{v_g}$$

$t_{particle}$ t_{photon}

- **reference time and vertex:** (t_{ref}, \hat{r}_{ref}) (any position on the track)

- **Analytical probability density functions:**

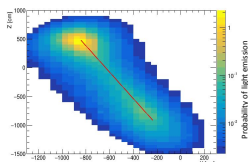
based on the scintillation average wavelength (436 nm) of direct light.



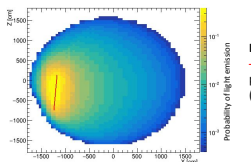
Results:

- Reconstruction of Charged Current interaction of ν_μ in the central detector (CD)
- Using 17612 LPMs
- Considering Monte Carlo time and vertex interaction point in the detector as reference point smeared with 25 cm uncertainty.
- Selecting fully contained atmospheric neutrino events in the CD with $E = 3\text{ GeV}$

Case 1: hadron energy is negligible -> XZ projection



Case 2: hadron energy is non negligible -> XZ projection



Legend:
- neutrino
- primary track (Monte Carlo)

Resulting in promising directional resolution for GeV events

Energy Reconstruction Using Graph Convolution Neural Network (GCN)

Idea: Use convolution on charge detected by PMTs and on detector surface to reconstruct the energy of charged current atmospheric neutrino events.

Graph Convolution:

- Graph consists of nodes and edges
- Nodes represent PMTs of central detector
- Each Node connected to the four closest neighbors in space
- Using 5000 LPMs
- Convolution based on Kipf and Welling[2]

$$h_i^{(l+1)} = \sigma \left(b^{(l)} + \sum_{j \in N(i)} \frac{1}{c_{ij}} h_j^{(l)} W^{(l)} \right)$$

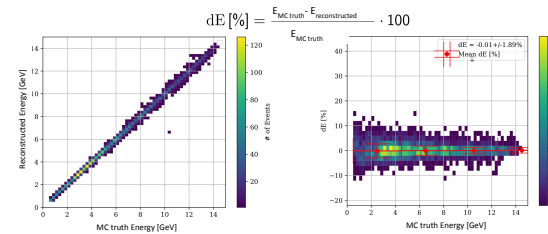
-> Graph represents detector geometry

Architecture:

- Inputs: First hit time, charge per PMT + charge over time distribution
- Charge summed over readout window select
- Graph Convolution with ResNet Blocks
- 1D convolution on Charge over time
- Combination of both convolution outputs
- Fully Connected Layers
- Activation function: SELU [2] Kipf and Welling, arXiv: 1609.02907

Results:

- Reconstruction of the visible energy in NMO range
- Linear bias correction on prediction applied to reduce offset
- Resolution defined as σ of dE distribution



Resulting energy resolution of ~ 2%, after bias correction

Summary and Outlook

- Energy and direction reconstruction for atmospheric neutrinos are feasible in JUNO, thus a sensitivity to NMO as well.
- JUNO sensitivity to NMO expected to be enhanced 1.4σ in 6 years via combined analysis of atmospheric neutrinos with reactor anti-neutrinos (main detection channel in JUNO).
- **Next steps:** Implementing both reconstruction methods in the JUNO official software.
- **Additional ongoing study!**
 - Particle identification of (anti-) neutrinos (ν_μ and ν_e) via machine learning (GCN).
 - Potential of JUNO to measure CP violating phase. (Aachen group)